

Electrochemical Sensors for the Detection and Quantification of Toxic Metal Ions

A thesis submitted for the degree of Doctor of Philosophy

in Physical and Theoretical Chemistry

Alex Lukmanto Suherman

St. John's College

Trinity Term 2019

Abstract

This thesis presents experimental work with the primary aim of developing sensors for the detection and quantification of the toxic metal ions Hg^{2+}, Al^{3+}, Zn^{2+}, and Li^{+} through electrochemical methods. Chapter 1 describes the fundamentals of electrochemistry, including voltammetric and nano-impact methods. Chapter 2 provides information about chemical reagents, instrumentation and experimental procedures used in this thesis. Chapter 3 outlines the development of a sensor for inorganic Hg^{2+} in aqueous solution using silver nanoparticles with galvanic displacement under a suitable applied potential.

Chapter 4 and Chapter 5 demonstrate the utilization of tannic acid (TA) as a capping agent of gold nanoparticles for the sensitive detection of Al^{3+} and Hg^{2+} toward complexation, respectively. Chapter 6 generalizes and extends these chapters, defining the role of the TA capping agent in the redox activity for Hg^{2+} and Zn^{2+} detection by using the nano-impact method. Chapter 7 outlines the electrochemical dissolution of the citrate-capped gold nanoparticle in cyanide-containing solution, where an understanding of the dissolution mechanism is of great importance for the optimization of gold nanoparticle recovery or refinery via oxidative cyanidation. Finally, Chapter 8 outlines the development of an electrochemical sensor for Li^{+} in authentic human saliva at lithium manganese oxide ($LiMn_2O_4$)-modified electrodes. The sensing strategy is based on an initial galvanostatic delithiation of $LiMn_2O_4$ followed by linear stripping voltammetry to detect Li^{+} in the sample.

Overall, the sensing methodology reported in this thesis makes a significant contribution to the application of voltammetric methods for the detection and quantification of toxic metal ions. All sensors reported in this thesis are specifically suitable for routine environmental monitoring, for drinking water and food products quality assessment, or for clinical monitoring and diagnosis applications.

Acknowledgments

I greatly thank my supervisor, Professor Dr. Richard G. Compton, for hosting me into his research group, for giving me full support and for trusting me. Thank you for providing me with such great opportunities and experiences during my time in Oxford.

A very special thanks to my lovely wife Kristiana Yuliyantie and my lovely son Immanuel Arga Suherman who always patiently accept the fact that I am far away from them while studying in Oxford. I am very proud to present this thesis to them, who made all this happen. I am also grateful to my parents (Papa/Mama in Cirebon and Bekasi) and my sisters/brothers (Ka Amina, Ka Maya, Edvan, Robby, Lae Yeremia and Lae Noki). Thank you very much for your endless love, encouragement, and ability to believe in me when I doubt myself.

Thank you for all mentors during my D.Phil, namely Dr. Eden Tanner, Dr. Sabine Kuss, Dr. Giorgia Zampardi, and Dr. Bertold Rasche. Thank you for all your guidance, support and for not giving up! Thank you to all the past and present members of the RGC Group, namely Raphael, Chris CBM, Wallans, Azhar Abbas, Enno Kätelhön, Hatem, Lifu, Yuki, Korbua, Danlei, Collin, Jake, Ryan, Yuanzhe, Grace, Annie, Mengjiang, and Rachel**.** Thank you also to the staff at the Department of Chemistry (Paul Mitchell, Philip Hurst, and Leigh Bennet) for supporting my research here is become easier.

I gratefully acknowledge the financial support from the Indonesia government through Indonesian Endowment Fund for Education (LPDP) scholarships. I am also thankful to St. John's College for providing me accommodations, academic grants, and part-time jobs. Finally, thank you to all the peoples of this lovely university and Oxford!

Contents

Abstract i

Acknowledgments ii

Contents iii

Glossary vii

Publications xi

Chapter 1. Introduction to Electrochemistry 1

1.1. Electrochemical Equilibrium 1

1.2. Electrode Kinetics 3

1.3. Mass Transport 5

1.3.1. Diffusion 5

1.3.2. Convection 8

1.3.3. Migration 9

1.4. Faradaic and Non-Faradaic Processes 9

1.5. Electrochemical Cell 12

1.6. Electrochemical Methods 16

1.6.1. Cyclic Voltammetry (CV) 18

1.6.2. Linear Sweep Voltammetry (LSV) 21

1.6.3. Square Wave Voltammetry (SWV) 23

1.6.4. Chronoamperometry 26

1.6.5. Nano-impacts 27

Bibliography 31

Chapter 2. Experimental 36

2.1. Chemical Reagents 36

2.2. Electrochemical Instrumentations 39

2.3. Non-electrochemical Instrumentation 41

Bibliography 47

Chapter 3. A Sensor for Inorganic Hg^{2+} in Aqueous Solution Using Galvanic Displacement 49

3.1. Introduction 50

3.2. Experimental 51

3.3. Results and Discussion 53

3.4. Conclusions 65

Bibliography 66

Chapter 4. Electrochemical Sensor for Al^{3+} Using Tannic Acid-capped Gold Nanoparticles 70

4.1. Introduction 71

4.2. Experimental 73

4.3. Results and Discussion 74

4.4. Conclusions 88

Bibliography 89

Chapter 5. Tannic Acid-capped Gold Nanoparticle-Modified Screen-printed Electrode: an Electrochemical Sensor of Hg^{2+} for Real-World Samples 93

5.1. Introduction 94

5.2. Experimental 96

5.3. Results and Discussion 97

5.4. Conclusions 110

Bibliography 111

Chapter 6. Tannic Acid-Capped Gold Nanoparticles: Capping Agent Chemistry Controls the Redox Activity 114

6.1. Introduction 115

6.2. Experimental 117

6.3. Results and Discussion 119

6.4. Conclusions 134

Bibliography 135

Chapter 7. Understanding Gold Nanoparticle Dissolution in Cyanide-Containing Solution via the Nano-impacts Method 138

7.1. Introduction 139

7.2. Experimental 141

7.3. Results and Discussion 141

7.4. Conclusions 156

Bibliography 157

Chapter 8. A Sensor for the Detection and Quantification of Li^+ in Authentic Human Saliva 162

8.1. Introduction 163

8.2. Experimental 166

8.3. Results and Discussion 170

8.4. Conclusions 189

Bibliography 189

Chapter 9. Overall Conclusions 193

Appendix A. Calculation Details 195

Appendix B. Characterisation of the Materials 207

Appendix C. Nano-impacts Analysis 210

Glossary

Roman Symbols

Symbol	Meaning	Units
a_A	The Activity of the Oxidized Species	mol dm^{-3}
a_B	The Activity of the Reduced Species	mol dm^{-3}
A_e	Area of Electrode	cm^2
A_{NP}	Surface Area of a Nanoparticle	m^2
A_{TA}	Surface Area of a Tannic Acid Molecule	m^2
C	Concentration of a Species	mol dm^{-3}
C_d	Double Layer Capacitance	F m^{-2}
D	Diffusion Coefficient	cm^2 s^{-1}
E	Electrode Potential	V
E^0	Standard Electrode Potential	V
E_1	Start Potential	V
E_2	End Potential	V
E_f^0	Formal Potential	V
f	Frequency	Hz
F	Faraday Constant, 96,485	C mol^{-1}
I	Current	A
I_0	Initial Current	A
I_p	Peak Current	A
I_{ox}	Oxidation Current	A
I_{re}	Reduction Current	A
I_c	Capacitative Current	A
I_{ss}	Steady-State Current	A
IR	Ohmic Drop	V
J	Flux	mol cm^{-2} s^{-1}
k_0	Standard Electrochemical Rate Constant	cm s^{-1}
k_{ox}	Rate Constant for the Oxidation Reaction	cm s^{-1}

k_{red}	Rate Constant for the Reduction Reaction	cm s^{-1}
$Log\,\beta$	Stability Constants of Complexes	
$[A]_0$	The Concentration of Species A at the Electrode Surface	mol cm^{-3}
$[B]_0$	The Concentration of Species B at the Electrode Surface	mol cm^{-3}
m_T	Mass Transport Coefficient	m s^{-1}
N_A	Avogadro Constant, 6.022 x 10^{23}	mol^{-1}
N_{NP}	Number of Nanoparticles on Electrode Surface	Dimensionless
n	Number of Electrons Transferred	Dimensionless
n'	Number of Electrons Before Rate Determining Step	Dimensionless
Q	Charge	C
R	Universal Gas Constant, 8.314	J K^{-1} mol^{-1}
r_e	The Radius of an Electrode	m
r_P	The Radius of a Nanoparticle	m
T	Temperature	K
t	Time	s
v	Scan Rate	V s^{-1}
V_{NP}	The volume of a Single Nanoparticle	m^3
z	Number of Electrons Transferred (Faraday 1st Law)	Dimensionless

Greek Symbols

Symbol	Meaning	Units
α	Reductive Transfer Coefficient	Dimensionless
β	Oxidative Transfer Coefficient	Dimensionless
δ	Diffusional Layer Thickness	m
φ_{RE}	Electrostatic Potential at Reference Electrode	V
φ_S	Electrostatic Potential at Solution Phase	V
φ_{WE}	Electrostatic Potential at Working Electrode	V
Γ	Electrode Surface Coverage	mol cm^{-2}

γ_A	Activity Coefficient of Species A	Dimensionless
γ_B	Activity Coefficient of Species B	Dimensionless
η	Overpotential ($E - E^0_f$)	V
ρ	Density	gm^{-3}
Λ	The Matsuda and Ayabe Parameter	
∇	Vector Operator in Cartesian Space	Dimensionless

Abbreviations

Symbol	Meaning
AdSV	Adsorptive Stripping Voltammetry
AgNPs	Silver Nanoparticles
ASV	Anodic Stripping Voltammetry
AuNPs@CA	Citrate-capped Gold Nanoparticles
AuNPs@TA	Tannic Acid-capped Gold Nanoparticles
ca.	Circa (about, roughly, or approximately)
CE	Counter Electrode
CSV	Cathodic Stripping Voltammetry
CV	Cyclic Voltammetry
DLS	Dynamic Light Scattering
GCE	Glassy Carbon Electrode
GCD	Glassy Carbon Disc
IHP	Inner Helmholtz Plane
LMO	Lithium Manganese Oxide
LMO-GCE	Lithium Manganese Oxide-Modified Glassy Carbon Electrode
LMO-SPE	Lithium Manganese Oxide-Modified Screen-Printed Electrode

LSV	Linear Sweep Voltammetry
MSE	Mercury/Mercurous Sulphate Electrode
NTA	Nanoparticle Tracking Analysis
OHP	Outer Helmholtz Plane
PXRD	Powder X-Ray Diffraction
RE	Reference Electrode
RSD	Relative Standard Deviation
SCE	Saturated Calomel Electrode
SHE	Standard Hydrogen Electrode
SPE	Screen-Printed Electrode
SEM	Scanning Electron Microscopy
SWV	Square Wave Voltammetry
TA	Tannic Acid
TEM	Transmission Electron Microscopy
UPD	Underpotential Deposition
UV-Vis	Ultra-violet Visible
WE	Working Electrode

Publications

This thesis is organized on the basis of seven publications that listed in chronological order as follows:

(1) Suherman, A. L.; Ngamchuea, K.; Tanner, E. E. L.; Sokolov, S. V; Holter, J.; Young, N. P.; Compton, R. G. Electrochemical Detection of Ultratrace (Picomolar) Levels of Hg^{2+} Using a Silver Nanoparticle-Modified Glassy Carbon Electrode. *Anal. Chem.* 2017, *89* (13), 7166–7173.

(2) Suherman, A. L.; Tanner, E. E. L.; Compton, R. G. Recent Developments in Inorganic Hg^{2+} Detection by Voltammetry. *TrAC Trends Anal. Chem.* 2017, *94*, 161–172.

(3) Suherman, A. L.; Tanner, E. E. L.; Kuss, S.; Sokolov, S. V; Holter, J.; Young, N. P.; Compton, R. G. Voltammetric Determination of Aluminium(III) at Tannic Acid Capped-Gold Nanoparticle Modified Electrodes. *Sensors Actuators B Chem.* 2018, *265*, 682–690.

(4) Suherman, A. L.; Kuss, S.; Tanner, E. E. L.; Young, N. P.; Compton, R. G. Electrochemical Hg^{2+} Detection at Tannic Acid-Gold Nanoparticle Modified Electrodes by Square Wave Voltammetry. *Analyst* 2018, *143* (9), 2035–2041.

(5) Suherman, A. L.; Zampardi, G.; Kuss, S.; Tanner, E. E. L.; Amin, H. M. A.; Young, N. P.; Compton, R. G. Understanding Gold Nanoparticle Dissolution in Cyanide-Containing Solution via Impact-Chemistry. *Phys. Chem. Chem. Phys.* 2018, *20* (44), 28300–28307.

(6) Suherman, A. L.; Zampardi, G.; Amin, H. M. A.; Young, N. P.; Compton, R. G. Tannic Acid Capped Gold Nanoparticles: Capping Agent Chemistry Controls the Redox Activity. *Phys. Chem. Chem. Phys.* 2019, *21* (8), 4444–4451.

(7) Suherman, A. L.; Rasche, B.; Godlewska, B.; Nicholas, P.; Herlihy, S.; Caiger, N.; Cowen, P. J.; Compton, R. G. Electrochemical Detection and Quantification of Li^{+} in Authentic Human Saliva Using $LiMn_2O_4$-Modified Electrodes. *ACS Sens.* 2019, 4, 2497-2506.

Chapter 1

Introduction to Electrochemistry

This thesis is concerned with the use of electrochemistry for the detection and quantification of toxic metal ions. This chapter outline some basic concepts and insights into electrochemical processes, underpinning the work presented in this thesis. Electrochemical equilibrium, electrode kinetics, mass transport, Faradaic and non-Faradaic processes, and the electrochemical cell configuration are presented first. Following this, several electrochemical methods, including the nano-impacts method, employed in this thesis are discussed. A fuller discussion appears in the later chapters.

1.1. Electrochemical Equilibrium

Electrochemistry studies the interaction of electrical and chemical effects at an electrode-solution interface.[1] Consider the following electrochemical equilibrium,

$$\text{A (aq)} + e^- \rightleftharpoons \text{B (aq)} \tag{1.1}$$

where *A* is the oxidized species in a bulk solution, which gains an electron from the electrode to form *B*, the reduced species. The electrode potential is influenced by the concentration of *A* and *B*. To define the equilibrium potential of these two electroactive species (redox couple, *A* and *B*), the Nernst equation[1,2] relates the potential and activities of species *A* and *B*,

$$E = E^0 + \frac{RT}{F} ln \frac{a_A}{a_B} \tag{1.2}$$

where E is the potential, E^0 is the standard electrode potential (measured with respect to the standard hydrogen electrode at standard conditions of 1 atm, 298 K), R is the universal gas constant (8.314 J K^{-1} mol^{-1}), T is the absolute temperature (unit in Kelvin), F is the Faraday constant (96485 C mol^{-1}) and a_A and a_B represent the activities of the oxidized and reduced species respectively. The activities for species A and B can be expressed in respect to their concentration[1,2], C_A and C_B, by

$$a_A = \gamma_A C_A \tag{1.3}$$

$$a_B = \gamma_B C_B$$

where γ_A and γ_B are the activity coefficients of species A and B, respectively. The activities of species are not measurable experimentally since activity coefficients are often unknown.[2] Therefore, equation 1.2 can alternatively be written in terms of concentrations as follows[1,2]:

$$E = E_f^0 + \frac{RT}{F} ln\frac{C_A}{C_B} \tag{1.4}$$

where E_f^0 is the formal potential that reflects the composition of the solution under study (pressure, temperature and other electrolytes present). The formal potential with respect to the standard potential, E^0, and activity coefficient, γ, can be expressed as follows[1,2]:

$$E_f^0 = E^0 + \frac{RT}{F} ln\frac{\gamma_A}{\gamma_B} \tag{1.5}$$

Note that the Nernst equation is only applicable to a system at a dynamic equilibrium (no current flows through the system). However, most of the electrochemical experiments, in reality, are performed under non-equilibrium conditions. This will be described further in the following sections.

1.2. Electrode Kinetics

This section deals with the rate of electron transfer at the electrode-solution interface. To discuss this, the following reaction is considered,

$$A\ (aq) + e^- \underset{k_{ox}}{\overset{k_{red}}{\rightleftarrows}} B\ (aq) \tag{1.6}$$

where k_{red} and k_{ox} represent the rate constants for reduction and oxidation respectively for a heterogeneous electron transfer. Note that reaction 1.6 differs from reaction 1.1 by the use of arrow instead of the harpoon, indicating the absence of equilibrium. The electron transfers result in the passage of a Faradaic current, I, through the electrode, which can be expressed by the equation[2],

$$I = I_{re} + I_{ox} = FA_eJ \tag{1.7}$$

$$J = J_{re} + J_{ox} = k_{re}[A]_0 - k_{ox}[B]_0 \tag{1.8}$$

where A_e is the electrode area (cm^2), J is the heterogeneous reaction flux at the electrode-solution interface (mol cm^{-2} s^{-1}), k_{re} and k_{ox} are the electron transfer rate constants (cm s^{-1}) for the reduction and the oxidation, respectively. $[A]_0$ and $[B]_0$ are the surface concentrations (mol cm^{-3}) of oxidized and reduced species, respectively. The surface concentrations are usually different from their bulk concentrations since electrolysis locally depletes or builds up material near the interface. The rate constants k_{re} and k_{ox} can be defined as[1,2]

$$k_{red} = k_0\ exp\left[\frac{-\alpha F\eta}{RT}\right] \tag{1.9}$$

$$k_{ox} = k_0\ exp\left[\frac{\beta F\eta}{RT}\right] \tag{1.10}$$

where k_0 is the standard electrochemical rate constant (cm s^{-1}), α and β are the reductive and oxidative transfer coefficients respectively (ranging from zero to 1 in the case of one-electron transfer, with $\alpha + \beta = 1$). If α value is close to zero, the transition

state is reactant-like (oxidative) and if α value is close to 1, the transition state is product-like (reductive). However, the α value is usually close to 0.5 indicating the transition state has intermediate behavior.[1] The overpotential, η, is the potential applied, E, relative to the formal potential, E_f^0, defined as[1,2]

$$\eta = (E - E_f^0) \tag{1.11}$$

The rate of reaction is strongly dependent on the η value and the rate constant of k_{re} and k_{ox}, where the overpotential is the driving force required for the oxidation or reduction reaction to occur. Therefore, the net current, I, can be expressed by the Butler-Volmer equation,[1]

$$I = FA_e k_0 \left[[A]_0 exp\left(\frac{-\alpha F\eta}{RT}\right) - [B]_0 exp\left(\frac{\beta F\eta}{RT}\right)\right] \tag{1.12}$$

where A_e is the area of the electrode (cm^2), k_0 is the standard electrochemical rate constant and $[A]_0$ and $[B]_0$ are the surface concentration (mol cm^{-3}) of species A and B at the electrode surface, respectively. This equation explains how the observed current varies as a function of the transfer coefficient (α and β) and overpotential (η).

Following this Butler-Volmer equation, the Tafel law can be derived. When the reduction process in the reaction 1.6 is sufficiently fast that the oxidation becomes negligible, the flux can be expressed as[2]

$$J_{re} = k_0[A]_0 exp\left(\frac{-\alpha F\eta}{RT}\right) \tag{1.13}$$

Meanwhile, when the oxidation is sufficiently fast relative to the reduction, the flux can be expressed as[2]

$$J_{ox} = k_0[B]_0 exp\left(\frac{\beta F\eta}{RT}\right) \tag{1.14}$$

Assuming $[A]_0$ and $[B]_0$ are not greatly changed from their constant bulk values, the above equations can be rearranged as[2]

$$ln\,|I_{re}| = \frac{-\alpha FE}{RT} + \text{constant} \quad (1.15)$$

$$ln\,|I_{ox}| = \frac{\beta FE}{RT} + \text{constant}$$

where I_{re} and I_{ox} are the reduction and oxidation currents, respectively. Meanwhile, plots of $ln\,|I_{ox}|$ vs E or $ln\,|I_{re}|$ vs E, named Tafel plots, which can be used to determine the value of transfer coefficients α and β.[1,2]

$$\frac{\partial\, ln|I_{re}|}{\partial E} = \frac{-\alpha F}{RT} \quad (1.16)$$

$$\frac{\partial\, ln|I_{ox}|}{\partial E} = \frac{\beta F}{RT}$$

1.3. Mass Transport

In an electrochemical reaction, the reaction kinetics may not only be controlled by the rate of electron transfer, but also by the rate of mass transport.[2] Mass transport is the movement of a species in solution, either diffusively due to random molecular motion or resulting from an applied external stimulus, such as a mechanical force, a concentration gradient or an electric field.[1,2] In this section, three main modes of mass transport, namely diffusion, convection, and migration are discussed.[1,3]

1.3.1. Diffusion

Diffusion is the spontaneous movement of species in solution as a result of a change in concentration gradient to maximize entropy.[1] Diffusion allows species from the bulk solution to be renewed at the electrode surface. The rate of this process, in the case of linear diffusion to a planar electrode surface (one dimension), is modeled mathematically by Fick's first law[1,2],

$$J = -D \frac{\partial C}{\partial x} \tag{1.17}$$

where J is the flux (moles cm^{-2} s^{-1}), $\frac{\partial C}{\partial x}$ is the concentration gradient at point x and D is the diffusion coefficient (cm^2 s^{-1}). The diffusion coefficient determines how fast a species move across the solution and the negative sign involved in Fick's first law accounts for the species is moving from an area of higher concentration to lower concentration.

For the diffusive flux in three dimensions (x, y, z), Fick's first law becomes

$$J = -D \nabla C \tag{1.18}$$

where ∇ is a vector operator in a three-dimensional Cartesian space[2],

$$\nabla = i\frac{\partial}{\partial x} + j\frac{\partial}{\partial y} + k\frac{\partial}{\partial z} \tag{1.19}$$

where i, j and k are the unit vector along the x, y, and z-axis, respectively[2].

To express the flux in terms of measured current, I, in respect to the number of moles passing through a unit area in a unit time, is expressed by[2]

$$J = \frac{I}{nFA_e} \tag{1.20}$$

where n is the number of electrons transferred in the reaction $A + ne^- \rightleftharpoons B$, F is the Faraday constant (96485 C mol^{-1}) and A_e is the area of the electrode. In the case of diffusion only conditions, Fick's second law[1,2] describes the rate of species concentration change in solution over time in one dimension, by the equation as

$$\frac{\partial C}{\partial t} = D \frac{\partial^2 C}{\partial x^2} \tag{1.21}$$

Meanwhile, in three dimensions (x, y, z), Fick's second law becomes

$$\frac{\partial C}{\partial t} = D \nabla^2 C \tag{1.22}$$

$$\text{where } \nabla^2 = \frac{\partial}{\partial x^2} + \frac{\partial}{\partial y^2} + \frac{\partial}{\partial z^2} \tag{1.23}$$

There are two types of diffusion to an electrode surface, linear and convergent. These two limiting cases are determined by comparing the size of the electrode radius, r, and the diffusion layer, δ. The latter describes the thickness of the depletion region near the electrode surface through which electroactive material diffuses to reach the electrode surface. The diffusion layer[1,2] is a result of a charge transfer reaction and a function of time given by the following equation,

$$\delta = \sqrt{6Dt} \tag{1.24}$$

where t is the experimental time. Linear diffusion dominates if $\delta << r$. Linear diffusion takes in experiments at short experimental durations and/or using a macroelectrode (with dimensions of millimeters or more).[1] Convergent diffusion occurs when $\delta >> r$, which takes place at longer experimental times or at microelectrodes (with a dimension of micrometres).[1] These two limits are schematically shown in Figure 1.1.

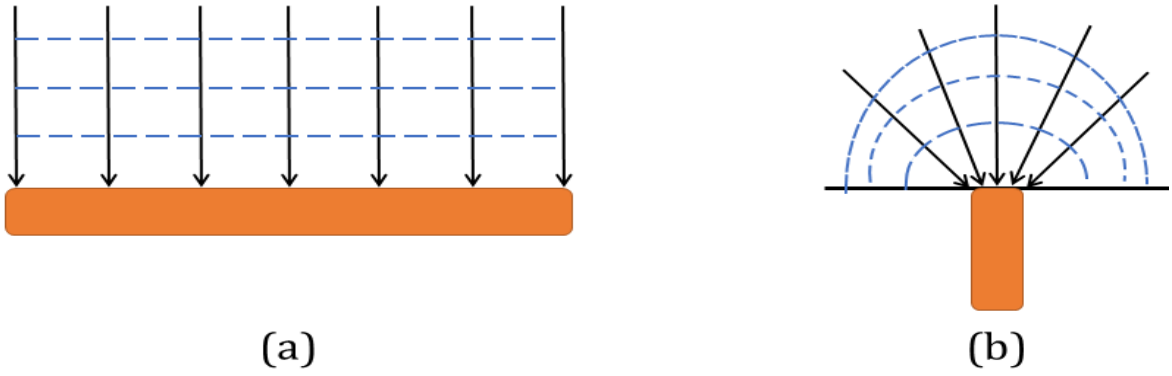


Figure 1.1. Diffusion to an electrode. (a) Linear diffusion at macroelectrode and (b) convergent diffusion at microelectrode (disc). Blue dashed lines are the diffusion layers.

At macroelectrodes (Figure 1.1a) the diffusion layers are normal to the electrode surface and when electrolysis proceeds the thickness of the diffusion layers becomes progressively larger. Meanwhile, at microelectrodes during the experimental

time scale, hemispherical diffusion layers are developed and therefore electroactive species are drawn towards the electrode surface from all directions (Figure 1.1b). The convergent diffusion is more efficient than linear diffusion. The former results in steady-state conditions over shorter time scales. The steady-state current, I_{ss}, at a microelectrode is given by equation[2]

$$I_{ss} = 4nFCDr_e \tag{1.25}$$

where n is the number of electrons transferred, C is the concentration of electroactive species, D is the diffusion coefficient and r_e is the radius of the microelectrode (disc).

1.3.2. Convection

Convection is the movement of species in solution due to external (mechanical) forces. There are two types of convection namely natural convection and forced convection.[1] Natural convection can occur either from random vibrations in the laboratory, density and thermal gradients in the bulk solution due to a chemical change at the electrode surface when a potential is applied. Natural convection is usually unpredictable and undesirable, which can cause experimental irreproducibility. To minimize natural convection effects, the electrochemical cell can be kept under thermostatted to minimize the differences in temperature and to distribute any heat formed at the electrodes due to electrolysis.

Forced convection can arise from actions such as solution stirring, sonication, agitation and forcing an inert gas to bubble through the solution in order to deliver fresh electroactive species to the electrode surface at a known rate. Forced convection is often designed to be part of the experiment so as to control the mass transport in the system (controlled convective mass transport), which can, for example, be achieved using rotating disc electrodes[4,5], the sonoelectrochemistry technique[6] or channel

electrode voltammetry (by flow of a solution over a stationary electrode in a channel)[7,8]. In summary, forced convection keeps the diffusion layer to a minimum and improves the mass transport rate as the diffusion layer since compressed.[1]

1.3.3. Migration

Migration is the movement of a charged species under the influence of an electric field. The potential drop across the electrode-solution interface generates an electrical field which leads to the migration of charged species. Generally, this condition becomes a problem during the experiment as the movement of charged species is not easily predictable. To overcome this, a chemically and electrochemically inert electrolyte is added to the bulk solution at high concentrations (usually at 0.1 M or above)[1] to suppress any migration effects. The large quantity of electrolyte increases the conductivity of the solution and thus decreases the resistivity for the passing current. In addition, adding supporting electrolyte decreases the potential drop at the electrode-solution interface and maintains a constant ionic strength in the solution during electrolysis. Adding supporting electrolyte also fixes the activity coefficients in order to facilitate the use of formal potentials and it compresses the diffusion layer to a distance that is compatible with electron tunneling (approximately 10-20 Å)[1,2], which is how electrons transfer between the electrode and solution phase species. If the full potential drop is not confined to this distance then some driving force for the transfer is lost.

1.4. Faradaic and Non-Faradaic Processes

There are two types of processes that might occur at the electrode-solution interface, namely Faradaic and non-Faradaic. When electrons are transferred across

the electrode-solution interface during the electrolysis of the electroactive species, this process is Faradaic. This is expressed by Faraday's law of electrolysis,[2]

$$n = \frac{Q}{zF} \tag{1.26}$$

where n is moles of species formed or consumed reactant, Q is the total electric charge passed (C), z is the number of electrons passed per ion and F is the Faraday constant (96485 C mol^{-1}). A number of processes can influence the observed Faradaic current response for a simple reaction, most importantly the mass transport (see Section 1.3) of reactants and products to and from the electrode surface respectively and the rate of electron transfer across the electrode-solution interface. Faraday's law assumes that the flow of electrons via the external circuit results entirely from the Faradaic process. However, in fact, not all the observed current passed at the electrode-solution interface is purely Faradaic. Non-Faradaic processes can also contribute.

Non-Faradaic processes do not involve electrochemical reactions or charge transfers at the electrode-solution interface, as they occur due to the charging and discharging of the double-layer capacitance. Non-Faradaic currents can result from adsorption and desorption at the electrode surface as well as changes in the solution composition at the interface when the potential of the electrode is changed.[1,2]

The electrical double layer charging occurs where an array of different ions and solution dipoles adjacent to the charged electrode surface reorganizes when a potential is applied.[2] A number of models have been developed to describe the structure of the double layer with the simplest one being proposed by Helmholtz. As shown in Figure 1.1., in the first region closest to the electrode there are ions and solvent molecules that are specifically adsorbed onto the electrode surface. The distance, *x1*, from the electrical centers of these molecules to the electrode surface is referred to as the Inner

Helmholtz Plane (IHP). If the potential applied at the electrode is more positive than the bulk solution, anions and solvent molecules will adsorb onto the electrode surface at the IHP. The next layer is referred to as the Outer Helmholtz Plane (OHP), this is the closest distance, *x2*, to which solvated ions can approach the electrode surface, which is attracted electrostatically or non-specifically adsorbed to the electrode surface. The extent of the double layer from the electrode surface varies with potential and electrolyte concentration. The double-layer compresses with increasing supporting electrolyte concentrations. The potential decreases approximately linearly with distance from the electrode surface to the OHP then decreases approximately exponentially from the OHP to the bulk solution.

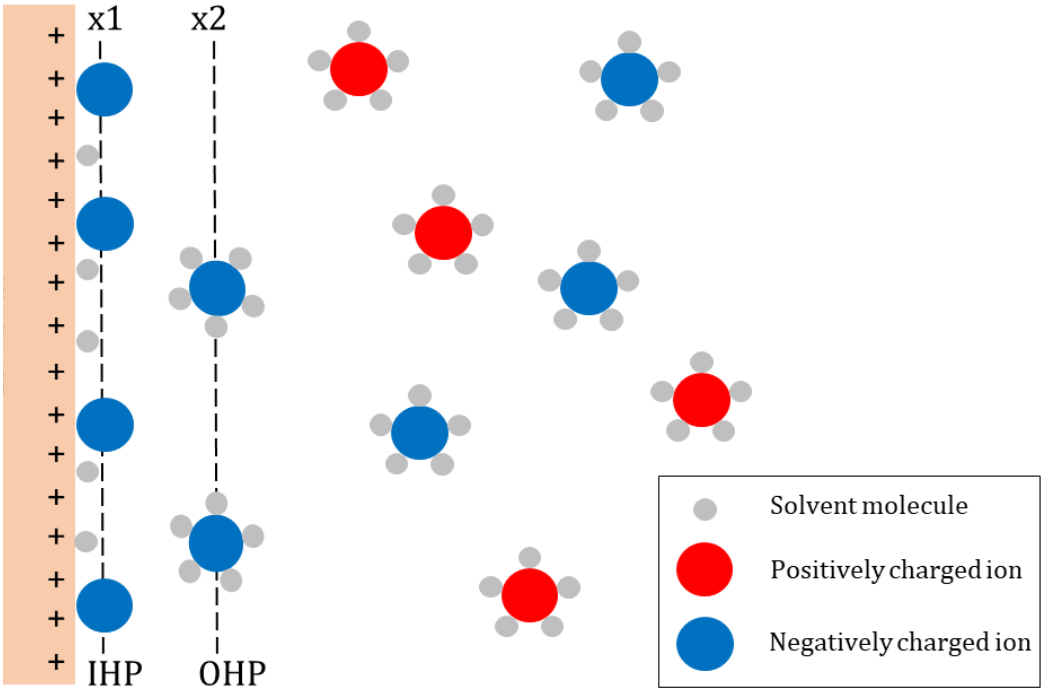


Figure 1.1. Schematic representation of the electrical double layer according to Helmholtz.

The Helmholtz model was later improved by Gouy and Chapman before being further developed by Stern and Grahame. Gouy and Chapman suggested a new model of the double-layer structure taking into account a continuous distribution of

electrolyte solution (the diffuse layer), which is simultaneously subject to random thermal motion and electrostatic interaction with the electrode surface charge. Finally, Stern developed a new double-layer structure model with both a compact layer and a diffuse layer where the former includes solvent molecules and strongly adsorbed ions. The boundary between the compact layer and the diffuse layer corresponds to the Outer Helmholtz Plane (OHP).

1.5. Electrochemical Cell

To observe an electrochemical reaction under the influence of electrode kinetics and/or mass transport, an electrochemical cell containing electrodes must be set-up such that a closed circuit is established. It is impossible to pass a current or apply a potential difference using a single electrode. The simplest electrochemical cell includes a working electrode (WE) and a reference electrode (RE) to complete a circuit. The potential is applied to the WE relative to the RE so that the potential at the RE is constant and provided no current is passed through it. The applied potential[1,2], E, is

$$E = (\phi_{WE} - \phi_s) - (\phi_{RE} - \phi_s) + IR \qquad (1.27)$$

where ϕ_{WE}, ϕ_{RE} and ϕ_s refer to the electrical potentials (V) of the working electrode, the reference electrode, and the solution phase, respectively, and IR is the ohmic drop due to the current passed through the bulk solution. IR value reflects the unknown and undesirable electrical resistance, R, of the bulk solution phase (see Section 1.3). It is essential to maintain a known value of $(\phi_{WE} - \phi_s)$ since this is the driving force for the electron transfer.

For experiments involving electrodes of large surface areas, large currents are passed through the electrode-solution interface. The ohmic drop in the solutions is no longer negligible and varies with time. Furthermore, the potential difference at the RE

is not constant since the large current can change the surface and the chemical composition of the RE. Therefore, the applied potential in a two-electrode system does not allow control of that applied at the WE-solution interface, $(\phi_{WE} - \phi_s)$. To overcome this problem, a third electrode, a counter electrode (CE), is introduced. In this situation, the current is only passed through the WE and the CE but no current passed through the RE, so the value of *IR* falls to zero whilst $(\phi_{RE} - \phi_s)$ is maintained at a constant value. A three-electrode system (Figure 1.2a) is commonly applied with macroelectrodes, whereas a two-electrode system can sometimes be employed with a microelectrode, but not with a macroelectrode since microelectrode currents are much smaller with a corresponding minimal input on *IR* and $(\phi_{RE} - \phi_s)$. Although a microelectrode is used in Chapters 6 and 7, a three-electrode configuration is employed for all systems studied in this thesis to minimize potential shifts from the ohmic drop.

In this thesis, screen-printed electrodes (SPEs, Figure 1.2b) were employed in Chapter 5 and Chapter 8. SPEs have a three-electrode configuration as with the conventional three-electrode configuration (Figure 1.2a). SPEs can be customized with various surface modifier agents, such as polymers[9], Prussian Blue[10], gold nanoparticles[11,12,13] or silver nanoparticles[14,15], or carbon[16,17] with various low-cost printing substrates such as plastic, paper or ceramic-based materials.[18,19] For example in Chapter 8, the lithium manganese oxide (LMO)-modified screen-printed electrode is used to determine lithium ions in authentic human saliva samples. This SPE comprised of three-electrode configuration with carbon/LMO as WE, carbon black/graphite as CE and *quasi* silver-silver chloride electrode as RE. The latter was formed using a 60:40 weight ratio of silver to silver chloride, stabilized by natural chloride content found in the analyte. Recent advances in voltammetry using SPEs have provided a simple sensing platform for the in situ monitoring of toxic metal ions.[20,21]

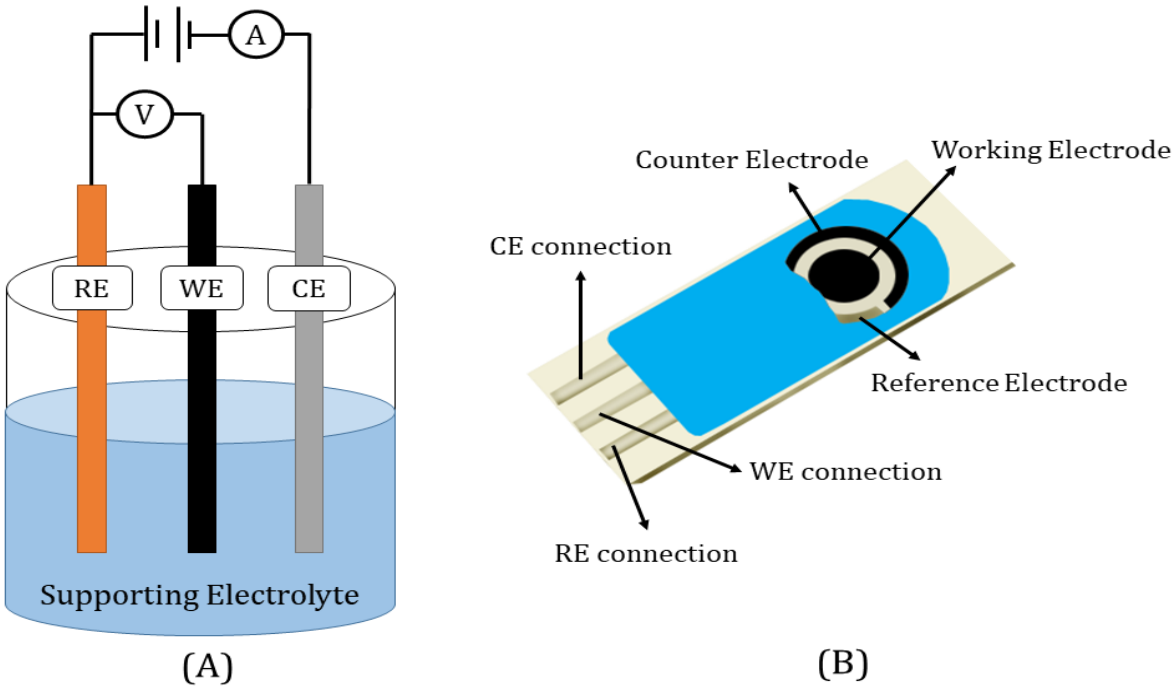


Figure 1.2. Schematic for a three-electrode setup, comprised of working (WE), reference (RE), and counter (CE) electrodes. (a) Electrochemical cell with all electrodes immersed in analyte-containing supporting electrolyte, (b) screen-printed electrode (SPE) with the analyte deposited onto SPE surface, covering all three electrodes.

The solution in the conventional electrochemical cell must be sufficiently ionic to allow the passage of the charged species of interest to the electrode-solution interface. To avoid the effects of solution resistance, mass transport limitations, large double-layer capacitance, and inconsistent ionic strength, a supporting electrolyte is often added to the analyte. The supporting electrolytes must be selected for their chemical and electrochemical inertness at the potentials of interest in the experiments and should not have reactions with both the electrode surface and the analyte. Supporting electrolytes such as inorganic salts, mineral acids or a buffer can be used, typically with concentrations of 0.1 M or greater.[1,2]

The reaction of interest occurs at the interface of the working electrode and the solution phase. In general, working electrodes are made of inert materials such as gold, glassy carbon or platinum to avoid interference with the reaction of interest.[2,22]

The function of the counter electrode is to pass the same current seen flowing through the working electrode. The counter electrode, often a carbon/graphite rod, a platinum wire/mesh or a gold foil, is important as it should be inert against the target of interest and sufficiently large enough to pass the required currents. With a counter electrode in the circuit, no current needs to flow through the reference electrode and a stable reference potential can be maintained.

The reference electrode is important in an electrochemical system as its purpose is to provide a stable and accurate reference potential value against the measurement of the working electrode. The standard hydrogen electrode (SHE) is the primary reference[2] the potential of which is zero (by convention). However, SHE is not ideal for regular experimental practice due to the difficulty of handling hydrogen gas. Currently, a range of alternative reference electrodes is available. A saturated calomel reference electrode (SCE) is comprised of a sealed tube containing a saturated KCl solution with solid KCl to maintain a stable potential of +0.242 V vs SHE at 25 ^{o}C. The solution is in contact with the mercurous chloride mixed with liquid mercury. The potential determining equilibrium of the SCE is $\frac{1}{2}Hg_2Cl_2$ (s) + e^- $\rightleftharpoons$ Hg (l) + Cl^- (aq). A mercury/mercurous sulfate electrode (MSE) is comprised of a sealed tube containing a saturated K_2SO_4 solution to maintain a stable potential of +0.62 V vs SHE at 25 ^{o}C. The potential determining equilibrium of MSE is Hg_2SO_4 (s) + $2e^-$ $\rightleftharpoons$ 2Hg (l) + SO_4^{2-} (aq). Quasi silver-reference electrodes are built into many screen-printed electrodes (SPEs, Figure 1.2b). The potential equilibrium is not well-defined against the SHE due to its sensitive dependence on the electrolyte environment. The term *quasi* suggests that it is essential or almost a reference electrode. It is often used when it is undesirable for the solution to be contaminated with species (chloride or sulfate ions). The work

reported in this thesis was performed with an SCE in Chapter 4 to Chapter 8, an MSE in Chapter 3 and a quasi silver-reference electrode in Chapter 5 and Chapter 8.

1.6. Electrochemical Methods

This section describes the fundamental aspects of voltammetric methods notably cyclic voltammetry (CV), linear sweep voltammetry (LSV), square wave voltammetry (SWV) and chronoamperometry (nano-impacts method). Voltammetric methods offer high sensitivity and, in niche applications, selectivity. More importantly, the voltammetric method is low-cost, allows rapid analysis and is highly suitable for in situ applications. In this thesis, stripping voltammetry is widely used.

In general, stripping voltammetric methods can be categorized into three main groups, which are adsorptive stripping voltammetry (AdSV), anodic stripping voltammetry (ASV), and cathodic stripping voltammetry (CSV). AdSV is a two-step process. The first step is a pre-concentration or accumulation step, which is performed by allowing the analyte to adsorb onto the working electrode surface (or complex with an electrode surface modifying agent). The second step involves the use of voltammetry to remove or *strip* the adsorbed analyte. When using AdSV, the pre-concentration time affects the detection limit and sensitivity of the electrode.

The pre-concentration time in voltammetry, specifically in AdSV, can be tuned depending on the analyte concentration in solution. Very low analyte concentrations (trace to ultra-trace levels) may require very long pre-concentration times to build up enough adsorbed analyte on the electrode surface to be accurately measured. However, it has the disadvantage of limiting the number of samples that can be analyzed. Thus, an important improvement in AdSV is decreasing the pre-concentration time without compromising the sensitivity, selectivity and linear range of the response.

Second, anodic stripping voltammetry (ASV) is another well-known sensitive stripping voltammetric method, and again has two steps for the detection of the target analyte. The first step is also a pre-concentration step, but which now involves holding the electrode at a sufficiently negative potential for a set length of time, resulting in the electrochemical reduction of metal cations to the elemental form at the electrode surface. In the second step, a voltammetric sweep of the potential from reductive to oxidative potentials is made, which oxidizes elemental form usually back to metal cation, resulting in a characteristic stripping peak. The magnitude of the resulting anodic peak current is proportional to the amount of the analyte electro-deposited onto the working electrode surface during the pre-concentration step, which in turn reflects the metal ion concentration in solution. The choice of deposition potential and length of pre-concentration time can be optimized to achieve a lower detection limit. Optimizing the deposition potential, generally by shifting the potential to a more negative value, may increase the stripping peak current. However, applying very negative deposition potentials may result in the signal being distorted by hydrogen evolution. An optimum deposition potential may be obtained where the stripping peak currents are maximized and there are no peak distortions.[22] Several voltammetric methods such as CV, LSV and SWV can be done in conjunction with AdSV, ASV or CSV.

Third, cathodic stripping voltammetry (CSV) is stripping voltammetry based on the pre-concentration step and the measurement of a reductive current response as a function of a potential scan toward more negative potentials.[1,2] During the pre-concentration step the analyte is collected on the surface of the working electrode.[23,24] The use of ultrasonically-assisted CSV has successfully determined the lead content of a contaminated sample of river sediment at a boron-doped diamond electrode (BDD).[25] The lead, Pb^{2+}, is first pre-concentrated as lead dioxide, PbO_2, according to the reaction

Pb^{2+} (aq) + $2H_2O$ (aq) → PbO_2 (electrode) + $4H^+$ + $2e^-$ followed by cathodic stripping as the reverse process.

1.6.1. Cyclic Voltammetry (CV)

In cyclic voltammetry, a potential is applied to the working electrode and is varied linearly with time from an initial potential, *E1*, to a second potential, *E2*, at a scan rate, *v*, and then back to *E1*. In practice, digitally generated small potential steps or staircase waves are made and the current is measured as the potential is applied.[1,26,27] The potentials *E1* and *E2* are chosen to embrace the process of interest. Figure 1.3 shows how the triangular potential sweep relates to the voltage scan rate, *v*, and shows the resulting cyclic voltammogram profile for a reversible system. Depending on the scan direction selected, an oxidation or reduction reaction will occur.[28] The current, *I*, measurements are plotted against the potential to give a cyclic voltammogram.

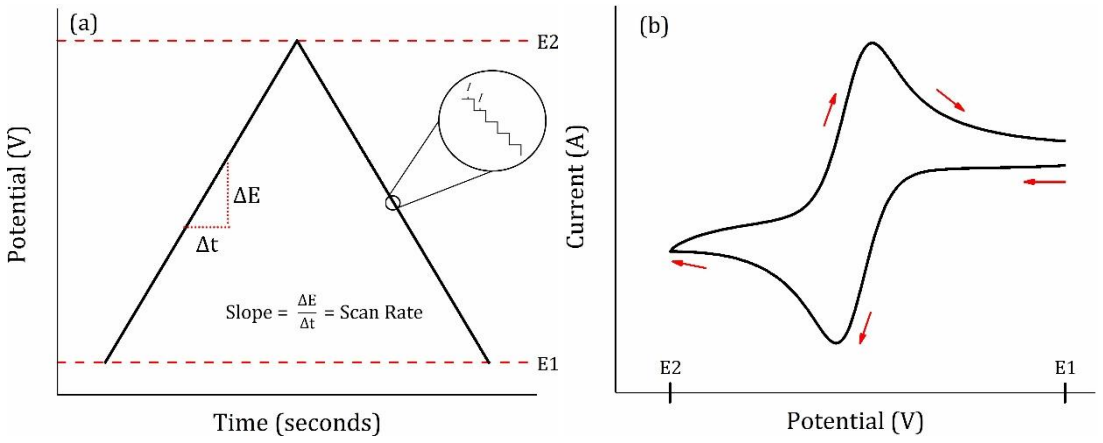


Figure 1.3. Cyclic voltammetry profile. (a) A triangular potential sweep used in CV, (b) example of cyclic voltammogram at a macroelectrode for a reversible reaction.

There are three generic voltammetric profiles for a simple voltammogram for the reaction $A + ne^- \rightleftarrows B$, which can be observed at a macroelectrode using a CV,

namely reversible, quasi-reversible and irreversible (Figure 1.4). The interpretation of these classifications is based on two criteria, namely the peak current, I_p, as a function of scan rate and the peak-to-peak separation of the forward and backward scans. In the reversible process, the electrode kinetics is fast relative to the mass transport on the experimental time scale.[1,2] The peak current, I_p, is described by the Randles-Ševčik[1,2] equation as follows

$$I_p = (2.69\ x\ 10^5)n^{1.5}A_eD^{0.5}Cv^{0.5} \quad (1.28)$$

where *n* is the number of electrons transferred, A_e is the surface area of the electrode, *D* is the diffusional coefficient of a species, *C* is the concentration of the electroactive species, and *v* is the scan rate. The peak-to-peak potential separation of the forward and backward peaks is can be calculated as *2.3RT/nF*, where the difference of those potentials is *57/n* mV at 298 K.[1,2]

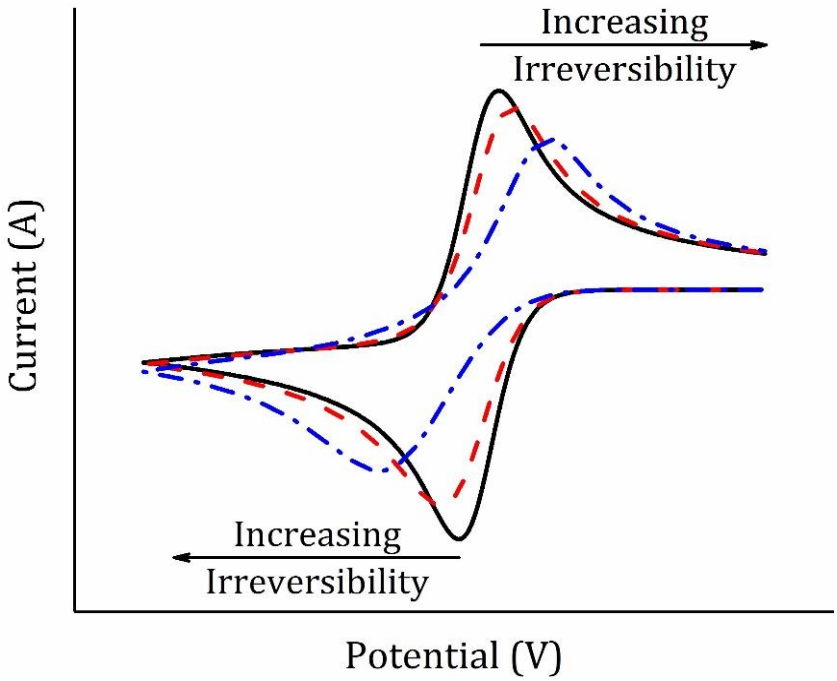


Figure 1.4. Illustration of cyclic voltammogram resulting in a macroelectrode with varying degree of electrochemical reversibility (solid black curve: reversible, dashed red curve: quasi-reversible and dashed-dot blue curve: irreversible)

In an irreversible process, where the electrode kinetics is slow compared to mass transport, the peak current, I_p, in this process is given by the Randles-Ševčik equation for an irreversible process[1,2],

$$I_p = (2.99\ x\ 10^5)n(n' + \alpha_{n'})^{1/2}AD^{0.5}Cv^{0.5} \quad (1.29)$$

where α is the transfer coefficient of the rate-determining step and n' is the number of electrons transferred before the rate-determining step. The forward and backward peaks become more separated as compared to the reversible process due to slower electrode kinetics which hence requires a larger overpotential to drive the reaction. Meanwhile, the case of a quasi-reversible process has intermediate characteristics between the two extremes of reversible and irreversible.

In general, these three different reversibility profiles can be explained in terms of electrode kinetics, measured by the standard electrochemical rate constant, k_0, and the rate of mass transport, measured by the mass transport coefficient[1], m_T,

$$m_T = \frac{D}{\delta} \quad (1.30)$$

where D is the diffusion coefficient ($cm^2\ s^{-1}$) and δ is the diffusion layer thickness (cm). The experimental time can be related to the scan rate through the equation below[1,2],

$$t \sim \frac{RT}{Fv} \quad (1.31)$$

Therefore m_T can be estimated from the following equation[1,2],

$$m_T \sim \sqrt{\frac{DFv}{RT}} \quad (1.32)$$

when $k_0 >> m_T$, the process is *reversible* whilst for $k_0 << m_T$, it is an *irreversible* process.

The limits of reversible and irreversible processes (at a macroelectrode and assuming $\alpha \sim 0.5$) have been evaluated by Matsuda and Ayabe[29] via a parameter Λ,

$$\Lambda = \frac{k_0}{\sqrt{\frac{DFv}{RT}}} \tag{1.33}$$

In summary, Table 1.1 shows the relation between v and k_0, which determines the electrochemical reversibility of a system at 298 K, assuming $\alpha \sim 0.5$.

Table 1.1. Three types of electrochemical reversibility with their classification boundary

Electrochemical Process	**Classification Boundary**
Reversible ($\Lambda \geq 15$)	$k_0 \geq 0.3\ v^{0.5}$ cm s^{-1}
Quasi-Reversible ($15 > \Lambda > 10^{-3}$)	$0.3\ v^{0.5} > k_0 > 2 \times 10^{-5}\ v^{0.5}$ cm s^{-1}
Irreversible ($\Lambda \leq 10^{-3}$)	$k_0 \leq 2 \times 10^{-5}\ v^{0.5}$ cm s^{-1}

The CV method and the influence of reversibility, diffusion and reaction mechanism on the voltammogram have been discussed in the present section. In the next section, linear sweep voltammetry is discussed.

1.6.2. Linear Sweep Voltammetry (LSV)

Linear sweep voltammetry (LSV) works in the same way as CV but the potential only swept in one direction over a potential range that encompasses the start, *E1*, and end potential, *E2*, as a function of time whilst the current passed, *I*, is measured (Figure 1.5). The mass transfer coefficient in LSV is as discussed previously. The potential held upon the electrode is varied linearly as a function of time and expressed as follows,

$$E = E_i + vt \tag{1.34}$$

where E_i is the initial electrode potential, v is the scan rate (v is negative for reduction) and t is the time. LSV is widely used in stripping voltammetry to quantify the amount of material on an electrode surface.

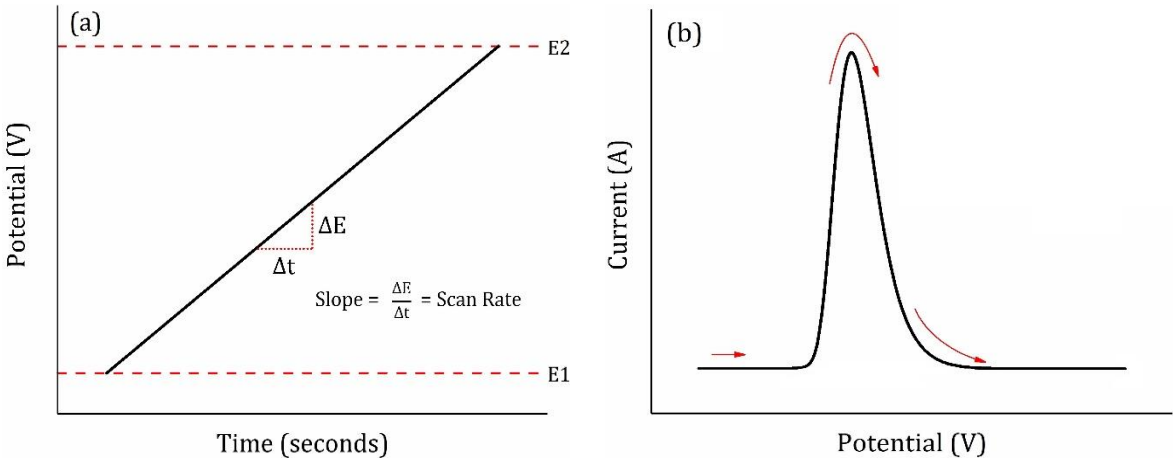


Figure 1.5. LSV profile. (a) A waveform of linear sweep voltammetry, (b) linear sweep voltammogram for a surface species.

As shown in Figure 1.5a, the scan rate is calculated from the slope of the line. Integrating the voltammogram (Figure 1.5b), $Q = \int I\,dt$, gives the charge, Q, which is directly proportional to the number of moles (Faraday's law of electrolysis, equation 1.26) involved in the transfer, and hence the amount of material on an electrode surface. Assuming that both chemical species A and B in the following redox process remain adsorbed, bound to the electrode surface, through the reaction

$$A\,(ads) + ze^- \rightleftarrows B\,(ads) \qquad (1.35)$$

the amount of A and B on the electrode surface is quantified by the surface coverage, Γ (mol cm^{-2}), where $\Gamma = Q/zFA_e$ and z is the number of electrons transferred. If the total surface coverage is constant throughout, $\Gamma_A + \Gamma_B = \Gamma_{Total}$, where Γ_A and Γ_B is the coverage of species A and species B, respectively.[1,2]

For a surface species on an electrode the resulting peak current, I_p, is directly proportional to the scan rate ($I_p \propto v$), in contrast to the case of solution-phase voltammetry. Note that in solution phase species it scales with the square root of the

scan rate. The total current increases linearly with increasing scan rate, given by equation as follows[1],

$$I_p = \frac{F^2}{4RT} v A_e \Gamma \tag{1.36}$$

The width of the peak at half-height can be calculated as follows[1],

$$3.53 \frac{RT}{F} = 90.6 \text{ mV at } 298 \text{ K} \tag{1.37}$$

For rapid electron transfer kinetics the potential of the reversible peak current, E_p, is independent of scan rate. For slow electron transfer kinetics, quasi-reversible or irreversible electron transfer reactions, the overall form of the voltammogram recorded is similar to that *reversible*, but the peak potential shifts depending on the oxidation/reduction rate constant and the scan rate used.

1.6.3. Square Wave Voltammetry (SWV)

Square wave voltammetry (SWV) is a pulse technique based on the series of potential steps and pulses as shown in Figure 1.6a.[2,26] In terms of sensitive detection of analytes, the SWV method is more sensitive than CV and LSV usually reaching detection limits of 1.0×10^{-8} M.[2] The greater sensitivity results from using a pulsed waveform in addition to scanning the potential.[30] The current differences between the pulsed steps are plotted against potential between WE and RE to give a square wave voltammogram. This subtraction allows the background current to be better offset, resulting in a greater resolution of the peaks. This gives a larger measured charged under the voltammetric signal. However, SWV requires careful and systematic optimisation of many analytical parameters, such as pre-concentration time (if performed in combination with AdSV method), accumulation potential, frequency, modulation pulse amplitude, square wave step potential (step height of the staircase), equilibration time

(time between deposition and stripping) and cleaning potential. It is important to note that all these parameters need to be optimized in order to find a clearly visible stripping peak, optimal signal-to-noise ratio, and the lowest background current.[22,30]

The square wave parameters are characterized by pulse height (ΔE_p), staircase height (ΔE_s), pulse time (t_p) and cycle period (t_s) as shown in Figure 1.6a. The term of pulse time can often be expressed as frequency, f, which correspond to $0.5t_p$, and, because of the staircase changes with ΔE_s at the start of each cycle, the scan rate can be expressed as[1,2]

$$\frac{\Delta E_s}{2t_p} = f.\Delta E_s \tag{1.38}$$

The capacitative component of the current resulting from each pulse or step decays much faster than the Faradaic current because capacitative current falls as a function of e^{-t} whilst the Faradaic current decreases by $t^{-\frac{1}{2}}$. The Faradaic current is given by Cottrell's equation[1,2] as:

$$I = \frac{nFA_e\sqrt{D}C}{\sqrt{\pi t}} \tag{1.39}$$

where I is current at the electrode measured as a function of time, n is the number of electrons passed in the electrode reaction, F is the Faraday constant (96485 C mol^{-1}), A_e is the electrode surface area, D is the diffusion coefficient, C is the bulk concentration and t is time. The capacitative current[1,2], I_c, decays exponentially as

$$I_c(t) = I_0\, exp\left(\frac{-t}{RC_d}\right) \tag{1.40}$$

where I_0 is the initial current, R is the resistance and C_d is the double layer capacitance (F m^{-2}). Therefore it is possible to minimize the capacitive contribution by sampling the current at the end of each step.

As shown in Figure 1.6a, the measurement is made at two points of each cycle (point 1 and 2). These points represent the end of the forward and backward peaks respectively, where the difference (resultant current, Figure 1.6b) can be expressed as[2]

$$\Delta I = I_1 - I_2 \tag{1.41}$$

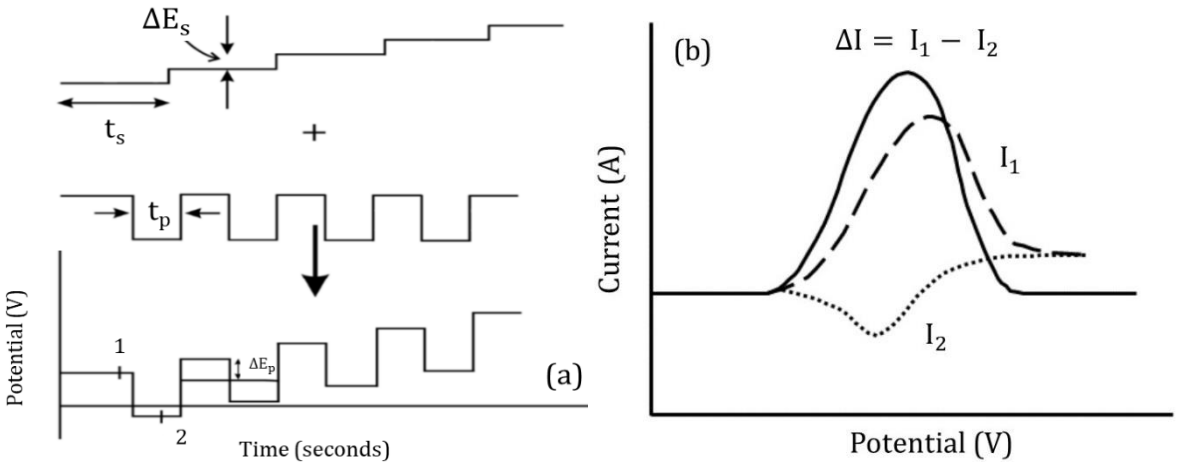


Figure 1.6. (a) Square waveform and measurement schematic and (b) general depiction of a square wave voltammogram.

Assuming the capacitative currents at regions 1 and 2 are approximately equal, the current due to the non-Faradaic process is reduced. This produces an advantage to using SWV as the subtraction of I_1 from I_2 and the potential steps between the forward and backward interval is small, resulting in high measurement sensitivity and the minimization of the capacitative contribution. In summary, SWV is a large amplitude differential technique, the waveform applied to the working electrode is a symmetric square wave superimposed on a base staircase potential and the current is sampled twice during each square-wave cycle (one at the end of the forward pulse and one at the end of the reverse pulse). This method is employed to detect inorganic Al^{3+} and Hg^{2+} in Chapter 4 and Chapter 5, respectively.

1.6.4. Chronoamperometry

Chronoamperometry is an electrochemical method that studies the change in current with time as a potential step is applied to the working electrode.[1,2] All of the species near the electrode surface will be consumed if the applied potential is held at a suitably high overpotential.

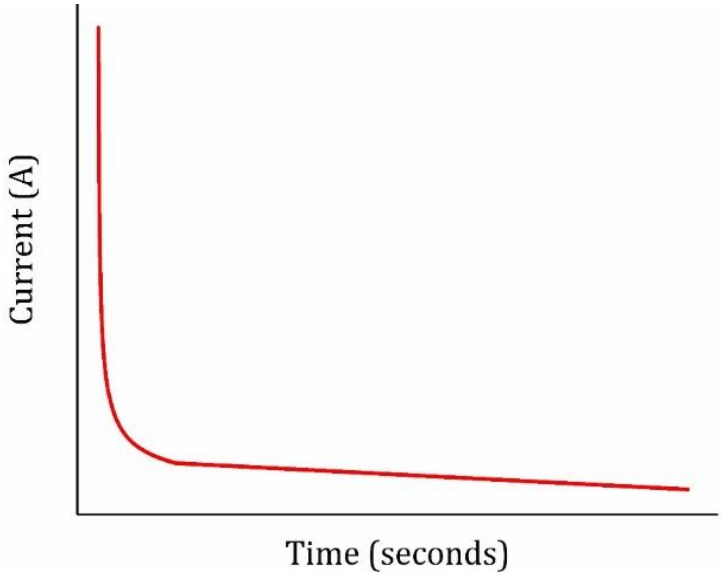


Figure 1.7. A typical chronoamperogram which plots current versus time.

As shown in Figure 1.7, huge current flows at the start of the chronoamperogram, then as the diffusion layer groups the current decreases as time passes. At a macroelectrode, the Cottrell equation[1,2] (equation 1.38) derived from Fick's second law shows the response to a potential step from zero current to a diffusion-controlled current. As the time approaches infinity, the current decays to zero as all the reactant is fully converted into product.

At a microelectrode, convergent diffusion should be considered. The equation below determines the current decay at a fixed potential following a potential step.

$$I = 4nFCDr_e f(\tau) \qquad (1.42)$$

where r_e is the electrode radius and $\tau = 4Dt/r_e^2$ (dimensionless time). Further, Shoup and Szabo[31,32] have estimated $f(\tau)$ at all times to be:

$$f(\tau) = 0.7854 + 0.8862\tau^{-1/2} + 0.2146\, exp^{-0.7823\tau^{-\frac{1}{2}}} \quad (1.43)$$

For short times (τ<1), $f(\tau)$ can be approximated as

$$f(\tau) = \left(\frac{\pi}{4\tau}\right)^{0.5} + \frac{\pi}{4} + 0.094\,\tau^{0.5} \quad (1.44)$$

and for a long time (τ>1), $f(\tau)$ can be approximated as

$$f(\tau) = 1 + 0.71835\tau^{-0.5} + 0.0562\,\tau^{-1.5} - 0.0064\,\tau^{-2.5} \quad (1.45)$$

As τ becomes infinite ($\tau \rightarrow \infty$), the $f(\tau)$ value becomes one so that a steady-state current, I_{ss}, is reached and expressed as,

$$I_{ss} = 4nFCDr_e \quad (1.46)$$

For both macroelectrode and microelectrode, the current is exclusively determined by the mass transport process, making chronoamperometry an attractive option for mass transport studies.

In this thesis, the chronoamperometry method (current-time transients) is employed for the nano-impacts experiments and discussed in the following section.

1.6.5. Nano-impacts

In this thesis, the nano-impacts method was employed to understand the role of the TA capping agent in the redox activity for Hg^{2+} and Zn^{2+} detection (Chapter 6) and to understand the reactivity and the mechanism of citrate-capped gold nanoparticle (AuNPs@CA) dissolution at the single-particle level in cyanide medium (Chapter 7). The study was mainly focussed on, but not limited to, the analysis of the resulting spikes shape, charge, current, duration and frequency of a statistically relevant number of single collision events.

The motion of the nanoparticles in solution is expected to be approximately Brownian so over time nanoparticles are brought close to or in physical contact (electrode-particle collision) with the potentiostated electrode (either stick or rebound). If the electrode is held at a sufficient potential, current spikes are seen corresponding to the oxidation or reduction of the impacting nanoparticles. Studying the electrode-particle collision phenomenon (hereafter referred to as nano-impacts) allows the characterization of single particles[33,34] and their reactivity (mechanistic and kinetic insights) in various solutions.[35,36]

The initial observation of the nano-impacts phenomenon was made by Micka[37] in the 1950s and then revitalized by Heyrovsky *et al*.[38,39] in 1995, later by Bard and Xiao[40] in 2007 and Compton[41,42]. The nano-impacts method provides analysis of single-particle level by detecting transient current peaks which result when suspended nanoparticles in solution, by virtue of their Brownian motion, stochastically collide with an electrode surface in which the electrode is held at a suitable potential. The stochastic collisions of the nanoparticles against the electrode surface typically result in spikes or steps in the background current recorded at the electrode (typically microelectrode). The spikes can be short or long-lived, which reflects the period of time that the particle is in contact with the electrode. In favorable cases, the magnitude of the current yields a direct measure of the reaction rate at the single-particle, hence short-lived electrochemical events may reflect a particle leaving the electrode surface or a decrease in the catalytic activity of the material as the reaction keep progresses. Numerous stochastic collisions or impact events are capable of providing specific information regarding the nature of the nanoparticle, the kinetics of the electron transfer and the catalytic activity of a given nanoparticle. Therefore, it is important to understand the types or mechanism of nano-impacts that may occur.

In the nano-impacts method, the electrode-particle collisions can be classified into four categories depending on the reaction taking place, namely (a) direct Faradaic, (b) mediated Faradaic, (c) capacitive and (d) blocking impacts.[42]

In *direct Faradaic impacts*, the process involves electron transfer between the nanoparticle and the electrode surface which results in the occurrence of a redox reaction.[43-45] Direct Faradaic impact involves the electrolysis of the nanoparticle itself. For example, single silver nanoparticles in aqueous solution impact a microelectrode surface that held at a suitable potential and become oxidized to soluble silver cations (Ag^+) or to form AgCl. The charge obtained by integrating the current transients (spikes) via Faraday's first law reflects directly the number of atoms or molecules in the silver nanoparticles thus giving its size.[46]

The colliding species (nanoparticles) in some cases may dissolve. For example, typical oxidative dissolution behavior is observed for metallic nanoparticles such as citrate-capped gold nanoparticle (AuNP@CA).[35] The near-complete oxidative dissolution of the single AuNP@CA level was achieved at the cyanide-containing solution of 35.0 mM and higher, at an applied potential of 1.0 V vs SCE. In this case, the oxidative dissolution of single AuNP@CA was shown to be controlled by a pre-adsorption step of CN^- onto the surface of individual particles before the electron was transferred.

In *mediated Faradaic impacts*, the reaction relies on the presence of a redox-active couple in the bulk solution (catalytically-amplified impact events), in which the redox state of the nanoparticles is unchanged and the nanoparticles serve to mediate a redox reaction of interest. For example is proton reduction[36,47], when a nanoparticle impacts on and formed an electrical contact with a microelectrode surface. The measurement of the kinetics of proton reduction has been reported for individual

silver nanoparticles.[48] Other examples of the use of mediated Faradaic impacts can be found in the oxidation of hydrazine at gold[49] and platinum[50] nanoparticles and the oxidation of water at iridium oxide nanoparticles.[51]

In *capacitative nano-impacts*, the process can be categorized into two groups: (a) a process due to the displacement of charge from the electrode–solution interface (double layer) and (b) a process from the charging of an impacting nanoparticle. To maintain charge neutrality, the electrons can leave or enter the electrode in response to the changes in ionic charge distribution at the interface. Large capacitive nano-impacts are therefore observed for particles featuring large surface areas. Capacitative nano-impacts have been successfully observed for graphene platelets and used to estimate the potential of zero charge (PZC) and their diffusion coefficient.[52]

Blocking nano-impacts occur when the electrode is blocked by the arriving nanoparticles. Lemay *et al*.[53] reported that during amperometric detection of single carboxylated micro- and nano- spheres these are adsorbed on micro- and nano-electrodes. An impacting non-conductive particle can cause a decrease or block in the electrode surface area and a corresponding reduction in the diffusion-limited current of the redox species is observed.[54,55]

As described earlier in this section, several types of information can be extracted through the study of nano-impacts, such as physical characterization of the nanoparticles (sizing, shape and aggregation/agglomeration state)[56,44] , mechanistic and kinetics of the reaction[48,57], etc. First, the sizing of the nanoparticle is crucial for efficient applications and rational system design.[58] The nano-impacts method has also shown the ability to size both spherical and non-spherical particles (such as nanorods[59] or icosahedra[60]). In addition, nano-impacts can observe the agglomeration and aggregation states of the particles. Understanding of agglomeration or aggregation

states of the particles is important as it can have a significant effect on the mass transport and physical properties of a particulate system.[61,62] One of the advantages of the nano-impact method is that it is an in situ technique.

In summary, the nano-impacts method has started to revolutionize single nanoparticle detection and characterization. For example, the work presented in this thesis has shown that incomplete stripping of citrate-capped gold nanoparticles (at the ensemble level, drop-casted onto glassy carbon electrode) in cyclic voltammetry can lead to issues of partial oxidative dissolution in cyanide-containing solution when aggregation of the nanoparticles takes place on the electrode surface (see Chapter 7). For this reason, nano-impacts experiments may be preferred.

Bibliography

(1) Compton, R. G.; Banks, C. E. *Understanding Voltammetry 3rd Edition*; World Scientific Publishing Co Pte Ltd., 2018.

(2) Bard, A. J.; Faulkner, L. R. *Electrochemical Methods: Fundamentals and Applications, 2nd Edition*; Wiley, 2001.

(3) Tobias, C. W.; Eisenberg, M.; Wilke, C. R. Fiftieth Anniversary: Diffusion and Convection in Electrolysis—A Theoretical Review. *J. Electrochem. Soc.* 1952, *99* (12), 359C-365C.

(4) Concepcion, J. J.; Binstead, R. A.; Alibabaei, L.; Meyer, T. J. Application of the Rotating Ring-Disc-Electrode Technique to Water Oxidation by Surface-Bound Molecular Catalysts. *Inorg. Chem.* 2013, *52* (19), 10744—10746.

(5) Lu, Y.-C.; He, Q.; Gasteiger, H. A. Probing the Lithium–Sulfur Redox Reactions: A Rotating-Ring Disk Electrode Study. *J. Phys. Chem. C* 2014, *118* (11), 5733–5741.

(6) Compton, R. G.; Eklund, J. C.; Marken, F. Sonoelectrochemical Processes: A Review. *Electroanalysis* 1997, *9* (7), 509–522.

(7) Snowden, M. E.; Unwin, P. R.; Macpherson, J. V. Single Walled Carbon Nanotube Channel Flow Electrode: Hydrodynamic Voltammetry at the Nanomolar Level. *Electrochem. commun.* 2011, *13* (2), 186–189.

(8) Prado, C.; Murcott, G. G.; Marken, F.; Foord, J. S.; Compton, R. G. Detection of Chlorophenols in Aqueous Solution via Hydrodynamic Channel Flow Cell Voltammetry

Using a Boron-Doped Diamond Electrode. *Electroanalysis* 2002, *14* (14), 975–979.

(9) Congur, G.; Erdem, A. PAMAM Dendrimer Modified Screen Printed Electrodes for Impedimetric Detection of MiRNA-34a. *Microchem. J.* 2019, *148*, 748–758.

(10) Aller-Pellitero, M.; Fremeau, J.; Villa, R.; Guirado, G.; Lakard, B.; Hihn, J.-Y.; del Campo, F. J. Electrochromic Biosensors Based on Screen-Printed Prussian Blue Electrodes. *Sensors Actuators B Chem.* 2019, *290*, 591–597.

(11) Hassani, S.; Akmal, M. R.; Salek-Maghsoudi, A.; Rahmani, S.; Ganjali, M. R.; Norouzi, P.; Abdollahi, M. Novel Label-Free Electrochemical Aptasensor for Determination of Diazinon Using Gold Nanoparticles-Modified Screen-Printed Gold Electrode. *Biosens. Bioelectron.* 2018, *120*, 122–128.

(12) Cinti, S.; Santella, F.; Moscone, D.; Arduini, F. Hg^{2+} Detection Using a Disposable and Miniaturized Screen-Printed Electrode Modified with Nanocomposite Carbon Black and Gold Nanoparticles. *Environ. Sci. Pollut. Res.* 2016, *23* (9), 8192–8199.

(13) Suherman, A. L.; Kuss, S.; Tanner, E. E. L.; Young, N. P.; Compton, R. G. Electrochemical Hg^{2+} Detection at Tannic Acid-Gold Nanoparticle Modified Electrodes by Square Wave Voltammetry. *Analyst* 2018, 143, 2035-2041.

(14) Akl, Z. F.; Ali, T. A. A Novel Modified Screen-Printed Electrode with Triazole Surfactant Assembled on Silver Nanoparticles for Potentiometric Determination of Uranium. *J. Radioanal. Nucl. Chem.* 2017, *314* (3), 1865–1875.

(15) Palanisamy, S.; Thirumalraj, B.; Chen, S.-M.; Ajmal Ali, M.; Muthupandi, K.; Emmanuel, R.; Prakash, P.; Al-Hemaid, F. M. A. Fabrication of Silver Nanoparticles Decorated on Activated Screen Printed Carbon Electrode and Its Application for Ultrasensitive Detection of Dopamine. *Electroanalysis* 2015, *27* (8), 1998–2006.

(16) Fava, E. L.; do Prado, T. M.; Garcia-Filho, A.; Silva, T. A.; Cincotto, F. H.; de Moraes, F. C.; Faria, R. C.; Fatibello-Filho, O. Non-Enzymatic Electrochemical Determination of Creatinine Using a Novel Screen-Printed Microcell. *Talanta* 2019, 120277.

(17) Mazzaracchio, V.; Tomei, M. R.; Cacciotti, I.; Chiodoni, A.; Novara, C.; Castellino, M.; Scordo, G.; Amine, A.; Moscone, D.; Arduini, F. Inside the Different Types of Carbon Black as Nanomodifiers for Screen-Printed Electrodes. *Electrochim. Acta* 2019, *317*, 673–683.

(18) Yamanaka, K.; Vestergaard, M. C.; Tamiya, E. Printable Electrochemical Biosensors: A Focus on Screen-Printed Electrodes and Their Application. *Sensors (Basel).* 2016, *16* (10), 1761.

(19) Barton, J.; García, M. B. G.; Santos, D. H.; Fanjul-Bolado, P.; Ribotti, A.; McCaul, M.; Diamond, D.; Magni, P. Screen-Printed Electrodes for Environmental Monitoring of Heavy Metal Ions: A Review. *Microchim. Acta* 2016, *183* (2), 503–517.

(20) Economou, A. Screen-Printed Electrodes Modified with “Green” Metals for

Electrochemical Stripping Analysis of Toxic Elements. *Sensors (Basel).* 2018, *18* (4), 1032.

(21) Li, M.; Li, D.-W.; Xiu, G.; Long, Y.-T. Applications of Screen-Printed Electrodes in Current Environmental Analysis. *Curr. Opin. Electrochem.* 2017, *3* (1), 137–143.

(22) Suherman, A. L.; Tanner, E. E. L.; Compton, R. G. Recent Developments in Inorganic Hg^{2+} Detection by Voltammetry. *TrAC Trends Anal. Chem.* 2017, *94*, 161–172.

(23) Ensch, M.; Wehring, B.; Landis, G. D.; Garratt, E.; Becker, M. F.; Schuelke, T.; Rusinek, C. A. Indium Tin Oxide Film Characteristics for Cathodic Stripping Voltammetry. *ACS Appl. Mater. Interfaces* 2019, *11* (18), 16991–17000.

(24) Fogg, A. G.; Zanoni, M. V. B.; Barros, A. A.; Rodrigues, J. A.; Birch, B. J. Aspects of Cathodic Stripping Voltammetry at the Hanging Mercury Drop Electrode and in Non-Mercury Disposable Sensors. *Electroanalysis* 2000, *12* (15), 1227–1232.

(25) Saterlay, A. J.; Agra-Gutiérrez, C.; Taylor, M. P.; Marken, F.; Compton, R. G. Sono-Cathodic Stripping Voltammetry of Lead at a Polished Boron-Doped Diamond Electrode: Application to the Determination of Lead in River Sediment. *Electroanalysis* 1999, *11* (15), 1083–1088.

(26) Brett, C. M. A.; Brett, A. M. O. *Step and Pulse Techniques*; Wiley-VCH Verlag GmbH & Co. KGaA: Weinheim, Germany, 2007.

(27) Van Benschoten, J. J.; Lewis, J. Y.; Heineman, W. R.; Roston, D. A.; Kissinger, P. T. Cyclic Voltammetry Experiment. *J. Chem. Educ.* 1983, *60* (9), 772.

(28) Kissinger, P. T.; Heineman, W. R. Cyclic Voltammetry. *J. Chem. Educ.* 1983, *60* (9), 702.

(29) Matsuda, H.; Ayabe, Y. Zur Theorie Der Randles-Sevčikschen Kathodenstrahl-Polarographie. *Zeitschrift für Elektrochemie, Berichte der Bunsengesellschaft für Phys. Chemie* 1955, *59* (6), 494–503.

(30) Laborda, E.; González, J.; Molina, Á. Recent Advances on the Theory of Pulse Techniques: A Mini Review. *Electrochem. commun.* 2014, *43*, 25–30.

(31) Shoup, D.; Szabo, A. Chronoamperometric Current at Finite Disk Electrodes. *J. Electroanal. Chem. Interfacial Electrochem.* 1982, *140* (2), 237–245.

(32) Xiong, L.; Aldous, L.; Henstridge, M. C.; Compton, R. G. Investigation of the Optimal Transient Times for Chronoamperometric Analysis of Diffusion Coefficients and Concentrations in Non-Aqueous Solvents and Ionic Liquids. *Anal. Methods* 2012, *4* (2), 371–376.

(33) Lees, J. C.; Ellison, J.; Batchelor-McAuley, C.; Tschulik, K.; Damm, C.; Omanović, D.; Compton, R. G. Nanoparticle Impacts Show High-Ionic-Strength Citrate Avoids Aggregation of Silver Nanoparticles. *ChemPhysChem* 2013, *14* (17), 3895–3897.

(34) Allerston, L. K.; Rees, N. V. Nanoparticle Impacts in Innovative Electrochemistry. *Curr.*

Opin. Electrochem. 2018., 10, 31-36.

(35) Suherman, A. L.; Zampardi, G.; Kuss, S.; Tanner, E. E. L.; Amin, H. M. A.; Young, N. P.; Compton, R. G. Understanding Gold Nanoparticle Dissolution in Cyanide-Containing Solution via Impact-Chemistry. *Phys. Chem. Chem. Phys.* 2018, *20* (44), 28300–28307.

(36) Robbs, P. H.; Rees, N. V. Nanoparticle Electrochemistry. *Phys. Chem. Chem. Phys.* 2016, *18* (36), 24812–24819.

(37) Micka K. *Depolarisation Der Quecksilbertropfelektrode Durch Suspensionen Unlöslicher Stoffe I. Allgemeine Beobachtungen*. *Collect Czechoslov Chem Commun* 1956, *21*, 647–651.

(38) Heyrovsky, M.; Jirkovsky, J. Polarography and Voltammetry of Ultrasmall Colloids: Introduction to a New Field. *Langmuir* 1995, *11* (11), 4288–4292.

(39) Heyrovsky, M.; Jirkovsky, J.; Struplova-Bartackova, M. Polarography and Voltammetry of Aqueous Colloidal TiO_2 Solutions. *Langmuir* 1995, *11* (11), 4300–4308.

(40) Xiao, X.; Bard, A. J. Observing Single Nanoparticle Collisions at an Ultramicroelectrode by Electrocatalytic Amplification. *J. Am. Chem. Soc.* 2007, *129* (31), 9610–9612.

(41) Rees, N. V; Banks, C. E.; Compton, R. G. Ultrafast Chronoamperometry of Acoustically Agitated Solid Particulate Suspensions: Nonfaradaic and Faradaic Processes at a Polycrystalline Gold Electrode. *J. Phys. Chem. B* 2004, *108* (48), 18391–18394.

(42) Sokolov, S. V.; Eloul, S.; Kätelhön, E.; Batchelor-McAuley, C.; Compton, R. G. Electrode–Particle Impacts: A Users Guide. *Phys. Chem. Chem. Phys.* 2017, *19* (1), 28–43.

(43) Sokolov, S. V; Bartlett, T. R.; Fair, P.; Fletcher, S.; Compton, R. G. Femtomolar Detection of Silver Nanoparticles by Flow-Enhanced Direct-Impact Voltammetry at a Microelectrode Array. *Anal. Chem.* 2016, *88* (17), 8908–8912.

(44) Li, X.; Batchelor-McAuley, C.; Compton, R. G. Silver Nanoparticle Detection in Real-World Environments via Particle Impact Electrochemistry. *ACS Sensors* 2019, *4* (2), 464–470.

(45) Zhou, Y.-G.; Rees, N. V; Compton, R. G. The Electrochemical Detection and Characterization of Silver Nanoparticles in Aqueous Solution. *Angew. Chemie Int. Ed.* 2011, *50* (18), 4219–4221.

(46) Saw, E. N.; Kratz, M.; Tschulik, K. Time-Resolved Impact Electrochemistry for Quantitative Measurement of Single-Nanoparticle Reaction Kinetics. *Nano Res.* 2017, *10* (11), 3680–3689.

(47) Ly, L. S. Y.; Batchelor-McAuley, C.; Tschulik, K.; Kätelhön, E.; Compton, R. G. A Critical Evaluation of the Interpretation of Electrocatalytic Nanoimpacts. *J. Phys. Chem. C* 2014, *118* (31), 17756–17763.

(48) Kahk, J. M.; Rees, N. V; Pillay, J.; Tshikhudo, R.; Vilakazi, S.; Compton, R. G. Electron Transfer Kinetics at Single Nanoparticles. *Nano Today* 2012, *7* (3), 174–179.

(49) Xiao, X.; Fan, F.-R. F.; Zhou, J.; Bard, A. J. Current Transients in Single Nanoparticle

Collision Events. *J. Am. Chem. Soc.* 2008, *130* (49), 16669–16677.

(50) Xiao, X.; Pan, S.; Jang, J. S.; Fan, F.-R. F.; Bard, A. J. Single Nanoparticle Electrocatalysis: Effect of Monolayers on Particle and Electrode on Electron Transfer. *J. Phys. Chem. C* 2009, *113* (33), 14978–14982.

(51) Kwon, S. J.; Fan, F.-R. F.; Bard, A. J. Observing Iridium Oxide (IrOx) Single Nanoparticle Collisions at Ultramicroelectrodes. *J. Am. Chem. Soc.* 2010, *132* (38), 13165–13167.

(52) Poon, J.; Batchelor-McAuley, C.; Tschulik, K.; Compton, R. G. Single Graphene Nanoplatelets: Capacitance, Potential of Zero Charge and Diffusion Coefficient. *Chem. Sci.* 2015, *6* (5), 2869–2876.

(53) Quinn, B. M.; van't Hof, P. G.; Lemay, S. G. Time-Resolved Electrochemical Detection of Discrete Adsorption Events. *J. Am. Chem. Soc.* 2004, *126* (27), 8360–8361.

(54) Lebègue, E.; Anderson, C. M.; Dick, J. E.; Webb, L. J.; Bard, A. J. Electrochemical Detection of Single Phospholipid Vesicle Collisions at a Pt Ultramicroelectrode. *Langmuir* 2015, *31* (42), 11734–11739.

(55) Dick, J. E.; Renault, C.; Bard, A. J. Observation of Single-Protein and DNA Macromolecule Collisions on Ultramicroelectrodes. *J. Am. Chem. Soc.* 2015, *137* (26), 8376–8379.

(56) Jiao, X.; Sokolov, S. V; Tanner, E. E. L.; Young, N. P.; Compton, R. G. Exploring Nanoparticle Porosity Using Nano-Impacts: Platinum Nanoparticle Aggregates. *Phys. Chem. Chem. Phys.* 2017, *19* (1), 64–68.

(57) Little, C. A.; Li, X.; Batchelor-McAuley, C.; Young, N. P.; Compton, R. G. Particle-Electrode Impacts: Evidencing Partial versus Complete Oxidation via Variable Temperature Studies. *J. Electroanal. Chem.* 2018, *823*, 492–498.

(58) Stark, W. J.; Stoessel, P. R.; Wohlleben, W.; Hafner, A. Industrial Applications of Nanoparticles. *Chem. Soc. Rev.* 2015, *44* (16), 5793–5805.

(59) Plowman, B. J.; Young, N. P.; Batchelor-McAuley, C.; Compton, R. G. Nanorod Aspect Ratios Determined by the Nano-Impact Technique. *Angew. Chemie* 2016, *128* (24), 7116–7119.

(60) Sokolov, S. V; Batchelor-McAuley, C.; Tschulik, K.; Fletcher, S.; Compton, R. G. Are Nanoparticles Spherical or Quasi-Spherical? *Chem. – A Eur. J.* 2015, *21* (30), 10741–10746.

(61) Shimizu, K.; Sokolov, S. V; Compton, R. G. Agglomeration Equilibria of Hematite Nanoparticles. *Colloid Interface Sci. Commun.* 2016, *13*, 19–22.

(62) Prasher, R.; Evans, W.; Meakin, P.; Fish, J.; Phelan, P.; Keblinski, P. Effect of Aggregation on Thermal Conduction in Colloidal Nanofluids. *Appl. Phys. Lett.* 2006, *89* (14), 143119.

Chapter 2

Experimental

This chapter summarises the experimental chemical reagents, electrochemical instrumentations and non-electrochemical instrumentation used within this thesis. A detailed description of each experiment performed can be found in the relevant experimental sections of Chapters 3 to Chapter 8.

2.1. Chemical Reagents

This section details all of the chemical reagents used within this thesis. They were used as received. All aqueous solutions were made up of deionized water with the resistivity of 18.2 MΩ cm at 298 K (Millipore, UK). A high purity nitrogen flow was used to degas all solutions thoroughly, exclude synthetic and authentic human saliva (Chapter 8), prior to the electrochemical measurements.

Table 2.1. List of chemicals used (in alphabetical order)

Chemical Name	Formula	Purity	Supplier
Aluminium sulphate	$Al_2(SO_4)_3.16H_2O$	> 97%	Alfa Aesar, Germany
Calcium chloride	$CaCl_2$	≥ 97.0%	Sigma Aldrich, UK
Carbon black (M1100)	-	-	Cabot, Billerica, USA
Citrate-capped gold nanoparticles (⌀ 12 nm)	AuNPs@CA	-	nanoComposix, San Diego, US

Citrate-capped gold nanoparticles (⌀ 20 nm)	AuNPs@CA	-	nanoComposix, San Diego, US
Citrate-capped gold nanoparticles (⌀ 60 nm)	AuNPs@CA	-	Nanopartz Inc., Loveland, US
Deionized water	H_2O	18.2 MΩ cm	Millipore, UK
Hydrochloric acid	HCl	~37%	Fisher Scientific, UK
Lithium chloride	LiCl	≥ 99.98%	Sigma Aldrich, UK
Lithium manganese oxide	$LiMn_2O_4$	≥99%	Sigma Aldrich, UK
Lithium manganese oxide	$LiMn_2O_4$	99.5%	Alfa Aesar, UK
Lithium perchlorate	$LiClO_4$	≥ 98.0%	Sigma Aldrich, UK
Magnesium chloride	$MgCl_2$	98%	Sigma Aldrich, UK
Mercury(II) nitrate	$Hg(NO_3)_2$	-	Sigma Aldrich, UK
Nitrogen	N_2	-	BOC Gases plc, UK
N-methyl-2-pyrrolidone	C_5H_9NO	> 99.5%	Sigma Aldrich, UK
Polyvinylidene difluoride	$-(C_2H_2F_2)_n-$	-	Solvay, Belgium
Potassium chloride	KCl	≥ 99.0%	Sigma Aldrich, UK
Potassium cyanide	KCN	≥ 97.0%	Sigma Aldrich, UK
Potassium nitrate	KNO_3	> 99.5%	Sigma Aldrich, UK
Potassium sulphate	K_2SO_4	> 99%	Sigma Aldrich, UK
Sodium chloride	NaCl	> 99.0%	Sigma Aldrich, UK
Sodium hydroxide	NaOH	≥ 97.0%	Sigma Aldrich, UK
Sodium perchlorate	$NaClO_4$	≥ 98.0%	Sigma Aldrich, UK
Silver nanoparticles (⌀ 50 nm)	AgNPs	-	nanoComposix, San Diego, US

Synthetic saliva (DIN53160-1)	-	-	Synthetic Urine e.k., Germany
Tannic acid	$C_{76}H_{52}O_{46}$	-	Sigma Aldrich, UK
Tannic acid-capped gold nanoparticles (⌀ 68.4 nm)	AuNPs@TA	-	nanoComposix, San Diego, US
Zinc nitrate hexahydrate	$Zn(NO_3)_2$	> 98%	Sigma-Aldrich, Germany

Synthetic and authentic human saliva samples are used for electrochemical experiments described in Chapter 8. The synthetic saliva (Synthetic Urine e.k., Germany) was used as received. The proprietary formulation of the synthetic saliva reflects the standardized production process pursuant to DIN 53160-1: 2010, which contains no lithium compounds.[1] The synthetic saliva used contains inorganic ions, such as Mg^{2+}, Ca^{2+}, K^{+}, Cl^{-}, CO_3^{2-} and HPO_4^{2-}, unknown organic substances and others in order to adjust the viscosity level and pH 6.8 ± 0.1.[1] Note that authentic human saliva is primarily composed of water (99%), several inorganic (Na^{+}, K^{+}, Ca^{2+}, Cl^{-}, HPO_4^{2-}, etc.) and organic (uric acid, creatine, etc.) substances and others.[2]

The collection of human saliva samples was made in accordance with the *Approved Procedure 24: IDREC 24 Version 3.0* from the Central University Research Ethics Committee (CUREC), Oxford University.[3] The samples were collected from three healthy volunteers using Salivetts® (Sarstedt, Germany). Each volunteer chewed the swabs from the Salivetts® for approximately 1 min and then the Salivetts® containing the respective swabs were centrifuged at 1,000 x *g* (2,400 rpm) for 2 minutes at 20 °C.[4] The analysis of authentic human saliva was conducted by the standard addition method in triplicate, each from the same time of sample collection.

2.2. Electrochemical Instrumentations

All electrochemical experiments were performed in a thermostatted Faraday cage at 25 ± 1 ^{o}C with a three-electrode configuration. For all the works in the thesis, a platinum (Pt) wire from Goodfellow Cambridge Ltd, Huntingdon, UK acted as a counter electrode. The electrochemical experiments were controlled by a μ-Autolab III potentiostat/galvanostat (Autolab B.V., Utrecht, The Netherlands) interfaced to a PC using GPES Version 4.9 for Windows.

All working electrodes, excluding the carbon screen-printed electrode (Dropsens, Llanera, Spain) and the lithium manganese oxide-modified screen-printed electrode (LMO-SPE), were first cleaned by mechanical polishing on soft lapping pads to a mirror finish using either diamond sprays (Kemet International Ltd, Kent, UK) in the sequence of size 3.0 μm, 1.0 μm and 0.1 μm or deionised water-alumina slurry (Buehler, Coventry, UK) in the sequence of size 1.0 μm, 0.3 μm and 0.05 μm. The diamond sprays were used for the experiments described in Chapters 3, 5 and 8, whilst the deionized water-alumina slurry was used in Chapters 4, 6 and 7. Table 2.2 summarises the working electrodes employed and their radii measured by optical microscopy. Table 2.3 summarises the reference electrodes used within this thesis and their potential against the standard hydrogen electrode (SHE).[5]

Table 2.2. Types of working electrode used

Electrode	Size	Supplier
Glassy carbon (GCE)	1.48 ± 0.02 mm radius	CH Instruments Inc., USA
Carbon microelectrode (disc)	nominally 7.0 μm diameter	ALS distributed by BASi, Japan

Gold macroelectrode	0.96 ± 0.02 mm radius	CH Instruments Inc., USA
Carbon screen-printed	4.0 mm diameter	Dropsens, Llanera, Spain
Glassy carbon disc (GCD)	nominally 10.0 mm radius (2 mm thick)	Hochtemperatur-Werkstoffe GmbH, Germany
$LiMn_2O_4$ screen-printed (LMO-SPE)	6.0 mm diameter	Sun Chemicals Ltd., Bristol, UK

Table 2.3. Types of reference electrode used

Electrode	Potential	Supplier
Standard Calomel Electrode (SCE), $Hg/Hg_2Cl_2/KCl$ (saturated)	+0.241 V vs SHE	ALS distributed by BASi, Japan
Mercury/Mercuous Sulphate Electrode (MSE), $Hg/Hg_2SO_4/K_2SO_4$ (saturated)	+0.620 V vs SHE	IJ Cambria Scientific Ltd., UK

The nano-impacts experiments are reported in Chapter 6 and Chapter 7. Nano-impacts experiments were performed within a double Faraday cage, where an in-house built low noise potentiostat was used with a 100 Hz Bessel-type low pass filter.[6] It should be noted that the potentiostat used accurately conserves the charge transferred due to a particle-impact process despite the possible distortion of the spike shape.[7,8] The analog-to-digital and digital-to-analog conversion were provided by a USB-6003 DAQ (National Instruments, TX, US). The control of these devices was performed by a script written in Python 2.7 with a graphical user interface and real-time electrochemical data visualization based upon the packages provided in the Enthought Tool Suite (Enthought, TX, US).

A carbon microelectrode disc with a nominally 7.0 μm diameter was employed as the working electrode for all nano-impacts experiments performed. Nitrogen was bubbled thoroughly into the solution prior to commencing the experiment. The glass cell used for all nano-impacts experiments were cleaned using aqua regia to ensure complete removal of all nanoparticles and organic impurities. Chronoamperometry was employed to observe nanoparticle-impact events. Chronoamperometric scans of 50 s duration with a sampling time of 0.0005 s were recorded. The number and magnitude of the spikes were determined by the "SignalCounter" software developed by Dr. Dario Omanović from Ruđer Bošković Institute, Zagreb, Croatia.[9] The "SignalCounter" is programmed to pick up spikes of a minimum intensity of 5.0 pA height. A linear baseline was taken and the charge underneath the peak calculated. The baseline was taken at the midpoint of the average noise to minimize the amount of background current taken as a signal. All signals were further checked by visual inspection to differentiate the actual spikes from noise via the signal shape. Statistical analysis on the measured spike current, charge, duration and frequency was performed with OriginPro 2017 Version 9.4.

2.3. Non-Electrochemical Instrumentation

Several non-electrochemical instrumentations were used to characterize the materials employed within this thesis. Each material was characterized by different co-workers using specific instrumentation as listed in Table 2.4. Dr. Neil P. Young and Ms. Jennifer Holter (Department of Materials, Oxford University) are acknowledged for the provision of electron microscopy and nanoparticle characterization facilities. Professor Simon J. Clarke (Department of Chemistry, Oxford University) is acknowledged for the provision of X-ray diffraction facilities. Details of experimental

procedures specific to each non-electrochemical instrumentation will be described in relevant chapters.

Table 2.4. List of non-electrochemical instrumentation used for specific material

Material	Chapter	Instrumentation	Performed by
AgNPs	3	SEM	Dr. Stanislav Sokolov
		TEM	
AuNPs@TA	4, 5, 6	SEM	Dr. Stanislav Sokolov
		TEM	Dr. Hatem M. Amin
		DLS	Dr. Hatem M. Amin
		NTA	Dr. Hatem M. Amin
		Zeta Potential	Dr. Stanislav Sokolov
AuNPs@CA	7	TEM	Dr. Hatem M. Amin
		SEM	
		DLS	
		NTA	
		Zeta Potential	
$LiMn_2O_4$	8	PXRD	Dr. Bertold Rasche

2.3.1. Transmission Electron Microscopy

Transmission electron microscopy (TEM) is a microscopy technique to measure the nanoparticle size whereby a beam of electrons is transmitted through the sample for imaging, which able to detect particles as small as 0.1 nm.[10,11] With aberration correction, TEM is capable of reaching a higher resolution where single atoms can be seen. In this thesis, TEM imaging analysis of the AgNPs, AuNPs@TA, and AuNPs@CA was carried out using a JEM-3000F instrument (JEOL Ltd., Japan) with a field-emission gun and an accelerating voltage of 300 kV.

Sample preparation consisted of modifying carbon grids (Agar Scientific Ltd., UK) by the drop-casting of AgNPs (2.5 x 10^{10} particles), AuNPs@TA (2.0 x 10^{9} particles) or AuNPs@CA (ca. 5.0 x 10^{8} particles), independently, then allowing them to completely dry under an N_2 flow. Different areas of the grid were imaged to ensure a representative view of the sample. Subsequent image extraction and analysis were performed using ImageJ software (National Institute of Health, US). The TEM micrographs and their analysis for AgNPs, AuNPs@TA and AuNPs@CA can be found in Chapter 3, Chapter 6 and Chapter 7, respectively.

2.3.2. Scanning Electron Microscopy

Scanning electron microscopy (SEM) imaging analysis was performed to determine the size, morphology and surface area of the nanoparticles. SEM is capable of measuring nanoparticles with a diameter not less than 1 nm.[12] However, often the nanoparticles are prone to change during SEM sample preparation and tend to aggregate on the sample holder.[12,13] In this thesis, SEM analysis of the AgNPs, AuNPs@TA, and AuNPs@CA were performed using a JSM-6500F instrument (JEOL Ltd., Japan) with an accelerating voltage of 5 kV and a secondary electron imaging mode. A glassy carbon plate (MFCD00133992, 3.0 mm thick, type 2, Lancashire, UK), cleaned in aqua regia, was used as an electron imaging substrate. After polishing steps (see above), SEM samples were prepared by drop-casting AgNPs (2.5 x 10^{10} particles), AuNPs@TA (2.0 x 10^{9} particles) or AuNPs@CA (5.0 x 10^{8} particles) onto the GC plate, separately. SEM images were analyzed for particle size and distributions using ImageJ (National Institute of Health, USA) and OriginPro 2017. The SEM micrographs and their analysis for AgNPs, AuNPs@TA and AuNPs@CA can be found in Chapter 3, Chapter 4 and Chapter 7, respectively.

2.3.3. Dynamic Light Scattering

Dynamic light scattering (DLS) is a laser scattering method that can be used to measure the hydrodynamic diameter size through the light scattered by the particles.[13] DLS can be used to size particles between 1 and 5,000 nm.[14] However, it is unable to determine the concentration or identity of nanoparticles in a solution. DLS analysis was performed to measure the hydrodynamic diameter of the AuNPs@TA and AuNPs@CA.

In this thesis, DLS measurements were carried out using a Malvern Zetasizer Nano ZS instrument with a 633 nm He-Ne laser. Each sample was diluted with deionized water and filtered using a sterile Whatman 0.2 μm filter to remove any contaminants before being placed in a disposable solvent-resistant micro-cuvette (path length of 10 mm). Three sets of 12 light scattering measurements were recorded and averaged to give three size distributions for the particles. Zetasizer software from Malvern (Malvern Panalytical Ltd., Malvern, UK) was used to analyze the data. The DLS analysis for the AuNPs@TA and AuNPs@CA can be found in Chapter 6 and Chapter 7, respectively.

2.3.4. Nanoparticle Tracking Analysis

Nanoparticle tracking analysis (NTA) uses a laser to illuminate the particles and a microscope to detect the movement of the individual particles, whilst DLS measures the particle size through the light scattered by the nanoparticles. NTA analysis is used to size and quantify nanoparticles in solution. The minimum nanoparticle diameter that can be detected is 10 nm.[15] However, this lower limit is dependent on the refractive index of the nanoparticle material. The sample does not have to undergo any special pre-treatment apart from dilution to the appropriate concentration (within the range of 10^7-10^9 particles mL^{-1}).

NTA was performed with a NanoSight LM10 (NanoSight, Amesbury, UK), equipped with a sample chamber and a red 642 nm laser to illuminate the particles so they could be tracked. A 500.0 µL sample of either AuNPs@TA or AuNPs@CA suspension was injected independently into the sample chamber with sterile syringes (BsD Discardit II, US) and the absence of air bubbles ensured. Three runs of 60 s each on three different portions of the samples was measured with an automatic setting of 30 frames per second. A microscope with an incorporated digital video recorder is used to visualize and record a video of the light being scattered by the nanoparticles. The particles appear as bright spots against a black background in the recorded video which can be analyzed by the NTA software suite. The NTA analysis for AuNPs@TA and AuNPs@CA can be found in Chapter 6 and Chapter 7, respectively.

2.3.5. UV-vis Spectroscopy

UV-vis spectroscopy measures the surface plasmon signals caused by the oscillating electron field of the nanoparticles.[16] Certain small changes on the nanoparticle surface, the stability, can be detected through UV-vis spectroscopy. In this thesis, a Shimadzu UV-1800 spectrophotometer with 20.0 µL High Precision Quartz Cells (Hellma Analytics, Germany) was used to measure the stability of the AuNPs@TA suspension in a solution of 10.0 to 100.0 mM HCl–KCl and AuNPs@CA in NaOH solution containing 5.0 mM to 50.0 mM KCN. Note that each solution was degassed with a nitrogen flow followed by performing baseline correction prior to the measurement. UV-vis spectra were recorded from 650 nm to 400 nm for the AuNPs@TA and from 650 nm to 450 nm for the AuNPs@CA; both with 1 min interval for 15 min measurement. The analysis of the stability of AuNPs@TA and AuNPs@CA suspensions can be found in Chapter 6 and Chapter 7, respectively.

2.3.6. Zeta Potential

Zeta potential measurement is used to quantify the magnitude of the charge of the particle and to assess the stability of colloidal dispersions. The magnitude of the zeta potential shows the degree of electrostatic repulsion between adjacent, similarly charged particles in a dispersion.[17] In this thesis, zeta potential measurements were performed using Zetasizer Nano ZS (Malvern Instruments, Ltd. Malvern, UK) with an irradiation wavelength of 638 nm (He laser). Disposable folded capillary cells were filled with the AuNPs@TA or AuNPs@CA suspension independently using a disposable syringe. Measurements were repeated six times during which the suspension was re-dispersed by brief ultrasonic agitation. The particle surface charge analysis for the AuNPs@TA and AuNPs@CA suspensions can be found in Chapter 4 and Chapter 7, respectively.

2.3.7. Powder X-ray Diffraction (PXRD)

PXRD analysis is used to determine the structural composition, phase, and orientation of lattice planes of the sample towards the different morphology of lattice planes. In Chapter 8, PXRD measurements were performed to analyze the structure of the lithium manganese oxide before and after the delithiation step at different times. The PXRD analysis was done on a PANalytical Empyrean instrument operating in Bragg-Brentano geometry with a curved Ge(111) Johansson monochromator to select $CuK_{\alpha 1}$ = 1.54060 Å radiation with a step size of 0.013° 2θ. A 5.0 µl of the slurry (see Chapter 8 for composition detail) drop cast onto 20.0 mm diameter – 2.0 mm thick glassy carbon disc (GCD) and annealing it at 65 ^{o}C for 10 min to evaporate the solvent. The GCD was directly mounted on a sample holder. The data was then evaluated with $WinX^{Pow}$ software.[18]

Bibliography

(1) Synthetic Urine e.K. https://www.synthetic-urine.de/en/produkt/synthetic-saliva-din-53160-1-din-en-6462006-07/. Accessed on 14 August 2019.

(2) Ngamchuea, K.; Chaisiwamongkhol, K.; Batchelor-McAuley, C.; Compton, R. G. Chemical Analysis in Saliva and the Search for Salivary Biomarkers – a Tutorial Review. *Analyst* 2018, *143* (1), 81–99.

(3) CUREC (Approved Procedure 24: IDREC 24 Version 3.0, University of Oxford). https://researchsupport.admin.ox.ac.uk/governance/ethics/resources/ap. Accessed on 14 August 2019.

(4) Instructions for use Salivetts® Cortisol. https://www.sarstedt.com/salivasputum/51.1534/. Accessed on 5 April 2019.

(5) W. M. Haynes. CRC Handbook of Chemistry and Physics 2012-2013, 93rd Ed. *CRC Press. Florida, USA* 2012.

(6) Batchelor-McAuley, C.; Ellison, J.; Tschulik, K.; Hurst, P. L.; Boldt, R.; Compton, R. G. In Situ Nanoparticle Sizing with Zeptomole Sensitivity. *Analyst* 2015, *140* (15), 5048–5054.

(7) Sokolov, S. V.; Eloul, S.; Kätelhön, E.; Batchelor-McAuley, C.; Compton, R. G. Electrode–Particle Impacts: A Users Guide. *Phys. Chem. Chem. Phys.* 2017, *19* (1), 28–43.

(8) Kätelhön, E.; Tanner, E. E. L.; Batchelor-McAuley, C.; Compton, R. G. Destructive Nano-Impacts: What Information Can Be Extracted from Spike Shapes? *Electrochim. Acta* 2016, *199*, 297–304.

(9) Ellison, J.; Tschulik, K.; Stuart, E. J. E.; Jurkschat, K.; Omanović, D.; Uhlemann, M.; Crossley, A.; Compton, R. G. Get More out of Your Data: A New Approach to Agglomeration and Aggregation Studies Using Nanoparticle Impact Experiments. *ChemistryOpen* 2013, *2* (2), 69–75.

(10) D. B. Williams and C. B. Carter, The transmission electron microscope (Springer, 1996).

(11) S. L. Flegler, J. W. Heckman Jr., and K. L. Klomparens, Scanning and Transmission Electron Microscopy: An Introduction, Oxford University Press, New York, 1993.

(12) Vernon-Parry, K. D. Scanning Electron Microscopy: An Introduction. *III-Vs Rev.* 2000, *13* (4), 40–44.

(13) P. Atkins and J. De Paula, Atkins' Physical Chemistry (Oxford University Press, Oxford, U.K., 2006), eighth edition.

(14) Lim, J.; Yeap, S. P.; Low, S. C. Characterization of Magnetic Nanoparticle by Dynamic Light Scattering. *Nanoscale Res. Lett.* 2013, *8* (1), 381.

(15) B. Carr and Wright, Nanoparticle Tracking Analysis (NanoSight, Amesbury, U.K., 2013).

(16) Haiss, W.; Thanh, N. T. K.; Aveyard, J.; Fernig, D. G. Determination of Size and

Concentration of Gold Nanoparticles from UV–Vis Spectra. *Anal. Chem.* 2007, *79* (11), 4215–4221.

(17) S. Bhattacharjee, DLS and zeta potential – what they are and what they are not? *J. Control. Release*. 2016, *235*, 337–351

(18) WinXPow. Program for the Collection and the Evaluation of X-Ray Powder Data. STOE & Cie GmbH, Darmstadt, Germany (1999).

Chapter 3

A Sensor for Inorganic Hg^{2+} in Aqueous Solution Using Galvanic Displacement

This chapter will focus on the detection and quantification of inorganic mercury (Hg^{2+}) in aqueous solutions at a silver nanoparticle-modified glassy carbon electrode by undertaking linear sweep voltammetry. This is achieved by monitoring the change in the silver stripping peak with Hg^{2+} concentration resulting from the galvanic displacement of silver by mercury. The sensor shows excellent linearity of 100.0 pM-10.0 nM Hg^{2+}, a detection limit of 28.0 pM (based on 3σ) and a "measurable lower limit" of 100.0 pM. This sensor is suitable for routine environmental monitoring and drinking water quality assessment, meeting the 30.0 nM guidelines issued by the World Health Organization (WHO) for inorganic mercury in drinking water.

This work has been published in *Analytical Chemistry* (*Anal. Chem*. 2017, *89* 13, 7166–7173). This chapter is also complemented with work that has been published in *Trends in Analytical Chemistry* (*TrAC Trends Anal. Chem*. 2017, *94*, 161–172). In this work, Dr. Kamonwad Ngamchuea and Dr. Eden Tanner helped with the interpretation of the experimental results. Dr. Stanislav Sokolov (in collaboration with Dr. Neil P. Young and Ms. Jennifer Holter from Department of Materials, Oxford University) recorded the scanning electron microscope (SEM) and transmission electron microscope (TEM) images on the silver nanoparticles.

3.1. Introduction

Exposure to mercury by the consumption of contaminated drinking water and food products may result in mortality, reproductive failure and other health effects in humans.[1-4] There are increasing awareness and necessity for detection of mercury and is considered by the World Health Organization (WHO) as one of the top ten chemicals of major public health concern.[1]

The WHO and the US Environmental Protection Agency (EPA) have issued guideline values for drinking water quality of 30.0 nM[5] and 10.0 nM[6] for inorganic mercury (Hg^{2+}), respectively. The development of a highly sensitive detection method that is reliable and simple for the routine detection of the Hg^{2+} in drinking water is urgently needed. Currently, common detection methods for Hg^{2+} include, but not limited to, UV-Vis spectrophotometry[7], atomic absorption spectrometry (AAS)[8], cold vapour atomic absorption spectrometry (CVAAS)[9], atomic emission spectrometry (AES)[10], X-ray fluorescence spectrometry (XFS)[11], inductive coupled plasma mass spectrometry (ICP-MS)[12], and colorimetric assay[13]. These methods generally have high sensitivity and selectivity. However, they require large sample volume, bulky instrumentation and extensive sample pre-treatment that limit their application to in situ analysis.[14-16]

Voltammetric techniques are promising alternatives for the determination of inorganic Hg^{2+} in aqueous samples due to their excellent sensitivity, low cost and short analysis time. Voltammetric analyses have been performed using different electrodes, including graphite[15,17], carbon paste[18,19], glassy carbon[20,21], screen-printed carbon[22,23], gold[24-26], platinum[27], titanium dioxide[28] and silver[29]. Anodic stripping voltammetry (ASV) has been used to detect micromolar levels of Hg^{2+} deposited on the titanium dioxide electrodes by photochemical reduction, but required significant pre-

concentration times to achieve reasonable sensitivity[28], whilst linear sweep voltammetry (LSV) has also been employed to detect trace level of Hg^{2+} at gold ultra-microelectrode arrays.[26] However, bulk gold, platinum, and silver electrodes are not suitable for Hg^{2+} detection since they suffer from structural changes of their surface caused by amalgam formation. This phenomenon can lead to decreasing sensor performance and loss of reproducibility[30], whilst the sensitivity of unmodified carbon electrodes is generally low and the detection limit and pre-concentration time are not acceptable for routine analyses.[14,15]

In this chapter, a glassy carbon electrode (GCE) was modified by drop-casting silver nanoparticles (AgNPs) without further surface modification. Under a suitable applied potential, the AgNPs interact with Hg^{2+} in the solution so as to galvanically dissolve silver via the reaction Ag (np) + ½ Hg^{2+} (aq) → Ag^{+} (aq) + ½ Hg (l). This leads to the loss of the stripping signal associated with the AgNPs. The large surface area of the drop cast AgNPs permits a high sensitivity analytical performance since only tiny amounts of Hg^{2+} are required to displace measurable amounts of silver. The use of nanoparticles thus permits the measurement of the loss of silver, which would not be possible with a bulk silver electrode. This proposed method is accessible for routine detection and quantification of Hg^{2+} for environment and drinking water quality purposes.

3.2. Experimental

Details about the chemical reagents here utilized can be found in Chapter 2, Section 2.1. Note that a standard mercury/mercurous sulfate electrode (MSE, Hg/Hg_2SO_4, K_2SO_4 (saturated), +0.62 V vs SHE) was used as a reference electrode (ALS distributed by BASi, Japan).

Size characterization of the AgNPs was carried out using a Transmission Electron Microscope (TEM), a JEOL 3000F instrument, which has a field-emission gun and is operated at 300 kV. Sample preparation consisted of modifying carbon grids by drop-casting the AgNPs suspension and allowing them to completely dry under an N_2 stream. Different areas of the grid were imaged to ensure a representative view of the sample. ImageJ software developed at the National Institute of Health, USA was used to size the particles recorded on the TEM images.

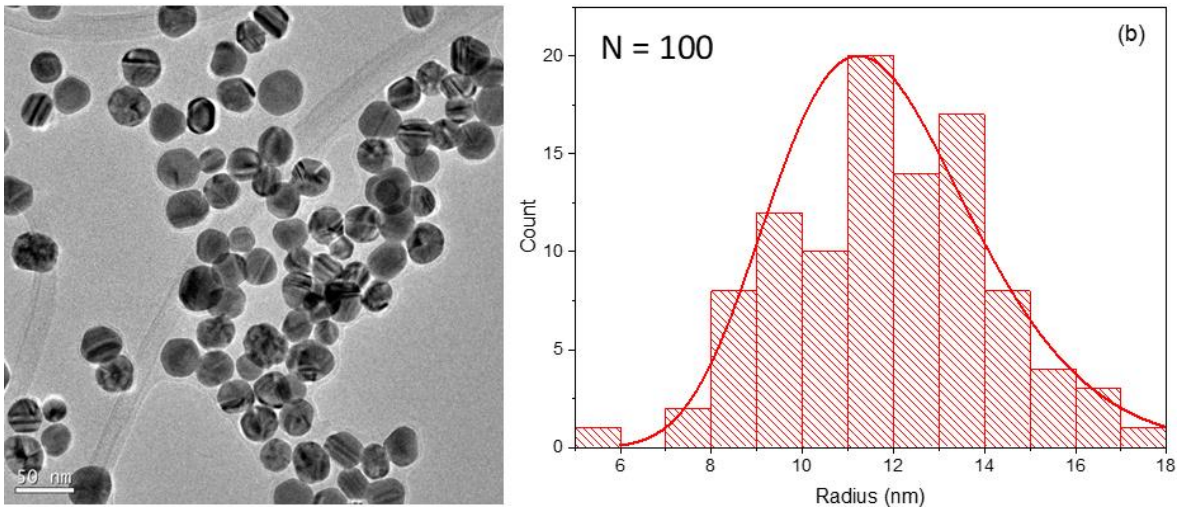


Figure 1. (a) TEM image of batch "A" AgNPs, (b) Statistical distribution of the AgNPs radius size as extracted from TEM images of 100 nanoparticles.

Figure 1a shows a TEM image of batch "A" of the AgNPs[31]. The data were processed to give a size distribution of the nanoparticle radii depicted in Figure 1b using OriginPro 2017 software for Windows. A lognormal curve is used to fit the data. The lognormal distribution of the particle size gave a mean radius of 11.9 (*/2.2) nm. For a lognormal distribution, the confidence interval is reported with a sign "*/" to indicate that it is obtained by multiplying or dividing the lognormal mean value by the standard deviation, as compared to sign "±" for a normal distribution.[32] To assess the

effect of size on Hg^{2+} detection, other sizes of AgNPs were used and sized to have a mean radius of 6.2 (*/1.5) nm and 22.5 (*/3.0) nm for batch B and nominally 50 nm diameter, respectively.

The aggregation/agglomeration state of the particles was characterized using a JEOL JSM-6500F is a field-emission Scanning Electron Microscope (SEM) with an accelerating voltage of 5 kV using a secondary electron imaging mode. A glassy carbon (GC) plate was used as an electron imaging substrate. The preparation of the GC plate involved treatment with aqua-regia in order to provide a clean metal-free surface, rinsing with deionized water and followed by the polishing procedure used for electrode preparation as described above.

3.3. Results and Discussion

This section outlines a method for the detection of ultra-trace levels of Hg^{2+} in aqueous solution by monitoring the reduction in the size of the silver stripping peak from the AgNPs-GCE with increasing Hg^{2+} concentration in the solution and exposure. First, the optimization of parameters that control the silver stripping peak is discussed. Second, the detection of ultra-trace levels of Hg^{2+} is undertaken by monitoring the magnitude of the silver stripping signal as a function of Hg^{2+} concentration. Third, the effect of the nanoparticle size towards the resulting signal or sensitivity is discussed.

3.3.1. Optimizing the Silver Stripping Peak

First, the glassy carbon electrode (GCE) was modified with 11.9 (*/2.2) nm AgNPs. This size of NPs is used throughout except for a brief comparison with nanoparticles of other sizes in Section 3.3.2 where they are shown to be optimal.

After placing a droplet containing 2.5 x 1010 NPs, leading to the formation of ca. 1.75-monolayer coverage (see Appendix A.1) onto the GCE surface, it was dried under an N_2 stream, resulting in a silver nanoparticle-modified glassy carbon electrode (AgNPs-GCE). The AgNPs-GCE was then immersed in 0.1 M KNO3 and cyclic voltammetry (CV) was recorded by sweeping the potential at a scan rate of 0.025 V s-1 from -0.50 V vs MSE to 0.40 V and back to -0.50 V (Figure 2a).

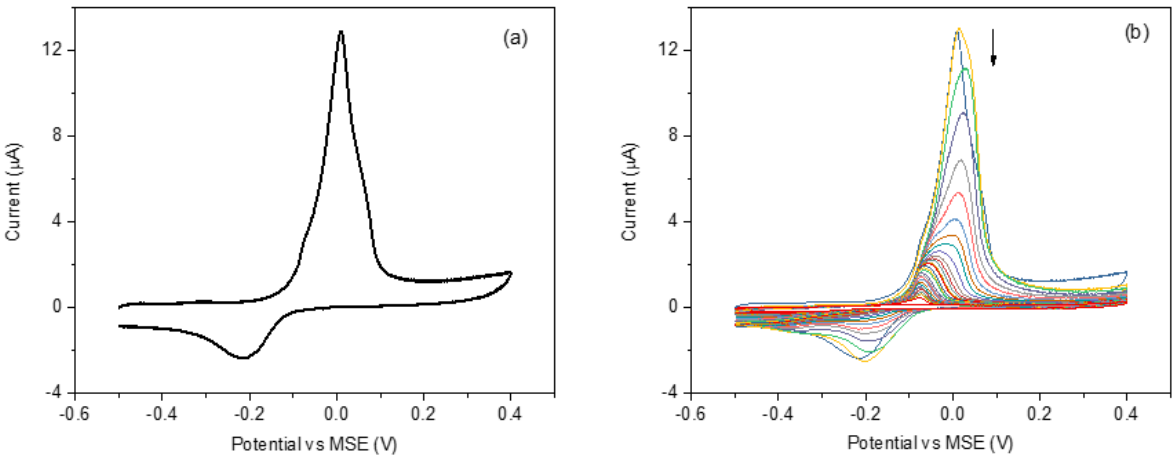


Figure 2. Cyclic voltammograms of the AgNPs-GCE immersed in 0.10 M KNO_3 at a scan rate of 0.025 V s^{-1} from -0.5 V to 0.4 V and back to -0.5 V vs SCE. (a) First scan, (b) 30 successive scans.

On the first forward scan, a peak corresponding to Ag to Ag^+ oxidation was observed with a peak potential of 0.0095 V vs MSE with a peak height of 12.9 μA, whilst on the reverse scan a reductive peak found at -0.2 V vs MSE.[33] The latter is a result of the oxidized silver being re-reduced on the electrode surface. Integrating the forward peak results in a peak charge of 119.0 μC. The expected charge (calculated from the number of nanoparticles drop cast and assuming that each atom transfers one electron) is ca. 1.8 mC, suggesting that ca. 7.0% was stripped from the GCE surface. This observation of partial stripping is consistent with literature reports documenting the oxidation of immobilized AgNPs on GCE.[34]

Next, a CV of thirty successive scans was undertaken on an electrode modified with 2.5 x 10^{10} NPs (Figure 2b). Over thirty scans, the net oxidative peak charge was ca. 340.0 μC, suggesting that ca. 19.0% of the silver had been stripped from the electrode surface. The cause of this incomplete stripping is discussed below.

The effect of electrode surface coverage on the resultant silver stripping peak was then investigated by altering the number of nanoparticles used to modify the electrode surface. Five thicknesses of nanoparticles were examined from approximately a one-monolayer to ca. 14-monolayers coverage, crudely estimated assuming close packing of 91%.[35] As above, the various amounts of silver nanoparticle were each drop cast onto a clean GCE surface and then the modified electrode (AgNPs-GCE) was immersed in 0.1 M KNO_3. Linear sweep voltammetry was then recorded at a scan rate of 0.1 V s^{-1} by sweeping the potential from -0.01 V to 0.5 V vs MSE and returning to -0.01 V (Figure 3).

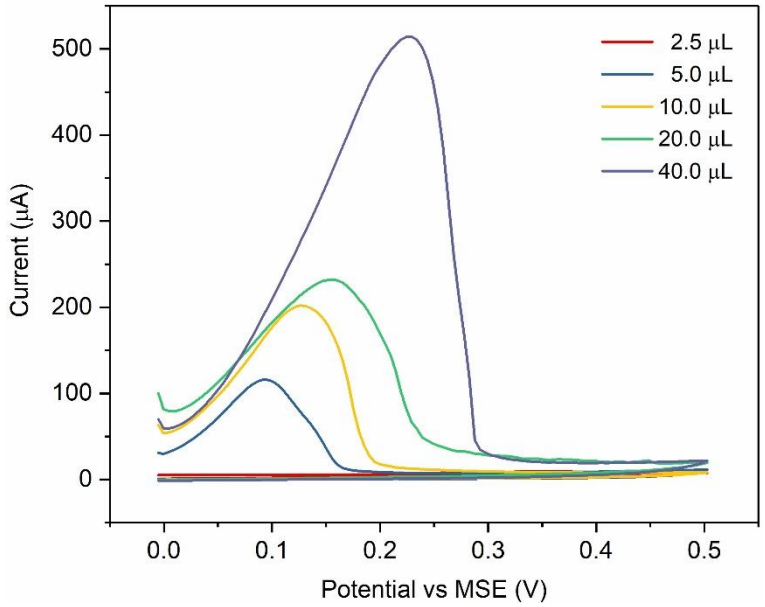


Figure 3. Linear sweep voltammogram of the AgNPs-GCEs immersed in 0.1 M KNO_3 with different drop cast masses, at a scan rate of 0.1 V s^{-1}.

Table 1 reports the peak charge for each surface coverage, along with the expected (maximum) charge and the percentage of silver successfully stripped on the first scan. Compared with the maximum theoretical stripping, the ca. 1.75-monolayer coverage achieved a stripping efficiency of ca. 7.0% from the first scan. This was approximately constant for ca. 1.75-monolayer coverage and above suggesting either only partial contact of the film with the electrode or significant aggregation/agglomeration of the nanoparticles.[36-39]

Table 1. Silver stripping peak charge at different drop cast masses

Surface Coverage	**Experimental Peak Charge**	**Expected Peak Charge**	**Stripping Efficiency**
1.0-monolayer	ca. 20.0 μC	ca. 0.9 mC	ca. 2.0%
1.75-monolayer	ca. 119.0 μC	ca. 1.8 mC	ca. 7.0%
3.5-monolayer	ca. 243.0 μC	ca. 3.5 mC	ca. 7.0%
7.0-monolayer	ca. 384.3 μC	ca. 6.9 mC	ca. 5.5%
14-monolayer	ca. 811.6 μC	ca. 13.8 mC	ca. 6.0%

To investigate the possible aggregation/agglomeration, a drop cast layer on a GCE surface was studied using SEM. Figure 4 shows the SEM image from a single droplet containing 2.5 x 10^{10} AgNPs, which shows a significant aggregation/ agglomeration state. The aggregation/agglomeration state of the particles drives the incomplete stripping of silver. Given the comparable efficiency of silver stripping peak, the ca. 1.75-monolayer surface coverage was selected for all further experiments to minimize the amount of silver required.

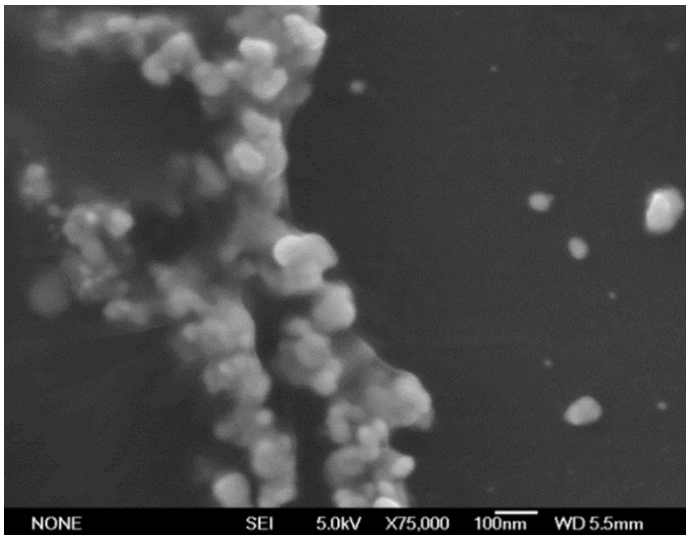


Figure 4. SEM image of 2.5 x 10^{10} AgNPs with scanning magnification of 75,000x.

Next, the effect of the scan rate was investigated. The AgNPs-GCE was immersed in 0.10 M KNO_3 and linear sweep voltammetry (LSV) was undertaken by sweeping the potential at -0.01 V to 1.0 V vs MSE and back to -0.01 V vs MSE at different scan rates. Figure 5 presents a plot of peak current vs scan rate with an R^2 = 0.980. The linear dependence of the peak current on the scan rate suggests that the species is surface-bound. For the analytical measurements reported below, a scan rate of 0.1 V s^{-1} was adopted for the reasons outlined in Section 3.3.2.

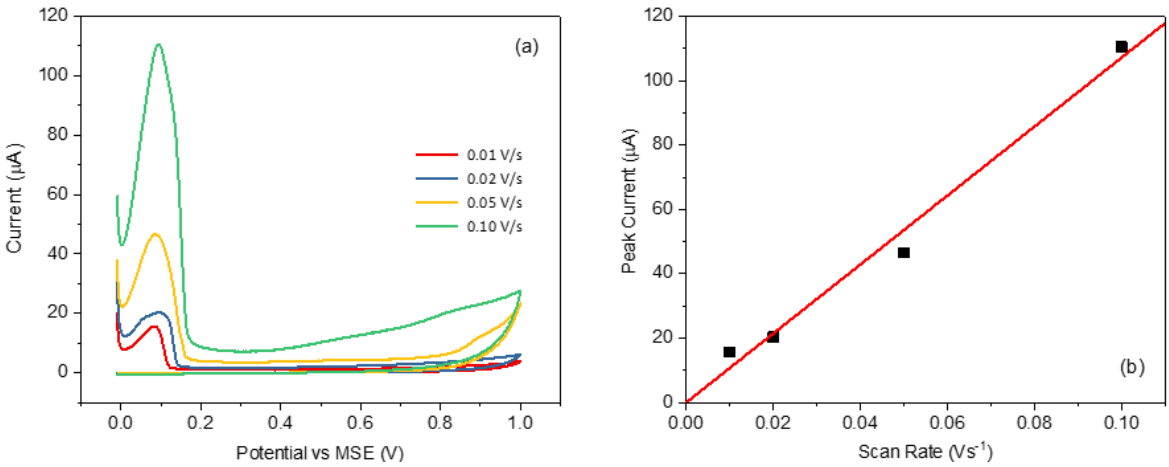


Figure 5. (a) Linear sweep voltammograms of AgNPs-GCEs immersed in 0.1 M KNO_3 at different scan rates and (b) a plot of scan rate vs peak current.

To assess the reproducibility, AgNPs-GCE was immersed in 0.1 M KNO_3 and held at a potential of -0.01 V vs MSE for 30 s. Next, an LSV was performed from -0.01 V to 1.0 V vs MSE and back to -0.01 V vs MSE at a scan rate of 0.1 V s^{-1} for three independent tests. The average peak current and peak charges are calculated to be 64.9 ± 0.3 μA and 59.6 ± 0.2 μC, respectively. As shown in Figure 6, a drop cast of 2.5 x 10^{10} AgNPs shows excellent reproducibility of the silver stripping peak.

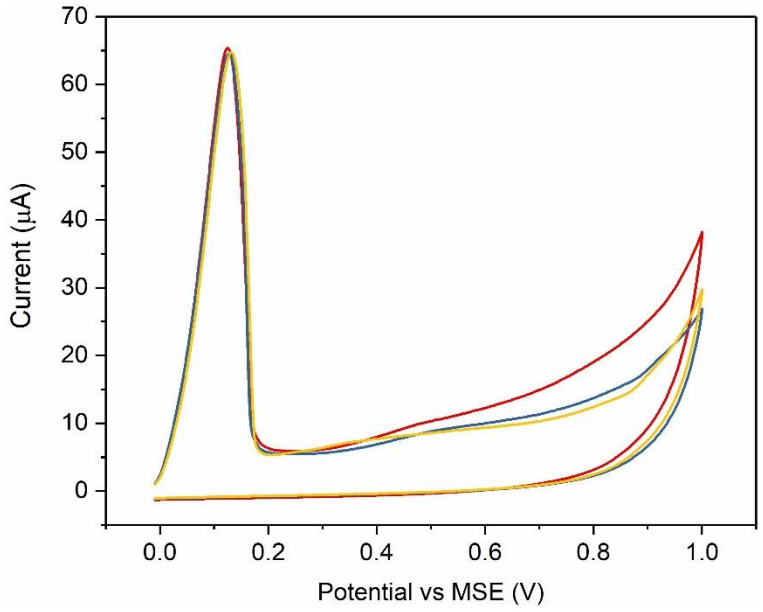


Figure 6. Reproducibility of three GCEs modified with 2.5 x 10^{10} AgNPs in 0.1 M KNO_3: 1st test (red), 2nd test (blue), 3rd test (yellow), at a scan rate of 0.1 V s^{-1}.

The pre-stripping time before the LSV being recorded plays a very important role to enable sensitivity of sensing performance. To assess the effect of pre-stripping time on the silver stripping peak, the AgNPs-GCE was immersed in 0.1 M KNO_3 and an LSV was undertaken in three independent tests with different pre-stripping times from zero to 500 seconds. As shown in Figure 7, a well-defined AgNPs stripping peak was found to decrease with time in solution. At a pre-stripping time of zero to 100 s, the peak is measurable, but at times of 200 s or above the peak is no longer discernible.

This is as a result of the AgNPs slowly dissolving from the GCE surface into the solution[40]. The dissolution is driven by the reduction of oxygen, which is even still present in micro-molar concentrations after extensive bubbling with nitrogen.[40] Compared to other pre-stripping times, 30 s allows for time for the silver to react without compromising the sensitivity, thus 30 s was selected for further experiments.

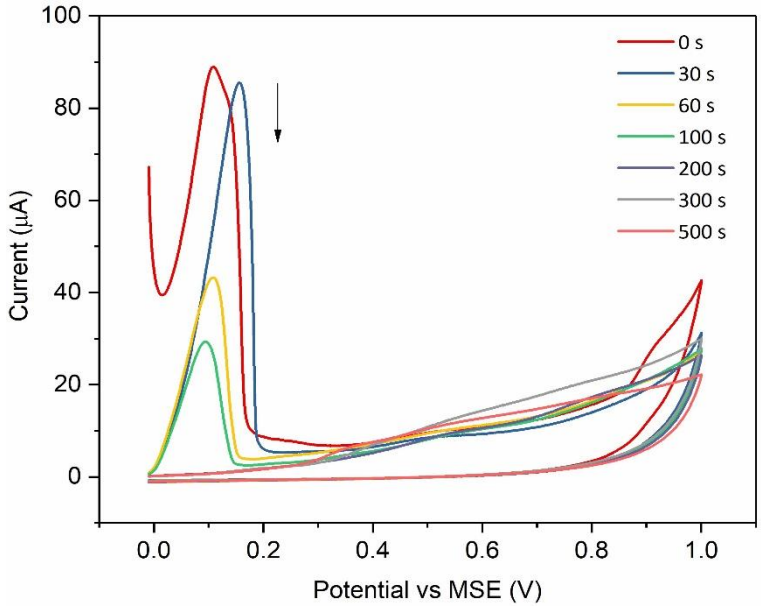


Figure 7. Linear sweep voltammograms of AgNPs-GCE in 0.1 M KNO_3 with different pre-stripping times at a scan rate of 0.1 V s^{-1}.

3.3.2. Electrochemical Detection of Ultra-trace Level of Hg^{2+}

With the silver stripping signal optimized in section 3.3.1., the use of the AgNPs-GCE to detect Hg^{2+} is next addressed. The stripping voltammetry detection approach has two steps; the first is a pre-stripping step, which involves holding the potential at a sufficiently negative value for a set length of time to allow the Hg^{2+} throughout the solution to react with the deposited silver without electro-deposition of mercury either in elemental form or as an amalgam. In this step, Hg^{2+} converts Ag to Ag^{+} and so the amount of material available for stripping is diminished by an amount reflecting the

concentration of Hg^{2+} in solution. The second step is the sweeping of the potential from -0.01 V to 1.0 V vs MSE, which results in the electrochemical oxidation of Ag^0 to Ag^+ at the GCE surface, allowing the detection of the Ag left unreacted by Hg^{2+} and thus by comparison with the stripping signal in the absence of Hg^{2+}, the Hg^{2+} concentration in the solution.

The deposition and subsequent stripping of Hg^{2+} on a GCE in the absence of AgNPs were investigated. An unmodified GCE was immersed in a 50.0 μM Hg^{2+} and held for two minutes at -0.5 V vs MSE such that Hg^{2+} deposition occurs[26]. The LSV was measured by sweeping the potential at a scan rate of 0.1 V s^{-1} from -0.50 V vs MSE to 1.0 V and back to -0.50 V (red curve, Figure 8). Two oxidation peaks appear at peak potentials of 0.046 V and 0.222 V vs MSE, which correspond to Hg^0 oxidation to Hg^+ and from Hg^+ to Hg^{2+} respectively[26,41]. The Hg(I) exists as Hg_2^{2+}. In the absence of Hg^{2+}, no oxidative features are present (yellow curve, Figure 8).

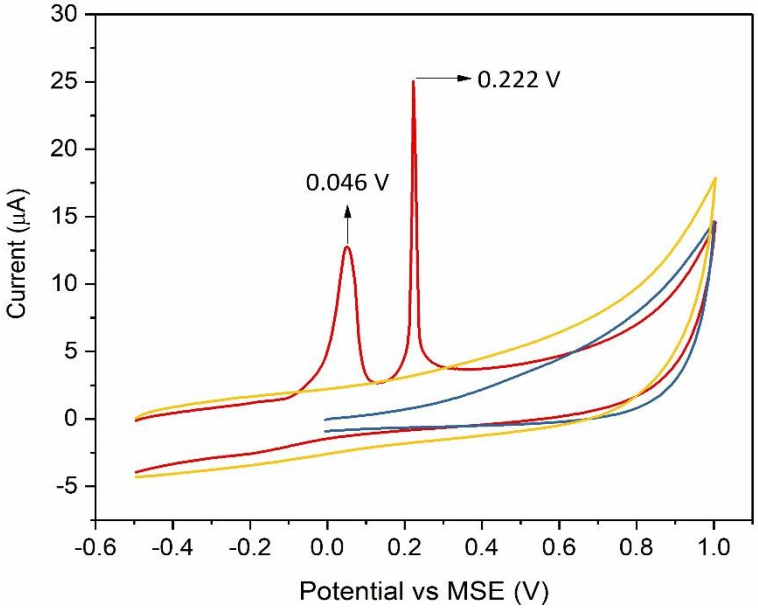


Figure 8. LSVs of unmodified GCE with starting potential of -0.5 V in 0.1 M KNO_3 (yellow curve), of -0.5 V in 50.0 μM Hg^{2+} (red curve) and of -0.01 V in 50.0 μM Hg^{2+} (blue curve).

To assess the effect of starting potential, an unmodified GCE was immersed in a solution containing 50.0 μM Hg^{2+} and an LSVs were recorded by sweeping the potential at a scan rate of 0.1 V s^{-1} from -0.01 V to 1.0 V vs MSE (blue curve, Figure 8). At these potentials, no mercury oxidation (Hg^{+} and Hg^{2+} stripping peaks) are observed. In the analytical determination of Hg^{2+} using AgNPs, the starting potential must be positive enough to ensure that any oxidative features present are as a result of the interaction between silver and Hg^{2+}, and not from the oxidation of mercury, which was electrochemically deposited (as would occur if the electrode was held at sufficiently negative potentials), and negative enough such that measurement of the full silver stripping peak is visible. With these constraints in mind, a starting potential of -0.01 V was selected. At this potential Hg(l) is not deposited from Hg^{2+} nor are the AgNPs stripped. Having optimized the starting potential, the analytical response of the AgNPs-GCE to different concentrations of Hg^{2+} was examined.

To assess the electroanalytical performance of AgNPs-GCE in the detection of ultra-trace levels of Hg^{2+}, a AgNPs-GCE was immersed in solutions of varying Hg^{2+} concentrations (100.0 pM to 10.0 nM) at pre-stripping time of 30 seconds, then an LSV was recorded at a scan rate of 0.1 V s^{-1} by sweeping the potential from -0.01 V vs MSE to 1.0 V and back to -0.01 V. As shown in Figure 9, in each case, two peaks appear. The first peak at ca. 0.1 V vs MSE and the second at ca. 0.3 V vs MSE. The first peak corresponds to the silver stripping, as established in section 3.3.1, whilst the second peak is related to mercury stripping as investigated earlier in this section. The decrease in the stripping peak as the Hg^{2+} concentration is increased, as explained above, is likely due to the reaction of Hg^{2+} with the AgNPs, which at least until the AgNPs are significantly oxidized, likely form an amalgam that is then oxidised at more positive potentials giving rise to the peak at ca. 0.3 V vs MSE. Due to the fact that the mercury

peak is heavily influenced by changes in kinetics and thermodynamics as the surface of the electrode changes with mercury deposition, the silver stripping peak was selected as the signal to be monitored rather than the mercury oxidation peak.

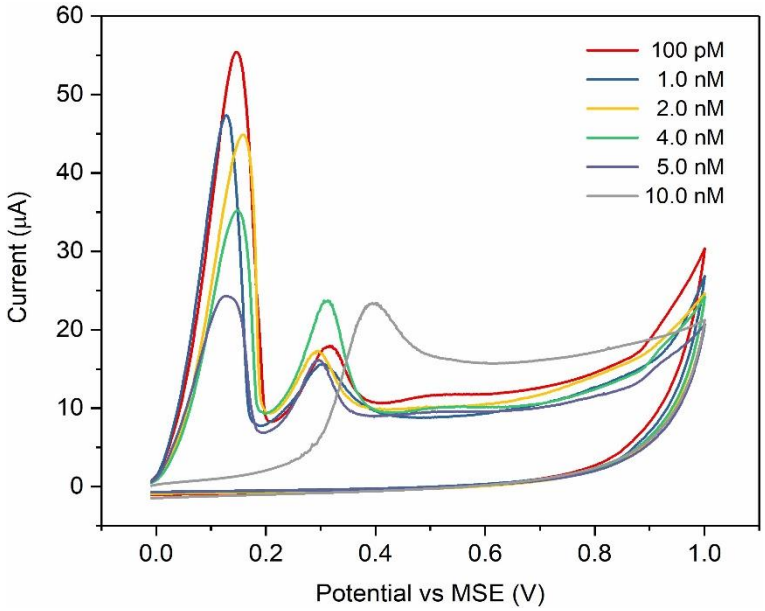


Figure 9. LSVs of AgNPs-GCE (2.5 x 10^{10} AgNPs) immersed in different Hg^{2+} concentrations with pre-stripping time of 30 s and at scan rate of 0.1 V s^{-1}.

To assess the relationship between the silver stripping peak and Hg^{2+} concentration, the AgNPs-GCE was immersed in 0.1 M KNO_3 and different concentrations of Hg^{2+} solutions. First, an AgNPs-GCE was immersed in a solution containing 100.0 pM Hg^{2+} and held at a potential of -0.01 V vs MSE for 30 s. Then, an LSV was recorded by sweeping the potential at a scan rate of 0.1 V s^{-1} from -0.01 V vs MSE to 1.0 V and back to -0.01 V. This procedure was repeated for eight others different Hg^{2+} concentrations in the range of 200.0 pM to 10.0 nM. The resulting data are shown in Figure 10 with a "normalized stripping signal" plotted against various Hg^{2+} concentrations. The reason for the normalization is as follows. In the absence of Hg^{2+}, the silver (AgNPs) stripping peak is affected by the pre-stripping time prior to the LSV

measurement, which allows sufficient time for the partial loss of silver via reduction of O_2. Note that the micro-molar concentration of O_2 is still present in the solution even after extensive bubbling with nitrogen.[42] The reduction of O_2 drives the oxidative dissolution of AgNPs from the GCE surface, thus decreasing the silver stripping peak. In the presence of Hg^{2+}, the silver stripping peak is affected by *both* the loss during the pre-stripping time and the Hg^{2+} in the solution. To measure the silver stripping peak such that it only reflects the Hg^{2+} concentration, the signal was normalized by dividing the peak obtained in the presence of Hg^{2+} by the peak obtained in the absence of Hg^{2+} with no pre-stripping time. The ratio is the normalized peak current or peak charge.

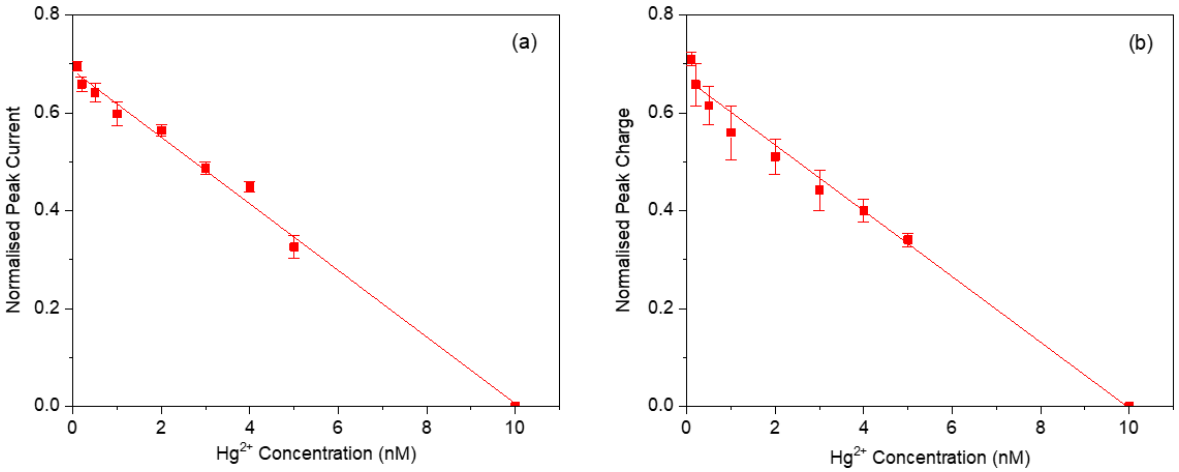


Figure 10. AgNPs-GCEs stripping peak in 100.0 pM-10.0 nM Hg^{2+} solutions in 0.1 M KNO_3. (a) Plot of normalized peak current, (b) plot of normalized peak charge.

Figure 10 shows how the normalized stripping peak current and the stripping peak charge on the first scan varies with the Hg^{2+} concentration. *Both* normalized peak current and peak charge ratios never reach a value of one because the pre-stripping time of 30 seconds enables the AgNPs to react with Hg^{2+} in the solution and decreases the silver stripping peak. Both figures show linear trends of AgNPs-GCE in the range of

100.0 pM to 10.0 nM Hg^{2+}. The linearity of measurement was found to be R^2 = 0.991 and R^2 = 0.982 for normalized peak current and peak charge, respectively.

3.3.3. The Effect of the Nanoparticle Size

The size of the nanoparticles used to modify the GCE was investigated in relation to the sensitivity of the measurement. To assess the effect of nanoparticle size on Hg^{2+} detection, AgNPs with a mean radius of 6.2 (*/1.50) nm (batch "B") or 22.5 (*/3.05) nm (nominally "50 nm diameter") were separately drop cast onto a GCE surface to give the same number of particles (2.5 x 10^{10} AgNPs). All experiments were performed in 0.1 M KNO_3, 500.0 pM, 2.0 nM and 5.0 nM Hg^{2+} solutions. There is no significant effect of AgNPs size on the resulting signal or sensitivity, suggesting that the process is controlled by diffusion of Hg^{2+} to the geometric area of the electrode rather than due to the surface area of silver available for oxidation. This result is confirmed by the analysis of variable surface coverages. A 2.5 x 10^{10} AgNPs with radius of 11.9 (*/2.2) nm, 1.25 x 10^{10} AgNPs with radius of 11.9 (*/2.2) nm and 2.5 x 10^{10} AgNPs with radius of 6.2 (*/1.5) nm were drop cast to form a 1.75-monolayer, 1.0-monolayer and 0.5-monolayer, respectively. All experiments were performed both in 0.1 M KNO_3 and at 500.0 pM, 2.0 nM, 5.0 nM Hg^{2+} solutions and the surface coverage were not found to affect the slope of the detection curve (Figure 11).

In summary, the proposed method for detection of ultra-trace levels of Hg^{2+} in aqueous solution monitors the loss of silver stripping peak from a drop cast ca. 1.75-monolayer of 11.9 (*/2.2) nm AgNPs in response to the Hg^{2+} concentrations. The limit of detection (LOD) based on 3σ[43,44] was calculated to be 28.0 pM. The latter compares favourably with alternative methods, which also involve much lengthier pre-treatment processes.[45-49]

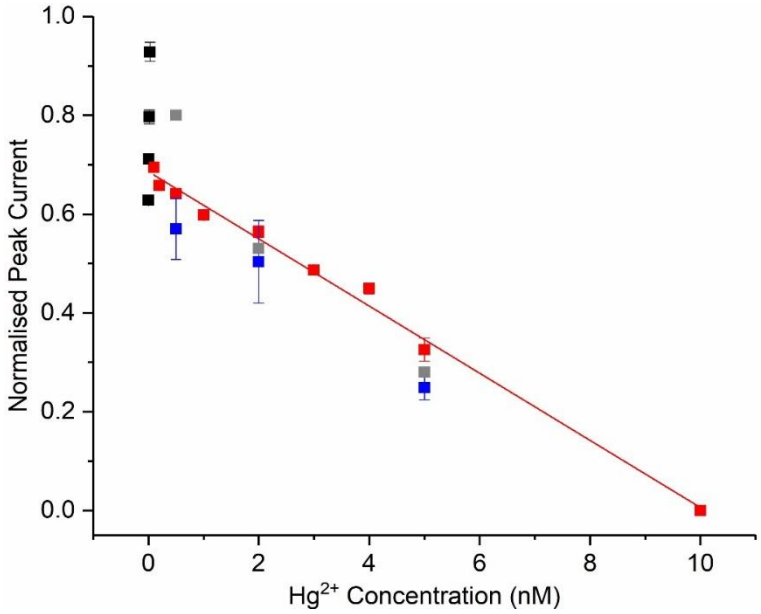


Figure 11. Normalized peak current of AgNPs stripping peak with different Hg^{2+} concentrations. Note that ca. 1.75-monolayer, r = 11.9 (*/2.2) nm (black, 1.0-30.0 pM Hg^{2+}), ca. 1.75-monolayer, r = 11.9 (*/2.2) nm (red, 100.0 pM-10.0 nM Hg^{2+}), ca. 1.0-monolayer, r = 11.9 (*/2.2) nm (blue) and ca. 0.5-monolayer, r = 6.2 (*/1.5) nm (grey).

3.4. Conclusions

A sensor for the detection and quantification of ultra-trace levels of Hg^{2+} in aqueous solutions has been developed by undertaking LSV using an AgNPs-GCE. This sensor is appropriate for routine environmental monitoring and drinking water quality assessment with the use of a disposable screen-printed electrode. The sensor is able to achieve a limit of detection of 28.0 pM and a linear range of 100.0 pM to 10.0 nM, meeting the 30.0 nM guidelines issued by the WHO[5] for inorganic mercury in drinking water. The transfer of the proposed methodology onto a disposable screen-printed electrode will make it accessible for routine monitoring and in situ applications. Future work needs to directly tackle issues of selectivity and heterogeneity. In addition to this, it is only by engaging with environmental samples that the full potential of voltammetry can be realized.

Bibliography

(1) WHO. Mercury and Health. www.who.int/en/news-room/fact-sheets/detail/mercury-and-health. Accessed on 2nd July 2019.

(2) Driscoll, C. T.; Chan, H. M.; Jacob, D. J.; Pirrone, N. Mercury as a Global Pollutant—Sources, Pathways, and Effects. *Environ. Sci. Technol.* 2013, *47* (10), 4967–4983.

(3) Wilhelm, S.; Bloom, N. Mercury in Petroleum. *Fuel Process. Technol.* 2000, *63* (1), 1–27.

(4) Gao, C.; Huang, X. J. Voltammetric Determination of Mercury(II). *TrAC - Trends Anal. Chem.* 2013, *51*, 1–12.

(5) WHO. Guidelines for Drinking-Water Quality, Fourth Edition. www.who.int/water_sanitation_health/publication/2011/dwq_guidelines/en/2011, Accessed on 2nd July 2019.

(6) US Environmental Protection Agency (EPA). EPA's Drinking Water Regulations for Mercury. www.safewater.zendesk.com/hc/en-us/articles/212076077-4-What-are-EPA-s-drinking-water-regulations-for-mercury. Accessed on 2nd July 2019.

(7) Ulusoy, H. İ.; Gürkan, R.; Ulusoy, S. Cloud Point Extraction and Spectrophotometric Determination of Mercury Species at Trace Levels in Environmental Samples. *Talanta* 2012, *88*, 516–523.

(8) Rey-Raap, N.; Gallardo, A. Determination of Mercury Distribution Inside Spent Compact Fluorescent Lamps by Atomic Absorption Spectrometry. *Waste Manag.* 2012, *32* (5), 944–948.

(9) Kopysc, E.; Pyrzynska, K.; Garbos, S.; Bulska, E. Determination of Mercury by Cold-Vapor Atomic Absorption Spectrometry with Preconcentration on a Gold-Trap. *Anal. Sci.* 2000, *16* (12), 1309–1312.

(10) Ioannidou, M. D.; Zachariadis, G. A.; Anthemidis, A. N.; Stratis, J. A. Direct Determination of Toxic Trace Metals in Honey and Sugars Using Inductively Coupled Plasma Atomic Emission Spectrometry. *Talanta* 2005, *65* (1), 92–97.

(11) Aranda, P. R.; Perino, E.; De Vito, I. E.; Raba, J. Solid-Phase Preconcentration and Determination of Mercury(II) Using Activated Carbon in Drinking Water by X-Ray Fluorescence Spectrometry. *X-Ray Spectrom.* 2013, *42* (2), 100–104.

(12) Fang, Y.; Pan, Y.; Li, P.; Xue, M.; Pei, F.; Yang, W.; Ma, N.; Hu, Q. Simultaneous Determination of Arsenic and Mercury Species in Rice by Ion-Pairing Reversed Phase Chromatography with Inductively Coupled Plasma Mass Spectrometry. *Food Chem.* 2016, *213*, 609–615.

(13) Jarujamrus, P.; Amatatongchai, M.; Thima, A.; Khongrangdee, T.; Mongkontong, C. Selective Colorimetric Sensors Based on the Monitoring of an Unmodified Silver

Nanoparticles (AgNPs) Reduction for a Simple and Rapid Determination of Mercury. *Spectrochim. Acta Part A Mol. Biomol. Spectrosc.* 2015, *142*, 86–93.

(14) Zaib, M.; Athar, M. M.; Saeed, A.; Farooq, U. Electrochemical Determination of Inorganic Mercury and Arsenic-A Review. *Biosensors and Bioelectronics*. 2015, pp 895–908.

(15) Martín-Yerga, D.; González-García, M. B.; Costa-García, A. Electrochemical Determination of Mercury: A Review. *Talanta*. 2013, pp 1091–1104.

(16) Daniel Martín-Yerga and Agustín Costa-García. Recent Advances in the Electrochemical Detection of Mercury. *Curr. Opin. Electrochem.* 2017, 3, 91-96.

(17) El Aroui, F.; Lahrich, S.; Farahi, A.; Achak, M.; El Gaini, L.; Manoun, B.; Bakasse, M.; Bouzidi, A.; El Mhammedi, M. A. Electrochemical Determination of Mercury(II) in Ambient Water at Palladium Oxide/Graphite Composite Electrodes. *J. Taiwan Inst. Chem. Eng.* 2014, *45* (5), 2725–2732.

(18) Wang, J.; Bonakdar, M. Preconcentration and Voltammetric Measurement of Mercury with a Crown-Ether Modified Carbon-Paste Electrode. *Talanta* 1988, *35* (4), 277–280.

(19) Afkhami, A.; Madrakian, T.; Sabounchei, S. J.; Rezaei, M.; Samiee, S.; Pourshahbaz, M. Construction of a Modified Carbon Paste Electrode for the Highly Selective Simultaneous Electrochemical Determination of Trace Amounts of Mercury(II) and Cadmium(II). *Sensors Actuators B Chem.* 2012, *161* (1), 542–548.

(20) Lu, J.; He, X.; Zeng, X.; Wan, Q.; Zhang, Z. Voltammetric Determination of Mercury(II) in Aqueous Media Using Glassy Carbon Electrodes Modified with Novel Calix[4]arene. *Talanta* 2003, *59* (3), 553–560.

(21) Ghanei-Motlagh, M.; Taher, M. A.; Heydari, A.; Ghanei-Motlagh, R.; Gupta, V. K. A Novel Voltammetric Sensor for Sensitive Detection of Mercury(II) Ions Using Glassy Carbon Electrode Modified with Graphene-Based Ion Imprinted Polymer. *Mater. Sci. Eng. C* 2016, *63*, 367–375.

(22) Cinti, S.; Santella, F.; Moscone, D.; Arduini, F. Hg^{2+} Detection Using a Disposable and Miniaturized Screen-Printed Electrode Modified with Nanocomposite Carbon Black and Gold Nanoparticles. *Environ. Sci. Pollut. Res.* 2016, *23* (9), 8192–8199.

(23) Somé, I. T.; Sakira, A. K.; Mertens, D.; Ronkart, S. N.; Kauffmann, J.-M. Determination of Groundwater Mercury(II) Content Using a Disposable Gold Modified Screen Printed Carbon Electrode. *Talanta* 2016, *152*, 335–340.

(24) Bonfil, Y.; Kirowa-Eisner, E. Trace Determination of Mercury by Anodic Stripping Voltammetry at the Rotating Gold Electrode. *Anal. Chim. Acta* 2000, *424* (1), 65–76.

(25) Wei, J.; Yang, D.; Chen, H.; Gao, Y.; Li, H. Stripping Voltammetric Determination of Mercury(II) Based on SWCNT-PhSH Modified Gold Electrode. *Sensors Actuators B Chem.* 2014, *190*, 968–974.

(26) Ordeig, O.; Banks, C. E.; Muñoz, F. X.; Compton, R. G. Trace Detection of Mercury(II) Using Gold Ultra-Microelectrode Arrays. *Electroanalysis* 2006, *18* (6), 573–578.

(27) Pinilla, J. M.; Hernández, L.; Conesa, A. J. Determination of Mercury by Open Circuit Adsorption Stripping Voltammetry on a Platinum Disk Electrode. *Anal. Chim. Acta* 1996, *319* (1–2), 25–30.

(28) Suárez, M. F.; Mills, A.; Egdell, R. G.; Compton, R. G. Anodic Stripping Voltammetry with Photochemical Preconcentration at Nanocrystalline TiO_2 Films: Detection of Ag^+ and Hg^{2+}. *Electroanalysis* 2000, *12* (6), 413–419.

(29) Farahi, A.; Lahrich, S.; Achak, M.; El Mhammedi, M. A. Effect of KNO_3 to Remove Silver Interferences in the Determination of Mercury(II): Application in Milk and Breast Milk Samples. *Sens. Bio-Sensing Res.* 2015, *4*, 90–95.

(30) Barrosse-Antle, L. E.; Xiao, L.; Wildgoose, G. G.; Baron, R.; Salter, C. J.; Crossley, A.; Compton, R. G. The Expansion/Contraction of Gold Microparticles during Voltammetrically Induced Amalgamation Leads to Mechanical Instability. *New J. Chem.* 2007, *31* (12), 2071–2075.

(31) Lees, J. C.; Ellison, J.; Batchelor-McAuley, C.; Tschulik, K.; Damm, C.; Omanović, D.; Compton, R. G. Nanoparticle Impacts Show High-Ionic-Strength Citrate Avoids Aggregation of Silver Nanoparticles. *ChemPhysChem* 2013, *14* (17), 3895–3897.

(32) Limpert, E.; Stahel, W. A.; Abbt, M. Log-Normal Distributions across the Sciences: Keys and Clues: On the Charms of Statistics, and How Mechanical Models Resembling Gambling Machines Offer a Link to a Handy Way to Characterize Log-Normal Distributions, Which Can Provide Deeper Insight into Variability and Probability—Normal or Log-Normal: That Is the Question. *Bioscience* 2001, *51* (5), 341–352.

(33) Zahid, A.; Lashin, A.; Rana, U. A.; Ullah, I.; Dionysiou, D. D.; Qureshi, R.; Waseem, A.; Kraatz, H. B.; Shah, A. Development of Surfactant Based Electrochemical Sensor for the Trace Level Detection of Mercury. *Electrochim. Acta* 2016, *190*, 1007–1014.

(34) Toh, H. S.; Batchelor-McAuley, C.; Tschulik, K.; Damm, C.; Compton, R. G. A Proof-of-Concept - Using Pre-Created Nucleation Centres to Improve the Limit of Detection in Anodic Stripping Voltammetry. *Sensors Actuators, B Chem.* 2014, *193*, 315–319.

(35) Kätelhön, E.; Cheng, W.; Batchelor-McAuley, C.; Tschulik, K.; Compton, R. G. Nanoparticle-Impact Experiments Are Highly Sensitive to the Presence of Adsorbed Species on Electrode Surfaces. *ChemElectroChem* 2014, *1* (6), 1057–1062.

(36) Toh, H. S.; Batchelor-McAuley, C.; Tschulik, K.; Uhlemann, M.; Crossley, A.; Compton, R. G. The Anodic Stripping Voltammetry of Nanoparticles: Electrochemical Evidence for the Surface Agglomeration of Silver Nanoparticles. *Nanoscale* 2013, *5* (11), 4884–4893.

(37) Cloake, S. J.; Toh, H. S.; Lee, P. T.; Salter, C.; Johnston, C.; Compton, R. G. Anodic Stripping

Voltammetry of Silver Nanoparticles: Aggregation Leads to Incomplete Stripping. *ChemistryOpen* 2015, *4* (1), 22–26.

(38) Toh, H. S.; Jurkschat, K.; Compton, R. G. The Influence of the Capping Agent on the Oxidation of Silver Nanoparticles: Nano-Impacts versus Stripping Voltammetry. *Chem. - A Eur. J.* 2015, *21* (7), 2998–3004.

(39) Neumann, C. C. M.; Laborda, E.; Tschulik, K.; Ward, K. R.; Compton, R. G. Performance of AgNPs in the Catalysis of the Oxygen Reduction Reaction in Neutral Media: Efficiency Limitation Due to Hydrogen Peroxide Escape. *Nano Res.* 2013, *6* (7), 511–524.

(40) Plowman, B. J.; Tschulik, K.; Walport, E.; Young, N. P.; Compton, R. G. The Fate of Nano-Silver in Aqueous Media. *Nanoscale* 2015, *7* (29), 12361–12364.

(41) Korolczuk, M. Sensitive and Selective Determination of Mercury by Differential Pulse Stripping Voltammetry after Accumulation of Mercury Vapour on a Gold Plated Graphite Electrode. *Fresenius. J. Anal. Chem.* 1997, *357* (4), 389–391.

(42) Clark, R. O. D.; Ngamchuea, K.; Batchelor-McAuley, C.; Compton, R. G. Electrochemical Measurement of the Dissolved Oxygen Concentration in Water in the Absence of Deliberately Added Supporting Electrolyte. *Electroanalysis* 2017, *29* (5), 1418–1425.

(43) Long, G. L.; Winefordner, J. D. Limit of Detection A Closer Look at the IUPAC Definition. *Anal. Chem.* 1983, *55* (07), 712A-724A.

(44) Laffont, L.; Hezard, T.; Gros, P.; Heimburger, L. E.; Sonke, J. E.; Behra, P.; Evrard, D. Mercury(II) Trace Detection by a Gold Nanoparticle-Modified Glassy Carbon Electrode Using Square-Wave Anodic Stripping Voltammetry Including a Chloride Desorption Step. *Talanta* 2015, *141*, 26–32.

(45) Tyszczuk-Rotko, K.; Barczak, M. Thiol-Functionalized Polysiloxanes Modified by Lead Nanoparticles: Synthesis, Characterization and Application for Determination of Trace Concentrations of Mercury(II). *Microporous Mesoporous Mater.* 2016, *230*, 109–117.

(46) Lahrich, S.; Manoun, B.; Mhammedi, M. A. El. Catalytic Effect of Potassium in $Na_{1-x}K_xCdPb_3(PO_4)_3$ to Detect Mercury(II) in Fish and Seawater Using a Carbon Paste Electrode. *Talanta* 2016, *149*, 158–167.

(47) Mahmoudian, M. R.; Aliasac, Y. A Sensitive Electrochemical Hg^{2+} Sensor Based on Polypyrrole Coated Nanospherical Platinum. *RSC Adv.* 2016, *6* (43), 36459–36466.

(48) Zhang, Y.; Zeng, G. M.; Zhu, Y.; He, X. X.; He, Y. Electrochemical Sensor Based on Electrodeposited Graphene-Au Modified Electrode and Nanoau Carrier Amplified Signal Strategy for Attomolar Mercury Detection. *Anal. Chem.* 2015, *87* (2), 989–996.

(49) Amiri, S.; Navaee, A.; Salimi, A.; Ahmadi, R. Zeptomolar Detection of Hg^{2+} Based on Label-Free Electrochemical Aptasensor: One Step Closer to the Dream of Single Atom Detection. *Electrochem. commun.* 2017, *78*, 21–25.

Chapter 4

Electrochemical Sensor for Al^{3+} Using Tannic Acid-capped Gold Nanoparticles

The previous chapter of this thesis dealt with the detection and quantification of metal ion through galvanic displacement (under a suitable applied potential) and using linear sweep voltammetry. In this chapter, the determination of aluminum ions (Al^{3+}) is achieved by utilizing tannic acid-capped gold nanoparticles through complexation and by employing square-wave voltammetry (SWV). The combination of gold nanoparticles and tannic acid as a capping/chelating agent (AuNPs@TA) results in the accurate and sensitive detection of inorganic Al^{3+} in aqueous solutions. The presented methodology gives clear measurable signals even at the measurable lower limit of 10.0 pM, markedly and usefully lower than the permissible level of 7.4 μM for inorganic Al^{3+} in drinking water as defined by the World Health Organization (WHO) and which compares favorably with alternative detection methods.

The work herein presented has been published in *Sensors and Actuators B: Chemical* (*Sensors Actuators B Chem.* 2018, *265*, 682–690) and was carried out in collaboration with Dr. Eden Tanner and Dr. Sabine Kuss, who helped with the interpretation of the experimental results. Dr. Stanislav Sokolov (in collaboration with Dr. Neil P. Young and Ms. Jennifer Holter from the Department of Materials, Oxford University) obtained the scanning electron microscope images and measurement of the zeta potential of the AuNPs@TA.

4.1. Introduction

The contamination of drinking water and food products by aluminum ions (Al^{3+}) represents a serious health issue[1], as it has been associated with the occurrence of Alzheimer's disease[2], Parkinson's dementia[3], renal osteodystrophy[4], and chronic kidney disease[5]. The World Health Organization (WHO) has reported acceptable levels for aluminum of ≤3.7 μM and ≤7.4 μM in treated water for large and small water treatment facilities, respectively.[6] Thus, a highly sensitive detection method that is reliable and simple for the routine monitoring of Al^{3+} in drinking water and food products is needed.

The analytical determination of Al^{3+} has conventionally been performed, but not limited to, using inductively coupled plasma atomic emission spectrometry (ICP-AES)[7], electrothermal atomic absorption spectrometry (ETAAS)[8], UV-vis diffuse reflectance spectroscopy (UV-vis DRS)[9] and spectrophotometry[10]. Although these methods offer reasonable sensitivity and reliability, their drawbacks such as extensive sample preparation, required expertise in handling, expensive instrumentation and the limitation to *ex-situ* analysis cannot be avoided. Voltammetry with its high sensitivity, rapid analysis time, low cost and possible adaptation for *in situ* analysis is an ideal technique for the routine monitoring of samples contaminated by Al^{3+}. In the literature, the determination of Al^{3+} in aqueous solution by voltammetry was achieved via metal-complexation in the presence of complexing agents, such as 1,2-dihydroxyanthraquinone-3-sulfonic acid[11], alizarin S[12], alizarin violet[13], pyrogallol red[14], 8-hydroxyquinoline[15] and ionophore JS-1[17]; using thin mercury film electrodes, renewable silver amalgam film electrodes, multi-walled carbon nanotube-modified carbon paste electrodes, mercury electrodes, hanging mercury dropping electrodes and screen-printed carbon electrodes, respectively. Although these chelating agents

have shown the capability to form a metal-complex with Al^{3+}, it is desirable to use alternative materials with a stronger and more selective binding with Al^{3+}.

Herein, this chapter reports the electrochemical determination of Al^{3+} in aqueous solutions at a tannic acid-capped gold nanoparticle-modified glassy carbon electrode (AuNPs@TA-GCE) using cyclic voltammetry (CV) and square wave voltammetry (SWV). Because of their high activity towards many chemical reactions, including molecular adsorption[18], reduction process[19], and metal complexes[20,21], metallic nanoparticles are extensively studied in areas of catalysis, sensing, and electronic applications. In this chapter, the large surface area to mass ratio of nanoparticles is exploited alongside their use to support chemically selective capping agents. Specifically, by drop-casting nanoparticles, the surface area of an electrode is much increased and permits an enhanced analytical performance, resulting in lower levels of detection during sensing applications. Moreover, since the aggregation/agglomeration state of the gold nanoparticles ideally needs to be avoided[22-24], employing gold nanoparticles (AuNPs) in combination with tannic acid ($C_{76}H_{52}O_{46}$,) as a capping agent has been shown to minimize this effect[25,26].

In plants, tannic acid (TA) is a naturally occurring polymer, exhibiting a range of structures, molecular masses, and physicochemical and biological properties[27,28]. TA consists of a central glucose core and surrounding covalently attached digalloyl ester groups, containing reactive functional groups such as hydroxyl and phenolic hydroxyl, which can bind metals.[28,29] Generally, the catechol or galloyl groups of TA provide binding sites for metal ions, ranging from mono-type to tris-type complexes[27,30]. Diverse metals and heavy metal ions such as Fe(III)[29], Ti(IV)[31], Hg(II)[32], Pb(II)[33], Cu(II)[34], Ni(II)[35], and Al(III)[36] are reported to complex with TA by adsorption. Stability constants of these complexes, indicating the affinity of the metal with TA, differ, and

much higher values have been reported in the literature for Al^{3+} than for other ions.[27,31,37-39] This suggests the use of TA for the selective detection of Al^{3+}. The proposed methodology below is based on the complexation process between Al^{3+} and TA, at AuNPs@TA-GCE. No strategy for the determination of Al^{3+} in combination with TA by voltammetry has been suggested in the past.

This chapter demonstrates a sensitive, reliable and low-cost alternative method for the detection of Al^{3+} in aqueous solutions. All voltammetric experiments were achieved using a freshly modified electrode. The reusability of the electrode was not assessed, as sensing principles are commonly transferred onto disposable screen-printed electrodes in later steps. Employing the presented methodology clear measurable signals are seen even at the low limit of 10.0 pM and a linear range up to 10.0 μM, evidencing the excellent utility of the sensor for practical purposes.

4.2. Experimental

Details about the chemical reagents here utilized can be found in Chapter 2, Section 2.1. Note that tannic acid (TA) solutions were prepared freshly for all experiments since the compound can be oxidized and decomposed by exposure to light and atmospheric oxygen.[27,40] HCl-KCl solution solutions of pH 1.0 and pH 2.0 were prepared by mixing 97.0 mL of 0.1 M HCl and 3.0 mL of 0.1 M KCl (pH 1.0) or by mixing 10.6 mL of 0.1 M HCl and 89.4 mL of 0.1 M KCl (pH 2.0). The GCE was modified by drop-casting ca. 25.0 μL of AuNPs@TA, which approximately corresponds to a surface concentration of one-monolayer (see Appendix A.2), resulting in the AuNPs@TA-GCE. Note that a gold electrode was used without further surface modification. The gold electrodes were used to study the solution phase electrochemistry of the tannic acid (see Section 4.3.1).

4.3. Results and Discussion

In this section, the electrochemical characterization of solution-phase tannic acid and of immobilized AuNPs@TA is first presented. Subsequently, the complexation of Al^{3+} and the AuNPs@TA-GCE is discussed by analyzing the resulting peak currents during cyclic voltammetry (CV) and evaluating the effects of scan rate, the concentration of target analyte and the electrode exposure time to sample solutions. Finally, an evaluation of the experimental parameters for square wave voltammetry (SWV) is presented, optimizing the electroanalytical performance of the chemical sensor.

4.3.1. Solution Phase Electrochemistry of Tannic Acid

Solution phase TA was electrochemically characterized in aqueous acid by CV using a 0.96 ± 0.02 mm radius gold electrode at varying pH, TA concentrations, scan rates, and electrode exposure times. After polishing, the gold electrode was exposed to TA concentrations, ranging from 1.0 to 15.0 mM. The CV measurements revealed an oxidation peak of TA to TA-quinone at a peak potential of 0.58 V vs SCE at pH 1.0 (Figure 1a) and peak potential of 0.54 V vs SCE at pH 2.0. The shift in peak potential with pH is consistent with the need for deprotonation prior to electron transfer and the difference of ca. 40 mV suggests the loss of fewer protons than electrons. For a particular concentration of TA, the current was approximately independent of pH, consistent with the TA being fully protonated at the pHs studied and with literature reports[28,41] of the pK_a of TA (range from 2.5 to 8.5), which were independently verified in this chapter which suggested the effective pK_a of TA is ca. 3.7.

A linear peak current behavior on the scan rate was observed (Figure 1b), suggesting the TA oxidation on the gold electrode surface is a surface-controlled

process. Furthermore, the exposure time of the gold electrode in a 1.0 mM TA solution prior to CV analysis was found to play an important role to maximize the oxidation of TA, as the prolonged exposure time of the gold electrode to TA results in the increased adsorption of TA to the electrode surface. By varying the exposure time from zero to 30 minutes at open circuit potential, a maximum peak current at 10 min was identified. The adsorption of TA onto the gold electrode surface and its electrochemical reaction is represented in Equation 1, where *x* and *y* are discussed below (Section 4.3.2.). Next, the understanding of the electrochemical behavior of TA in its combination with AuNPs is addressed in the following section.

$$\text{TA (aq)} \rightleftharpoons \text{TA (ads)} \xrightarrow{-xH^+,\ -ye^-} \text{Products} \qquad \text{(Equation 1)}$$

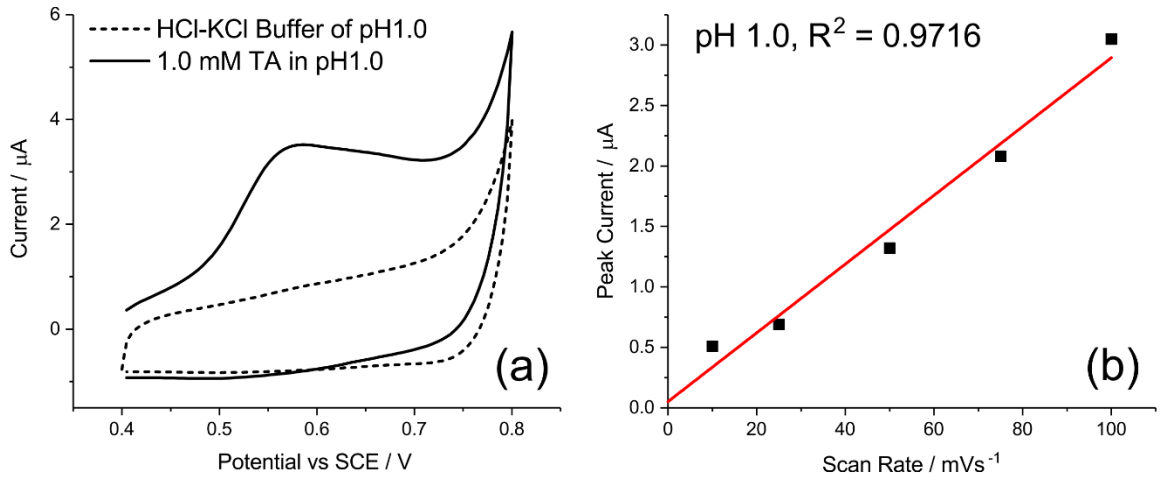


Figure 1. Electrochemical characterization of solution-phase TA using gold electrode by CV at a scan rate of 0.1 V s^{-1}, (a) cyclic voltammogram of 1.0 mM TA in HCl-KCl solution (pH 1.0) and (b) linear peak current behavior at various scan rates.

4.3.2. Characterization of AuNPs@TA

The size characterization of the AuNPs@TA was performed by scanning electron microscope (SEM). Figure 2 shows an SEM image of AuNPs@TA, where a mean

diameter size distribution of 60.0 ± 3.0 nm was obtained (Figure 2, inset). The particle surface charge was quantified by measuring the zeta potential in the water at 25 °C, whereby an average zeta potential of -30.9 ± 1.3 mV, conductivity of 0.023 mS cm^{-1}, was obtained. This value shows high stability of the colloidal gold dispersion.[42]

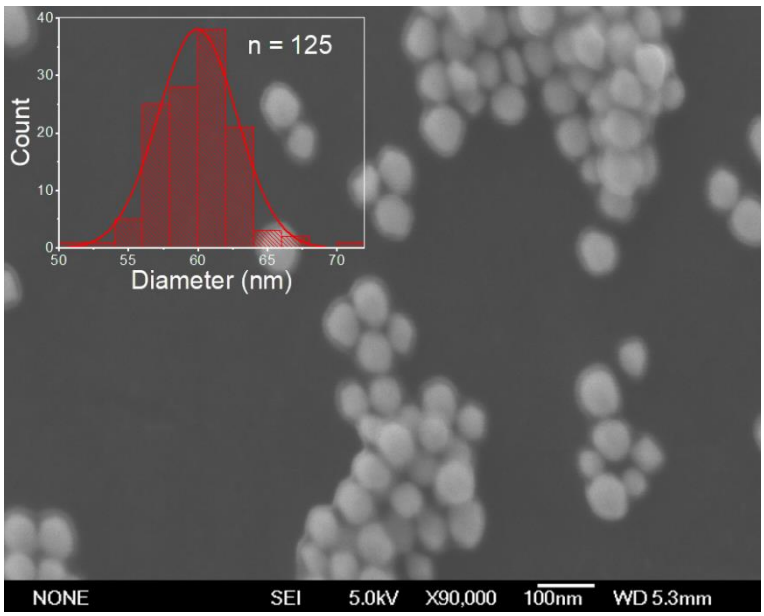


Figure 2. SEM micrograph of AuNPs@TA (inset: size distribution of the AuNPs@TA)

In agreement with literature[40,41], an estimated effective radius of the TA molecules of 1.3 nm was calculated from the structure and known bond lengths and angles, corresponding to an area of 6.46 x 10^{-18} m^2 of TA molecule (see Appendix A.2). Therefore, the amount of TA in one-monolayer surface coverage was estimated to be ca. 1,750 molecules per nanoparticle.

Next, the AuNPs@TA-GCE was electrochemically characterized by CV. For this purpose, a GCE was modified by drop-casting ca. 5.6 x 10^8 AuNPs@TA, corresponding to a surface concentration of ca. one-monolayer. This volume contains ca. 10^{12} TA molecules in total (see Appendix A.2). AuNPs@TA-GCE was immersed in HCl-KCl solution (pH 1.0) and CV was performed by sweeping the potential from 0.0 to 0.7 V vs

SCE and back to 0.0 V vs SCE, at a scan rate of 0.1 V s^{-1}. At the first forward scan, an oxidation peak was observed at a potential of 0.31 V vs SCE attributed to the oxidation of TA as illustrated in Equation 1 (see below for Figure 4a, blue curve).[43]

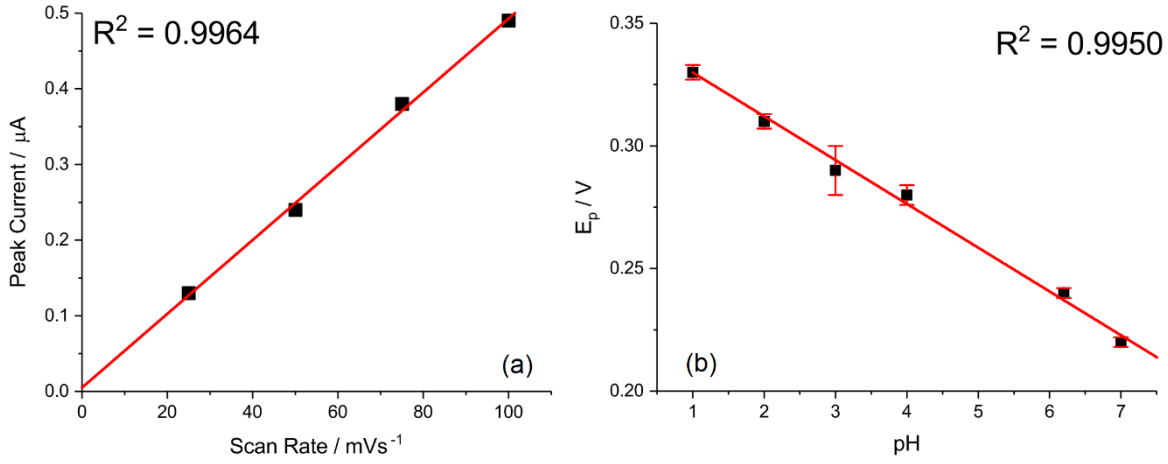


Figure 3. Electrochemical analysis of the AuNPs@TA by CV. (a) linear relationship between peak current and scan rate, (b) dependence of peak potential on pHs.

Following this, AuNPs@TA-GCE immersed in HCl-KCl solution (pH 1.0) and analogous CV was performed but at different scan rates, from 25 to 100 mV s^{-1}. As shown in Figure 3a, a linear relationship between peak current of AuNPs@TA and scan rate was found, suggesting that the oxidation of AuNPs@TA at the GCE is a surface-controlled process. An investigation of the electrochemical current behavior in dependence of the pH reveals a decrease in peak potential with increasing pH values (Figure 3b), along with a decrease in the peak currents. The response reflects the loss of protons on oxidation, but the complexity of the TA structure precludes the quantification of the exact number of electrons and protons being transferred, except the sub-Nernstian slope of Figure 3b suggests $y >> x$ related to Equation 1.

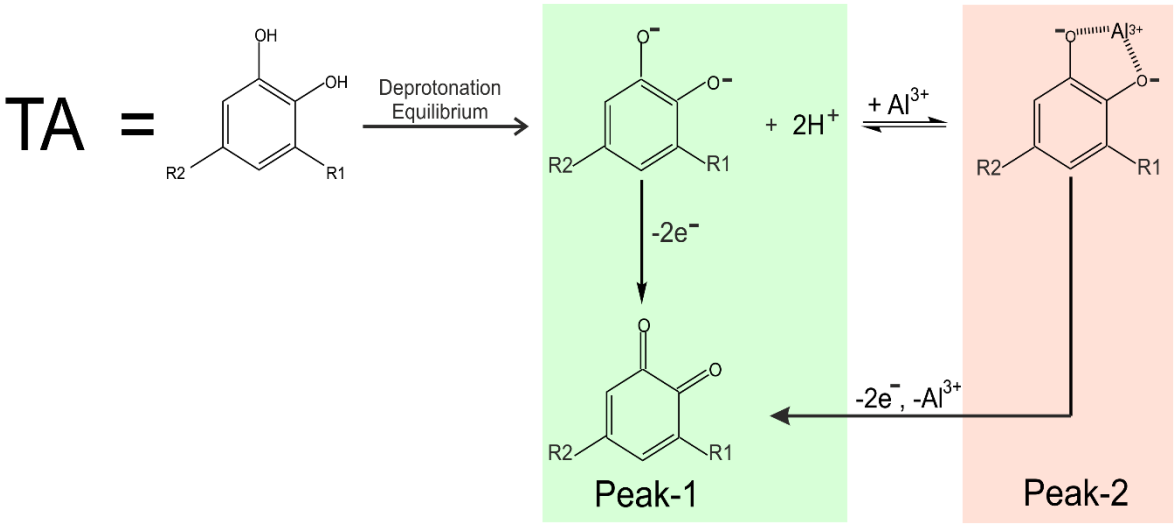
Further, the effect of exposure time of the AuNPs@TA-GCE to the HCl-KCl solution (pH 1.0), prior to voltammetric measurements were studied immediately and

after 30 min. The resulting peak at the potential of 0.31 V vs SCE exhibits a higher charge at 30 min compared to zero exposure time, suggesting the swelling of the TA capping layers on the AuNPs over prolonged exposure times. The exposure time prior to the CV being recorded plays a very important role to enable sensitivity of sensing performance, since it allows to improve the accessibility of the capping layers and to increase the possibility of Al^{3+} being complexed. However, the length of exposure time needs to meet a reasonable time scale of analysis without compromising the sensitivity and linear range of the response.

4.3.3. Complexation of Al^{3+} by AuNPs@TA

To explore the complexation of Al^{3+} by AuNPs@TA, a CV experiment was performed in the HCl-KCl solution (pH 1.0) using first an unmodified GCE in the presence of 2.0 mM Al^{3+}. The CV was recorded by sweeping the potential from 0.0 V to 0.7 V vs SCE and back to 0.0 V vs SCE at a scan rate of 0.1 V s^{-1}. As shown in Figure 4a (red curve), no Al^{3+} related signal was seen. After immobilisation of AuNPs@TA at an approximate coverage of one-monolayer, the cyclic voltammogram exhibited an oxidation peak (peak 1) at a potential of 0.31 V vs SCE (Figure 4a, blue curve), which, as above, is attributed to the oxidation of TA to form the TA-quinone (Scheme 1, green). By exposing the AuNPs@TA-GCE to 2.0 mM Al^{3+} solution, a second oxidation peak (peak 2) becomes apparent at a potential of 0.52 V vs SCE (Figure 4a, green curve), which is attributed to the oxidation of TA complexed with Al^{3+} (Scheme 1, orange). The possibility of a peak contribution from sulfate anions SO_4^{2-} of $Al_2(SO_4)_3$ (Al^{3+} source) was excluded after a control measurement in the K_2SO_4 solution (Figure 4a, black curve). A peak charge of 0.14 μC related to the number of TA oxidized per nanoparticle (Figure 4a, green curve, peak-1) and peak charge of 0.23 μC related to the complexation

of TA with Al^{3+} (Figure 4a, green curve, peak-2) were obtained by cyclic voltammetry at the scan rate of 100 ms^{-1}.



Scheme 1. TA exhibits several phenyl rings with acidic hydroxyl groups. These may be oxidized at ca. 0.31 V vs SCE to yield peak-1 (Figure 4a, green curve). Solution Al^{3+} can be complexed by TA, raising its oxidation potential to that of "peak 2". Note the complexation of Al^{3+} may involve more than two deprotonated OH^- groups.

Next, the effect of the scan rate was addressed to identify whether the AuNPs@TA in the presence of Al^{3+} is a surface-controlled or diffusion-controlled process. To assess this, AuNPs@TA-GCE was immersed in an HCl-KCl solution (pH 1.0) containing 2.0 mM Al^{3+}. The CV was recorded by sweeping the potential from 0.0 V to 0.7 V vs SCE and back to 0.0 V vs SCE, at different scan rates from 10 to 120 mV s^{-1}. Figure 4b presents the linear dependence of both peak currents on the scan rate, which suggests that the oxidation of AuNPs@TA/Al complex is a surface-controlled process, as with the oxidation of the uncomplexed TA. The peak 1 is considerably enhanced in the presence of Al^{3+}, suggesting partial complexation of the TA leads to greater accessibility of the capping layers. The peak potentials for both peaks were essentially scan rate independent hinting at an electrochemically reversible process.

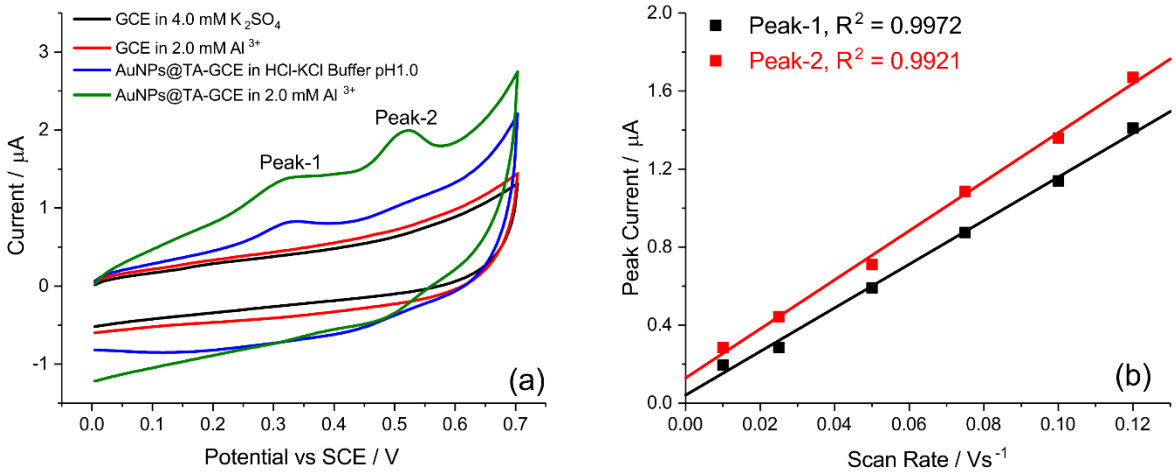


Figure 4. (a) CVs of the GCE and AuNPs@TA-GCE immersed in different solutions at a scan rate of 0.1 V s^{-1}, (b) Plot of the peak current of peak-1 and peak-2 at different scan rates.

The electrochemical response with respect to Al^{3+} concentration during the complexation process was investigated by CV. The AuNPs@TA-GCE was immersed in HCl-KCl solution (pH 1.0) containing Al^{3+} at concentration range between 0.1 mM and 10.0 mM. Figure 5a shows that peak 2, resulting from AuNPs@TA/Al complex, increased linearly with Al^{3+} concentration, within the concentration range studied.

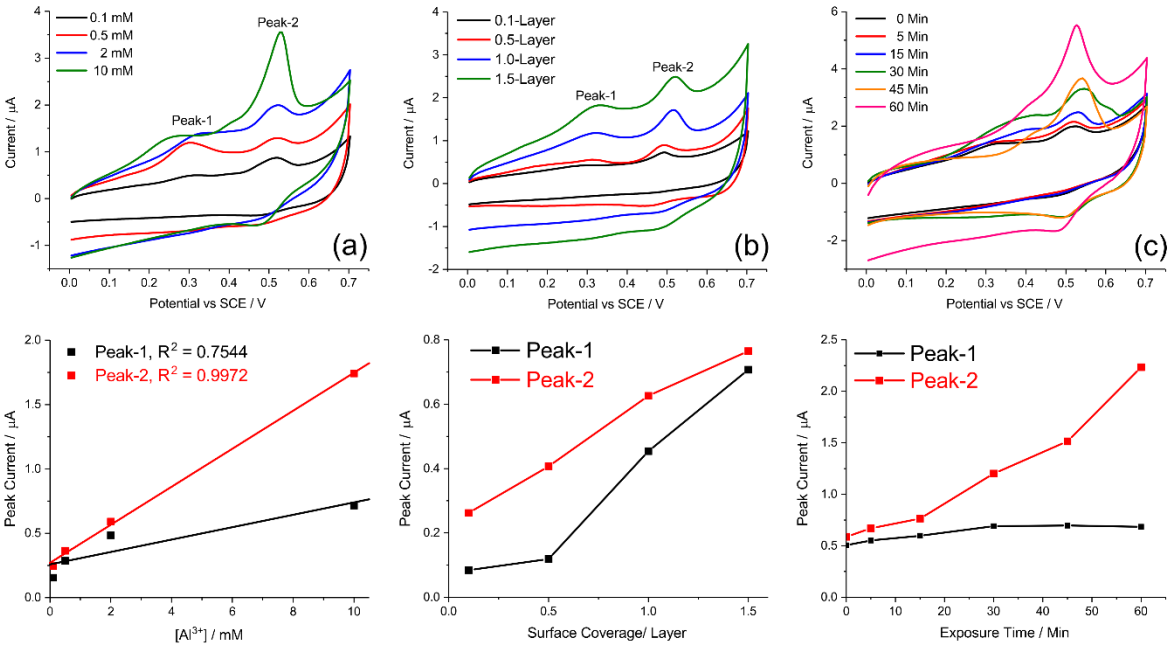


Figure 5. CVs of AuNPs@TA-GCE immersed in various Al^{3+} concentrations (a) and 2.0 mM Al^{3+} at different electrode surface concentrations (b), exposure times (c); at a scan rate of 0.1 V s^{-1}.

Furthermore, various surface concentrations of AuNPs@TA on the GCE were analyzed to find the optimal condition for Al^{3+} uptake during voltammetric measurements. The GCE surface was modified by drop-casting varying amounts of AuNPs@TA, corresponding to surface concentration in a range of 0.1 to 1.5-monolayer. To assess this, AuNPs@TA-GCE was immersed in the HCl-KCl solution (pH 1.0) containing 2.0 mM Al^{3+} and CV was recorded at a scan rate of 100 mV s^{-1}. Figure 5b shows that increasing the amount of AuNPs@TA resulted in an increase in *both* peak currents during the CV. However, considering the cost of AuNPs@TA and the time required to modify the electrode, one-monolayer surface coverage was selected for further experiments.

Finally, the time of exposure of the AuNPs@TA-GCE to the analyte solution, prior to voltammetric measurements (hereafter referred to as the exposure time), plays an important role during the optimization of the sensitivity of the sensing performance. The exposure time that generates a significant peak current increase, related to the detection of Al^{3+} within a reasonable timescale during CV, was evaluated by immersing the AuNPs@TA-GCE in HCl-KCl solution (pH 1.0) containing 2.0 mM Al^{3+} at various exposure times. The peak current of peak 2 increased continuously, 30 min of exposure time was selected as giving good sensitivity.

To assess the complexation process for analytical purposes, an AuNPs@TA-GCE was immersed into the HCl-KCl solution (pH 1.0) containing different Al^{3+} concentrations, ranging from 10.0 pM to 10.0 mM with an exposure time of 30 min. CVs were recorded by sweeping the potential from 0.0 V to 0.7 V vs SCE and back to 0.0 V vs SCE at a scan rate of 100 mV s^{-1} (Figure 6). The peak current value of peak-2 was plotted against the Log_{10} of Al^{3+} at different concentrations, resulting in a linearity trend with $R^2 = 0.9798$ (Figure 6b).

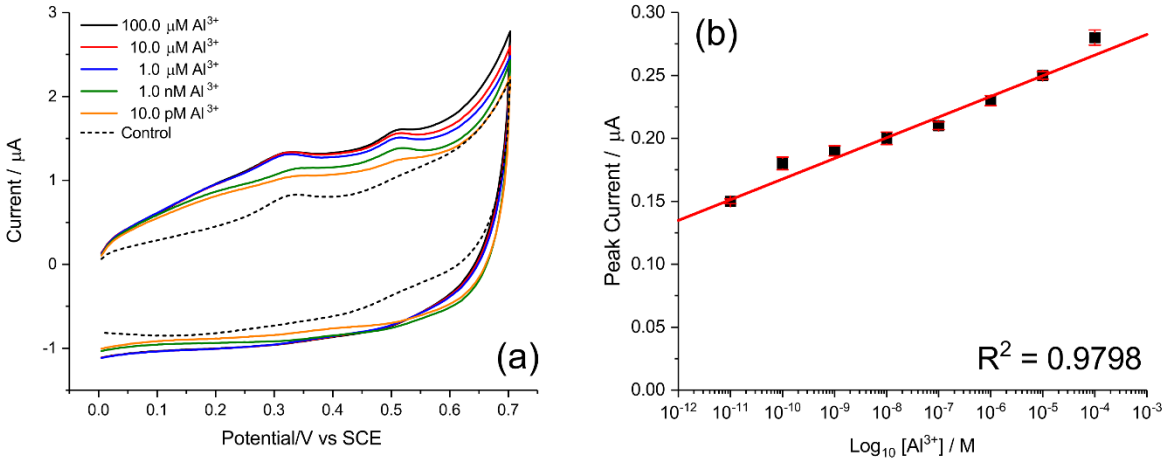


Figure 6. (a) CVs of AuNPs@TA-GCE immersed in different Al^{3+} concentrations at a scan rate of 0.1 V s^{-1}, (b) Plot of the resulting current of peak-2 versus Al^{3+} concentrations.

The amount species involved in the "peak 2" reaction, *n* (moles), was calculated from the peak charge, *Q* (Coulomb), obtained from the CV (Figure 6a) based on Faraday's law of electrolysis. To obtain the *effective* electrode coverage, *Γ* (mol cm^{-2}), the calculated number of moles was divided by the geometric area of the electrode, *A* (cm^2), as shown in Equation 2,

$$\Gamma = \frac{Q}{zFA} \qquad \text{(Equation 2)}$$

where *z* is the number of transferred electrons (*z* = 2) and *F* is the Faraday constant (96485.33 C mol^{-1}).

To determine effective electrode coverage, a linear baseline correction was performed to measure the charge under the voltammetric peaks. As shown in Figure 7, a linear log-log relationship between the effective electrode coverage and the concentration of Al^{3+} in solution was observed for *both* peak 1 and peak 2, with an intercept of -10.79 ± 0.02 and -10.67 ± 0.02, respectively. In the HCl-KCl solution (pH 1.0) and with 30 min exposure time, the presence of Al^{3+} resulted in significantly higher effective electrode coverage, compared to a control solution, lacking Al^{3+}. At a low

concentration of Al^{3+} (10.0 pM to 0.1 mM), the closely similar positive slope values of 0.097 ± 0.003 and 0.100 ± 0.002 were obtained for peak 1 and peak 2, respectively, indicate that the response of the TA capped is likely to reflect Al^{3+} induced swelling of the capping layer with an increased accessibility of chelating and oxidizable sites. The fact that the slope is below unity may indicate that the surface of the TA capping layer is partly saturated with Al^{3+}. Note that at higher concentrations of Al^{3+} (0.5 to 10.0 mM), peak 2 increased strongly while peak 1 remained relatively constant. For concentration above 0.1 mM Al^{3+}, the effective electrode coverage of peak 2 increased much more rapidly than peak 1.

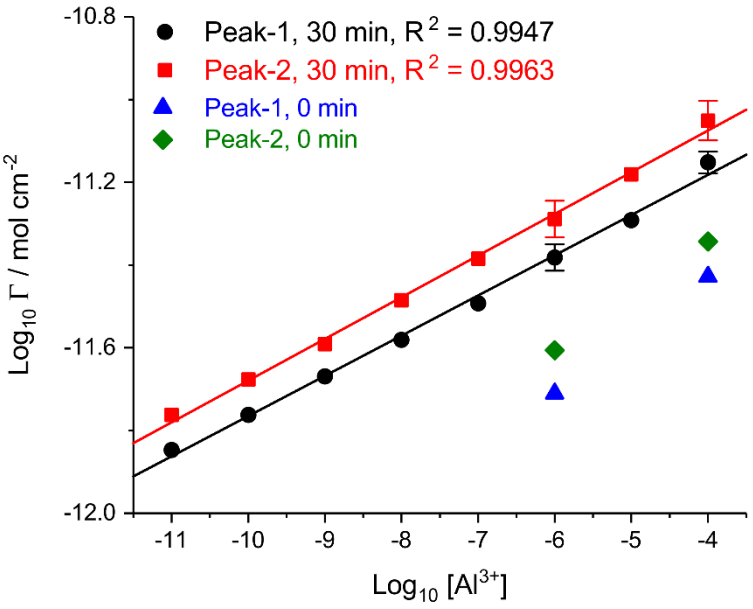


Figure 7. Dependence of the effective electrode coverage of the AuNPs@TA/Al complex on the solution containing Al^{3+}. Note the log-log scale.

It should be noted that TA can form complexes with other ions. To address possible interferences from other ions, the experimental stability constants (Log_{10} β) of various ions with TA were carefully reviewed from the literature. Table 1 shows that the TA/Al^{3+} complex is reported to have the highest stability constant (Log_{10} β) of all

TA/metal complexes. Moreover, an experimental validation shows the Al^{3+} detection at the AuNPs@TA-GCE is significantly more sensitive than Zn^{2+} at lengthier exposure times, above 15 min (Figure 8). Where no stability constants are recorded for ions, such as Cu^{2+}, $Ni^{2+,}$ and Ca^{2+}, available literature suggests no significant influence is expected due to insufficient binding of ions to TA at low pH.[27,35,44]

Table 1. Experimental stability constants reported in the literature for several ions

Complex Formation	pH	Stability Constant (Log_{10} β)	Reference
TA/Al^{3+}	6.0	23.0	(37)
TA/Al^{3+}	4.0	20.7	(45)
TA/TI^{4+}	4.0	16.5	(31)
TA/Fe^{3+}	5.0-7.0	9.0	(38)
TA/ Fe^{3+}	< 3.0	5.0-17.0	(39)
TA/Zn^{2+}	5.0	4.64	(27)
TA/Pb^{2+}	5.0	5.56	(27)

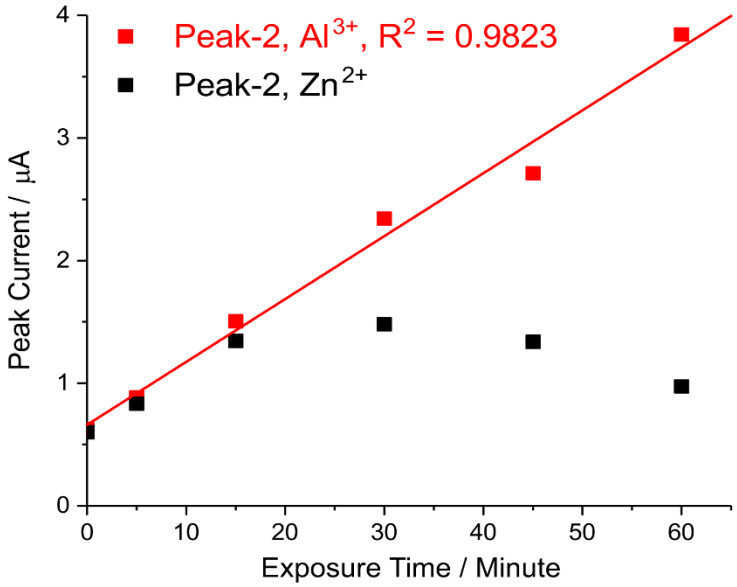


Figure 8. Evaluation of possible interference by Zn^{2+}. The Al^{3+} detection (red dot) at the AuNPs@TA is significantly more sensitive than Zn^{2+} at lengthier exposure times.

The effect of the exposure time of the AuNPs@TA-GCE to the analyte and a control solution was investigated. At zero exposure time (as represented by 1.0 μM and 0.1 mM Al^{3+}, Figure 7), the coverage of both peak 1 and peak 2 was lower compared to an exposure time of 30 min, suggesting the swelling degree of TA capping layers, as noted above, was affected by lengthier exposure time and increased accessibility of the chelating sites.

The above demonstrates a possible new analytical sensing method for Al^{3+}. However, the identified required exposure time of 30 minutes is disadvantageous for the routine monitoring and assessment of samples. In the following section, this aspect can be improved by conducting square-wave voltammetry (SWV) analyses with the established sensing strategy.

4.3.4. Optimized Parameters of the Chemical Sensor

Given the high surface area of the AuNPs@TA-GCE, capacitive and background currents can hide currents due to TA/Al^{3+} complex oxidation. By using square wave voltammetry (SWV), the capacitive current can be reduced. SWV is a pulse technique based on a series of potential steps and heights on a linear time scale. In SWV, the signal consists of a symmetrical square wave pulse of amplitude superimposed on a staircase waveform of step height. The current is sampled twice during each square-wave cycle, one at the end of the forward pulse and again at the end of the reverse pulse, therefore resulting in very high sensitivity.

SWV in the present system requires careful optimization of several analytical parameters, namely exposure potential and time, frequency and pulse amplitude. To determine an optimum exposure time, a AuNPs@TA-GCE was immersed in HCl-KCl solution (pH 1.0) containing 2.0 mM Al^{3+} and a holding potential of 0.0 V vs SCE was

applied for exposure times ranging from 5 to 300 s. A potential sweep was performed at a frequency of 40 Hz and amplitude of 0.02 V. Figure 9a shows that peak 2 was increased up to an exposure time of 300 s, after which a strong analytically useful signal is seen. This demonstrates a significant improvement in terms of time over the CV approach and is reasonable for routine monitoring.

Analysis of the operating frequency during SWV (Figure 9b) showed an increasing peak current for peak-2 up to 80 Hz, indicating optimal sensitivity for this parameter. Finally, the amplitude for SWV was examined. In the presence of 2.0 mM Al^{3+}, the pulse amplitude was varied from 0.01 to 0.1 V. As shown in Figure 9c, peak currents of peak-2 increased upon an increase of the pulse amplitude up to 0.04 V, which was therefore selected as the optimum pulse amplitude for all subsequent experiments.

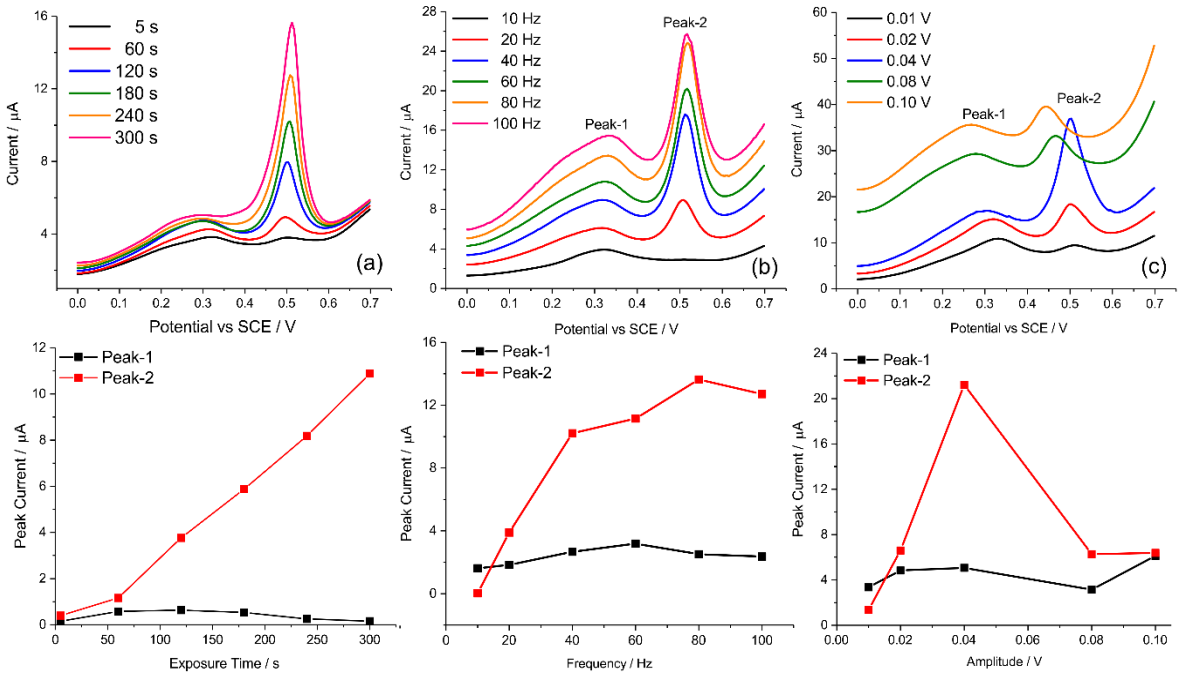


Figure 9. Parameter optimisation for square wave voltammetry (SWV), evaluating: (a) exposure time, (b) frequency, and (c) amplitude for the AuNPs@TA-GCE immersed in HCl-KCl solution (pH 1.0) containing of 2.0 mM Al^{3+}.

4.3.5. Measurement of Low Concentrations of Al^{3+}

Having established a successful sensing strategy for the detection of Al^{3+} at AuNPs@TA-GCEs, a measurable lower limit was determined by SWV in HCl-KCl solution (pH 1.0) by selecting a frequency of 80 Hz, a pulse amplitude of 0.04 V, and applying a holding potential of 0 V vs SCE for an exposure time of 300 s. Figure 10a shows that very clear signals are seen for concentrations of Al^{3+} in the range between 0.1 μM and 10.0 μM corresponding to the range of interest for drinking water. A measurable lower limit of the signal was also extracted. The determined measurable lower limit here represents the lowest concentration that can be distinguished significantly from the background signal.

In order to determine a measurable lower limit for the proposed system, a polynomial (typically of order 3) fit was performed to extract the signal from the baseline. Subtracting the polynomial baseline from the original data, an electrochemical signal significantly greater than the background can be seen for concentrations as low as 10.0 pM with a relative standard deviation (RSD) of less than 4% across triplicate experiments (Figure 10b).

As shown in Figure 10b, a linear log-log relationship between the electrode surface coverage (mol cm^{-2}) and the concentration of Al^{3+} in solution was observed for peak 2 at concentrations ranging from 10.0 pM to 2.0 mM Al^{3+}. A linear trend was observed from 10.0 pM to 10.0 μM Al^{3+}. At concentrations exceeding 10.0 μM Al^{3+}, the modified electroactive area of the electrode probably tends to be saturated with Al^{3+}. A measurable lower limit of 10.0 pM compares favorably with alternative methods[12,17] while offering lower costs and the potential to be applicable in routine water quality assessments.

In this chapter, however, that for use in heavily contaminated water, as opposed to drinking water, the possible effect of humic acid and/or surfactants might need to be investigated.

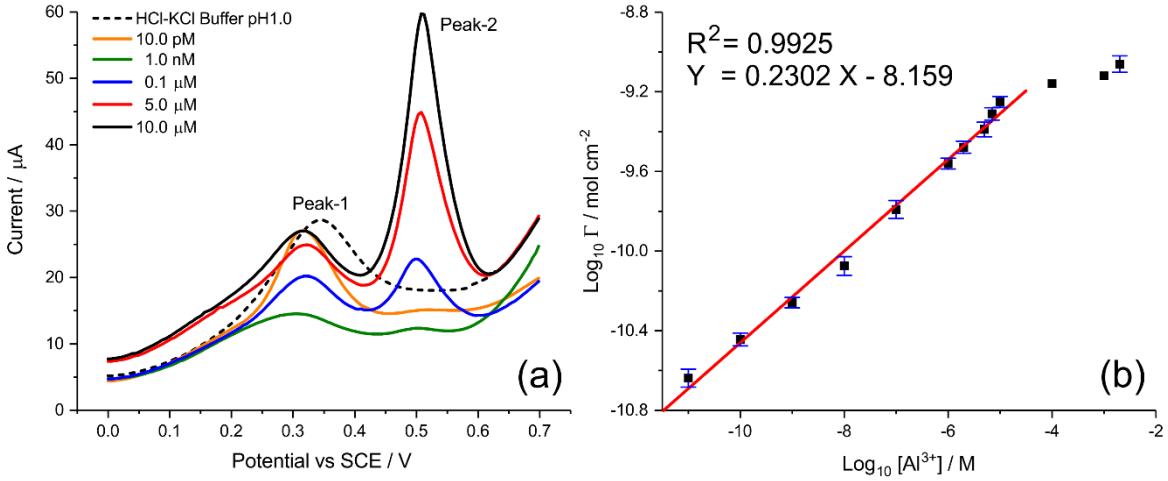


Figure 10. Determination of Al^{3+} by SWV. (a) Representative square-wave voltammograms of AuNPs@TA-GCE in the presence of Al^{3+}. (b) A linear log-log relationship between the effective electrode coverage and various Al^{3+} concentrations. Error bars represent the relative standard deviation, corresponds to an error of < 4%.

4. Conclusions

An electrode modification method is presented, employing tannic acid-capped gold nanoparticles (AuNPs@TA) for the sensitive detection of inorganic Al^{3+} in water. The starting potential and optimization of SWV parameters become essential to achieve selectivity, sensitivity and to eliminate other possible interference ions. The suitable starting potential during voltammetry measurement controls which species are taken up by the tannic acid capping agent and/or are electrochemically visible. SWV measurements revealed a measurable lower limit of 10.0 pM and a linear range up to 10.0 μM (meet the permissible level of ≤7.4 μM as declared by the WHO), evidencing the excellent utility of the proposed analytical method.

Bibliography

(1) Krewski, D.; Yokel, R. A.; Nieboer, E.; Borchelt, D.; Cohen, J.; Harry, J.; Kacew, S.; Lindsay, J.; Mahfouz, A. M.; Rondeau, V. Human Health Risk Assessment for Aluminium, Aluminium Oxide, and Aluminium Hydroxide. *J. Toxicol. Environ. Health. B. Crit. Rev.* 2007, *10 Suppl 1*, 1–269.

(2) Wang, Z.; Wei, X.; Yang, J.; Suo, J.; Chen, J.; Liu, X.; Zhao, X. Chronic Exposure to Aluminum and Risk of Alzheimer's Disease: A Meta-Analysis. *Neurosci. Lett.* 2016, *610*, 200–206.

(3) Chin-Chan, M.; Navarro-Yepes, J.; Quintanilla-Vega, B. Environmental Pollutants as Risk Factors for Neurodegenerative Disorders: Alzheimer and Parkinson Diseases. *Front. Cell. Neurosci.* 2015, *9*, 124.

(4) Ott, S. M. Renal Osteodystrophy—Time for Common Nomenclature. *Curr. Osteoporos. Rep.* 2017, *15* (3), 187–193.

(5) Wasana, H. M. S.; Perera, G. D. R. K.; De Gunawardena, P. S.; Bandara, J. The Impact of Aluminum, Fluoride, and Aluminum–Fluoride Complexes in Drinking Water on Chronic Kidney Disease. *Environ. Sci. Pollut. Res.* 2015, *22* (14), 11001–11009.

(6) WHO. Guidelines for Drinking-Water Quality, Fourth Edition. www.who.int/water_sanitation_health/publications/2011/dwq_guidelines/en/. Accessed on 2nd July 2019.

(7) Frankowski, M.; Zioła-Frankowska, A.; Kurzyca, I.; Novotný, K.; Vaculovič, T.; Kanický, V.; Siepak, M.; Siepak, J. Determination of Aluminium in Groundwater Samples by GF-AAS, ICP-AES, ICP-MS and Modelling of Inorganic Aluminium Complexes. *Environ. Monit. Assess.* 2011, *182* (1), 71–84.

(8) Qadir, M. A.; Ahmed, M.; Shahzad, S. Determination of Aluminium by Electrothermal Atomization Atomic Absorption Spectrometry in Serum to Characterize Hemodialysis Toxicity. *Anal. Lett.* 2015, *48* (1), 147–153.

(9) Zanjanchi, M. A.; Noei, H.; Moghimi, M. Rapid Determination of Aluminum by UV–Vis Diffuse Reflectance Spectroscopy with Application of Suitable Adsorbents. *Talanta* 2006, *70* (5), 933–939.

(10) Ahmed, M. J.; Hoque, M. R.; Bhattacharjee, S. C. A Simple Spectrophotometric Method for the Determination of Aluminum in Some Real, Environmental, Biological, Soil and Pharmaceutical Samples Using 2-Hydroxynaphthaldehydebenzoylhydrazone. *Eurasian J. Anal. Chem.* 2010, *5* (1), 1–15.

(11) Thomas, S. D.; Davey, D. E.; Mulcahy, D. E.; Chow, C. W. K. Determination of Aluminum by Adsorptive Cathodic Stripping Voltammetry with 1,2-Dihydroxyanthraquinone-3-Sulfonic Acid (DASA): Effect of Thin Mercury Film Electrode. *Electroanalysis* 2006, *18*

(22), 2257–2262.

(12) Zuziak, J.; Jakubowska, M. Voltammetric Determination of Aluminum-Alizarin S Complex by Renewable Silver Amalgam Electrode in River and Waste Waters. *J. Electroanal. Chem.* 2017, *794* (C), 49–57.

(13) Deng, P.; Fei, J.; Zhang, J.; Feng, Y. Determination of Trace Aluminum by Anodic Adsorptive Stripping Voltammetry Using a Multi-Walled Carbon Nanotube Modified Carbon Paste Electrode. *Anal. Lett.* 2011, *44* (8), 1521–1535.

(14) Arancibia, V.; Muñoz, C. Determination of Aluminium in Water Samples by Adsorptive Cathodic Stripping Voltammetry in the Presence of Pyrogallol Red and a Quaternary Ammonium Salt. *Talanta* 2007, *73* (3), 546–552.

(15) Santos, L. B.; de Souza, M. T. F.; Paulino, A. T.; Garcia, E. E.; Nogami, E. M.; Garcia, J. C.; de Souza, N. E. Determination of Aluminum in Botanical Samples by Adsorptive Cathodic Stripping Voltammetry as Al-8-Hydroxyquinoline Complex. *Microchem. J.* 2014, *112*, 50–55.

(16) Qiong, L.; Lirong, W.; Danli, X.; Guanghan, L. Determination of Trace Aluminum in Foods by Stripping Voltammetry. *Food Chem.* 2006, *97* (1), 176–180.

(17) Rana, S.; Mittal, S. K.; Singh, N.; Singh, J.; Banks, C. E. Schiff Base Modified Screen Printed Electrode for Selective Determination of Aluminium(III) at Trace Level. *Sensors Actuators B Chem.* 2017, *239*, 17–27.

(18) Wong, K.; Zeng, Q.; Yu, A. Gold Catalysts: A New Insight into the Molecular Adsorption and CO Oxidation. *Chem. Eng. J.* 2009, *155* (3), 824–828.

(19) Aswathy Aromal, S.; Philip, D. Facile One-Pot Synthesis of Gold Nanoparticles Using Tannic Acid and Its Application in Catalysis. *Phys. E Low-dimensional Syst. Nanostructures* 2012, *44* (7), 1692–1696.

(20) Wilton-Ely, J. D. E. T. The Surface Functionalisation of Gold Nanoparticles with Metal Complexes. *Dalt. Trans.* 2008, No. 1, 25–29.

(21) Pezzato, C.; Maiti, S.; Chen, J. L.-Y.; Cazzolaro, A.; Gobbo, C.; Prins, L. J. Monolayer Protected Gold Nanoparticles with Metal-Ion Binding Sites: Functional Systems for Chemosensing Applications. *Chem. Commun.* 2015, *51* (49), 9922–9931.

(22) Cloake, S. J.; Toh, H. S.; Lee, P. T.; Salter, C.; Johnston, C.; Compton, R. G. Anodic Stripping Voltammetry of Silver Nanoparticles: Aggregation Leads to Incomplete Stripping. *ChemistryOpen* 2015, *4* (1), 22–26.

(23) Ngamchuea, K.; Tschulik, K.; Eloul, S.; Compton, R. G. In Situ Detection of Particle Aggregation on Electrode Surfaces. *ChemPhysChem* 2015, *16* (11), 2338–2347.

(24) Sokolov, S. V; Tschulik, K.; Batchelor-McAuley, C.; Jurkschat, K.; Compton, R. G. Reversible or Not? Distinguishing Agglomeration and Aggregation at the Nanoscale.

Anal. Chem. 2015, *87* (19), 10033–10039.

(25) Untener, E. A.; Comfort, K. K.; Maurer, E. I.; Grabinski, C. M.; Comfort, D. A.; Hussain, S. M. Tannic Acid Coated Gold Nanorods Demonstrate a Distinctive Form of Endosomal Uptake and Unique Distribution within Cells. *ACS Appl. Mater. Interfaces* 2013, *5* (17), 8366–8373.

(26) Tsai, C. Y.; Lee, D. S.; Tsai, Y. H.; Chan, B.; Luh, T. Y.; Chen, P. J.; Chen, P. H. Shrinking Gold Nanoparticles: Dramatic Effect of a Cryogenic Process on Tannic Acid/Sodium Citrate-Generated Gold Nanoparticles. *Mater. Lett.* 2004, *58* (14), 2023–2026.

(27) Cruz, B. H.; Díaz-Cruz, J. M.; Ariño, C.; Esteban, M. Heavy Metal Binding by Tannic Acid: A Voltammetric Study. *Electroanalysis* 2000, *12* (14), 1130–1137.

(28) Rahim, M. A.; Ejima, H.; Cho, K. L.; Kempe, K.; Müllner, M.; Best, J. P.; Caruso, F. Coordination-Driven Multistep Assembly of Metal–Polyphenol Films and Capsules. *Chem. Mater.* 2014, *26* (4), 1645–1653.

(29) Fan, L.; Ma, Y.; Su, Y.; Zhang, R.; Liu, Y.; Zhang, Q.; Jiang, Z. Green Coating by Coordination of Tannic Acid and Iron Ions for Antioxidant Nanofiltration Membranes. *RSC Adv.* 2015, *5* (130), 107777–107784.

(30) Üçer, A.; Uyanik, A.; Aygün, Ş. F. Adsorption of Cu(II), Cd(II), Zn(II), Mn(II) and Fe(III) Ions by Tannic Acid Immobilised Activated Carbon. *Sep. Purif. Technol.* 2006, *47* (3), 113–118.

(31) Surleva, A.; Atanasova, P.; Kolusheva, T.; Costadinnova, L. Study of the Complex Equilibrium between Titanium(IV) and Tannic Acid. *J. Chem. Technol. Metall.* 2014. *49* (6), 594-600.

(32) Luo, H.; Zhang, S.; Li, X.; Liu, X.; Xu, Q.; Liu, J.; Wang, Z. Tannic Acid Modified Fe_3O_4 Core–Shell Nanoparticles for Adsorption of Pb^{2+} and Hg^{2+}. *J. Taiwan Inst. Chem. Eng.* 2017, *72*, 163–170.

(33) Badawi, M. A.; Negm, N. A.; Abou Kana, M. T. H.; Hefni, H. H.; Abdel Moneem, M. M. Adsorption of Aluminum and Lead from Wastewater by Chitosan-Tannic Acid Modified Biopolymers: Isotherms, Kinetics, Thermodynamics and Process Mechanism. *Int. J. Biol. Macromol.* 2017, *99*, 465–476.

(34) Kraal, P.; Jansen, B.; Nierop, K. G. J.; Verstraten, J. M. Copper Complexation by Tannic Acid in Aqueous Solution. *Chemosphere* 2006, *65* (11), 2193–2198.

(35) Meethale Kunnambath, P.; Thirumalaisamy, S. Characterization and Utilization of Tannin Extract for the Selective Adsorption of Ni(II) Ions from Water. *J. Chem.* 2015, Article ID 498359.

(36) Kinraide, T. B.; Hagermann, A. E. Interactive Intoxicating and Ameliorating Effects of Tannic Acid, Aluminum (Al^{3+}), Copper (Cu^{2+}), and Selenate (SeO_4^{2-}) in Wheat Roots: A

Descriptive and Mathematical Assessment. *Physiol. Plant.* 2010, *139* (1), 68–79.

(37) Zhang, L.; Liu, R.; Gung, B. W.; Tindall, S.; Gonzalez, J. M.; Halvorson, J. J.; Hagerman, A. E. Polyphenol–Aluminum Complex Formation: Implications for Aluminum Tolerance in Plants. *J. Agric. Food Chem.* 2016, *64* (15), 3025–3033.

(38) Kim, S.; Philippot, S.; Fontanay, S.; Duval, R. E.; Lamouroux, E.; Canilho, N.; Pasc, A. PH- and Glutathione-Responsive Release of Curcumin from Mesoporous Silica Nanoparticles Coated Using Tannic Acid–Fe(III) Complex. *RSC Adv.* 2015, *5* (110), 90550–90558.

(39) Sungur, Ş.; Uzar, A. Investigation of Complexes Tannic Acid and Myricetin with Fe(III). *Spectrochim. Acta Part A Mol. Biomol. Spectrosc.* 2008, *69* (1), 225–229.

(40) Poncet-Legrand, C.; Cabane, B.; Bautista-Ortín, A.-B.; Carrillo, S.; Fulcrand, H.; Pérez, J.; Vernhet, A. Tannin Oxidation: Intra- versus Intermolecular Reactions. *Biomacromolecules* 2010, *11* (9), 2376–2386.

(41) Shutava, T.; Prouty, M.; Kommireddy, D.; Lvov, Y. pH Responsive Decomposable Layer-by-Layer Nanofilms and Capsules on the Basis of Tannic Acid. *Macromolecules* 2005, *38* (7), 2850–2858.

(42) Bhattacharjee, S. DLS and Zeta Potential – What they are and what they are not? *J. Control. Release* 2016, *235*, 337–351.

(43) Vu, D. L.; Ertek, B.; Dilgin, Y.; Červenka, L. Voltammetric Determination of Tannic Acid in Beverages Using Pencil Graphite Electrode. *Czech J. Food Sci.* 2015, 33 (1), 72–76.

(44) Barbehenn, R. V; Martin, M. M. Formation of Insoluble and Colloidally Dispersed Tannic Acid Complexes in the Midgut Fluid of *Manduca sexta* (Lepidoptera: Sphingidae): An Explanation for the Failure of Tannic Acid to Cross the Peritrophic Envelopes of Lepidopteran Larvae. *Arch. Insect Biochem. Physiol.* 1998, *39* (3), 109–117.

(45) T. Kolusheva, M. Hristova, L. C. Study of the Complex Formation Reaction Between Al(III) and Tannic Acid. *J. Univ. Chem. Tech. Met.* 2012, *47* (5), 570–573.

Chapter 5

Tannic Acid-capped Gold Nanoparticle-modified Screen-printed Electrode: an Electrochemical Sensor of Hg^{2+} for Real-World Samples

This chapter further develops tannic acid-capped gold nanoparticle-modified carbon electrodes (see Chapter 4) as an electrochemical sensor, in this chapter for inorganic Hg^{2+} in real-world samples, such as tap water. Moreover, one key strategy is exploited to achieve an excellent selectivity performance of the sensor toward Hg^{2+} namely the starting potential during voltammetry, which controls which species are taken up by the capping agent and/or are electrochemically visible. Specifically, a starting potential of 0.3 V vs SCE allows the elimination of possible interference from Al^{3+} and Zn^{2+} studied. Under optimal conditions and using square-wave voltammetry, the presented methodology exhibits a measurable lower limit of 100.0 fM. The transfer of the established sensing protocol onto screen-printed electrodes shows its applicability to routine monitoring of inorganic Hg^{2+} in tap water.

The work presented in this chapter has been published in the *Analyst* (*Analyst* 2018, *143*, 9, 2035–2041) and was carried out in collaboration with Dr. Sabine Kuss and Dr. Eden Tanner, who helped with the interpretation of the experimental results. Dr. Stanislav Sokolov (in collaboration with Dr. Neil P. Young and Ms. Jennifer Holter from the Department of Materials, Oxford University) obtained the scanning electron microscope (SEM) images of the AuNPs@TA.

5.1. Introduction

The World Health Organisation (WHO) has declared mercury as one of the most toxic heavy metals to human health.[1] Inorganic mercury (Hg^{2+}) accumulates in the vital tissues and organs, interfering with proteins and enzymes[2], which can result in cellular dysfunctions and health issues, such as learning and memory impairments, as well as Alzheimer's disease.[3-5] In addition, individuals with congenital mercury toxicity are especially vulnerable to environmental mercury contaminations and may show severe mental retardation[6] and neurological abnormalities[7], as well as profound immunological and embryonic toxicological effects.[8] Therefore, the exposure to inorganic Hg^{2+} by the consumption of contaminated drinking water has become a global concern and a maximum permissible level of inorganic Hg^{2+} in drinking water of 6.0 $\mu g\ L^{-1}$ was declared by the WHO, which corresponds to an approximate concentration of 30.0 nM.[9]

The above-mentioned risks associated with inorganic Hg^{2+} in drinking water require sensitive and selective detection and monitoring strategies to assure public health. To date, various analytical methods have been developed for the detection of trace and/or ultra-trace levels of Hg^{2+}, such as gas chromatography-inductively coupled plasma analysis (GC-ICPMS)[10], atomic absorption spectrometry[11] and UV-Vis spectrophotometry[12], as well as voltammetric techniques.[13,14] Voltammetry has been widely accepted and is considered for the detection of metals, such as Hg^{2+}, because of its excellent sensitivity, low cost and its suitability for *in situ* applications. However, particular aspects, such as a reasonable time scale of analysis, electrode modifications and selectivity need to be thoroughly assessed[14], whereby straightforward and easy to implement electrode pre-treatment procedures have become desirable if not imperative. Electrode modifications using gold nanoparticles (AuNPs) are commonly

carried out for voltammetry.[15,16] AuNPs are easy to synthesize, highly conductive, and increase the electrode surface area, making AuNPs an excellent choice in sensing applications. Employing AuNPs in combination with chemically selective capping agents, aggregation/agglomeration effects[17,18] can be minimized and selectivity of the modified electrode towards Hg^{2+} improved.

In this chapter, tannic acid ($C_{76}H_{52}O_{46}$, TA) is employed both as a stabilizing agent for AuNPs and as a selective capping agent for Hg^{2+}. TA is found in plant tissues, such as leaves, gallnuts, and pods of certain plants[19], where it exhibits various structures, molecular masses, and physicochemical and biological properties.[20,21] In addition, TA molecules contain a large number of reactive functional groups, such as hydroxyl and phenolic hydroxyl groups, which can form complexes with heavy metal ions, such as Hg^{2+}.[20,22] As an example, Luo *et al*[23] have used TA modified Fe_3O_4 core-shell nanoparticles for the adsorption and detection of Hg^{2+} from contaminated water, and it has recently shown that the combination of AuNPs and TA results in the sensitive detection of Al^{3+} in aqueous solutions with a measurable lower limit of 10.0 pM (see Chapter 4).[24] Furthermore, in biological related voltammetry applications, TA has been used as an electrode surface modifier for the detection of dopamine[25], glucose[26], bisphenol A[27], and epinephrine[28]. The role of TA appears to be either as a dopant[25], as a biocompatible host for an enzyme[26] or the target[27], or alternatively "electron mediation"[28] with TA is suggested. Despite apparent success in various applications, voltammetric strategies in connection with TA for the detection of inorganic Hg^{2+} have not been reported in the literature.

This chapter reports the electrochemical detection of inorganic Hg^{2+} in aqueous solutions and tap water at a tannic acid-capped gold nanoparticle-modified glassy carbon electrode (AuNPs@TA-GCE) by square-wave voltammetry. The influence of

coexisting ions on the detection of inorganic Hg^{2+} is investigated and Hg^{2+}-spiked tap water samples analyzed. The developed sensing strategy is then transferred onto disposable AuNPs@TA-modified screen-printed carbon electrodes (AuNPs@TA-SPE), demonstrating the ability to detect Hg^{2+} in tap water with a measurable lower limit of 100.0 fM, showing distinct signals above background, as well as making it accessible for routine monitoring applications.

5.2. Experimental

Details about the chemical reagents here utilized can be found in Chapter 2, Section 2.1. Analyte solutions were prepared in a HCl-KCl solution (pH 1.0) by mixing 97.0 mL of 0.1 M HCl and 3.0 mL of 0.1 M KCl.[29] GCE was modified by drop-casting ca. 25.0 μL of AuNPs@TA, which approximately corresponds to a surface concentration of one-monolayer (see Appendix A.2), then dried under a N_2 stream resulting in a tannic acid-capped gold nanoparticle-modified glassy carbon electrode (AuNPs@TA-GCE).

The water sample used in this chapter was collected from the laboratory water tap (Rodney Porter Building, Oxford, OX1 3RQ). The collected tap water was spiked with various concentrations of Hg^{2+}. The influence of interfering metal ions was investigated using mixtures of tap water solutions containing Zn^{2+} and/or Al^{3+} at different concentrations. The transfer of the established method to disposable screen-printed carbon electrodes was realized using DropSens screen-printed carbon electrodes (DRP-110, DropSens, Llanera, Spain, SPE), with a built-in carbon (4.0 mm diameter) working electrode, carbon counter electrode and silver reference electrode - all printed on a L33 x W10 x H0.5 mm ceramic substrate. SPEs were modified by drop-casting ca. 25.0 μL of AuNPs@TA suspension and dried under N_2 flow, resulting in

AuNPs@TA-SPE. A 50.0 μL of the sample was deposited onto the SPE surface, covering all three electrodes. Each sample was analyzed in triplicate under optimized experimental conditions as discussed below.

5.3. Results and Discussion

The electrochemical detection of Hg^{2+} using cyclic voltammetry (CV) was first discussed. The characterization of AuNPs@TA-GCE in the absence and presence of Hg^{2+} at different scan rates, surface coverages and at various exposure times leads to the determination of a measurable lower limit for Hg^{2+}. The selectivity performance of the AuNPs@TA-GCE towards possible interfering ions is discussed, before evaluating the detection of Hg^{2+} using square-wave voltammetry (SWV). As proof of concept, this chapter demonstrates the application of the established sensing strategy to screen-printed electrodes (AuNPs@TA-SPE) and tap water analysis.

5.3.1. Mercury Detection by Cyclic Voltammetry

The electrochemical characterization of TA in the solution phase has been studied previously in Chapter 4, whereby an oxidation peak at a potential of 0.58 V vs SCE was revealed.[24] The CV of AuNPs@TA-GCE exposed to HCl-KCl (pH 1.0) solution results in an oxidation peak potential of TA at 0.31 V vs SCE and describing a surface-controlled process.[24] In addition, prolonged exposure time of the AuNPs@TA-GCE to the solution of HCl-KCl (pH 1.0), prior to CV measurements, revealed the swelling of the TA layers on the AuNP.[24]

Before assessing the oxidation behavior of Hg^{2+} at AuNPs@TA-GCEs, the unmodified GCE was immersed in a solution of HCl-KCl (pH 1.0), containing 2.0 mM Hg^{2+} and CV was performed by sweeping the potential from 0.3 V to 0.7 V vs SCE, at a

scan rate of 0.1 V s^{-1}. No electrochemical current signal related to Hg^{2+} was observed (Figure 1, black-solid curve), demonstrating the necessity for the proposed electrode modifications. To obtain a fully functionalized AuNPs@TA-GCE sensor, AuNPs@TA suspension were drop cast onto a GCE surface at a concentration of ca. 5.6 x 10^8 nanoparticles, corresponding to a surface concentration of approximately one-monolayer (see Appendix A.2). Next, the AuNPs@TA-GCE was immersed in a solution containing 2.0 mM Hg^{2+}, whereby CV (Figure 1, red-solid curve) reveals two oxidation peaks at potentials of 0.40 V and 0.58 V vs SCE, respectively. The first oxidation peak (peak-1) is attributed to the oxidation of tannic acid (TA) capping agent[24,30] and the second peak (peak-2) is attributed to the oxidation of AuNPs@TA/Hg^{2+} complex. TA is likely to reflect Hg^{2+} induced swelling of the capping layer with increased accessibility of chelating and oxidizable sites to uptake Hg^{2+} and results in peak-2 (see Chapter 4).

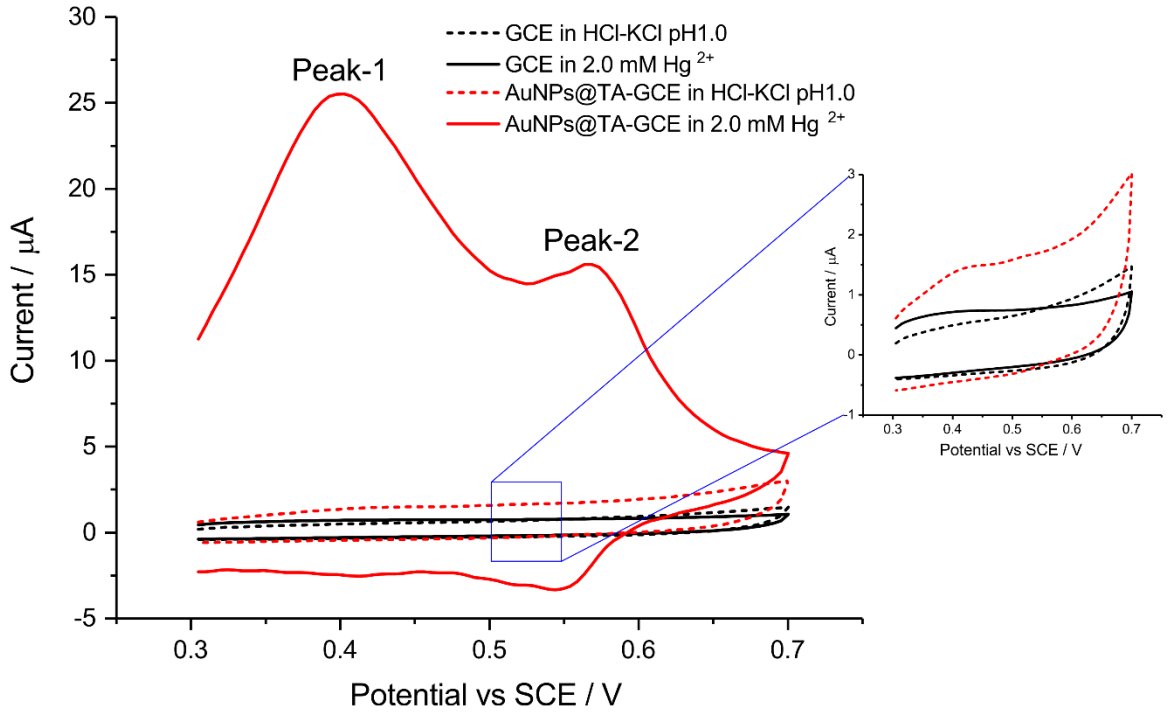


Figure 1. Detection of Hg^{2+} at unmodified and modified GCE by CV at a scan rate of 0.1 V s^{-1}.

The effect of scan rate was studied. To assess this, the AuNPs@TA-GCE was immersed into a 2.0 mM Hg^{2+} solution and CVs were performed at scan rates of up to 0.12 V s^{-1}. As shown in Figure 2a, peak currents of peak-1 and peak-2 increased monotonically with scan rate. The linear dependence of the peak currents of peak-1 and peak-2 on the scan rate (Figure 2b) suggests that both the oxidation process of TA and of the AuNPs@TA/Hg^{2+} complex are surface-controlled processes. In addition, peak-1 substantially increases in the presence of Hg^{2+}, suggesting that the partial complexation of TA leads to greater accessibility of the TA layers. The peak potential positions of peak-2 at 0.58 V vs SCE were found to be independent of the scan rate, indicating a reversible electrochemical process for the oxidation of the AuNPs@TA/Hg^{2+} complex. For further analytical measurements reported below, a scan rate of 0.1 V s^{-1} was selected.

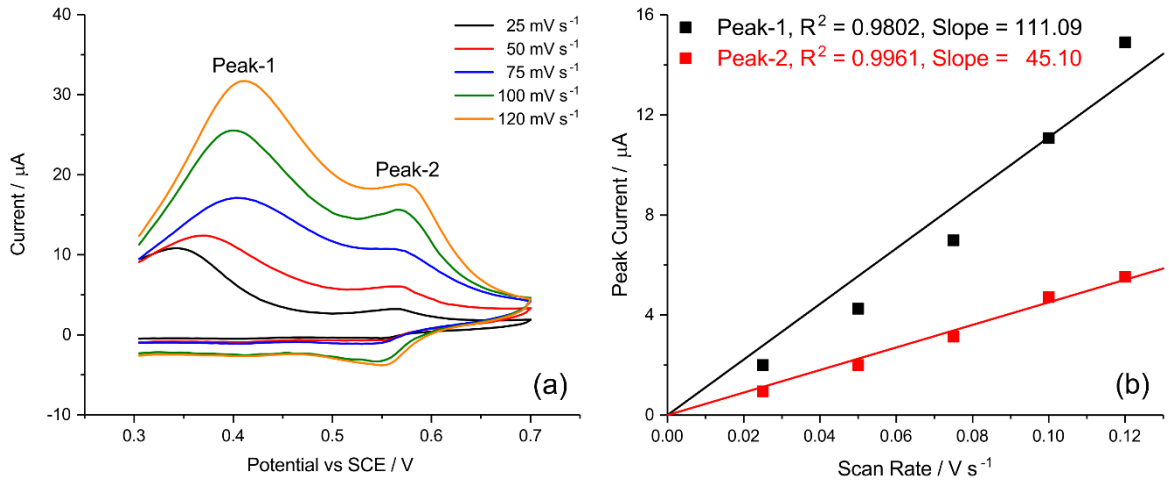


Figure 2. Scan rate dependence of Hg^{2+} detection. (a) CVs of AuNPs@TA-GCE at various scan rates. (b) Linear peak current behavior at scan rates shown in (a).

Next, the effect of the electrode surface concentration of AuNPs@TA on the Hg^{2+} uptake was studied. Surface coverages between 0.1- and 1.5-monolayer of AuNPs@TA were evaluated by crudely estimating a close packing of 91% (Figure 3a).[31] All modified

AuNPs@TA-GCE with specific surface coverages were exposed to 2.0 mM Hg^{2+} in HCl-KCl (pH 1.0). Figure 3b shows that peak currents of both peak-1 and peak-2 enhanced monotonically with increasing AuNPs@TA concentrations at the GCE surface. This is attributed to the greater number of accessible complexation sites of the AuNPs@TA-GCE. Considering the cost of AuNPs@TA, a one-monolayer surface coverage was found to be sufficient for good analytical performance and thus was selected for further experiments.

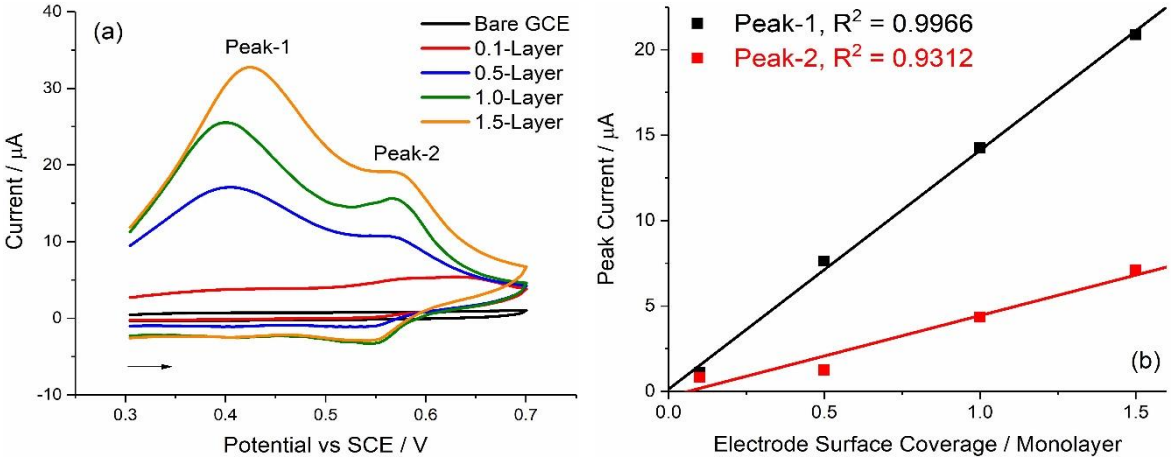


Figure 3. (a) CVs of the AuNPs@TA-GCE immersed in 2.0 mM Hg^{2+} at various electrode surface coverages. (b) Linear peak current behavior at various surface coverages shown in (a).

One of the key aspects for achieving sufficient sensitivity and thus lowering the detection limit is the exposure time of the AuNPs@TA-GCE to Hg^{2+} ions in solution before voltammetric measurements. To assess this, a AuNPs@TA-GCE was exposed to 1.0 μM Hg^{2+} in HCl-KCl solution at varying exposure times between zero to 30 min. CVs were recorded by sweeping the potential from 0.3 V to 0.7 V vs SCE and back to 0.3 V vs SCE at a scan rate of 0.1 V s^{-1}. As shown in Figure 4, the peak current of peak-2 increased up to an exposure time of 10 min and significantly decreased at lengthier time. This effect can be attributed to the swelling of TA capping layers, which reaches

its maximum at 10 min when the effective electrode surface becomes saturated with Hg^{2+}. This suggests that with a practical exposure time of 10 min good sensitivity of the AuNPs@TA-GCE towards the detection of Hg^{2+} by CV can be achieved.

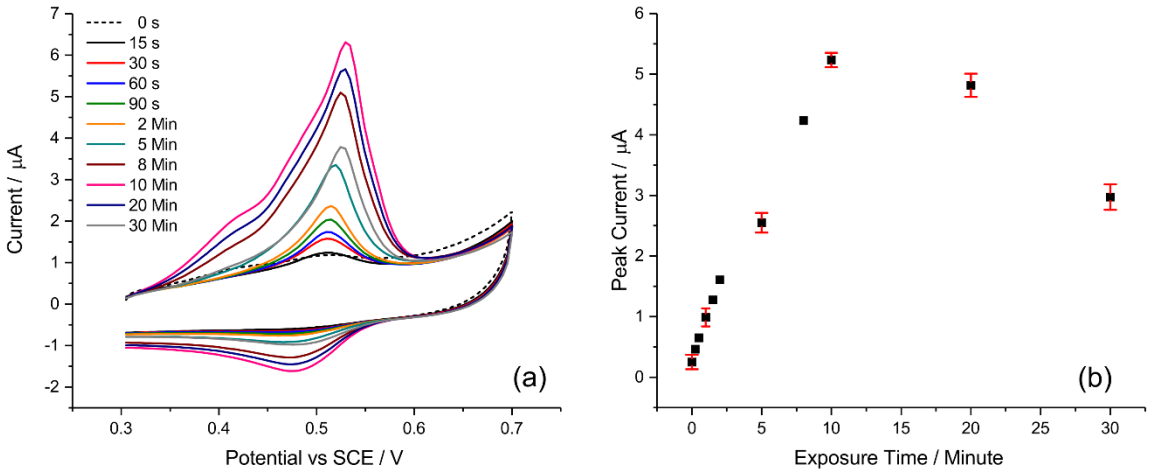


Figure 4. Study of the electrode exposure times to 1.0 µM Hg^{2+} by CV at a scan rate of 0.1 V s^{-1}. (a) CVs of AuNPs@TA-GCE at various exposure times. (b) Current behavior at peak-2 at exposures ranging from zero to 30 minutes.

5.3.2. Measurable Lower Limit for Hg^{2+} at AuNPs@TA-GCE Using CV

An exposure time of 10 min was applied to determine a measurable lower limit, representing the lowest concentration that can be distinguished from the background signal, for the detection of Hg^{2+} by CV. As discussed in Section 5.3.1., a one-monolayer of AuNPs@TA and a scan rate of 0.1 V s^{-1} were selected. The AuNPs@TA-GCE was immersed in an HCl-KCl solution (pH 1.0) containing various Hg^{2+} concentrations, ranging from 10.0 pM to 10.0 µM (Figure 5a). A linear baseline correction was performed, which revealed two effective linear regions at concentrations of 10.0 pM-10.0 nM (Figure 5b, black line) and 10.0 nM-10.0 µM (Figure 5b, red line). These linear relationships indicate the potential for sensitive Hg^{2+} detection at low concentrations.

Notably, a measurable lower limit was determined at 10.0 pM Hg^{2+}, considerably lower than the guideline value of 30.0 nM for Hg^{2+} in drinking water, as defined by the WHO.

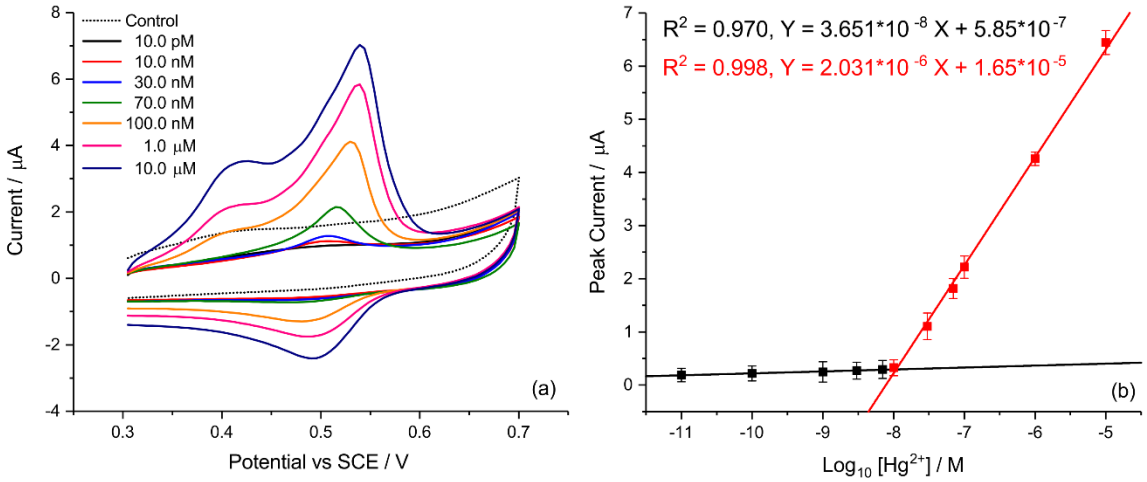


Figure 5. (a) CVs of AuNPs@TA-GCE immersed in various Hg^{2+} concentrations at a scan rate of 0.1 V s^{-1}, (b) Linear peak current behavior at various Hg^{2+} concentrations.

5.3.3. Selectivity Performance of the AuNPs@TA-GCE Using CV

In order to develop an efficient sensor for the detection of Hg^{2+} in the environment, possible interferences from other ions need to be excluded. As an example, a fully functionalized AuNPs@TA-GCE was exposed to 10.0 µM Al^{3+} or Zn^{2+} and CV measurements were performed applying the previously established optimal parameters. As shown in Figure 6, a strong oxidation signal for Hg^{2+} was found without a significant contribution by neither Al^{3+} nor Zn^{2+} ions.

The proposed Hg^{2+} detection strategy, based on AuNPs@TA-GCE as described above, has shown the capability to selectively detect low concentrations of inorganic Hg^{2+} in aqueous solutions by cyclic voltammetry. In the following section, the possibility of avoiding exposure time as high as 10 min by conducting square-wave voltammetry (SWV), which offers reliable and more sensitive detection of Hg^{2+} for the routine monitoring and assessment of real-world samples, is discussed.

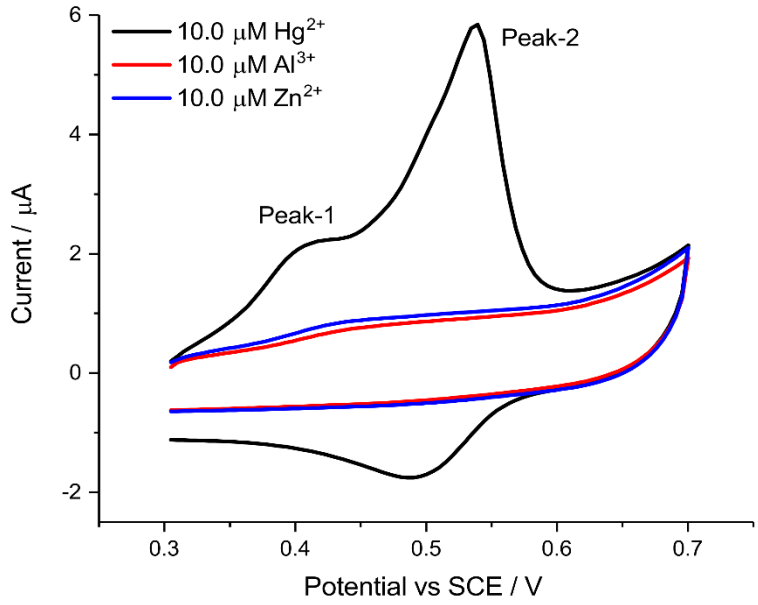


Figure 6. Selectivity studies of the AuNPs@TA-GCE for Al^{3+} and Zn^{2+} at a scan rate of 0.1 V s^{-1} and exposure time of 10 min.

5.3.4. Mercury Detection by Square-Wave Voltammetry

In order to reduce capacitive and background currents by square-wave voltammetry (SWV), several analytical parameters, such as exposure potential and time, frequency and pulse amplitude need to be optimized. To assess these parameters, the AuNPs@TA-GCE was exposed to 1.0 nM Hg^{2+} in the HCl-KCl solution (pH 1.0). First, the effect of frequency on the current intensity was studied at a range of 10 to 50 Hz, while maintaining all other parameters constant (preliminary selection of amplitude of 0.03 V and an exposure time of 60 s). As shown in Figure 7a, the peak current increased up to a value of 30 Hz and subsequently decreased at higher frequencies. Hence, 30 Hz was selected as the optimal frequency for Hg^{2+} detection. Second, the effect of amplitude variation on the AuNPs@TA sensitivity was studied at different values, ranging from 0.01 V to 0.05 V, while maintaining an optimal frequency of 30 Hz and a preliminarily selected exposure time of 60 s. As shown in Figure 7b, the optimal amplitude of 0.04 V was found for the Hg^{2+} detection, maximizing the electrochemical

current signal. Finally, the exposure time was re-assessed for SWV in the range of zero to 90 s, while maintaining all other optimum parameters constant. The limiting value of peak current was obtained with an exposure time of 30 s (Figure 7c). In summary, optimal parameters for the detection of Hg^{2+} using SWV selected to be at a frequency of 30 Hz, an amplitude of 0.04 V, and an exposure time of 30 s for all subsequent experiments.

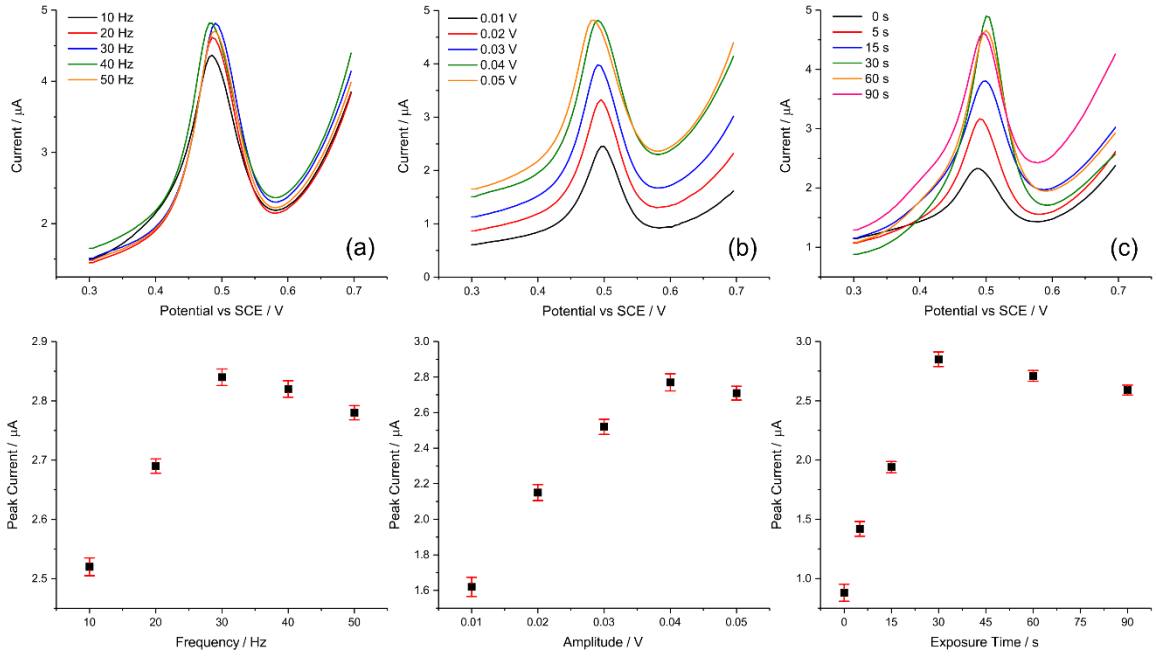


Figure 7. Parameter optimisation for SWV. Evaluating: (a) frequency, (b) amplitude, and (c) exposure time for the AuNPs@TA-GCE immersed in HCl-KCl (pH1.0) containing 1.0 nM Hg^{2+}.

Having defined the optimum conditions of SWV, the selectivity and sensitivity of the sensor are evaluated in the following section.

5.3.5. Selectivity Performance of the AuNPs@TA-GCE Using SWV

To assess the possible influence of various ions on the detection of inorganic Hg^{2+}, solution mixtures of Hg^{2+}, Zn^{2+}, and Al^{3+} in HCl-KCl solution (pH 1.0) in varying

concentrations from 3.0 nM to 10.0 nM were prepared. SWVs (at optimal parameters, see Section 5.3.4) were performed in triplicate to ensure reproducibility of the measurement. As shown in Figure 8, both peak current and peak charge of the AuNPs@TA-GCE in the presence of these cations and Hg^{2+} remained relatively constant. To obtain peak current values, a polynomial baseline correction (typically order 3) was performed and subtracted from the raw data. The resulting peak current and peak charge remains constant, indicating only minimal interference by these ions with the proposed Hg^{2+} sensor.

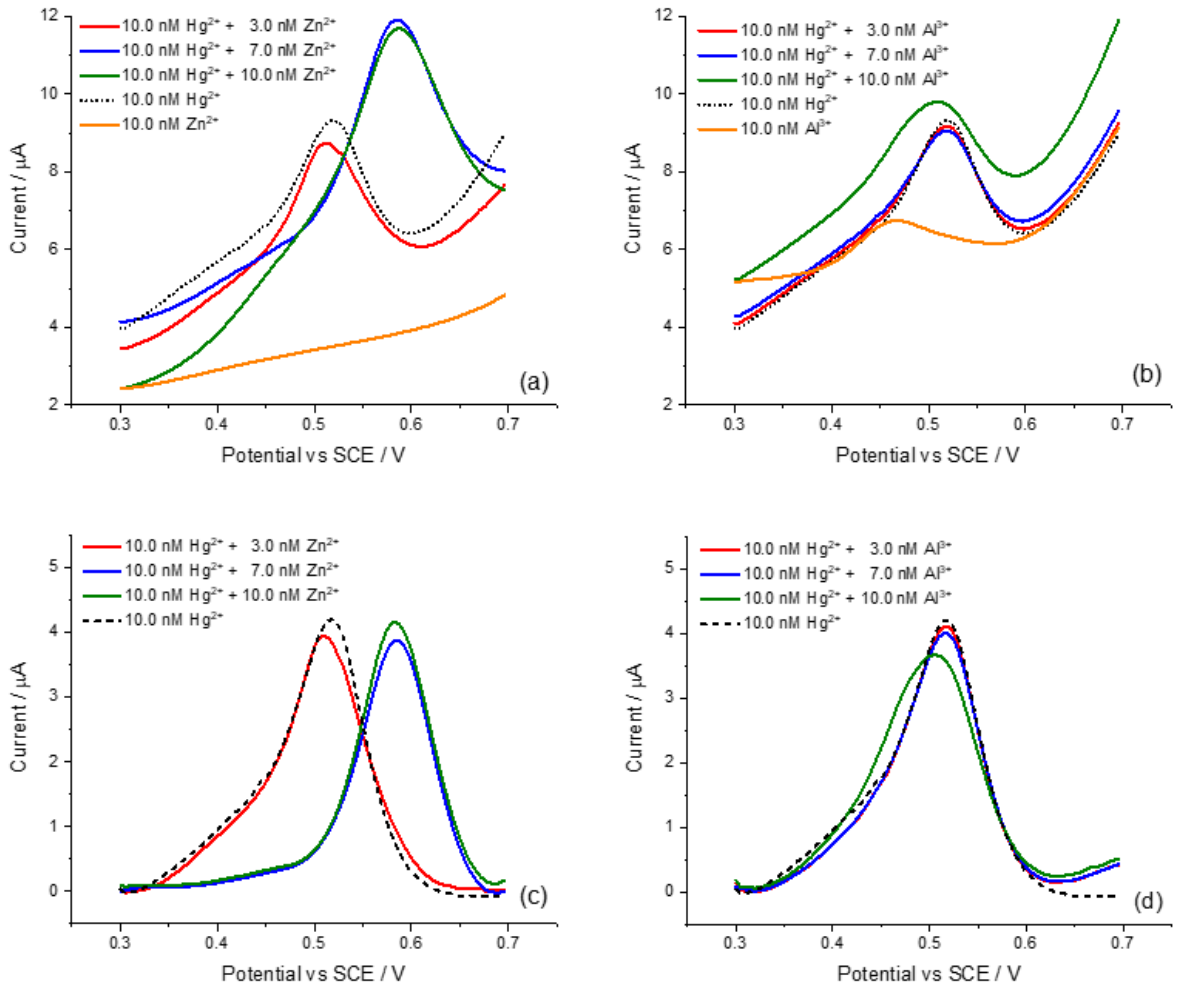


Figure 8. Selectivity performance analysis of the AuNPs@TA-GCE by SWV. (a) and (b) showing raw data acquired at mixture solution with three different concentrations of Zn^{2+} and Al^{3+}, respectively. (c) and (d) showing a new curve after subtraction of polynomial baseline.

5.3.6. Measurable Lower Limit for Hg^{2+} at AuNPs@TA-GCE Using SWV

The sensitivity of the sensor was evaluated by immersing AuNPs@TA-GCEs in the HCl-KCl solution (pH 1.0), containing various Hg^{2+} concentrations, ranging from 100.0 fM to 100.0 nM (Figure 9). A polynomial baseline correction was conducted to determine peak current values. In the absence of Hg^{2+}, no peak current could be detected (Figure 9a, dotted line). As shown in Figure 9b, a linear peak current behavior was observed for peak-2 at concentrations ranging from 100.0 fM to 100.0 nM Hg^{2+}, revealing a measurable lower limit, representing the lowest concentration that can be distinguished from the background signal, of 100.0 fM. This result is presented in Figure 9a with data showing a relative standard deviation (RSD) of less than 3% across triplicate experiments. Given the sensitivity of the proposed strategy, significantly below the permissible level of inorganic Hg^{2+} in drinking water of 30.0 nM[9], and outperforming the system during CV, SWV compares favorably over other voltammetry approaches[32-34], in addition to other methods, which require lengthier analysis time.[35,36]

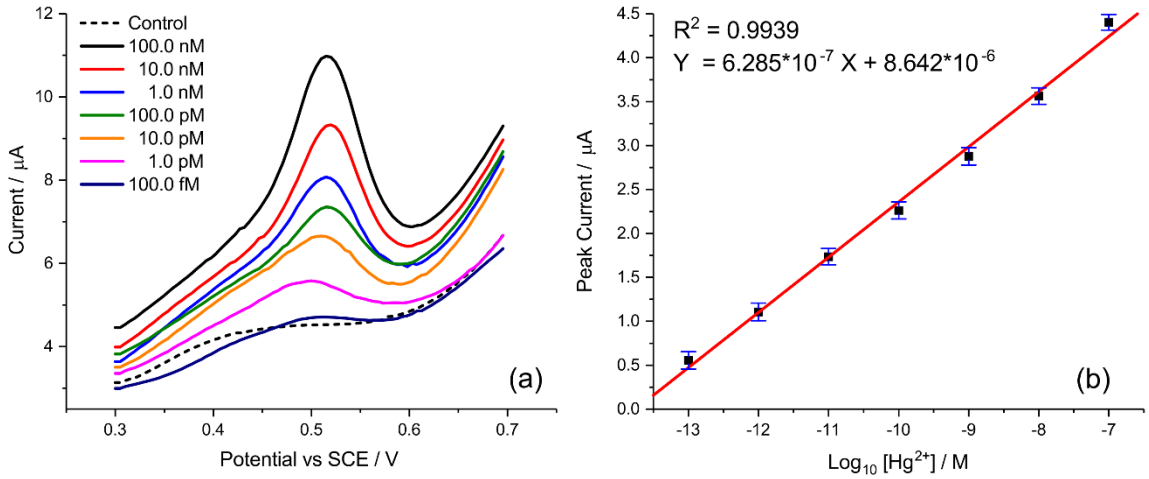


Figure 9. Detection of Hg^{2+} by SWV. (a) SWVs of the AuNPs@TA-GCE immersed in various concentrations of Hg^{2+}. (b) Linear peak current behavior (error bars represent relative standard deviation, with an error of < 3%).

5.3.7. Tap Water Analysis by AuNPs@TA-GCE and AuNPs@TA-SPE

As a proof of concept, the characterized and optimized the system for the detection of Hg^{2+} ions at AuNPs@TA-GCE was exposed to Hg^{2+}-spiked tap water and SWV measurements were carried out. Tap water samples were collected in the laboratory and spiked with 20.0 µM, 2.0 µM, and 20.0 nM Hg^{2+}. As shown in Figure 10a, the oxidation peak (oxidation of TA bound to Hg^{2+}) at a potential of roughly 0.60 V vs SCE, increased with increasing Hg^{2+} concentrations in solution. Even a concentration of just 20.0 nM resulted in a significant peak current value in the presence of Hg^{2+}, in contrast to Al^{3+} and Zn^{2+} ions (Figure 10b).

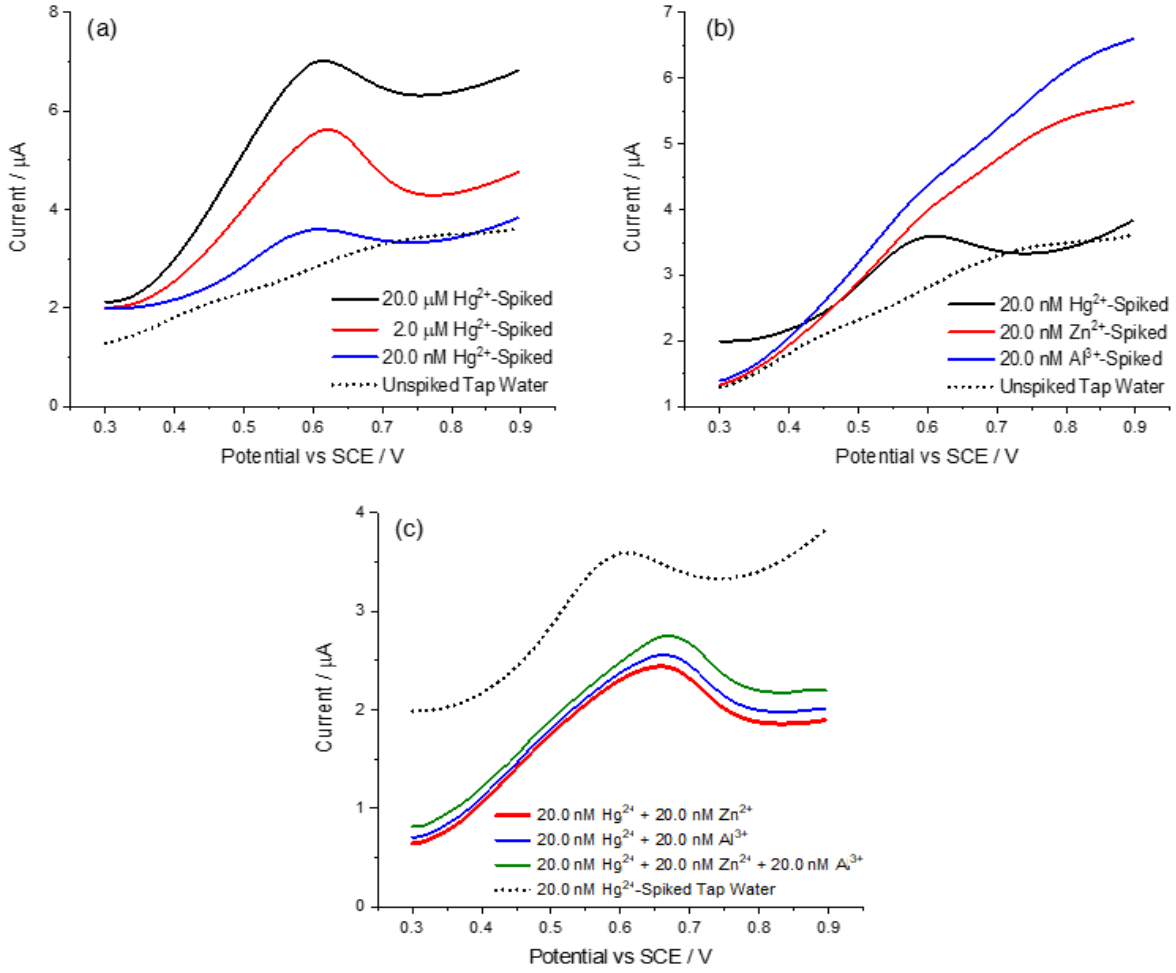


Figure 10. Detection of Hg^{2+} at AuNPs@TA-GCE in (a) spiked tap water with varying Hg^{2+} concentrations, (b) spiked tap water with different metal ions of 20.0 nM each and (c) binary and ternary mixtures of different metal ions, using optimized SWV parameters.

To validate the sensor's selectivity further, the AuNPs@TA-GCE was assessed in the presence of binary and ternary mixtures of tap water solutions, containing Zn^{2+} and/or Al^{3+} ions at a selected concentration of 20.0 nM for each ion. As shown in Figure 10c, the presence of Zn^{2+} and/or Al^{3+} in mixtures leads to an anodic peak current shift to a potential of ca. 0.67 V vs SCE. The polynomial (typically order 3) baseline correction revealed both peak current and peak charge of the binary and ternary solutions remained constant to the value in the presence of 20.0 nM Hg^{2+}-spiked tap water. These results demonstrate that the AuNPs@TA-GCE sensor retains its selectivity towards Hg^{2+}, even if applied to more complex media, such as tap water.

Finally, the transfer of this strategy onto disposable screen-printed carbon electrodes may facilitate the utilization of the demonstrated analytical method in portable devices for routine monitoring purposes. A screen-printed carbon electrode was modified by drop-casting AuNPs@TA suspension at an approximate surface concentration of one-monolayer (assuming the particles are uniformly dispersed on the SPE surface). The CV was conducted to assess whether the oxidation of the AuNPs@TA in the absence of Hg^{2+} is a surface-controlled or diffusion-controlled process. The AuNPs@TA-SPE was immersed into the HCl-KCl solution (pH 1.0) and CV measurements were carried out at scan rates from 10 to 125 mV s^{-1}. As shown in Figure 11, a linear dependence of the peak current on the scan rate was observed, suggesting a surface-controlled process. Furthermore, the peak potential positions at ca. 0.04 V vs SCE were found to be independent of the scan rate, indicating an electrochemically reversible process.

To detect Hg^{2+} at AuNPs@TA-SPE and to establish a calibration curve, functionalised sensors were immersed in HCl-KCl solution (pH 1.0), containing various Hg^{2+} concentrations from 10.0 pM to 1.0 μM (Figure 12a). As shown in Figure 12b, a

linear dependence of the peak current as a function of $\log_{10}$ of Hg^{2+} concentrations was observed, whereby this relationship might be used to determine possible Hg^{2+} contamination in tap water.

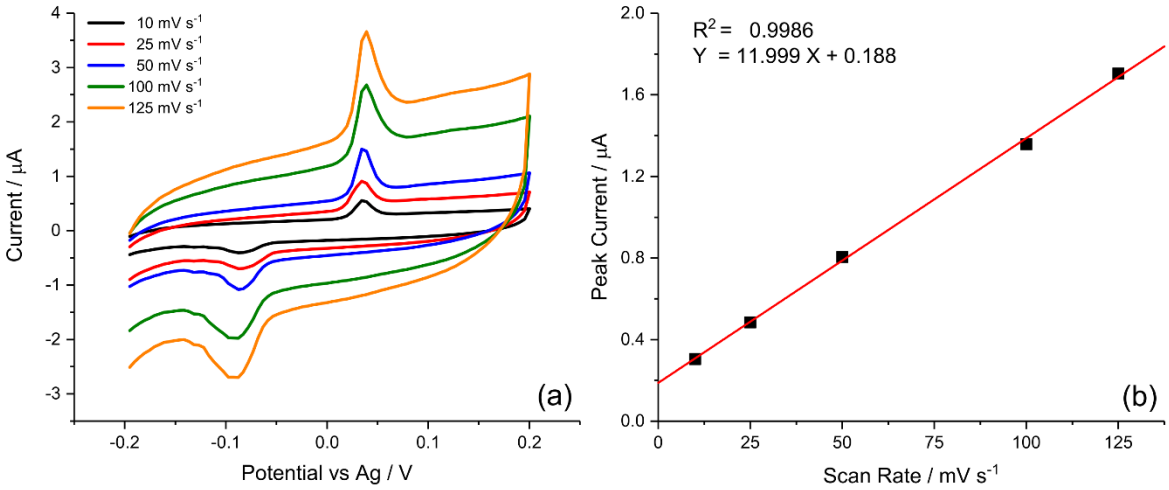


Figure 11. Characterization of AuNP@TA-SPE in HCl-KCl solution (pH 1.0). (a) CVs recorded at AuNP@TA-SPE at various scan rates. (b) Linear peak current behavior at various scan rates.

The detection of inorganic Hg^{2+} in tap water using AuNPs@TA-SPE was conducted by exposing the sensor to tap water, spiked with 10.0 nM Hg^{2+}. SWV was performed in triplicate and experimental parameters were selected in accordance with the optimization procedures outlined above. As shown in Figure 12c, a clear electrochemical oxidation peak current can be seen at a potential of 0.45 V vs Ag, with an average peak current value of 9.08 ± 0.17 µA. Figure 12d presents the resulting curve after subtraction of polynomial (typically order 3) baseline from raw data in Figure 12c. Note that error bars represent the relative standard deviation from triplicate experiments According to the linear calibration function (see Figure 12b), this current value corresponds to an Hg^{2+} concentration in solution with an average of 9.27 nM, close to the expected value of 10.0 nM, showing a recovery above 90%.

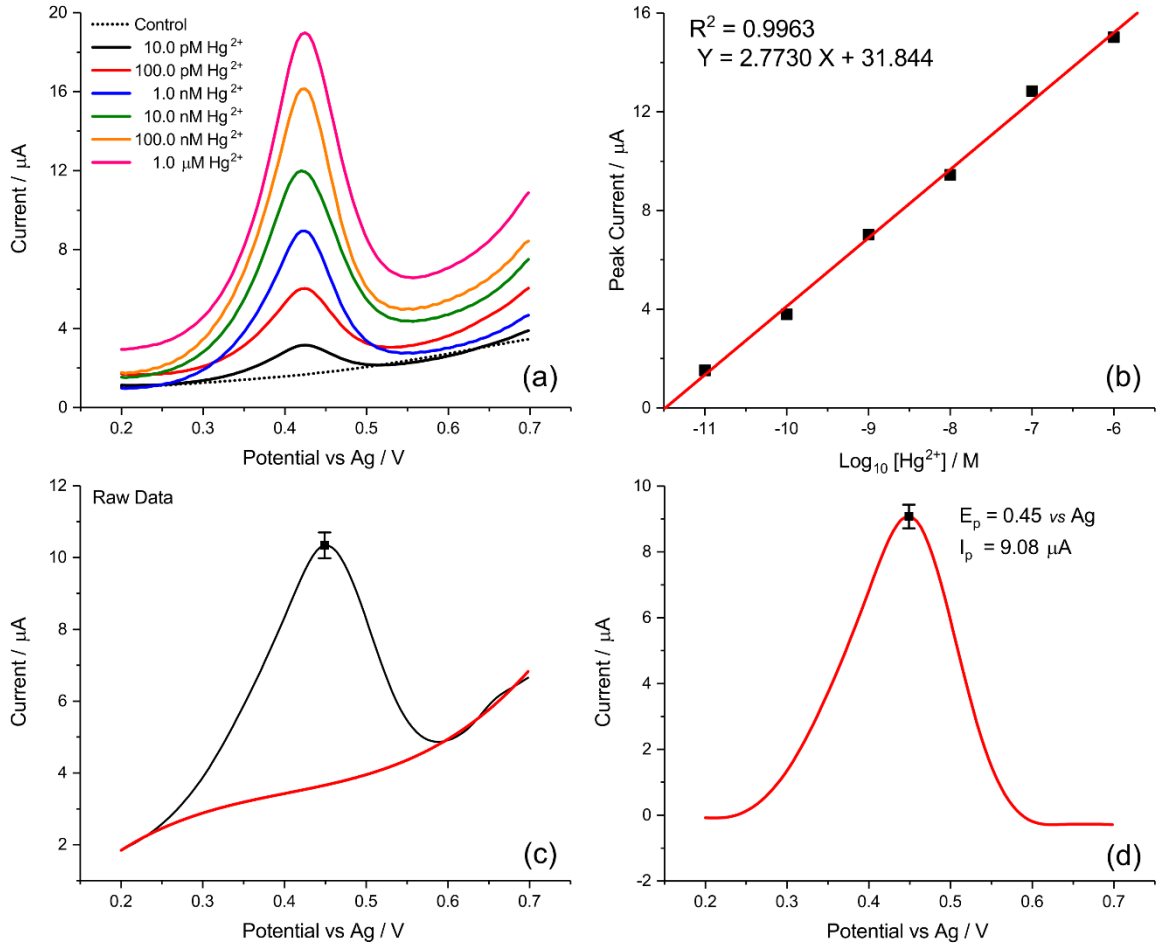


Figure 12. Detection of Hg^{2+} by SWV using AuNPs@TA-SPEs. (a) Voltammograms of AuNPs@TA-SPE exposed to various Hg^{2+} concentrations in HCl-KCl (pH 1.0), (b) linear peak current behaviour for various Hg^{2+} concentrations, (c) detection of 10.0 nM Hg^{2+} in tap water. Raw data (black curve) with polynomial baseline (red curve), (d) resulting curve after subtraction of polynomial baseline from raw data.

5.4. Conclusions

The work presented in this chapter demonstrates an effective analytical method for the sensitive and selective electrochemical detection of Hg^{2+} in aqueous solutions, based on tannic acid-capped gold nanoparticle at carbon electrodes. This strategy allows the quantitative analysis of Hg^{2+} in real samples, such as tap water. The electrochemical sensing parameters for CV and SWV measurements have been characterized and excluded signal contributions from possibly interfering Al^{3+} and Zn^{2+}

ions. This strategy for the detection of trace and/or ultra-trace levels of inorganic Hg^{2+} in aqueous solutions exhibits a measurable lower limit of 100.0 fM. The transfer of the analytical method onto screen-printed electrodes (AuNPs@TA-SPE) makes it suitable for the routine monitoring of inorganic Hg^{2+} in drinking water, as it meets the critical threshold value of 30.0 nM set by the WHO.

Bibliography

(1) WHO. Mercury and Health. www.who.int/en/news-room/fact-sheets/detail/mercury-and-health. Accessed on 2nd July 2019.

(2) Li, Y.; He, B.; Hu, L.; Huang, X.; Yun, Z.; Liu, R.; Zhou, Q.; Jiang, G. Characterization of Mercury-Binding Proteins in Human Neuroblastoma SK-N-SH Cells with Immobilized Metal Affinity Chromatography. *Talanta* 2018, *178*, 811–817.

(3) Chakraborty, P. Mercury Exposure and Alzheimer's Disease in India - An Imminent Threat? *Science of the Total Environment*. 2017, pp 232–235.

(4) Khan, A. T.; Atkinson, A.; Ali, S.; Shireen, K. F. Effects of Inorganic Mercury on Reproductive Performance of Mice. *Food Chem. Toxicol.* 2004, *42* (4), 571–577.

(5) Bjørklund, G.; Dadar, M.; Mutter, J.; Aaseth, J. The Toxicology of Mercury: Current Research and Emerging Trends. *Environmental Research*. 2017, pp 545–554.

(6) Liu, Y.; McDermott, S.; Lawson, A.; Marjorie Aelion, C. The Relationship between Mental Retardation and Developmental Delays in Children and the Levels of Arsenic, Mercury and Lead in Soil Samples Taken near Their Mother's Residence during Pregnancy. *Int. J. Hyg. Environ. Health* 2010, *213* (2), 116–123.

(7) Peplow, D.; Augustine, S. Neurological Abnormalities in a Mercury Exposed Population among Indigenous Wayana in Southeast Suriname. *Environ. Sci. Process. Impacts* 2014, *16* (10), 2415–2422.

(8) Rice, K. M.; Walker, E. M.; Wu, M.; Gillette, C.; Blough, E. R. Environmental Mercury, and Its Toxic Effects. *Journal of Preventive Medicine and Public Health*. 2014, pp 74–83.

(9) WHO. *Guidelines for Drinking-Water Quality: Fourth Edition Incorporating the First Addendum*; 2017. https://doi.org/9789241508087.

(10) Hu, J.; Pagliano, E.; Hou, X.; Zheng, C.; Yang, L.; Mester, Z. Sub-ppt Determination of Butyltins, Methylmercury and Inorganic Mercury in Natural Waters by Dynamic Headspace in-Tube Extraction and GC-ICPMS Detection. *J. Anal. At. Spectrom.* 2017, *32*

(12), 2447–2454.

(11) Senila, M.; Covaci, E.; Cadar, O.; Ponta, M.; Frentiu, M.; Frentiu, T. Mercury Speciation in Fish Tissue by Eco-Scale Thermal Decomposition Atomic Absorption Spectrometry: Method Validation and Risk Exposure to Methylmercury. *Chem. Pap.* 2018, *72* (2), 441–448.

(12) Ghasemi, E.; Kaykhaii, M. Determination of Zinc, Copper, and Mercury in Water Samples by Using Novel Micro Cloud Point Extraction and UV-Vis Spectrophotometry. *Eurasian J. Anal. Chem.* 2017, *12* (4).

(13) Daniel Martín-Yerga and Agustín Costa-García. Recent Advances in the Electrochemical Detection of Mercury. *Curr. Opin. Electrochem.* 2017, 3, 91-96.

(14) Suherman, A. L.; Tanner, E. E. L.; Compton, R. G. Recent Developments in Inorganic Hg^{2+} Detection by Voltammetry. *TrAC Trends Anal. Chem.* 2017, *94*, 161–172.

(15) Saha, K.; Agasti, S. S.; Kim, C.; Li, X.; Rotello, V. M. Gold Nanoparticles in Chemical and Biological Sensing. *Chem. Rev.* 2012, *112* (5), 2739–2779.

(16) Zeng, S.; Yong, K.-T.; Roy, I.; Dinh, X.-Q.; Yu, X.; Luan, F. A Review on Functionalized Gold Nanoparticles for Biosensing Applications. *Plasmonics* 2011, *6* (3), 491–506.

(17) Ngamchuea, K.; Tschulik, K.; Eloul, S.; Compton, R. G. In Situ Detection of Particle Aggregation on Electrode Surfaces. *ChemPhysChem* 2015, *16* (11), 2338–2347.

(18) Sokolov, S. V; Tschulik, K.; Batchelor-McAuley, C.; Jurkschat, K.; Compton, R. G. Reversible or Not? Distinguishing Agglomeration and Aggregation at the Nanoscale. *Anal. Chem.* 2015, *87* (19), 10033–10039.

(19) Wang, J.; Zheng, C.; Ding, S.; Ma, H.; Ji, Y. Behaviors and Mechanisms of Tannic Acid Adsorption on an Amino-Functionalized Magnetic Nanoadsorbent. *Desalination* 2011, *273* (2–3), 285–291.

(20) Rahim, M. A.; Ejima, H.; Cho, K. L.; Kempe, K.; Müllner, M.; Best, J. P.; Caruso, F. Coordination-Driven Multistep Assembly of Metal-Polyphenol Films and Capsules. *Chem. Mater.* 2014, *26* (4), 1645–1653.

(21) Cruz, B. H.; Díaz-Cruz, J. M.; Ariño, C.; Esteban, M. Heavy Metal Binding by Tannic Acid: A Voltammetric Study. *Electroanalysis* 2000, *12*, 1130–1137.

(22) Fan, L.; Ma, Y.; Su, Y.; Zhang, R.; Liu, Y.; Zhang, Q.; Jiang, Z. Green Coating by Coordination of Tannic Acid and Iron Ions for Antioxidant Nanofiltration Membranes. *RSC Adv.* 2015, *5* (130), 107777–107784.

(23) Luo, H.; Zhang, S.; Li, X.; Wang, Z. Tannic Acid Modified Fe_3O_4 Core-Shell Nanoparticles for Adsorption of Pb^{2+} and Hg^{2+}. *J. Taiwan Inst. Chem. Eng.* 2017, *72*, 163–170.

(24) Suherman, A. L.; Tanner, E. E. L.; Kuss, S.; Sokolov, S. V; Holter, J.; Young, N. P.; Compton, R. G. Voltammetric Determination of Aluminium(III) at Tannic Acid Capped-Gold

Nanoparticle Modified Electrodes. *Sensors Actuators B Chem.* 2018, *265*, 682–690.

(25) Jiang, L.; Xie, Q.; Li, Z.; Li, Y.; Yao, S. A Study on Tannic Acid-Doped Polypyrrole Films on Gold Electrodes for Selective Electrochemical Detection of Dopamine. *Sensors* 2005, *5* (4), 199–208.

(26) Çakiroğlu, B.; Özacar, M. Tannic Acid Modified Electrochemical Biosensor for Glucose Sensing Based on Direct Electrochemistry. *Electroanalysis* 2017, *29*, 1–9.

(27) Rajar, K.; Soomro, R. A.; Ibupoto, Z. H.; Sirajuddin; Balouch, A. Tannic Acid Assisted Copper Oxide Nanoglobules for Sensitive Electrochemical Detection of Bisphenol A. *Int. J. Food Prop.* 2017, *20* (6), 1359–1367.

(28) Manjunatha, J. G.; Kumara Swamy, B. E.; Mamatha, G. P.; Gilbert, O.; Chandrashekar, B. N.; Sherigara, B. S. Electrochemical Studies of Dopamine and Epinephrine at a Poly (Tannic Acid) Modified Carbon Paste Electrode: A Cyclic Voltammetric Study. *Int. J. Electrochem. Sci.* 2010, *5* (9), 1236–1245.

(29) Mohan, C. A Guide for the Preparation and Use of Buffers in Biological Systems. *Calbiochem* 2003, 18–21.

(30) Vu, D. L.; Ertek, B.; Dılgın, Y.; Červenka, L. Voltammetric Determination of Tannic Acid in Beverages Using Pencil Graphite Electrode. *Czech J. Food Sci.* 2015, *33* (1), 72–76.

(31) Kätelhön, E.; Cheng, W.; Batchelor-McAuley, C.; Tschulik, K.; Compton, R. G. Nanoparticle-Impact Experiments are Highly Sensitive to the Presence of Adsorbed Species on Electrode Surfaces. *ChemElectroChem* 2014, *1* (6), 1057–1062.

(32) Shah, A.; Sultan, S.; Zahid, A.; Aftab, S.; Nisar, J.; Nayab, S.; Qureshi, R.; Khan, G. S.; Hussain, H.; Ozkan, S. A. Highly Sensitive and Selective Electrochemical Sensor for the Trace Level Detection of Mercury and Cadmium. *Electrochim. Acta* 2017, 258, 1397-1403.

(33) Granado, E.; Gervais, E.; Gotti, G.; Meireles, M.; Gros, P.; Evrard, D. Mercury(II) Trace Detection Using a Glassy Carbon Electrode Functionalized by Chemically Prepared Gold Nanoparticles. Influence of Coating Process on Surface Reactivity and Analytical Performances. *Int. J. Electrochem. Sci.* 2017, *12* (7), 6092–6107.

(34) Nguyen, H. L.; Cao, H. H.; Nguyen, D. T.; Nguyen, V.-A. Sodium Dodecyl Sulfate Doped Polyaniline for Enhancing the Electrochemical Sensitivity of Mercury Ions. *Electroanalysis* 2017, *29* (2), 595–601.

(35) Asadpour-Zeynali, K.; Amini, R. A Novel Voltammetric Sensor for Mercury(II) Based on Mercaptocarboxylic Acid Intercalated Layered Double Hydroxide Nanoparticles Modified Electrode. *Sensors Actuators, B Chem.* 2017, *246*, 961–968.

(36) Bui, M. P. N.; Brockgreitens, J.; Ahmed, S.; Abbas, A. Dual Detection of Nitrate and Mercury in Water Using Disposable Electrochemical Sensors. *Biosens. Bioelectron.* 2016, *85*, 280–286.

Chapter 6

Tannic Acid Capped Gold Nanoparticles: Capping Agent Chemistry Controls the Redox Activity

This chapter generalizes and extends the discussion in chapters 4 and 5, exploring the role of the tannic acid capping agent in the redox activity for Hg^{2+} and Zn^{2+} detection through the nano-impacts method. The key role of the capping agent in the detection of metal cations is assessed for tannic acid-capped gold nanoparticles (AuNPs@TA) at both ensembles (using cyclic voltammetry) and single particles (using oxidative and reductive nano-impacts). The results show that the capping agent complexes with Zn^{2+} and Hg^{2+} in a reversible and Langmuirian manner in both cases. The sensitivity of detection is determined by the amount of capping agent present on the nanoparticles with similar values seen for both oxidation and reduction reactions. The optimization of the capping agent loading is, therefore, key to metal ion detection.

The work presented in this chapter has been published in *Physical Chemistry Chemical Physics* (*Phys. Chem. Chem. Phys.* 2019, *21* (8), 4444–4451) and was carried out in collaboration with Dr. Giorgia Zampardi, who helped with the interpretation of the experimental results. Dr. Hatem M. Amin (in collaboration with Dr. Neil P. Young and Ms. Jennifer Holter from the Department of Materials, Oxford University) obtained the dynamic light scattering (DLS) and nanoparticle tracking analysis (NTA) data and transmission electron microscope (TEM) images for AuNPs@TA.

6.1. Introduction

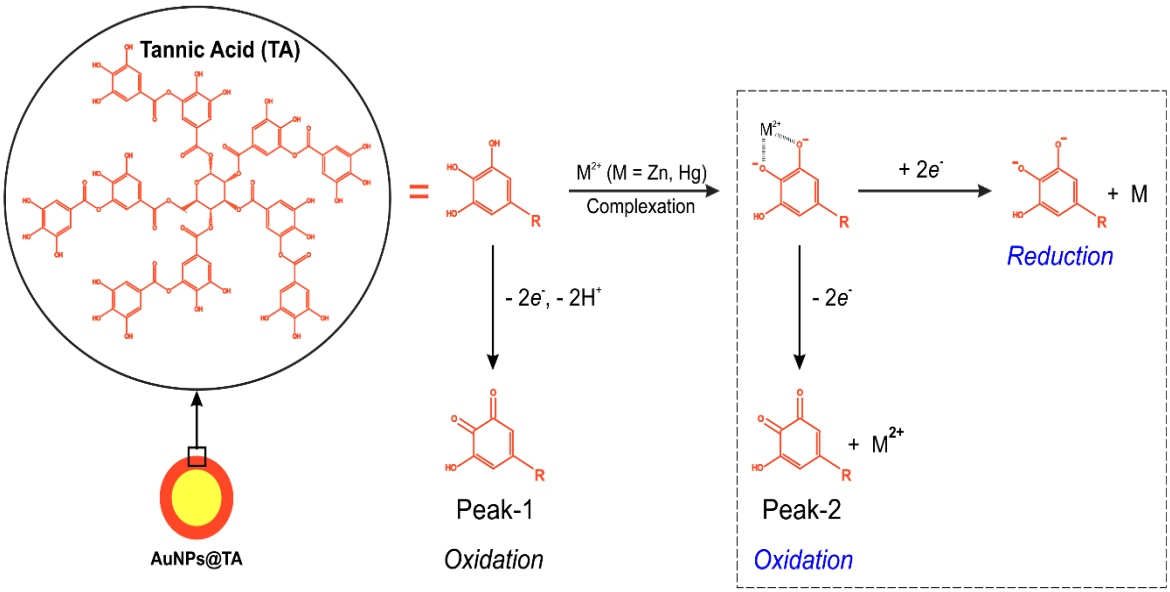
Understanding the role of the capping agent is important for the development of the controlled synthesis of nanoparticles[1], the prevention of nanoparticle aggregation/agglomeration[2], the attenuation of nanoparticle toxicity[3], the control of nanoparticle reactivity[4] and for understanding electron-transfer dynamics[5,6]. In addition, capped nanoparticles such as gold nanoparticle (AuNPs) are widely used notably for colorimetric analysis[7], electrocatalysis[8], and electroanalysis[9]. This chapter will define how the *quantity* of capping agents can control the electrochemical responses.

The interaction between the capping agent of nanoparticles and metal cations has been reported to influence the extent of agglomeration of nanoparticles.[10] The latter was found to have a correlation with the metal-capping agent complex formation constant. For example, in the presence of Pb^{2+}, silver nanoparticles reversibly form agglomerates and this is induced by the complexation between Pb^{2+} and citrate groups of the capping agent. The capping agent can also tune the electron transfer kinetics to/from the nanoparticle.[11,12] For example, whilst citrate capped silver nanoparticles are completely oxidized at low potentials, DNA capped particles require higher potentials for complete oxidation and which is enough to oxidize the quinine and adenine base pairs of DNA. This emphasizes the role of DNA capping agent as a tunnelling barrier to insulate the particle core, and thus selectively control of the oxidation process can be realised by adjusting the applied potential. An electron transfer-gated mechanism has been also observed for poly(ethylene glycol) capping agents, where a dynamic equilibrium between a wrapped and unwrapped silver nanoparticle exists.[13] Meanwhile, the reactivity of nanoparticles has been studied using

cetyl trimethylammonium bromide (CTAB) capping agent.[14] The CTAB shifted the nanoparticle oxidation to significantly lower potentials, resulting in the more facile oxidative dissolution of gold.

Macromolecular capping agents such as tannic acid (TA) have been exploited for the electrochemical detection of specific metal cations via ensembles of the gold nanoparticles.[15,16] However, the electrochemical analysis of the TA capping agent studied with an ensemble of AuNPs@TA (for example using stripping voltammetry) does not reflect necessarily its behavior at the single nanoparticle level. In particular, analysis of the nanoparticles using stripping voltammetry is unreliable because capping agent effects in drop-casting may lead to particle aggregation and partial oxidation.[17,18]

Recent advances in the nano-impacts method have demonstrated the possibility of electrochemistry at the single-particle level[19-23]. This method is performed by suspending nanoparticles in solution so that single nanoparticle can stochastically collide with an electrode surface due to their Brownian motion. Faradaic current-time transients (spikes) in the background reveal the collision events. Usually, the spike is produced from two possible sources: (1) an electrochemical reaction catalysed ("mediated") on the surface of the collided nanoparticles ("indirect impacts") and (2) the oxidation or reduction of the single nanoparticle itself when it hits the electrode surface ("direct impacts").[23-25] This chapter will in contrast focus on the electrochemistry of the capping agent on the nanoparticle surface using both oxidative and reductive nano-impacts to understand the role of a TA capping agent (Scheme 1) on gold particles for the detection of inorganic Zn^{2+} and Hg^{2+} and to generate mechanistic and kinetic insights.



Scheme 1. Schematic illustration shows that the tannic acid (TA) capping agent controls the redox activity of the gold nanoparticle.

6.2. Experimental

Details about the chemical reagents can be found in Chapter 2, Section 2.1. The tannic acid-capped gold nanoparticles (AuNPs@TA, 2.2 x 10^{10} particles mL^{-1}) colloid, with a hydrodynamic diameter of 68.4 nm as indicated by the manufacturer, were used as received (NanoComposix Inc., San Diego, US). The main ingredients of suspension are Au (0.005% mass), tannic acid (<0.001% mass) and water (>99% mass). The manufacturer declares that no residual reactants are present in the final formulation.[26] To ensure the reproducibility of all measured data, both glassy carbon electrode (GCE) and carbon microelectrode disc were regularly re-polished.[27]

For CV analysis of Zn^{2+}, a ca. 2.0 x 10^{9} particles of the AuNPs@TA suspension were drop cast on the GCE surface then allowing them to completely dry under N_2 flow. This resulted in approximately one-monolayer surface coverage of AuNPs@TA-GCE (see Appendix A.3). However, the possibility of particle agglomeration/aggregation is recognized in the drop-casting method and can drive the incomplete stripping

oxidation of the nanoparticles.[18,28,29] CVs were recorded by sweeping the potential from 0.0 V to 0.7 V and reversed back to 0.0 V vs SCE, at a scan rate of 0.1 V s^{-1}. The CV analysis of Hg^{2+} has been reported previously in Chapter 5.[16]

For nano-impacts experiments, the chronoamperometry was recorded at a carbon microelectrode disc with the same reference and counter electrodes as above, but using a home-built low noise potentiostat with a post-acquisition Bessel filtering of 100 Hz and PyFemto software (version 0.6).[30] This potentiostat accurately conserves the overall amount of charge transferred due to a particle impact process despite possible alteration in the spike shape.[15,31] A 10.0 pM of the AuNPs@TA suspension (ca. 8.8 x 10^9 particles) and various concentrations of either Zn^{2+} (10.0 to 300.0 mM) or Hg^{2+} (1.0 to 100.0 μM) were added into a solution of 10.0 mM KCl + 10.0 mM HCl. Chronoamperograms were recorded for 25 s at different oxidizing or reducing potentials. For Zn^{2+} analysis, potentials in the range from 0.4 V to 0.7 V and from -0.2 V to -0.5 V were applied for oxidative and reductive nano-impacts, respectively. For Hg^{2+} analysis, chronoamperograms were recorded at potentials between 0.6 V to 0.9 V and -0.2 V to -0.6 V for oxidative and reductive nano-impacts, respectively. The magnitude of the spike threshold is taken as either three or five times the estimate of the standard deviation of the background current.[32] The spikes were analyzed using "SignalCounter", which was developed by Dr. D. Omanović (Centre for Marine and Environmental Research Zagreb, Croatia).[33]

Scanning electron microscopy (SEM) and zeta potential analyses of the AuNPs@TA have been reported previously in Chapter 4.[15,16] In this chapter, transmission electron microscopy (TEM), dynamic light scattering (DLS) and nanoparticle tracking analysis (NTA) analyses were added and discussed.

6.3. Results and Discussion

The physical characterization of the AuNPs@TA using TEM, DLS, NTA, and UV-vis spectroscopy analyses was first reported. Following this, the electrochemical analysis of AuNPs@TA was conducted at the ensemble (using cyclic voltammetry) and single-particle (using nano-impacts) levels. Subsequently, both oxidative and reductive nano-impacts experiments were performed in the absence and presence of Zn^{2+} or Hg^{2+} on single particles of AuNPs@TA. Comparisons are used to infer the mechanisms underlying the redox responses observed and the key role of the tannic acid (TA) capping agent identified and defined.

6.3.1. Characterization of AuNPs@TA

Size characterization of the gold nanoparticle core and thickness of the tannic acid (TA) capping agent was carried out using TEM. As shown in Figure 1, the nanoparticle population exhibits qualitative homogeneity in their morphology, namely roughly spheroidal particles. The average diameter size of gold nanoparticle core and thickness of TA capping layers are 62.2 ± 1.4 nm and 8.3 ± 0.5 nm, respectively.

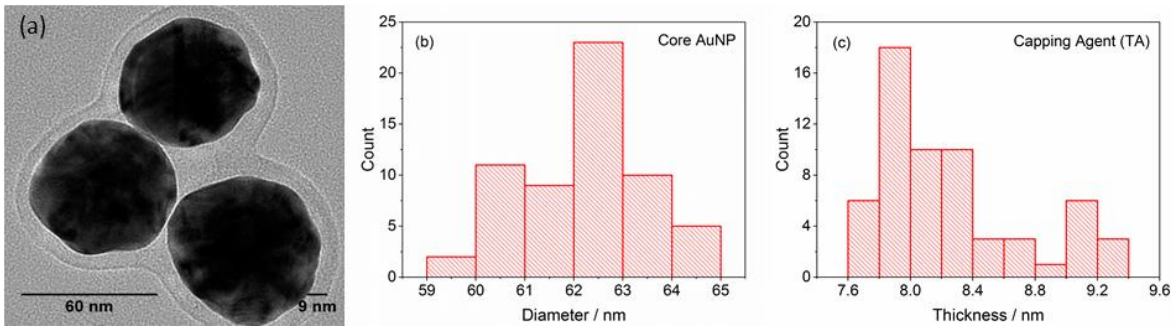


Figure 1. (a) TEM micrograph showing the gold nanoparticle core capped with TA layers. Statistical distributions of (b) diameter size of AuNP core and (c) layer thickness of TA, as extracted from TEM micrographs of 60 particles.

DLS and NTA analyses were undertaken to measure the average hydrodynamic diameter of the AuNPs@TA. The results give an average diameter of 68.1 ± 0.7 nm and 68.7 ± 0.4 nm for NTA and DLS analysis, respectively (see Appendix B.2). These results are in good agreement with the manufacturer size specification and related to previous chapters (see Chapter 4 and Chapter 5).[15,16]

The stability of the AuNPs@TA in various concentrations of electrolyte was assessed by UV-Vis spectroscopy in the range of 10.0 to 100.0 mM of KCl + HCl solutions (pH 1.0). Each electrolyte was degassed thoroughly with a N_2 before 10.0 pM of AuNPs@TA (ca. 8.8 x 10^9 particles) suspension was added. As shown in Figure 2, the most stable condition of AuNPs@TA was found in 10.0 mM KCl + 10.0 mM HCl solutions (pH 1.0) with only a ca. 2.0% decrease in maximum absorbance during 15 min observation, with the characteristic wavelength of 535 nm (see Appendix B.2).

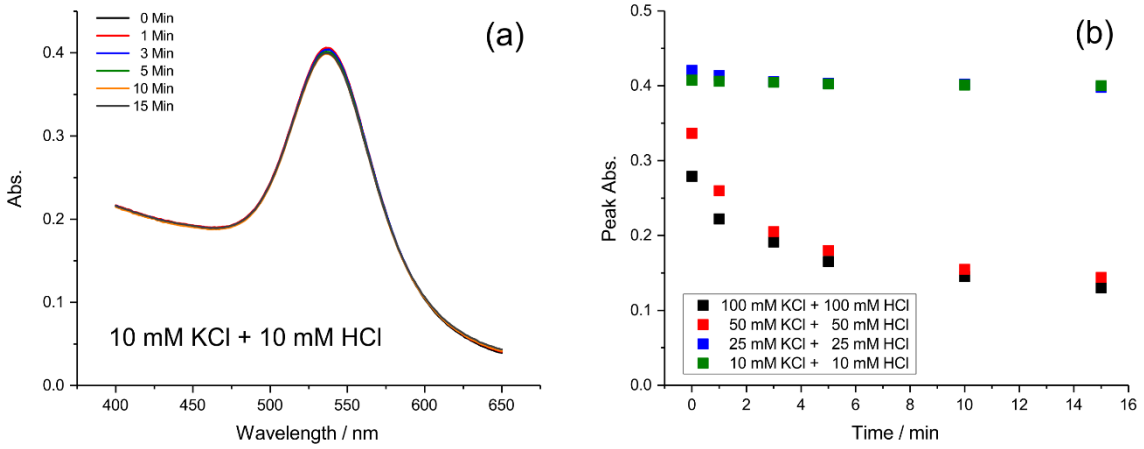


Figure 2. UV-vis analysis of AuNPs@TA. (a) UV-vis spectra of ca. 10.0 pM AuNPs@TA in a solution of 10 mM KCl + 10 mM HCl (pH 1.0) and (b) plot of peak absorbance of AuNPs@TA in various electrolyte concentrations during 15 minutes measurement.

The lowest stability was found in 100.0 mM KCl + 100.0 mM HCl solutions, with a ca. 53% decrease in maximum absorbance. It is reasonable to conclude that the

AuNPs@TA suspensions are stable over the time period (ca.15 min) of the subsequent nano-impacts experiments (see below).

6.3.2. Electrochemical Analysis of AuNPs@TA Using Cyclic Voltammetry

Having physically characterized the AuNPs@TA, electrochemical characterization of the ensemble of AuNPs@TA was investigated first using CV. This was achieved by drop-casting ca. 2.0 x 10^9 particles of AuNPs@TA suspension onto a GCE surface, leading to an approximately one-monolayer surface coverage of the AuNPs@TA-GCE (see Appendix A.3). AuNPs@TA-GCE was then immersed in a solution of 0.1 M KCl + 0.1 M HCl (pH 1.0) and CV was recorded by sweeping the potential from 0.0 V to 0.7 V and reversed back to 0.0 V vs SCE at a scan rate of 0.1 V s^{-1}.

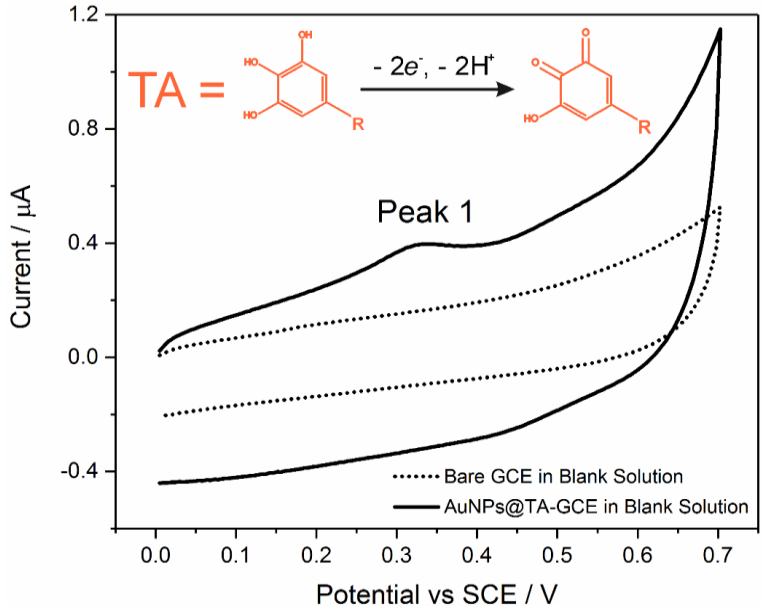


Figure 3. CV analysis of the ensemble of AuNPs@TA (oxidation of TA capping agent to TA-quinone, Scheme 1)

As shown in Figure 3 (solid black line), a single broad oxidative peak (peak 1) was observed at the potential of ca. 0.31 V vs SCE. This peak is consistent with the

previous reports on the oxidation of TA to TA-quinone with the peak currents of the peak 1 increased linearly with scan rate, ranging from 0.01 to 0.1 V s^{-1} (see Chapter 4 and Chapter 5).[15,16] The result confirms that the oxidation of the TA capping layers is a surface-controlled process. Furthermore, the peak potentials of the peak 1 essentially scan rate independent hinting at an electrochemically reversible process. Chapter 4 reports the peak potential and peak current of the peak-1 decreased with increasing pH solutions[15], suggesting the loss of protons on oxidation of the TA capping agent. However, analysis of the ensemble of AuNPs@TA via drop-casting method is recognized to effect experimental results by causing aggregation/agglomeration of the particles.[17,28] Therefore, to get an accurate understanding of the role the TA capping agent plays in the electron transfer process at a single particle level of AuNPs@TA, the nano-impacts method was next performed.

Single particles of AuNPs@TA were characterized via oxidative nano-impacts with the aim of calculating the number of electroactive quinone or hydroquinone species involved in the reaction at a single AuNPs@TA level. To assess this, a carbon microelectrode disc was immersed in 10.0 mM KCl + 10.0 mM HCl solutions (hereafter referred to as the blank solution) containing 10.0 pM (ca. 8.8 x 10^9 particles) of AuNPs@TA. Chronoamperograms were recorded at applied oxidizing potential ranging from 0.3 V to 0.7 V vs SCE. In the absence of AuNPs@TA (control experiment), featureless continuous time-current transients were observed at all potentials studied (see Appendix C.1). Subsequently, by introducing the AuNPs@TA into the system, the oxidative spikes were observed at an applied potential greater than or equal to 0.5 V vs SCE (Figure 4). The lower oxidizing potential (0.3 V and 0.4 V vs SCE) gave spike features too small to detect, suggesting the insufficient potential to oxidize the TA capping layers at the single AuNPs@TA level.

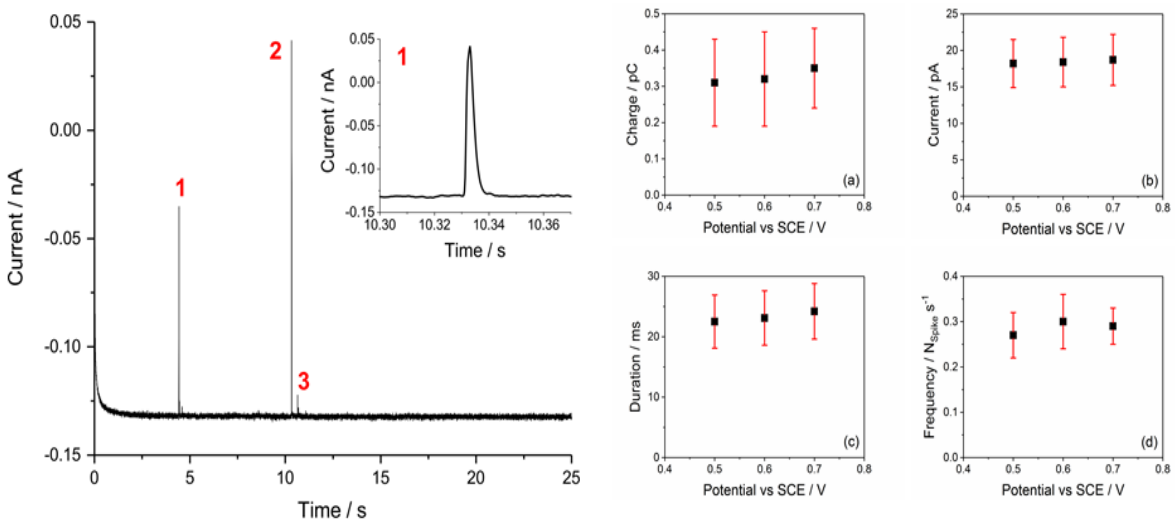


Figure 4. Representative chronoamperograms measured at a carbon microelectrode disc immersed in a blank solution containing 10.0 pM (ca. 8.8 x 10^9 particles) AuNPs@TA at the potential of 0.6 V vs SCE (inset image depicts the spike shape).

The average spikes charge, current, duration, and frequency, resulting from the TA oxidation, were found to be ca. 0.32 ± 0.1 pC, 18.4 ± 3.4 pA, 23.3 ± 4.5 ms, 0.3 ± 0.1 spike s^{-1}, respectively. These values are roughly constant at potentials of ≥0.5 V vs SCE (Figure 4). The experimental number of TA molecules incorporated on a single AuNP core is ca. 1.0 x 10^5 molecules, calculated by applying the Faraday's first law and considering a maximum of potentially 20 electron transfer from the TA molecular structure[15] (see Appendix A.3). This result is in good agreement with the apparent number of the TA molecules of ca. 1.2 x 10^5 molecules as calculated by dividing the volume of AuNP core with an estimated volume of a single tannic acid (TA) molecule (8.6 x 10^{-28} m^3) reported by Madhan *et al*[34] (see Appendix A.3).

Subsequently, reductive nano-impacts experiments of AuNPs@TA were undertaken by immersing a carbon microelectrode disc in either blank solution (control experiments) or blank solution containing 10.0 pM (ca. 8.8 x 10^9 particles) of AuNPs@TA. Chronoamperograms were recorded at applied reducing potential ranging

from -0.1 V to -0.5 V vs SCE in each case. As a result, *both* in the absence and in the presence of AuNPs@TA no reductive spike features were observed at all studied potentials (see Appendix C.1). The result suggests that the TA capping agent, incorporated on a single AuNP core, is not reduced under these potentials and thus is electrochemically inactive. This result is consistent with previously reported data in both Chapter 4 and Chapter 5.[15,16]

The following section considers the role of the TA capping agent in the presence of metal cations. The analysis was again carried out by exposing AuNPs@TA, either as ensembles (using CV) or as single particles (using nano-impacts), into an aqueous solution containing Zn^{2+} or Hg^{2+} ions.

6.3.3. Electrochemical Analysis of AuNPs@TA with Metal Cations

Ensembles of AuNPs@TA in the presence of Zn^{2+} were analyzed using CV. One-Monolayer surface coverage of AuNPs@TA-GCE was immersed in a blank solution containing 1.0 mM Zn^{2+} and CV was recorded by sweeping the potential from 0.0 V to 0.7 V and reversed back to 0.0 V vs SCE at a scan rate of 0.1 V s^{-1}. As shown in Figure 5 (solid black line), two oxidative peaks were observed at a peak potential of 0.31 V vs SCE (peak 1) and 0.48 V vs SCE (peak 2). The peak 1 was the result of the oxidation of TA to TA-quinone (see Chapter 4 and Chapter 5), whilst peak 2 is attributed to the oxidation of TA capping agent complexed with Zn^{2+}. This leads to some swelling of the TA layers during oxidation followed by some increased accessibility of the complexing sites to uptake Zn^{2+} and results in peak-2.[15,16] CV analysis of the Hg^{2+} has been reported in Chapter 5, with the peak 2 was observed at a more positive potential (0.58 V vs SCE). These results suggest that TA capping agent uptakes metal cations.

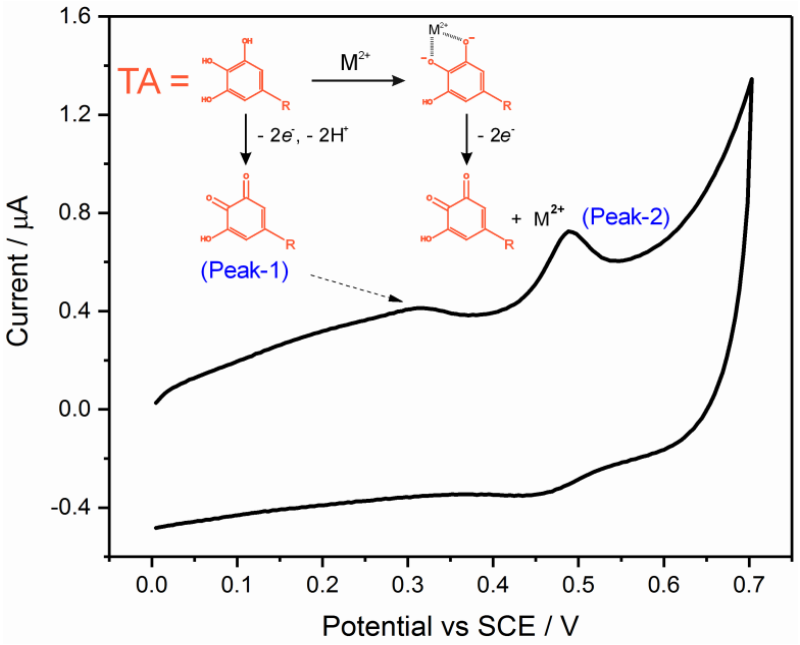


Figure 5. The CV of the ensemble of AuNPs@TA in 1.0 mM Zn^{2+} at a scan rate of 0.1 V s^{-1}.

Following this, the effect of the scan rate was studied to identify whether the oxidation of the TA/Zn^{2+} complexes in the ensemble of AuNPs@TA is a surface-controlled or diffusion-controlled process. To assess this, the AuNPs@TA-GCE was exposed to a solution containing 1.0 mM Zn^{2+} and then CVs were recorded at different scan rates between 0.01 and 0.1 V s^{-1}.

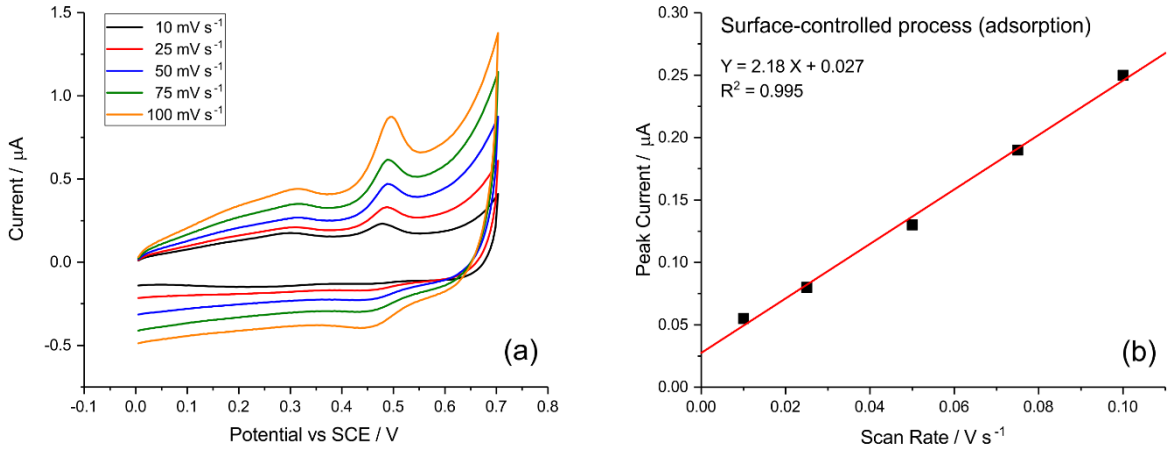


Figure 6. (a) CVs of one-monolayer surface coverage of AuNPs@TA-GCE immersed in 1.0 mM Zn^{2+} at various scan rates, (b) Linearity of the peak current of the peak 2 at various scan rates shown in (a).

As shown in Figure 6, the peak current value of peak 2, baseline-corrected by applying a polynomial fit (typically of order 4), increased linearly (R^2 = 0.995) with scan rates. The result suggests that the oxidation of AuNPs@TA complexed Zn^{2+} is a surface-bound; a similar process as seen with Hg^{2+} as has been reported in Chapter 5.[16] Moreover, the peak potentials of the peak 2 were scan rate independent, again suggesting an electrochemically reversible process, where the shift in peak potential between peak 1 and peak 2 reflects the strength of the binding of Zn^{2+} and TA.

Following this, the AuNPs@TA-GCE was immersed in a blank solution containing various Zn^{2+} concentrations ranging from 1.0 to 120.0 mM, at a scan rate of 0.1 V s^{-1}. Equilibration of the AuNPs@TA with the solution containing the ions, or not, was realized within a matter of minutes.[15,16] The peak current of peak 2 increased with the Zn^{2+} concentration and saturated for concentration above 75.0 mM (Figure 7).

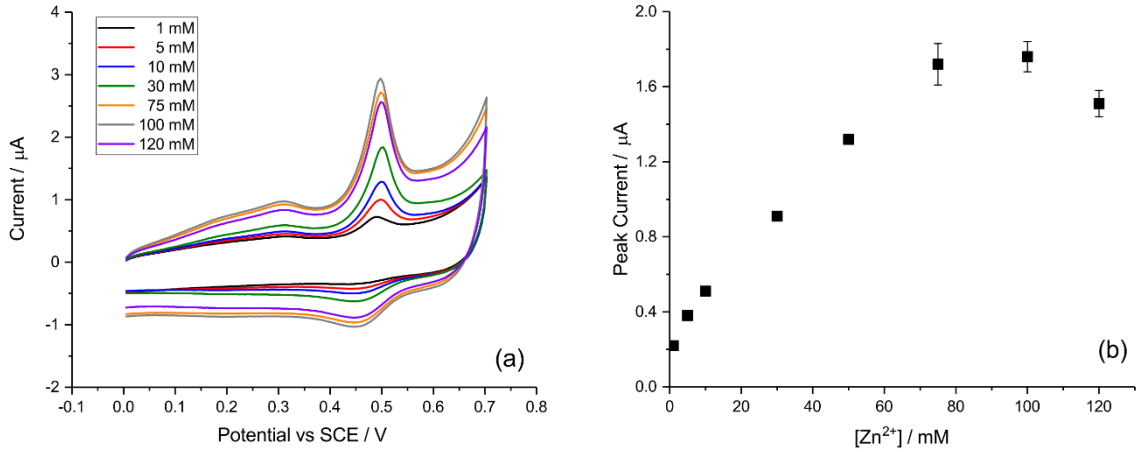


Figure 7. (a) CVs of one-monolayer surface coverage of AuNPs@TA-GCE immersed in various Zn^{2+} concentrations at a scan rate of 0.1 V s^{-1}. (b) The plot of the peak current of peak 2 at various Zn^{2+} concentrations.

This result indicates the limitation of the TA capping agent to uptake Zn^{2+} at concentration beyond 75.0 mM. In addition, CV analysis of the ensemble of AuNPs@TA in the presence of metal cations with different pre-equilibrium times has been reported

previously (see Chapter 4 for Al^{3+} and Chapter 5 for Hg^{2+}).[15,16] For example in the case of Hg^{2+}, the peak current of peak 2 increased during a pre-equilibrium time of 10 min. This result suggests that the swelling of the TA layer reached its maximum at 10 min when the electrode surface becomes saturated with Hg^{2+}.

Reductive CV scans were studied to identify whether the TA capping agent may mediate the underpotential deposition of zinc on the gold core surfaces within the AuNPs@TA ensemble. Underpotential deposition (UPD) is the deposition of a monolayer or sub-monolayer of metal onto the different metal surface at potentials more positive than the Nernst potential for bulk deposition of this metal.[35,36] A one-monolayer surface coverage of AuNPs@TA-GCE was immersed in a 0.2 mM Zn^{2+} solution. Next, the CV was recorded by sweeping the potential from 0.0 V to -1.2 V and reversed back to 0.0 V vs SCE at a scan rate of 0.02 V s^{-1}. The UPD peak was observed at the potential of -0.8 V vs SCE followed by a sharp increase in the cathodic current from the potential of ca. -1.0 V to -1.2 V vs SCE (bulk deposition of Zn).

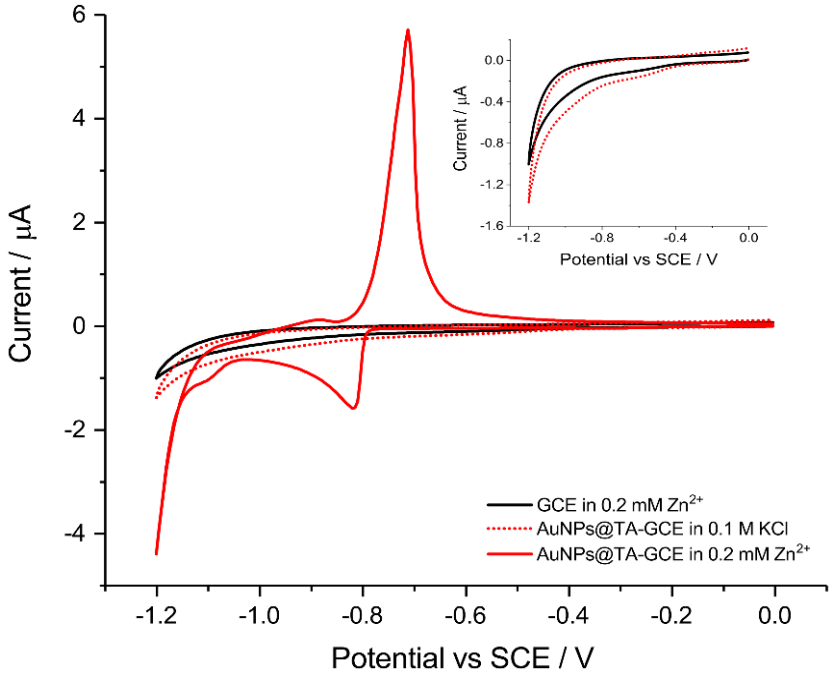


Figure 8. UPD analysis of Zn^{2+} at the ensemble of AuNPs@TA, at a scan rate of 0.1 V s^{-1}.

As shown in Figure 8, the sharp UPD peak shape indicates that the reaction is probably not controlled by mass transport to the ensembles of AuNPs@TA surface but suggests that under sufficient reducing potential the Zn^{2+} can complex with the TA layers and on reduction, zinc metal is deposited on the gold core surface. Integrating the UPD peak results in a peak charge of ca. 17.2 μC, with an apparent surface coverage of the Zn deposition is approximately 2.2 x 10^{14} atoms cm^{-2}. Note that no UPD signal was seen in the absence of AuNPs@TA.

Having characterized the ensemble of AuNPs@TA in the presence of metal cations using a CV, the next section will identify the role of the TA capping agent at single AuNPs@TA in the presence of either Zn^{2+} or Hg^{2+}. The analysis consists of both oxidative and reductive nano-impacts at various potentials and for different metal cation concentrations.

6.3.4. Oxidative Nano-impacts Analysis

Initially, control experiments were performed in the absence of the AuNPs@TA. A microelectrode was immersed in a blank solution containing various concentrations of metal cation, either 10.0 to 300.0 mM Zn^{2+} or 1.0 μM to 100.0 μM Hg^{2+}. The microelectrode disc was held at the potential of 0.4, 0.5, 0.6, and 0.7 V vs SCE for Zn^{2+} or 0.6, 0.7, 0.8 and 0.9 V vs SCE for Hg^{2+}, independently. No spike features were detected at any studied potential for these control experiments (see Appendix C). Following this, 10.0 pM (ca. 8.8 × 10^{9} particles) of AuNPs@TA was introduced into the blank solution containing either 100.0 mM Zn^{2+} or 10.0 μM Hg^{2+}, and the potential was applied as with the control experiments. Note that all analyte solutions were degassed thoroughly with N_2 flow prior to the measurement.

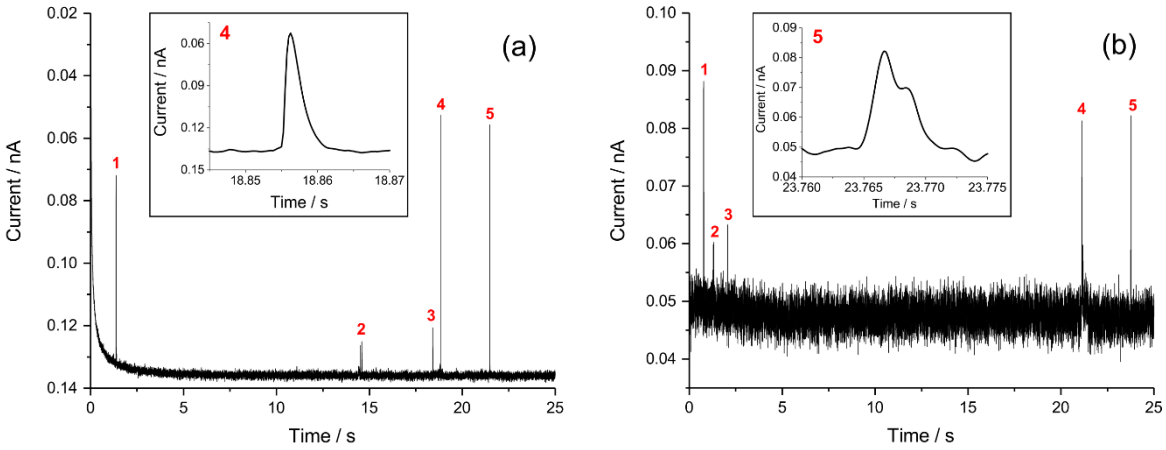


Figure 9. Representative chronoamperograms of oxidative nano-impacts. A carbon microdisc electrode immersed in solution containing of 10.0 pM AuNPs@TA (ca. 8.8 x 10^9 particles) and (a) 100.0 mM Zn^{2+}, (b) 10.0 μM Hg^{2+} at applied potential of 0.6 V and 0.7 V vs SCE, respectively.

As shown representatively in Figure 9, clear and sharp oxidative spikes were observed for both of the metal cations studied. The results suggest that the oxidative spikes resulted from the reduction of complexed metal cations upon collision of the nanoparticles with the electrode surface. As shown in Figure 9, the spike magnitude was found to be similar but a little larger in the presence of metal cations as compared to the case of the uncomplexed AuNPs@TA (Figure 4). The small increase in charge and current may reflect swelling of the TA layer promoting the oxidation of more quinone groups (as discussed above) whilst the duration and frequency may hint at electrostatic factors being drops by the complexation.

To study the potential dependency, the average charge of 2,114 spikes at four different potentials (0.4 V to 0.7 V vs SCE) were calculated and plotted as a function of different Zn^{2+} and Hg^{2+} concentrations. The average charge values were found to be roughly constant at all potentials studied. Note that potentials <0.4 V gave features too small to detect. The charge values increased up to 30.0 mM Zn^{2+} and then saturating at higher concentrations. In comparison, 1.0 μM to 100.0 μM of Hg^{2+} was assessed in the

same manner as with the Zn^{2+} ions, but at applied potentials of 0.6 to 0.9 V vs SCE. The average charge values were found to be roughly constant at all studied potentials (0.5, 0.6 and 0.7 for Zn^{2+} and 0.6, 0.7, 0.8 and 0.9 V for Hg^{2+}). The charge values in the presence of Hg^{2+} increased up to 25.0 μM Hg^{2+} (Figure 10a, red).

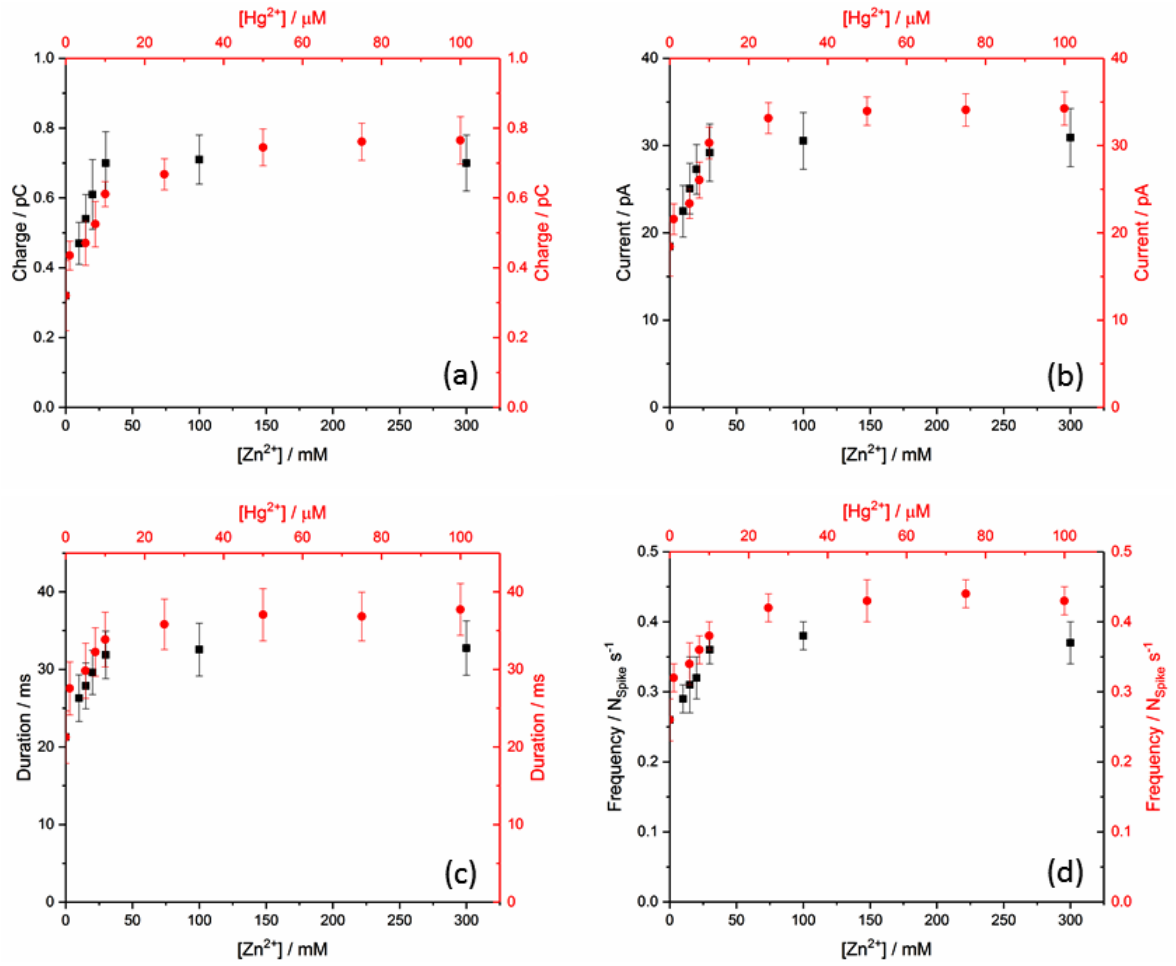


Figure 10. Overlaid plots of the oxidative spikes (a) charge, (b) current, (c) duration and (d) frequency in the presence of various Zn^{2+} (black) and Hg^{2+} (red) concentrations.

Figure 10 shows comparisons of the oxidative spikes charge, current, duration, and frequency for Zn^{2+} and Hg^{2+}. Notably, these characteristics were shown to have approximately similar qualitative behavior in both cases but, quantitatively, responding differently to the metal cation concentration. For example, similar behavior

of impact duration of 20-35 ms and frequency of ca. 0.3-0.4 spikes s^{-1} were observed at a concentration region of ≤30.0 mM Zn^{2+} and ≤25.0 μM Hg^{2+}, above which the value tend to plateau at higher concentrations but, significantly, with similar values for each case. These results suggest that TA controls the oxidation prior to the complexation with metals and undergo oxidation in a similar manner for both metals.

6.3.5. Reductive Nano-impacts Analysis

The reductive nano-impacts experiments were performed by immersing a carbon microelectrode disc in an outgassed solution containing the same concentrations of either Zn^{2+} or Hg^{2+} as in the oxidative nano-impacts experiments. The potential was applied at -0.2 to -0.5 V vs SCE for Zn^{2+} and -0.2 to -0.6 V vs SCE for Hg^{2+}. In the absence of the AuNPs@TA (control experiment), no reductive spikes were observed (Appendix C). By introducing a ca. 8.8 × 10^9 particles of AuNPs@TA, the sharp reductive spikes were found for both cations (Figure 11). The spikes result from the collision events of the single AuNPs@TA with the electrode surface, which subsequent deposition of Zn^0 or Hg^0 on the electrode surface during the impact residence time.

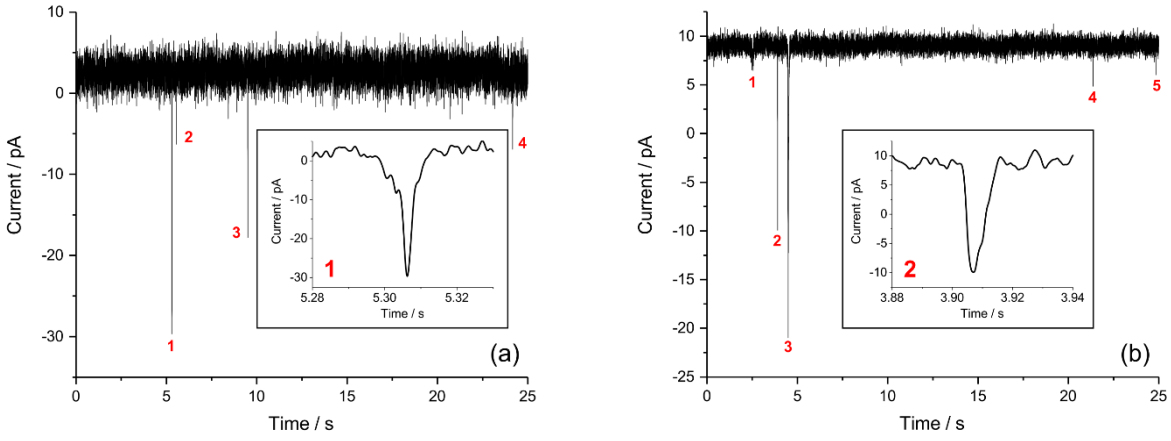


Figure 11. Representative chronoamperograms of reductive particle impacts. A microdisc electrode immersed in solution containing of 10.0 pM AuNPs@TA (ca. 8.8 x 10^9 particles) and (a) 100.0 mM Zn^{2+}, (b) 10.0 μM Hg^{2+} at applied potential of -0.2 V and -0.4 V vs SCE, respectively.

In the presence of Zn^{2+}, the average reductive charge values were found to be roughly constant at all studied potentials and, significantly, were similar to the values seen for the oxidative nano-impacts. Analogous behavior was found in the presence of Hg^{2+} with similar values of the reductive spikes current, duration, and frequency at oxidative and reductive nano-impacts. As shown in Figure 12, the average spikes charge, current, duration, and frequency were compared together as a function of different Zn^{2+} and Hg^{2+} concentrations. Importantly, these characteristics show roughly similar values as seen for the oxidative nano-impacts (Figure 10) but different onsets of with respect to the cation concentrations. These results suggest that TA controls both oxidation and reduction activity of the nanoparticle (Scheme 1).

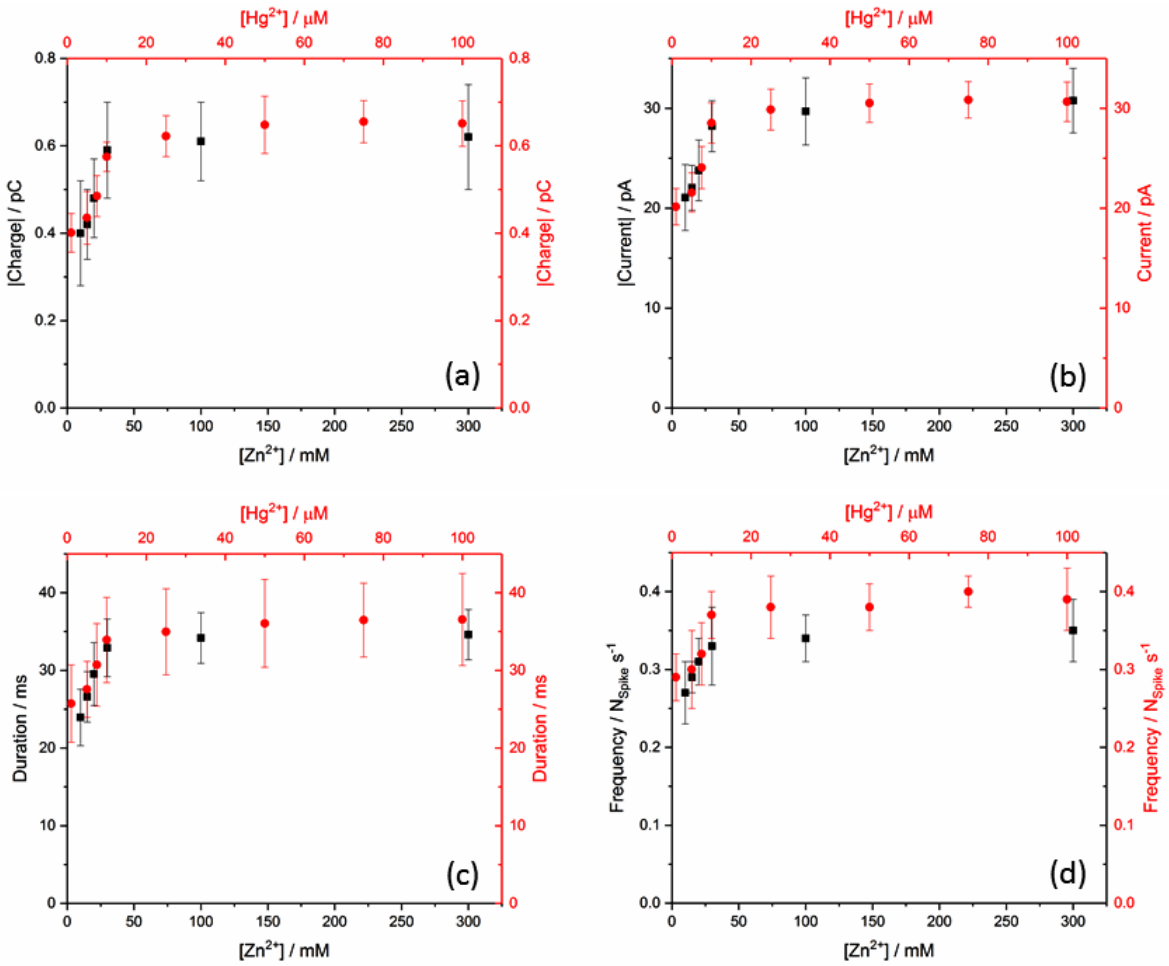


Figure 12. Overlaid plots of the reductive spikes charge (a), current (b), duration (c), and frequency (d) in the presence of various Zn^{2+} (black) and Hg^{2+} (red) concentrations.

6.3.6. Mechanistic Insights

The charge vs Zn^{2+} or Hg^{2+} concentration data for AuNPs@TA was analyzed using the Langmuir adsorption model. The Langmuir isotherm can be expressed as follows $\theta = KC / (1 + KC)$, where θ is the fractional coverage that is directly related to the charge, K is the equilibrium constant of adsorption and C is the metal cation concentrations. The data was analyzed by selecting the charge vs concentration data before saturation (≤30 mM for Zn^{2+} and ≤25 μM for Hg^{2+}).

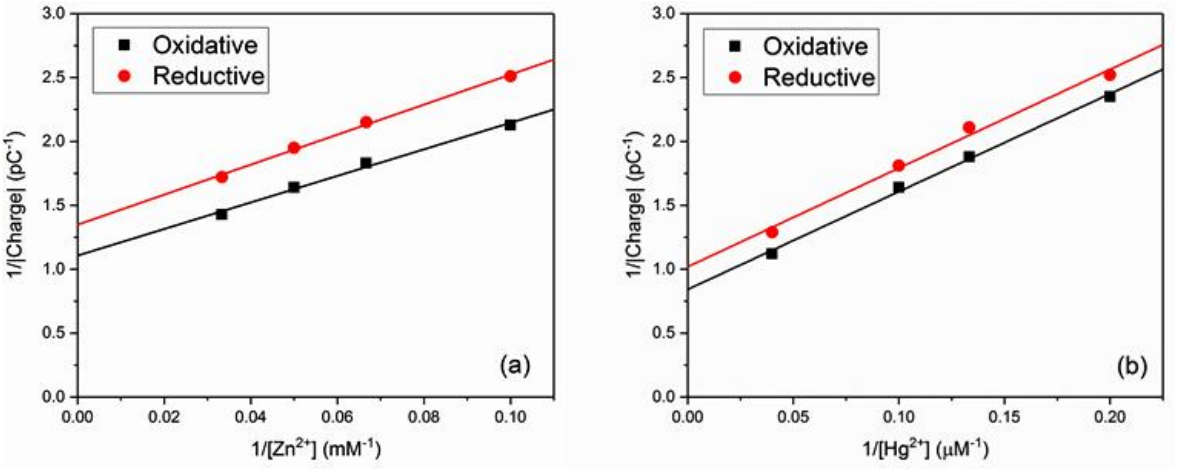


Figure 13. Langmuir plots of a) Zn^{2+} and b) Hg^{2+} on single particles AuNPs@TA for oxidative and reductive nano-impacts. Langmuir model applies with metal cation concentration before saturation (≤30.0 mM of Zn^{2+} and ≤25.0 μM of Hg^{2+}).

Figure 13a shows the reciprocal charge plotted against reciprocal of Zn^{2+} concentrations, giving linearity of $R^2 = 0.988$ and $R^2 = 0.995$ for oxidative and reductive nano-impacts, respectively. The linearity indicates that the complexation of Zn^{2+} onto TA at a single AuNPs@TA is consistent with the Langmuir model. The adsorption constant (K), as estimated from the reciprocal of the slope from oxidative and reductive nano-impacts, were seen to have a similar value of ca. 0.1 mM^{-1} for both the oxidative and reductive nano-impacts of Zn complexed particles. Interestingly, the complexation

of Zn^{2+} seen at the ensembles of AuNPs@TA was also Langmuirian at the concentration region of ≤75.0 mM Zn^{2+} with adsorption constant of K = 0.12 ± 0.003 mM^{-1} (see Appendix C.1). The similar value of the adsorption constant of Zn at both ensemble and single AuNPs@TA levels confirms the complexation mechanism, which is Langmuirian.

For comparison, the Langmuir adsorption model was also applied to Hg^{2+} for oxidative and reductive nano-impacts (Figure 13b). At the concentration region of ≤25.0 μM, the linearity was found with R^2 = 0.995 (K = 0.13 ± 0.003 μM^{-1}) and R^2 = 0.986 (K = 0.12 ± 0.002 μM^{-1}) for oxidative and reductive nano-impacts, respectively. The adsorption equilibration constant in the presence of Zn^{2+} or Hg^{2+}, for both oxidative and reductive nano-impacts, was found to be roughly similar values although the order of magnitude of the adsorption concentration differed by three orders of magnitude between the two metals. This result suggests that the complexation of both metal cations undergo a similar manner, in which TA controls the redox activity.

6.4. Conclusions

The TA capping agent markedly controls the redox activity of the nanoparticle, prior to and after the complexation with either Zn^{2+} or Hg^{2+}. The maximum uptake of these cations reflects the amount of capping agent that can undergo redox activity. Analogous redox behavior of the metal cation complex TA-coated particles was observed for both Zn^{2+} and Hg^{2+}, where the processes are Langmuirian, surface-controlled and an electrochemically reversible process (giving similar values for oxidative and reductive signals for both metals). It is evidenced that the quantity and detection limit of the metals is controlled by the amount of TA capping agent used to cap the nanoparticles.

Bibliography

(1) Zhang, N.; Luo, J.; Liu, R.; Liu, X. Tannic Acid Stabilized Silver Nanoparticles for Inkjet Printing of Conductive Flexible Electronics. *RSC Adv.* 2016, *6* (87), 83720–83729.

(2) Niu, Z.; Li, Y. Removal and Utilization of Capping Agents in Nanocatalysis. *Chemistry of Materials*. 2014, pp 72–83.

(3) Lopes, L. C. S.; Brito, L. M.; Bezerra, T. T.; Gomes, K. N.; Carvalho, F. A. D. A.; Chaves, M. H.; Cantanhede, W. Silver and Gold Nanoparticles from Tannic Acid: Synthesis, Characterization, and Evaluation of Antileishmanial and Cytotoxic Activities. *An. Acad. Bras. Cienc.* 2018, *90* (3), 2679–2689.

(4) Tanner, E. E. L.; Tschulik, K.; Tahany, R.; Jurkschat, K.; Batchelor-McAuley, C.; Compton, R. G. Nanoparticle Capping Agent Dynamics, and Electron Transfer: Polymer-Gated Oxidation of Silver Nanoparticles. *J. Phys. Chem. C* 2015, *119* (32), 18808–18815.

(5) Çakiroğlu, B.; Özacar, M. Tannic Acid Modified Electrochemical Biosensor for Glucose Sensing Based on Direct Electrochemistry. *Electroanalysis* 2017, *29*, 1–9.

(6) Tanner, E. E. L.; Sokolov, S. V.; Young, N. P.; Compton, R. G. DNA Capping Agent Control of Electron Transfer from Silver Nanoparticles. *Phys. Chem. Chem. Phys.* 2017, *19* (15), 9733–9738.

(7) Priyadarshini, E.; Pradhan, N. Gold Nanoparticles as Efficient Sensors in Colorimetric Detection of Toxic Metal Ions: A Review. *Sensors and Actuators, B: Chemical*. 2017, pp 888–902.

(8) Hutchings, G. J. Selective Oxidation Using Supported Gold Bimetallic and Trimetallic Nanoparticles. *Catal. Today* 2014, *238*, 69–73.

(9) Jin, W.; Maduraiveeran, G. Electrochemical Detection of Chemical Pollutants Based on Gold Nanomaterials. *Trends in Environmental Analytical Chemistry*. 2017, pp 28–36.

(10) Ngamchuea, K.; Batchelor-McAuley, C.; Sokolov, S. V.; Compton, R. G. Dynamics of Silver Nanoparticles in Aqueous Solution in the Presence of Metal Ions. *Anal. Chem.* 2017, *89* (19), 10208–10215.

(11) Tanner, E. E. L.; Sokolov, S. V.; Young, N. P.; Batchelor-McAuley, C.; Compton, R. G. Fluorescence Electrochemical Microscopy: Capping Agent Effects with Ethidium Bromide/DNA Capped Silver Nanoparticles. *Angew. Chemie - Int. Ed.* 2017, *56* (41), 12751–12754.

(12) Tanner, E. E. L.; Sokolov, S. V.; Young, N. P.; Compton, R. G. DNA Capping Agent Control of Electron Transfer from Silver Nanoparticles. *Phys. Chem. Chem. Phys.* 2017, *19* (15), 9733–9738.

(13) Tanner, E. E. L.; Tschulik, K.; Tahany, R.; Jurkschat, K.; Batchelor-McAuley, C.; Compton,

R. G. Nanoparticle Capping Agent Dynamics, and Electron Transfer: Polymer-Gated Oxidation of Silver Nanoparticles. *J. Phys. Chem. C* 2015, *119* (32), 18808–18815.

(14) Plowman, B. J.; Tschulik, K.; Young, N. P.; Compton, R. G.; Li, Z.; Compton, R. G.; Compton, R. G. Capping Agent Promoted Oxidation of Gold Nanoparticles: Cetyl Trimethylammonium Bromide. *Phys. Chem. Chem. Phys.* 2015, *17* (39), 26054–26058.

(15) Suherman, A. L.; Tanner, E. E. L.; Kuss, S.; Sokolov, S. V; Holter, J.; Young, N. P.; Compton, R. G. Voltammetric Determination of Aluminium(III) at Tannic Acid Capped-Gold Nanoparticle Modified Electrodes. *Sensors Actuators B Chem.* 2018, *265*, 682–690.

(16) Suherman, A. L.; Kuss, S.; Tanner, E. E. L.; Young, N. P.; Compton, R. G. Electrochemical Hg^{2+} Detection at Tannic Acid-Gold Nanoparticle Modified Electrodes by Square Wave Voltammetry. *Analyst* 2018, *143* (9), 2035–2041.

(17) Toh, H. S.; Jurkschat, K.; Compton, R. G. The Influence of the Capping Agent on the Oxidation of Silver Nanoparticles: Nano-Impacts versus Stripping Voltammetry. *Chem. - A Eur. J.* 2015, *21* (7), 2998–3004.

(18) Cloake, S. J.; Toh, H. S.; Lee, P. T.; Salter, C.; Johnston, C.; Compton, R. G. Anodic Stripping Voltammetry of Silver Nanoparticles: Aggregation Leads to Incomplete Stripping. *ChemistryOpen* 2015, *4* (1), 22–26.

(19) Robbs, P. H.; Rees, N. V. Nanoparticle Electrochemistry. *Phys. Chem. Chem. Phys.* 2016, *18* (36), 24812–24819.

(20) Allerston, L. K.; Rees, N. V. Nanoparticle Impacts in Innovative Electrochemistry. *Curr. Opin. Electrochem.* 2018, 10, 31-36.

(21) Zhou, Y. G.; Rees, N. V.; Compton, R. G. Nanoparticle-Electrode Collision Processes: The Underpotential Deposition of Thallium on Silver Nanoparticles in Aqueous Solution. *ChemPhysChem* 2011, *12* (11), 2085–2087.

(22) Stevenson, K. J.; Tschulik, K. A Materials Driven Approach for Understanding Single Entity Nano Impact Electrochemistry. *Curr. Opin. Electrochem.* 2017, *6* (1), 38–45.

(23) Sokolov, S. V.; Eloul, S.; Kätelhön, E.; Batchelor-McAuley, C.; Compton, R. G. Electrode–Particle Impacts: A Users Guide. *Phys. Chem. Chem. Phys.* 2017, *19* (1), 28–43.

(24) Kätelhön, E.; Feng, A.; Cheng, W.; Eloul, S.; Batchelor-McAuley, C.; Compton, R. G. Understanding Nano-Impact Current Spikes: Electrochemical Doping of Impacting Nanoparticles. *J. Phys. Chem. C* 2016, *120* (30), 17029–17034.

(25) Zampardi, G.; Batchelor-McAuley, C.; Kätelhön, E.; Compton, R. G. Lithium-Ion-Transfer Kinetics of Single $LiMn_2O_4$ Particles. *Angew. Chemie Int. Ed.* 2017, 56, 641-644.

(26) nanoComposix. www.nanocomposix.com/pages/gold-colloid. Accessed on 3 February 2019.

(27) Cardwell, T. J.; Mocak, J.; Santos, J. H.; Bond, A. M. Preparation of Microelectrodes:

Comparison of Polishing Procedures by Statistical Analysis of Voltammetric Data. *The Analyst*. 1996, 121, 357-362.

(28) Toh, H. S.; Batchelor-McAuley, C.; Tschulik, K.; Uhlemann, M.; Crossley, A.; Compton, R. G. The Anodic Stripping Voltammetry of Nanoparticles: Electrochemical Evidence for the Surface Agglomeration of Silver Nanoparticles. *Nanoscale* 2013, *5* (11), 4884–4893.

(29) Giorgia, Z.; Jorg, T.; Hendrik, N.; A., A. H. M.; Suman, P.; Lutz, M.; G., C. R. Electrochemical Behavior of Single CuO Nanoparticles: Implications for the Assessment of Their Environmental Fate. *Small* 2018, 14, 1801765.

(30) Batchelor-McAuley, C.; Ellison, J.; Tschulik, K.; Hurst, P. L.; Boldt, R.; Compton, R. G. In Situ Nanoparticle Sizing with Zeptomole Sensitivity. *Analyst* 2015, *140* (15), 5048–5054.

(31) Kätelhön, E.; Tanner, E. E. L.; Batchelor-McAuley, C.; Compton, R. G. Destructive Nano-Impacts: What Information Can Be Extracted from Spike Shapes? *Electrochim. Acta* 2016, *199*, 297–304.

(32) Little, C. A.; Xie, R.; Batchelor-McAuley, C.; Kätelhön, E.; Li, X.; Young, N. P.; Compton, R. G. A Quantitative Methodology for the Study of Particle-Electrode Impacts. *Phys. Chem. Chem. Phys.* 2018, *20* (19), 13537–13546.

(33) Ellison, J.; Tschulik, K.; Stuart, E. J. E.; Jurkschat, K.; Omanović, D.; Uhlemann, M.; Crossley, A.; Compton, R. G. Get More out of Your Data: A New Approach to Agglomeration and Aggregation Studies Using Nanoparticle Impact Experiments. *ChemistryOpen* 2013, *2* (2), 69–75.

(34) Madhan, B.; Dhathathreyan, A.; Subramanian, V.; Ramasami, T. Investigations on Geometrical Features in Induced Ordering of Collagen by Small Molecules. *J. Chem. Sci.* 2003, *115* (5–6), 751–766.

(35) Moniwa, S.; Aramata, A. Underpotential Deposition of Zn^{2+} Ions on Au(111), Au(100) and Au(110) Electrodes. *J. Electroanal. Chem.* 1994, *376* (1), 203–206.

(36) Taguchi, S.; Kondo, M.; Mori, H.; Aramata, A. Formation of Zinc-Oxianion Complex Adlayer by Underpotential Deposition of Zn on Au(111) Electrode: Preferential Formation of Zinc Monohydrogen Phosphate Complex in Weakly Acidic Solutions. *Electrochim. Acta* 2013, 111, 642-655.

Chapter 7

Understanding Gold Nanoparticle Dissolution in Cyanide-containing Solution via the Nano-impacts Method

In this chapter, citrate-capped gold nanoparticles (AuNPs@CA) are explored as a model to understand the reactivity and the mechanism of gold dissolution at the nanoscale in cyanide-containing solution and to contrast this with nanoparticle ensemble behavior. Clear insights into the kinetics and mechanism of the process at the single-particle level emerge. It was found that the AuNPs@CA showed different dissolution behavior as ensembles than as single particles. At the single-particle level, a nearly complete electrochemical oxidation of nominally 60 nm diameter AuNPs@CA was achieved at concentrations ≥35.0 mM KCN and at an applied potential of 1.0 V vs SCE. By studying single particle level using the nano-impacts method, the oxidation of the single AuNPs@CA was shown to be controlled by a pre-adsorption step of CN^- onto the surface of single AuNPs@CA before the electron was transferred.

The work presented in this chapter has been published in *Physical Chemistry Chemical Physics* (*Phys. Chem. Chem. Phys.* 2018, *20*, 44, 28300–28307) and was carried out in collaboration with Dr. Giorgia Zampardi, Dr. Sabine Kuss and Dr. Eden Tanner, who helped with the interpretation of the experimental results. Dr. Hatem M. A. Amin (in collaboration with Dr. Neil P. Young and Ms. Jennifer Holter from Department of Materials, Oxford University) obtained the TEM, SEM, DLS, NTA and zeta potential data of the AuNPs@CA.

7.1. Introduction

Gold nanoparticles have attracted much attention due to their use in catalysis and electrocatalysis[1-3], in electrochemical sensing[4], in medicine as drug delivery systems[5] and as therapeutic agents for cancer treatments[6]. Moreover, the applications have been recently extended to the electrochemical detection and quantification of pathogenic bacteria[7,8]. Nevertheless, much chemistry of gold and gold nanoparticles remains unclear.[9-12] Moreover, the challenges related to the technologies required to synthesize gold nanoparticles, such as cost, environmental impact, and toxicity issues, can potentially limit their use.[10,11] In order to minimize these effects, the recovery or refinery of gold nanoparticles from diverse sources is becoming increasingly important. The recovery of gold nanoparticles from aqueous solutions can be performed using extracting agents such as biogenic-sulphide[13], surfactants[14], polymers[15] and cyanide salts in conjunction with aerial oxidation[16]. Oxidative dissolution of gold in cyanide media remains the key industrial of gold leaching process[17,18] and is commonly used because of its relatively low cost and great effectiveness. The main advantages are the selectivity of free cyanide for gold dissolution and the high stability of the gold-cyanide complexes.[19,20] Recently, thiourea, thiosulfate, chlorine, and acid leaching techniques have been developed as an alternative to cyanide, but none of these has yet gained industrial application.[21,22]

In alkaline cyanide solutions, the aerial oxidation of gold is a pre-requisite for its dissolution, an electrochemical process. The gold dissolution in cyanide-containing solutions may be limited due to the passivation of the gold surface, resulting in the formation of gold oxide and sub-oxide surface species.[23,24] The gold dissolution oxidative process in cyanide-containing solution is a complex mechanism, which can be affected by a number of influential parameters such as the cyanide concentration,

availability of oxygen at the solid-liquid interface, the presence of ions other than CN^- in solution, pH and temperature.[25,26] Many studies have been carried out to investigate these factors, but there is less information regarding the behavior of gold at the nanoscale level.

In this chapter, the oxidative dissolution of citrate-capped gold nanoparticles (AuNPs@CA) in cyanide-containing solution is assessed both at nanoparticle ensembles and at the single-particle level. The analysis of ensembles of AuNPs@CA was performed through cyclic voltammetry of random arrays of AuNPs@CA drop cast onto a glassy carbon electrode surface, while the analysis of single AuNPs@CA was performed using the nano-impacts method.[27-32]

The nano-impacts method is a powerful technique that allows the study of the electrochemical behavior of single particles. With this technique, it is possible to characterize single nanoparticles and to study their reactivity in various solutions. In the nano-impacts method, the nanoparticles are suspended in solution and, by virtue of their Brownian motion, they randomly collide with the surface of a potentiostated electrode immersed in the solution. Upon collision, the nanoparticles may, for instance, adsorb, dissolve and promote various reactions, from catalytic to ion insertion, and complex ion formation.[27,33-35] The stochastic collisions of the nanoparticles against the electrode surface typically result in spikes or steps in the background current recorded at the electrode.

The oxidative dissolution of gold through nano-impacts has been given proof-of-concept in the presence of bromide (Br^-).[36] Moreover, oxidative dissolution of AuNPs@CA have been successfully detected and characterized using the nano-impacts method in aqueous 0.1 M HCl.[37] Sticking probabilities have also been measured.[38]

In this chapter, the analysis of the shape, charge, current, duration and frequency of a statistically relevant number of single collision events have been carried out in order to understand the reactivity and the mechanism of gold dissolution at the nanoscale in cyanide-containing solution and to contrast this with the nanoparticle ensemble behavior. Clear insights into the kinetics and mechanism of the process at the single-particle level emerge.

7.2. Experimental

Details about the chemical reagents here utilized can be found in Chapter 2, Section 2.1. Cyanide-containing solutions were prepared in 10.0 mM NaOH to avoid the formation and volatilization of HCN during the experiment.[39] For the nano-impacts experiment, all chronoamperograms were recorded at the potential of 0.3 to 1.2 V vs SCE for 25 s. An electrochemical cell was placed inside a double Faraday cage, where an in-house built low noise potentiostat was used with a 100 Hz Bessel-type low pass filter.[40] Note that the potentiostat used in this chapter accurately conserves the charge transferred due to a particle-impact process despite the possible distortion of the spike shape.[27,41,42] In this chapter, transmission electron microscopy (TEM), scanning electron microscopy (SEM), dynamic light scattering (DLS), nanoparticle tracking analysis (NTA), zeta potential and UV-vis spectroscopy analyses were performed to characterize the AuNPs@CA.

7.3. Results and discussion

This section outlines the characterization and electrochemical measurements of gold nanoparticles in cyanide-containing solutions. The voltammetry studies are

conducted at the nanoparticle ensemble and at the single-particle levels. Studies of nanoparticle ensembles are undertaken with cyclic voltammetry (CV) of drop cast AuNPs@CA onto a GCE surface (AuNPs@CA-GCE). The presence of a gold stripping peak, the effect of the scan rate and the surface concentration, the maximum peak charge during successive scans and the percent conversion of oxidized AuNPs@CA are investigated. Following this, the nano-impacts method in a suspension of single particles of AuNP@CA was undertaken, and the observed spikes in the current-time trace were integrated and sized. Finally, the AuNP@CA oxidation, and dissolution mechanism and rate are discussed.

7.3.1. Characterization of Gold Nanoparticles

Initially, the physical characterization of the commercially sourced nominally 60 nm diameter citrate-capped gold nanoparticles (AuNPs@CA) was conducted using transmission electron microscopy (TEM), scanning electron microscopy (SEM), dynamic light scattering (DLS), nanoparticle tracking analysis (NTA), zeta potential measurement and UV-vis spectroscopy (UV-vis). As shown in Figure 1a, the AuNPs@CA exhibit a spheroidal shape with an average diameter size of 62.9 ± 2.7 nm, as extracted from TEM micrographs of 100 particles, in accordance with the manufacturer's size specification of nominally 60 nm diameter.

The SEM analysis of the AuNPs@CA suspension drop cast onto a GC plate shows numerous clusters due to particle aggregation/agglomeration (Figure 1b). This can cause incomplete stripping oxidation of the AuNPs@CA.[43,44] Therefore, these effects must be considered when the study of ensemble AuNPs@CA, through drop-casting AuNPs@CA suspension onto GCE surface is undertaken (see below).

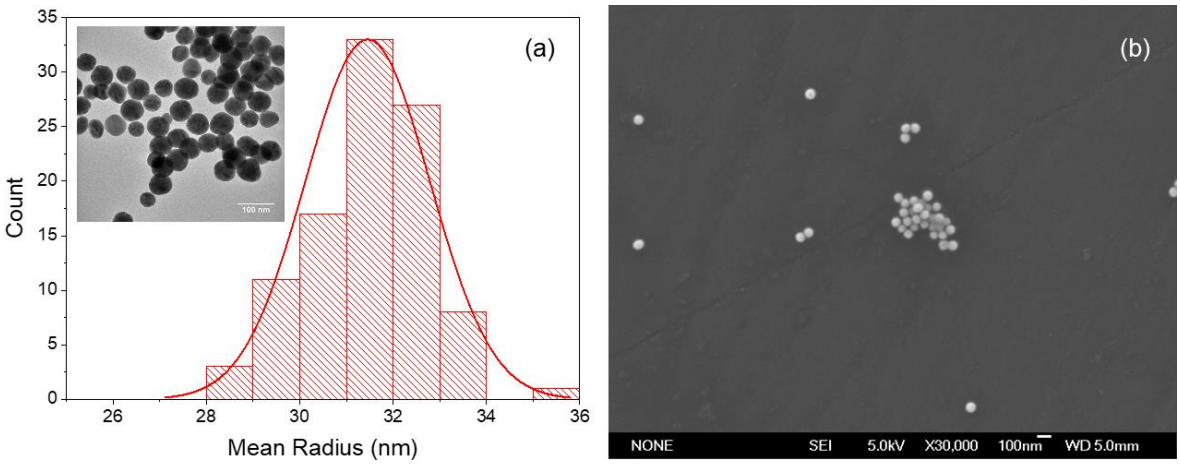


Figure 1. (a) Statistical distribution of the AuNPs@CA radius size (inset: TEM micrograph of the AuNPs@CA). (b) SEM micrograph of AuNPs@CA showing the aggregation/agglomeration state of the particles.

DLS was undertaken to measure the hydrodynamic diameter of the AuNPs@CA. This analysis revealed that the average hydrodynamic diameter of the particles is 64.0 ± 0.3 nm (see Appendix B.3). The polydispersity index for all measurements was 0.07 ± 0.01, indicating that particle size was closely monodispersed. The NTA analysis exhibited an average size of 65.0 ± 0.9 nm (Appendix B.3). Meanwhile, zeta potential analysis showed the values of -43.6 ± 2.3 mV, -45.6 ± 1.4 mV and -36.7 ± 0.7 mV for the overall electro-kinetic potential of each sample of AuNPs@CA in deionized water, in 10.0 mM NaOH and in 10.0 mM NaOH containing 50.0 mM KCN, respectively (see Appendix B.3). The results suggest that AuNPs@CA suspension are electrically less stabilized in cyanide-containing solution. This stability behavior will be discussed further in the following section.

In order to gain information about the stability of the AuNPs@CA in cyanide-containing solution, UV-Vis spectroscopy analysis was performed. Each sample was degassed thoroughly with a high purity N_2 flow prior to the measurements. Note that in this context, stability means that the AuNPs@CA suspension is resistant to

aggregation/agglomeration state. The stability of the AuNPs@CA can be monitored using UV-Vis spectroscopy due to the presence of a surface plasmon resonance absorption peak, which results in the observation of maximum absorbance at the characteristic wavelength of 520-535 nm, depending on the nanoparticle size.[45] As shown in Figure 2, the AuNPs@CA showed higher stability in the solution containing 5.0 mM KCN than 25.0 and 50.0 mM KCN, over the time range studied. The result suggests that AuNPs@CA stability in the colloidal phase decreased by increasing the CN^- concentrations.

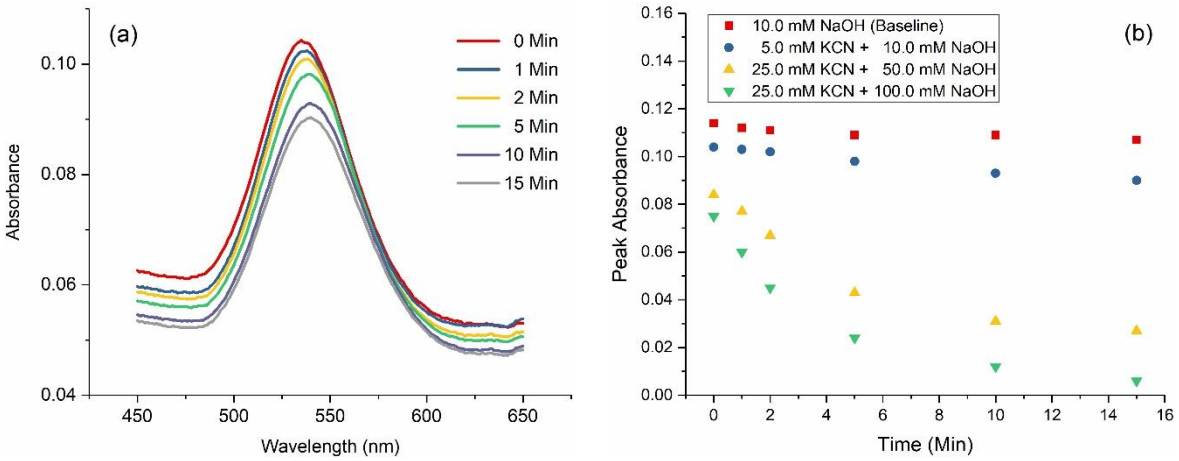


Figure 2. UV-vis spectroscopy analysis. (a) UV-vis spectra of the AuNPs@CA in a solution of 10.0 mM NaOH containing 5.0 mM KCN. (b) The plot of peak absorbance against time at different KCN concentrations.

7.3.2. Electrochemical Analysis of Ensembles of AuNPs@CA

The redox properties of an ensemble of AuNPs@CA were assessed by CV performed at a AuNPs@CA-GCE immersed into a solution of 5.0 mM KCN + 10.0 mm NaOH. First, an unmodified GCE was immersed in a solution of 5.0 mM KCN + 10.0 mM NaOH and CV was recorded by sweeping the potential from –0.6 to 0.5 V vs SCE at a scan rate of 0.1 V s^{-1}. In the absence of AuNPs@CA (Figure 3, solid black curve), the

voltammetric response of an unmodified GCE did not exhibit any oxidative features in the potential range studied. Subsequently, the GCE surface was modified by drop-casting 20.0 µL of AuNPs@CA suspension, resulting in approximately one-monolayer surface coverage that corresponded to ca. 5.0 x 10^8 particles (Appendix A.4). Then, analogous CV experiments as with the unmodified GCE were performed.

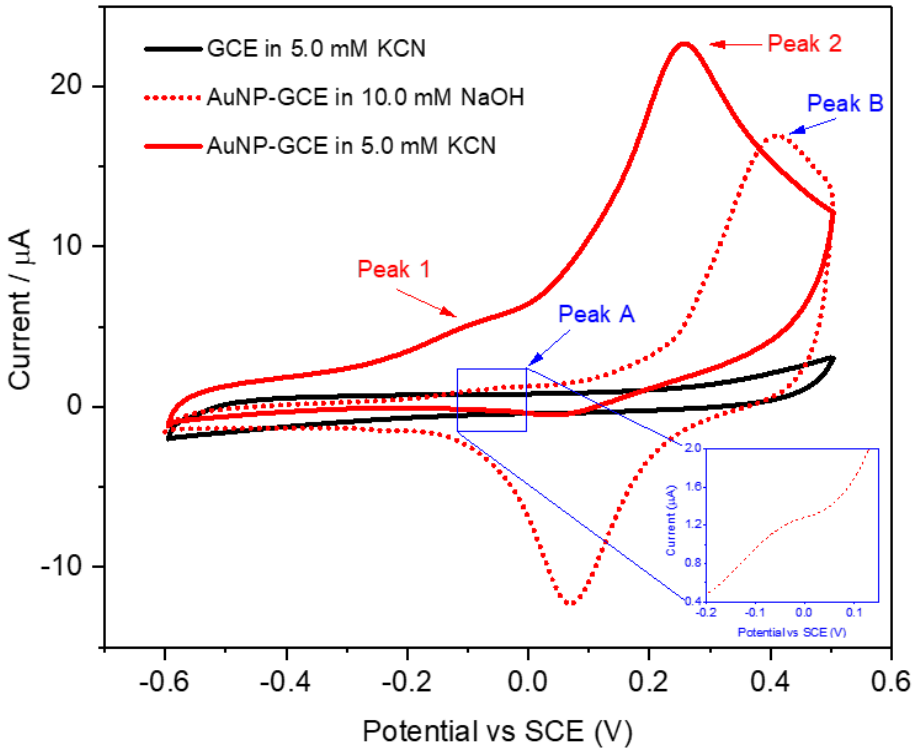


Figure 3. CVs of the unmodified GCE immersed in a solution of 5.0 mM KCN (solid black curve) and AuNPs@CA-GCE immersed in 10.0 mM NaOH (red dotted c) or in 5.0 mM KCN (red solid curve) at a scan rate of 0.1 V s^{-1}.

In the absence of CN^- (Figure 3, dotted red curve), two oxidative peaks in the first forward scan of the voltammogram were observed at peak potentials of –0.05 V and 0.40 V vs SCE, respectively. These peaks have been assigned to the oxidation of gold to gold hydroxide $Au(OH)_{ads}$ (hereafter referred to as peak A) and to gold oxide Au_2O_3 (hereafter referred to as peak B).[46-48] The $Au(OH)_{ads}$ species is formed due to the

reaction of AuNPs@CA with OH^- from the electrolyte (Reaction 1). A further oxidation process leads to the formation of Au_2O_3 layers at more positive potentials (Reaction 2). The peak current of Au_2O_3 species increased linearly as a function of the scan rate, suggesting a surface-controlled process involving the passage of a constant charge within a fixed potential range.

$$Au\ (s) + OH^- \longrightarrow AuOH\ (ads) + e^- \quad (R1)$$

$$2Au\ (s) + 3H_2O \longrightarrow Au_2O_3 + 6H^+ + 6e^- \quad (R2)$$

In the presence of 5.0 mM KCN, the AuNPs@CA-GCE exhibits two oxidative features at peak potentials of ca. –0.10 V and ca. 0.28 V vs SCE (Figure 3, solid red curve). These peaks are reported to correspond to the formation of $AuCN_{ads}$ (hereafter referred to as peak 1) and $Au(CN)_2^-$ (hereafter referred to as peak 2), respectively, which are formed through the following reaction pathways.[49-51]

$$Au\ (s) + CN^-\ (aq) \rightleftharpoons AuCN^-\ (ads) \quad (R3)$$

$$AuCN^-\ (ads) \rightleftharpoons AuCN\ (ads) + e^- \quad (R4)$$

$$AuCN\ (ads) + CN^- \rightleftharpoons Au(CN)_2^- \quad (R5)$$

According to Kirk *et al.*[49], the reaction occurring at peak 2 is consistent with the reactions R3 to R5, with reaction R5 as the rate-determining step. Meanwhile, the reaction at peak 1 involves the same dissolution scheme as for peak 2, but with reaction R4 likely to be the rate-determining step. The dissolution of gold in cyanide-containing solution through the reaction pathways described above is suggested to be terminated at potentials more positive than potential of peak 2 by the formation of $Au(OH)_3$.[49] It

has been suggested that $AuOH_{ads}$ species (R1) can potentially block the reaction with CN^- causing gold passivation[50,51], whilst the adsorption of CN^- facilitates the dissolution of the AuNPs@CA and leads to the complexation between AuNPs@CA and CN^-, promoting the oxidative dissolution of AuNPs@CA. The dicyanoaurate(I) complex ion, $Au(CN)_2^-$, is known for its high stability. It has an equilibrium constant value for the formation of a complex Au-CN estimated in the range of 1.0×10^{37} to 2.8×10^{39}.[20]

The coverage of AuNPs@CA drop cast onto the GCE surface was varied in the range of 0.1-to 1.0-monolayer. Analogous measurements were performed to these as described above. As shown in Figure 4, the peak current of peak 2 increased monotonically on increasing surface coverage in the range studied. This is attributed to the greater number of nanoparticles readily available for complexation with CN^- and subsequent oxidation. A one-monolayer surface concentration was selected for further experiments, in particular, to calculate the total charge of the peak 2 after successive scans and to determine the percent conversion of the oxidized AuNPs@CA (see below).

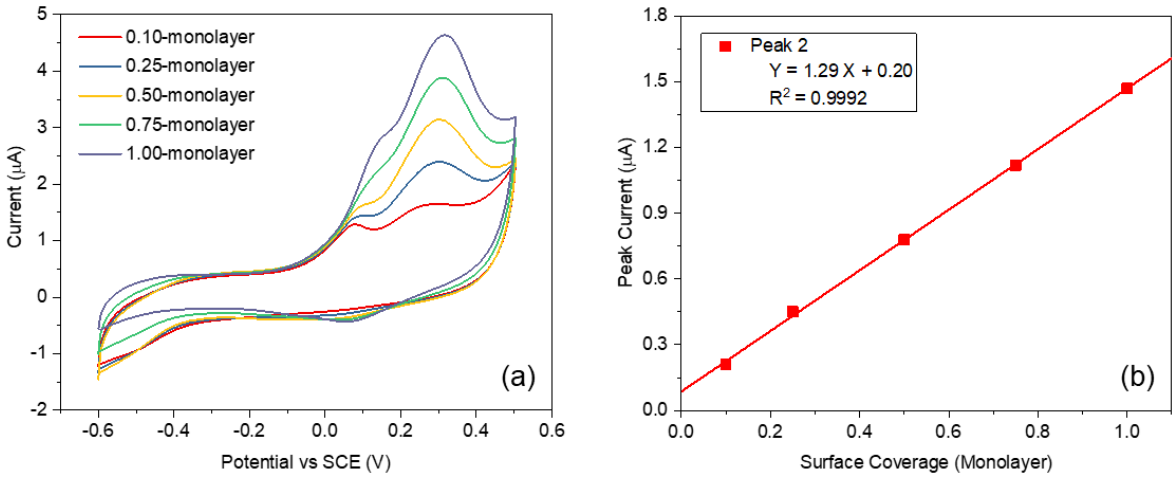


Figure 4. Surface concentration study of AuNPs-GCE immersed in 5.0 mM KCN + 10.0 mM NaOH at a scan rate of 0.1 V s^{-1}. (a) CVs of AuNPs-GCE at various surface concentrations. (b) The plot of the linear peak current of peak 2 at the various surface concentrations shown in (a).

The effect of the scan rate at different fixed CN^- concentrations were evaluated. A one-monolayer of AuNPs@CA-GCE was immersed into solutions of 10.0 mM NaOH, 5.0 mM KCN + 10.0 mM NaOH and 50.0 mM KCN + 10.0 mM NaOH, independently. Following this, CVs were recorded by sweeping the potential from -0.6 to 1.0 V vs SCE at a scan rate of 0.02 to 0.2 V s^{-1}. The peak currents were determined by applying a polynomial fit (typically of order 6) to extract the signal from the baseline.

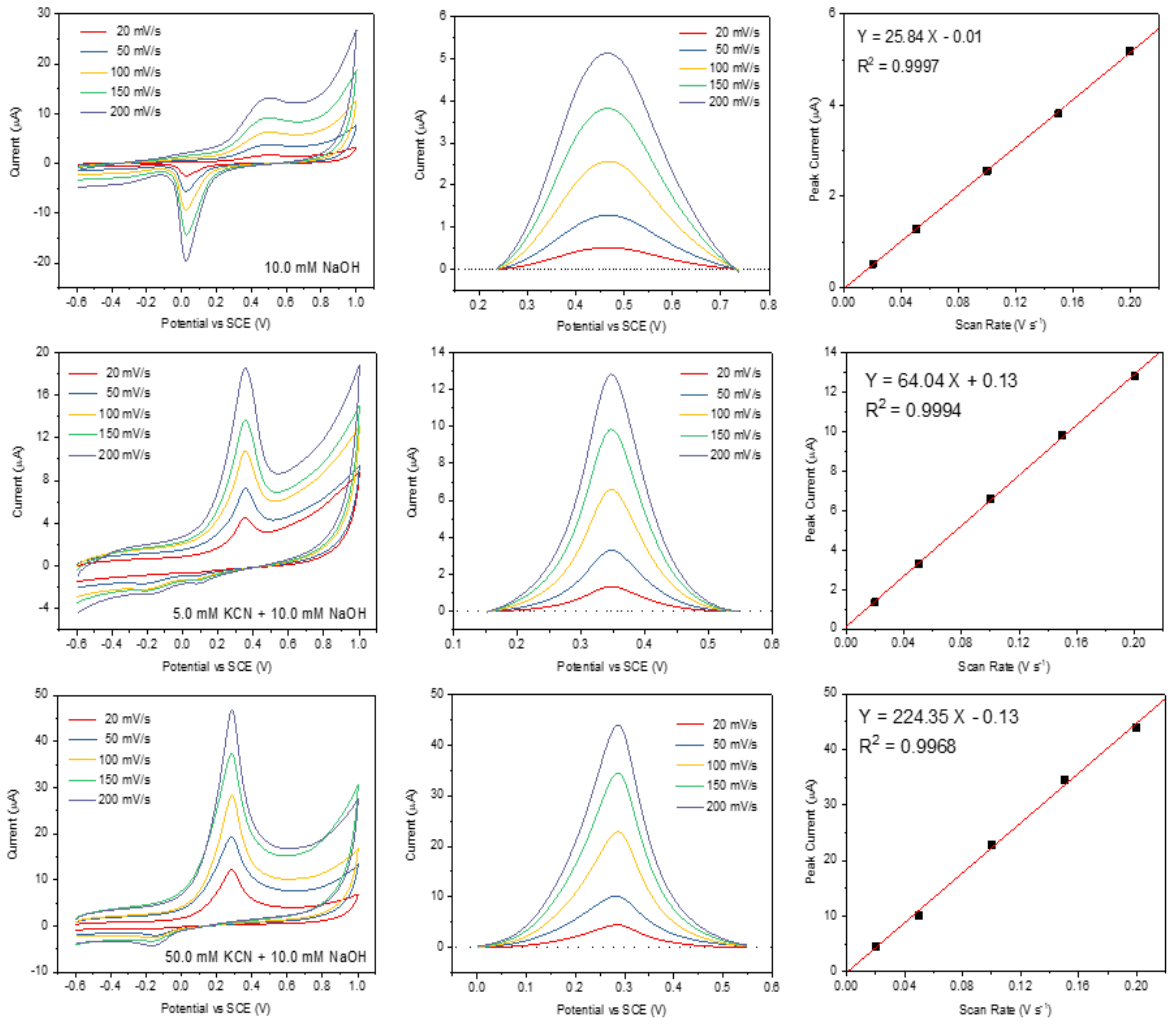


Figure 5. Scan rate study of one-monolayer AuNPs@CA-GCE immersed in a solution of 10.0 mM NaOH, 5.0 mM, and 50.0 mM KCN at different scan rates (showing the original voltammograms, after polynomial (typically order-6) baseline correction and linear peak current behavior at different scan rates).

As shown in Figure 5, the peak currents increased linearly with scan rate, consistently for all CN^- concentrations. The linear dependence of the peak current on the scan rate suggests that the oxidation is a surface-controlled process. Further, a one-monolayer AuNPs@CA-GCE was immersed into a solution of 10.0 mM NaOH containing five different CN^- concentrations, from 1.0 to 50.0 mM. The first forward scan of CVs recorded at a scan rate of 0.1 V s^{-1} (Figure 6a) shows that the peak current values of peak 2 increased linearly on increasing the CN^- concentration. However, the peak potential of peak 2 was shifted to more negative potentials by increasing CN^- concentrations (Figure 6b). This likely arises from an increased rate of reaction at higher levels of CN^-, leading to fuller stripping at lower potentials.

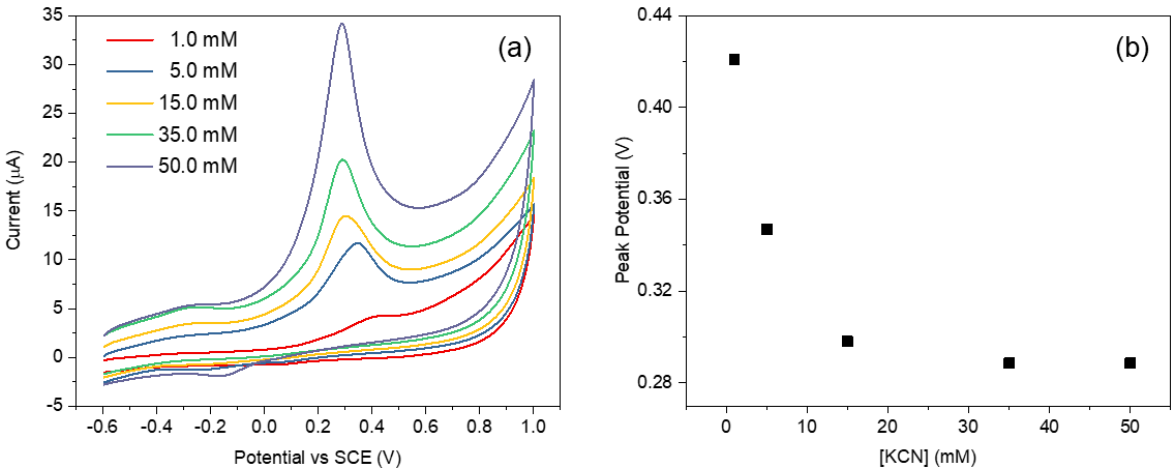


Figure 6. (a) CVs of AuNPs@CA-GCE immersed in 10.0 mM NaOH containing various CN^- concentrations at a scan rate of 0.1 V s^{-1}, (b) The plot of the peak potential of peak 2 against different CN^- concentrations.

Finally, the charges associated with peak 2 were measured to calculate the percent conversion of oxidized AuNPs@CA. The percent conversion is determined as a ratio between the experimental charges of the peak 2 recorded from the CVs and the expected charges for complete particle oxidative dissolution (see Appendix A.4). To

determine the total experimental charge of peak 2, a one-monolayer AuNPs@CA-GCE was immersed into a solution of 10.0 mM NaOH with five different CN^- concentrations, and then a multiple cycle-CV was performed until the oxidative features were no longer discernible. The total charge from successive CV scans was determined by integrating the area of peak 2 until no oxidative features were observed (Figure 7).

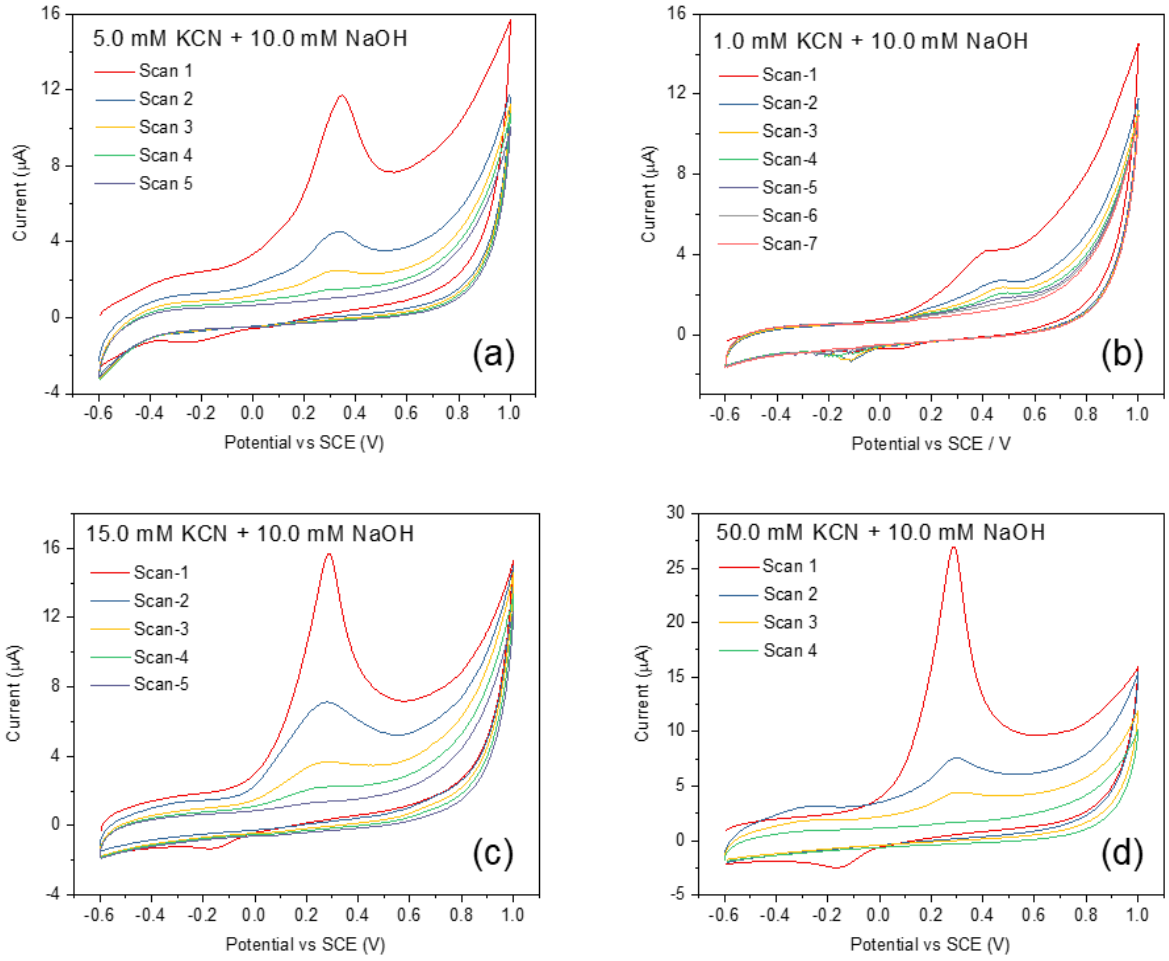


Figure 7. Successive CV scans of the one-monolayer AuNPs@CA-GCE immersed in a solution of (a) 1.0 mM KCN, (b) 5.0 mM KCN, (c) 15.0 mM KCN, and (d) 50 mM KCN-containing 10.0 mM NaOH at a scan rate of 0.1 V s^{-1}.

The charge expected from the number of drop cast AuNPs@CA was estimated to be ca. 600 μC (see Appendix A.4). The ratio between experimental and expected

charge values, assuming one electron was transferred per gold atom, was then considered as the yield of oxidized AuNPs@CA. The percent conversions of ensembles of AuNPs@CA were found to be small, ranging from 1.6% to 7.8% throughout the five different CN^- concentrations studied (see Appendix A.4). These small percentages correspond to the incomplete stripping of the AuNPs@CA, which is strongly affected by the aggregation/agglomeration states of particles[52,53] as verified by the SEM image (Figure 1b).

7.3.3. Nano-impacts Analysis of Single AuNP@CA

In this section, the spike shape, charge, current, duration, frequency and oxidation rate resulting from the nano-impacts experiments are reported. The results are obtained from stochastic single collision events of single AuNPs@CA with a potentiostated carbon microelectrode disc immersed in the solution and polarised at a fixed potential. A nominally 7.0 μm diameter carbon microelectrode disc was immersed into a solution containing 10.0 mM NaOH and a ca. 42.0 pM AuNPs@CA suspension (ca. 1.8×10^{10} particles mL^{-1}). Chronoamperograms were then recorded by applying a fixed potential ranging from 0.3 to 1.1 V vs SCE for 25 s. A series of chronoamperograms were recorded in order to obtain at least 100 spikes for the analysis. First, in the absence of CN^- in the system, a featureless continuous time-current transient was observed at all potentials studied (see Appendix C.2). This procedure was repeated in the absence of AuNPs@CA, in which the system contained 10.0 mM NaOH and five different CN^- concentrations, from 1.0 to 50.0 mM. Featureless continuous time-current transients were also observed in this case (see Appendix C.2). Subsequently, both ca. 42.0 pM AuNPs@CA suspension and particular CN^- concentrations were introduced together in the system and analogous experiments

conducted. Figure 8 depicts four representative chronoamperograms with their zoomed spikes (inset) at an applied potential of 1.0 V vs SCE. The resulting spikes features in the transient current are attributed to single AuNP@CA stochastically colliding with the carbon microelectrode disc surface in the presence of CN^-, consistent with the oxidation of AuNP@CA occurring through surface complexation with CN^- and subsequent oxidative dissolution reaction. Note that smaller nanoparticles (nominally 12 nm and 20 nm diameter) gave features too small to detect (see Appendix C.2).

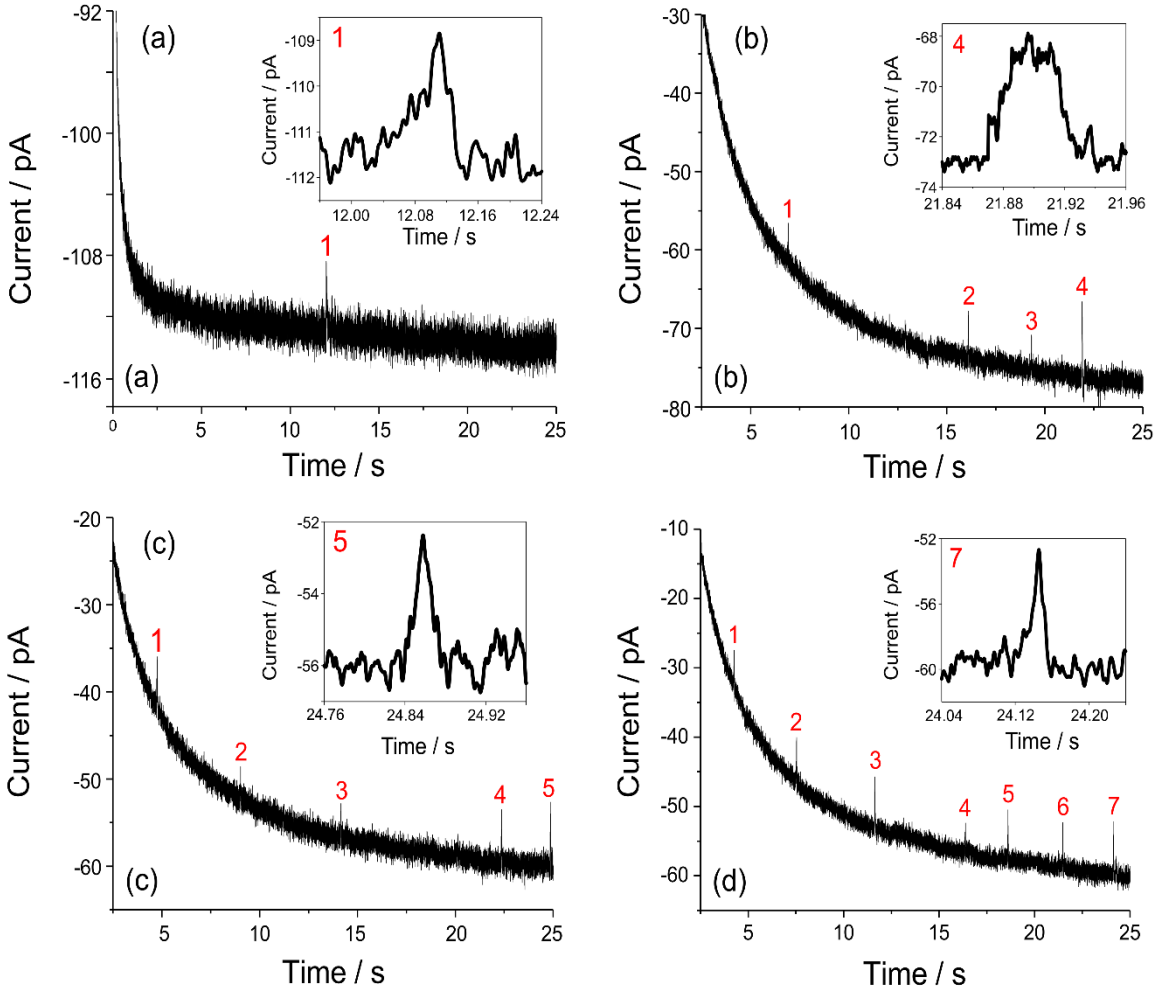


Figure 8. Representative chronoamperograms of carbon microelectrode disc immersed in a solution containing ca. 42.0 pM AuNPs@CA (ca. 1.8×10^{10} particles mL^{-1}) and (a) 1.0 mM, (b) 5.0 mM, (c) 15.0 mM and (d) 50.0 mM KCN at applied potential of 1.0 V vs SCE.

Chronoamperograms at nine different potentials (0.3 V to 1.1 V) were measured to analyze the potential dependency of the nano-impacts. Figure 9 shows that the spikes were exclusively observed at potentials >0.4 V and ≤1.0 V. For 1.0 mM CN^-, spikes were only seen at potentials >0.8 V. For the other CN^- concentrations, the charge and current per spike tends to a plateau on increasing the potential to a maximum of 1.0 V. The absence of spikes at potentials <0.5 V is attributed to insufficient overpotential for the particle oxidation. The absence of spikes at >1.0 V is probably due to the formation of non-conductive hydroxide or oxide layers on the AuNP@CA surface, which inhibiting particle dissolution.

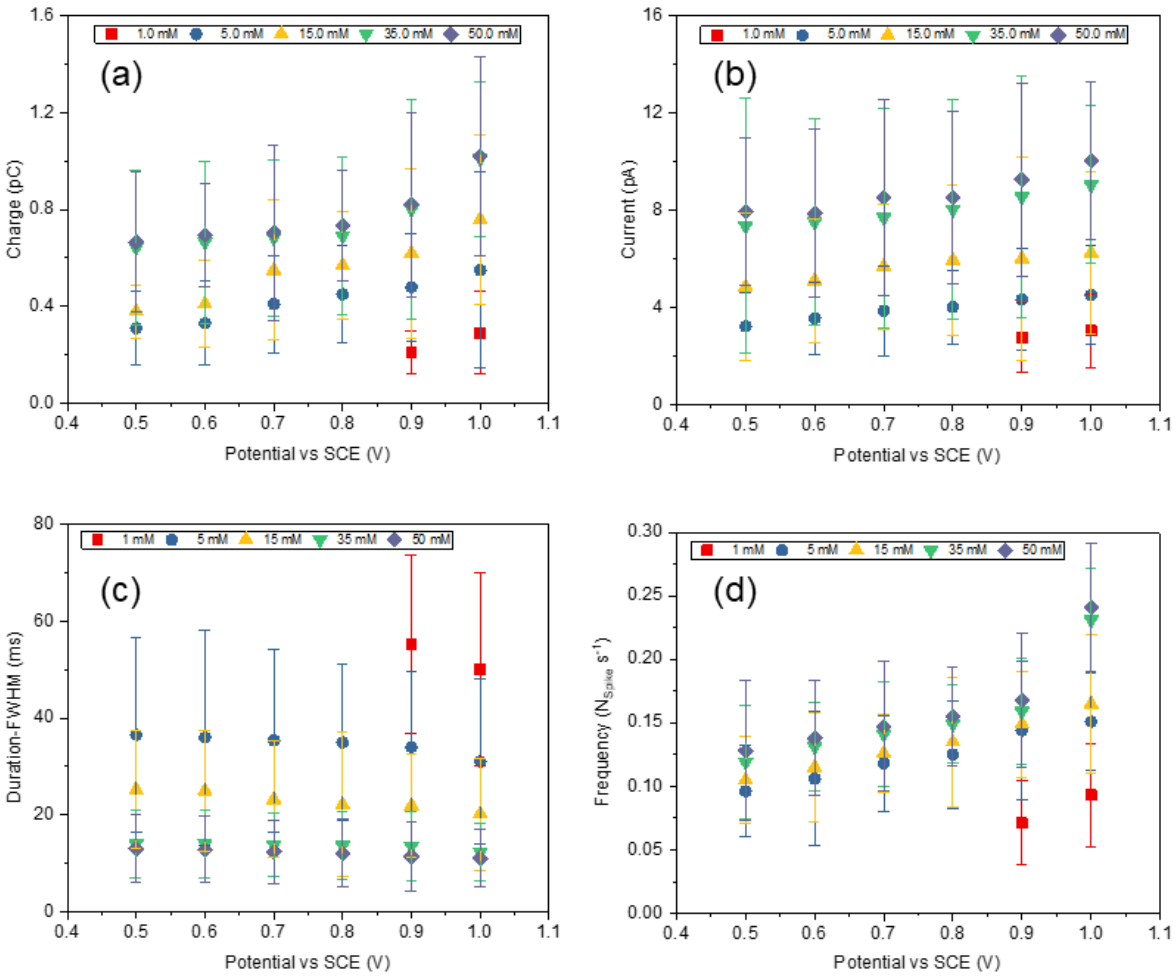


Figure 9. Linear relationship of average spikes (a) charge, (b) current, (c) duration at full width at half-maximum, (d) frequency with CN^- concentrations at different potentials.

The average spike duration was determined as the full width at half-maximum (FWHM), the width of a single spike at half of the maximum current amplitude. The average duration was found to be shorter with increasing CN^- concentrations, namely ca. 30 ± 17 ms, 20 ± 12 ms, 12 ± 6 ms and 11 ± 6 ms for 5.0, 15.0, 35.0 and 50.0 mM, respectively (Figure 9c). In addition, the spike shape was found to be independent of the CN^- concentration. The shorter nano-impacts duration implies a faster reactivity of the single AuNPs@CA in higher CN^- concentrations, leading to a quicker dissolution reaction (see below).

The nano-impacts is stochastic in nature, thus the number of collision events observed per one chronoamperogram may vary. The average impact frequency, number of single collision events per second, was found to be roughly constant with increasing CN^- concentrations and applied potentials (Figure 9d). This suggests that the frequency of nano-impacts is essentially independent of CN^- concentration, at least in the concentration range studied.

The expected charge from the oxidation of the average AuNPs@CA, assuming a one-electron transfer, was calculated to be ca. 1.1 pC (see Appendix A.4). The ratio between the experimental and expected charge values was considered as the percent conversion of the average AuNPs@CA. The percent conversion was calculated to be ca. 94 ± 5% in the presence of 35.0 mM CN^- or higher (Table 1). The nearly complete oxidation process at 35.0 mM CN^- or higher, also suggests the near-complete gold particle dissolution into CN^- solution. These results suggest that at the single-particle level, nearly complete oxidation of nominally 60 nm diameter AuNPs@CA was achieved at concentrations greater than or equal to 35.0 mM CN^- and at an applied potential of 1.0 V vs SCE.

Table 1. Percent conversion of AuNPs@CA at ensemble and single particle levels

KCN Concentration	Cyclic Voltammetry		Nano-impacts
	First Scan	Total Scan	
1.0 mM	0.6%	1.6%	26.4%
5.0 mM	1.3%	2.2%	50.0%
15.0 mM	2.7%	4.8%	69.1%
35.0 mM	4.6%	6.2%	93.6%

Assuming a rate law of the form: rate/mole s^{-1} = k [CN^-], as suggested by the linearity of Figure 10 (a) and (b), the rate constant, k / cm^3 s^{-1}, can be inferred and the values are shown as insets in the figures. For potentials in the range of 0.5 to 0.8 V, the rate constant is approximately independent of potential, whilst for the range of 0.8 to 1.0 V is higher (Figure 10b, inset). A comparison between Figures 3, 9 and 10 show that significantly higher potentials are required for particle oxidation in the case of single AuNPs@CA over ensembles. This likely reflects partly a high electrical contact resistance in the case of solution-phase impacts as compared to dried drop casted deposits as noted in related cases through direct measurement of contact resistance via *bridging* impacts[54], coupled with a possible loss of driving force for electron transfer resulting from the citrate capping agent on the particles and also possibly from oxide layer formation. Assuming a significant contact resistance, the two kinetic regimes evidenced in Figure 10 might be tentatively attributed to the change in rate-determining step identified by Kirk *et al.*[49] and discussed above on the basis of reaction R3, R4, and R5 (see Section 7.3.2.).

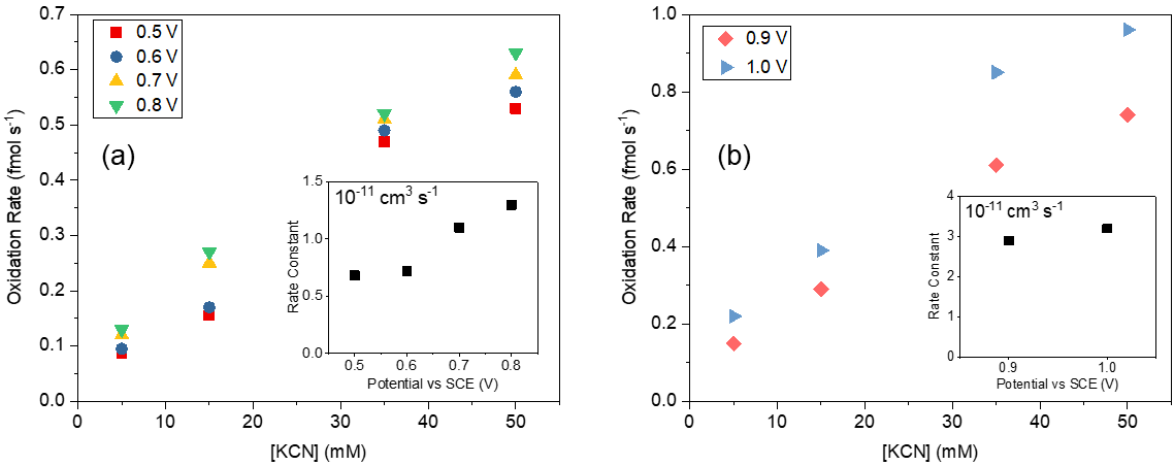


Figure 10. The oxidation rate of the single AuNPs@CA. The linear relationship between oxidation rate and CN^- concentrations at an applied potential of (a) 0.5 V to 0.8 V. and (b) greater than 0.8 V. The rate constant is reported as an inset.

The complete or near-complete dissolution of the single AuNPs@CA for high CN^- concentrations contrasts strongly with the corresponding behavior seen for AuNPs@CA ensembles as reported above. As an ensemble, the AuNPs@CA did not achieve complete oxidation, at least partly due to the particle aggregation or agglomeration states, and thus the gold particle dissolution is limited. In contrast, nano-impacts experiments revealed that a nearly complete oxidation process occurred at 35.0 mM CN^- and higher, at a potential of 1.0 V for a single AuNPs@CA level. The data in Figure 10b shows CN^- is involved in the rate-determining step and since the reaction is oxidative the CN^- likely pre-adsorbs on the AuNPs@CA surface prior to oxidative dissolution.

7.4. Conclusions

The electrochemical dissolution behavior of AuNPs@CA was evaluated at the ensemble and at the single-particle level in cyanide-containing solutions, through CV and nano-impacts experiments, respectively. The CV experiments of the nanoparticles

ensemble exhibited incomplete oxidation of the single AuNPs@CA. In contrast, the nano-impacts experiments revealed that a nearly complete oxidation of the AuNPs@CA was achieved at 35 mM CN^- and higher with an applied potential of 1.0 V. Moreover, by studying single particles, the oxidation of the AuNPs@CA was shown to be controlled by a pre-adsorption step of CN^- onto the surface of single AuNPs@CA before the electron was transferred. This further understanding of the AuNPs@CA dissolution and their reactivity in cyanide-containing solution is of great importance for the optimization of the AuNPs@CA recovery and refinery through the cyanidation process.

Bibliography

(1) A.S.K. Hashmi, Gold-Catalyzed Organic Reactions. *Top. Organomet. Chem*., 2013, 44, 143-164.

(2) R. Ciriminna, E. Falletta, C. Della Pina, J.H. Teles, M. Pagliaro. Industrial Application of Gold Catalysis. *Angew. Chemie-Int. Ed.*, 2016, 55, 14210-14217.

(3) G. J. Hutchings. Selective Oxidation Using Supported Gold Bimetallic and Trimetallic Nanoparticles. *Catalysis Today*, 2014, 238, 69-73.

(4) W. Jin, G. Maduraiveeran. Electrochemical Detection of Chemical Pollutants Based on Gold Nanomaterials. *Trends Environ. Anal. Chem.,* 2017*,* 14, 28-36.

(5) M.E. Kyriazi, D. Giust, A.H. El-Sagheer, P.M. Lackie, O.L. Muskens, T. Brown, A.G. Kanaras. Multiplexed mRNA Sensing and Combinatorial-Targeted Drug Delivery Using DNA-Gold Nanoparticle Dimers. *ACS Nano*., 2018, 12, 3333-3340.

(6) Y. Il Yoon, X. Pang, S. Jung, G. Zhang, M. Kong, G. Liu, X. Chen. Smart Gold Nanoparticle-Stabilized Ultrasound Microbubbles as Cancer Theranostics. *J. Mater. Chem. B*., 2018, 6, 3235-3239.

(7) S. Campuzano, P. Yáñez-Sedeño, J. Manuel Pingarrón. Electrochemical Genosensing of Circulating Biomarkers. *Sensors*, 2017, 17, 866.

(8) S. Kuss, E.E.L. Tanner, M. Ordovas-Montanes, R.G. Compton. Electrochemical Recognition and Quantification of Cytochrome C Expression In *Bacillus Subtilis* and Aerobe/Anaerobe *Escherichia Coli* Using *N*,*N*,*N*′,*N*′-Tetramethyl-*Para*-Phenylene-Diamine (TMPD). *Chem. Sci.,* 2017*,* 8, 7682-7688.

(9) P. Pyykkö, Theoretical Chemistry of Gold. Angew. *Chemie-Int. Ed*., 2004, 43, 4412-4456.

(10) R. Sardar, A.M. Funston, P. Mulvaney, R.W. Murray. Gold Nanoparticles: Past, Present, and Future. *Langmuir*, 2009, 25, 13840-13851.

(11) Y.P. Jia, B.Y. Ma, X.W. Wei, Z.Y. Qian. The *In Vitro* and *In Vivo* Toxicity of Gold Nanoparticles. *Chinese Chem. Lett.*, 2017, 28, 691-702.

(12) P. Knittel, O. Bibikova, C. Kranz. Challenges in Nanoelectrochemical and Nanomechanical Studies of Individual Anisotropic Gold Nanoparticles. *Faraday Discuss*. 2016, 193, 353-369.

(13) A. Assunção, B. Vieira, J.P. Lourenço, M.C. Costa. Recovery of Gold(0) Nanoparticles from Aqueous Solutions Using Effluents from a Bioremediation Process. *RSC Adv*., 2016, 6, 112784-112794.

(14) S. Krishnamurthy, Y.S. Yun. Recovery of Microbially Synthesized Gold Nanoparticles Using Sodium Citrate and Detergents. *Chem. Eng. J.,* 2013*,* 214, 253-261.

(15) A.M. Lazim, J. Eastoe, M. Bradley, K. Trickett, A. Mohamed, S.E. Rogers. Recovery of Gold Nanoparticles Using pH-Sensitive Microgels. *Soft Matter*. 2010, 6, 2050-2055.

(16) A.D. Bas, E. Ghali, Y. Choi. A Review on Electrochemical Dissolution and Passivation of Gold during Cyanidation in Presence of Sulphides and Oxides. *Hydrometallurgy*, 2017, 172, 30-44.

(17) P.D. Kondos, G. Deschênes, R.M. Morrison. Process Optimization Studies in Gold Cyanidation. *Hydrometallurgy,* 1995, 39, 235-250.

(18) F. Xie, D.B. Dreisinger. Use of Ferricyanide for Gold and Silver Cyanidation. *Trans. Nonferrous Met. Soc. China*, 2009, 19, 714-718.

(19) D. M. Mac Arthur. A Study of Gold Reduction and Oxidation in Aqueous Solutions. *J. Electrochem. Soc*., 1972, 119, 672-677.

(20) X. Bin Wang, Y.L. Wang, J. Yang, X.P. Xing, J. Li, L.S. Wang. Evidence of Significant Covalent Bonding in $Au(CN)_2^-$. *J. Am. Chem. Soc.,* 2009*,* 131, 16368-16370.

(21) M. Tanriverdi, H. Mordoğan, Ü. Ipekoğlu. Leaching of Ovacık Gold Ore with Cyanide, Thiourea, and Thiosulphate. *Miner. Eng.,* 2005*,* 18, 363-365.

(22) I. De Michelis, A. Olivieri, S. Ubaldini, F. Ferella, F. Beolchini, F. Vegliò. Roasting and Chlorine Leaching of Gold-Bearing Refractory Concentrate: Experimental and Process Analysis. *Int. J. Min. Sci. Technol*., 2013, 23, 709-715.

(23) A.D. Bas, F. Safizadeh, W. Zhang, E. Ghali, Y. Choi. Active and Passive Behaviors of Gold in Cyanide Solutions. *Trans. Nonferrous Met. Soc. China,* 2015, 25, 3442-3453.

(24) D. Kirk, F. Foulkes, W. Graydon. Gold Passivation in Aqueous Alkaline Cyanide. *J. Electrochem.* 1980, 605, 1962-1969.

(25) A. J. McCarthy, R. G. Coleman, and M. J. Nicol. The Mechanism of the Oxidative Dissolution of Colloidal Gold in Cyanide Media. *J. Electrochem. Soc*., 1998, 145, 408.

(26) M.I. Jeffrey, I.M. Ritchie. The Leaching of Gold in Cyanide Solutions in the Presence of Impurities II. The Effect of Silver. *J. Electrochem. Soc.*, 2000, 147, 3272.

(27) S. V. Sokolov, S. Eloul, E. Kätelhön, C. Batchelor-McAuley, R.G. Compton. Electrode–particle Impacts: A Users Guide. *Phys. Chem. Chem. Phys.*, 2017, 19, 28-43.

(28) E. Kätelhön, A. Feng, W. Cheng, S. Eloul, C. Batchelor-McAuley, R.G. Compton. Understanding Nano-Impact Current Spikes: Electrochemical Doping of Impacting Nanoparticles. *J. Phys. Chem. C.,* 2016*,* 120, 17029-17034.

(29) M. Pumera. Impact Electrochemistry: Measuring Individual Nanoparticles. *ACS Nano*, 2014, 8, 7555-7558.

(30) P.H. Robbs, N. V Rees. Nanoparticle Electrochemistry. *Phys. Chem. Chem. Phys*., 2016, 18, 24812-24819.

(31) L.K. Allerston, N. V Rees. Nanoparticle Impacts in Innovative Electrochemistry. *Curr. Opin. Electrochem*. 2018, 10, 31-36.

(32) K.J. Stevenson, K. Tschulik. A Materials Driven Approach for Understanding Single Entity Nano Impact Electrochemistry. *Curr. Opin. Electrochem*. 2017, 6, 38-45.

(33) G. Zampardi, C. Batchelor-McAuley, E. Kätelhön, R.G. Compton. Lithium-Ion-Transfer Kinetics of Single $LiMn_2O_4$ Particles. *Angew. Chem.,* 2017, 129, 656-659.

(34) G. Zampardi, S. V. Sokolov, C. Batchelor-McAuley, R.G. Compton. Potassium De-insertion Processes in Prussian Blue Particles: Ensemble versus Single Nanoparticle Behaviour. *Chem. - A Eur. J.*, 2017, 23, 14338-14344.

(35) G Zampardi, J Thöming, H Naatz, H Amin, S Pokhrel, L Mädler, R.G. Compton. Electrochemical Behavior of Single CuO Nanoparticles: Implications for the Assessment of their Environmental Fate. *Small*, 2018, 14, 1801765.

(36) B.J. Plowman, K. Tschulik, N.P. Young, R.G. Compton. Capping Agent Promoted Oxidation of Gold Nanoparticles: Cetyl Trimethylammonium Bromide. *Phys. Chem. Chem. Phys.,* 2015, 17, 26054-26058.

(37) Y.G. Zhou, N. V Rees, J. Pillay, R. Tshikhudo, S. Vilakazi, R.G. Compton. Gold Nanoparticles Show Electroactivity: Counting and Sorting Nanoparticles upon Impact with Electrodes. *Chem. Commun*., 2012, 48, 224-226.

(38) Y.G. Zhou, E.J.E. Stuart, J. Pillay, S. Vilakazi, R. Tshikhudo, N. V. Rees, R.G. Compton. Electrode-Nanoparticle Collisions: The Measurement of the Sticking Coefficients of Gold and Nickel Nanoparticles from Aqueous Solution onto a Carbon Electrode. *Chem. Phys. Lett*., 2012, 551, 68-71.

(39) K. Chiang, R. Amal, T. Tran. Photocatalytic Oxidation of Cyanide: Kinetic and Mechanistic Studies. *J. Mol. Catal. A Chem*., 2003, 193, 285-297.

(40) C. Batchelor-McAuley, J. Ellison, K. Tschulik, P.L. Hurst, R. Boldt, R.G. Compton. *In Situ* Nanoparticle Sizing with Zeptomole Sensitivity. *Analyst*, 2015, 140, 5048-5054.

(41) E. Kätelhön, E.E.L. Tanner, C. Batchelor-McAuley, R.G. Compton. Destructive Nano-Impacts: What Information Can Be Extracted from Spike Shapes?, *Electrochim. Acta*. 2016, 199, 297-304.

(42) J. Ellison, K. Tschulik, E.J.E. Stuart, K. Jurkschat, D. Omanović, M. Uhlemann, A. Crossley, R.G. Compton. Get More Out of Your Data: A New Approach to Agglomeration and Aggregation Studies Using Nanoparticle Impact Experiments. *ChemistryOpen*. 2013, 2, 69-75.

(43) S.J. Cloake, H.S. Toh, P.T. Lee, C. Salter, C. Johnston, R.G. Compton. Anodic Stripping Voltammetry of Silver Nanoparticles: Aggregation Leads to Incomplete Stripping. *ChemistryOpen*. 2015, 4, 22-26.

(44) S. V. Sokolov, K. Tschulik, C. Batchelor-McAuley, K. Jurkschat, R.G. Compton. Reversible or Not? Distinguishing Agglomeration and Aggregation at the Nanoscale. *Anal. Chem.*, 2015, 87, 10033-10039.

(45) X. Huang, M.A. El-Sayed. Gold nanoparticles: Optical Properties and Implementations in Cancer Diagnosis and Photothermal Therapy. *J. Adv. Res*., 2010, 1, 13-28.

(46) M. Shamsipur, Z. Karimi, M. A. Tabrizi. A Novel Electrochemical Cyanide Sensor Using Gold Nanoparticles Decorated Carbon Ceramic Electrode. *Microchem. J.*, 2017, 133, 485-489.

(47) C.M. Welch, M.E. Hyde, O. Nekrassova, R.G. Compton. The Oxidation of Trivalent Chromium at Polycrystalline Gold Electrodes. *Phys. Chem. Chem. Phys.*, 2004, 6, 3153-3159.

(48) L.D. Burke. Scope for New Applications for Gold Arising from the Electrocatalytic Behaviour of Its Metastable Surface States. *Gold Bull*., 2004, 37, 125-135.

(49) D.W. Kirk, F.R. Foulkes, W.F. Graydon. A Study of Anodic Dissolution of Gold in Aqueous Alkaline Cyanide. *J. Electrochem. Soc.*, 1978, 125, 1436.

(50) H.K. Lin, X. Chen. Electrochemical Study of Gold Dissolution in Cyanide Solution. *Miner. Metall. Process*., 2001, 18, 147-153.

(51) A.D. Bas, F. Safizadeh, W. Zhang, E. Ghali, Y. Choi. Active and Passive Behaviors of Gold in Cyanide Solutions. *Trans. Nonferrous Met. Soc. China*, 2015, 25, 3442-3453.

(52) H.S. Toh, K. Jurkschat, R.G. Compton. The Influence of the Capping Agent on the Oxidation of Silver Nanoparticles: Nano-impacts versus Stripping Voltammetry. *Chem.-A Eur. J.*, 2015, 21, 2998-3004.

(53) H.S. Toh, C. Batchelor-McAuley, K. Tschulik, M. Uhlemann, A. Crossley, R.G. Compton. The Influence of the Capping Agent on the Oxidation of Silver Nanoparticles: Nano-impacts versus Stripping Voltammetry. *Nanoscale,* 2013, 5, 4884-4893.

(54) X. Li, C. Batchelor-McAuley, L. Shao, S. V. Sokolov, N.P. Young, R.G. Compton. Quantifying Single-Carbon Nanotube–Electrode Contact via the Nanoimpact Method. *J. Phys. Chem. Lett*., 2017, 8, 507-511.

Chapter 8

A Sensor for the Detection and Quantification of Li^+ in Authentic Human Saliva

This chapter reports the development of a sensor for lithium ions (Li^+) in authentic human saliva at lithium manganese oxide ($LiMn_2O_4$)-modified glassy carbon electrodes (LMO-GCE) and screen-printed electrodes (LMO-SPE). The sensing strategy is based on an initial galvanostatic delithiation of $LiMn_2O_4$ according to the reaction: $LiMn_2O_4 - x\,e^- \rightleftharpoons Li_{(1-x)}Mn_2O_4 + x\,Li^+$ followed by linear sweep voltammetry (LSV) to detect the re-insertion Li^+. The process was investigated using powder X-ray diffraction (PXRD) and voltammetry. Four different samples of authentic human saliva were analyzed with the established sensing strategy using LMO-SPEs, showing good linearity over a concentration range up to 5.0 mM, good reproducibility and applicability for routine monitoring purposes. The total time needed to analyze a sample is less than 3 minutes.

The work presented in this chapter has been published in the *ACS Sens.* 2019, 4, 2497-2506 and was carried out in collaboration with Dr. Bertold Rasche, who helped with the PXRD analysis and interpretation of the experimental results. The work was performed collaboratively with Prof. Dr. Philip J. Cowen and Dr. Beata Godlewska from the Department of Psychiatry, Oxford University. The LMO-SPE was fabricated by Sun Chemical Ltd (Bristol, UK). Professor Simon J. Clarke (Department of Chemistry, Oxford University) is acknowledged for the provision of the X-ray diffraction facilities.

8.1. Introduction

Bipolar disorder (BD), also known as manic-depressive illness, is a recurrent mood disorder that causes unusual changes in affect, energy and activity levels from one extreme to another.[1,2] According to the National Health Service (NHS) of the United Kingdom, lithium salts (normally administered as lithium carbonate) are the first-line treatment and officially approved for the management of BD.[3] Lithium is also included on the 20th World Health Organization (WHO) Essential Medicines List (EML) as one of the most effective and safe medicine needed to treat BD.[4] During treatment, it is necessary to monitor the level of lithium (Li^+) since the therapeutic range (0.5-0.8 mM in *blood*) is close to the levels associated with severe intoxication at ≥1.5 mM. Li^+ is lethal at concentrations of 2.0-2.5 mM.[5-6] The monitoring of the Li^+ level is clearly an important aspect of the treatment of BD, as toxicity and dose-related adverse effects can be avoided by dose adjustment or change in the dosage schedule. It is therefore currently necessary for clinicians to monitor their patient's levels of Li^+ regularly with repeated blood tests.

The monitoring of Li^+ ion levels in patients can also be achieved in saliva because it is correlated with the content in the blood. Specifically, the Li^+ ion level in saliva has been reported to be two/three times higher than in blood.[5,7] Moreover, saliva is a preferable and more practical matrix for monitoring of Li^+ levels because its collection is less stressful compared to the collection of blood and furthermore allows the patients to monitor their Li^+ level for themselves.[8-9] The effective therapeutic Li^+ range in the *saliva* is 1.5-2.5 mM.[6,10] This range must be accurately monitored by a highly sensitive analytical method that is reliable and simple to ensure adequate and safe treatment.

Several analytical methods have been described for Li^+ detection in different samples including, but not limited to, high-performance liquid chromatography (HPLC)[11], capillary electrophoresis[12], inductively coupled plasma-atomic emission spectroscopy (ICP-AES)[13], fluorescence-based sensor[14], secondary ion mass spectrometry[15], spectrophotometry[6], and potentiometry[16,17]. These methods are reliable and have good sensitivity. However, they may involve extensive sample pre-treatment and expensive instruments. In favorable cases, voltammetry could provide simpler, cost-effective, user-friendly and fast analysis and the possibility to adapt the process for *in situ* analysis; making it an ideal option for the routine monitoring purpose. The effective use of voltammetric methods has been reported for the detection of glucose[18], bisphenol A[19], silver nanoparticles[20], metal ions[21-22], cortisol[23,24], amphetamines[25], thiocyanate[26], Δ^9-tetrahydrocannabinol[27], glutathione[28,29], uric acid[30], selegiline[31] and modafinil[32] in either synthetic or authentic human saliva.

In this thesis, a linear sweep voltammetry (LSV) method is employed to detect Li^+ in aqueous solution, synthetic saliva, and authentic human saliva samples, using lithium manganese oxide ($LiMn_2O_4$)-modified electrodes. The spinel-type $LiMn_2O_4$ (LMO) is employed as a cathode material for high-performance lithium-ion rechargeable batteries.[33] LMO can also be used for lithium extraction and insertion from aqueous media due to its high selectivity for Li^+, chemical stability, low cost, and non-toxic nature.[34,35] Furthermore, the delithiation kinetics from single LMO particles has been studied in an aqueous solution by the nano-impacts method.[36] In this thesis, LMO is used as an electrode surface modifier for Li^+ detection (*lithiation*) through first a galvanostatic partial delithiation and a subsequent LSV measurement. In the novel approach described below, the LMO was first oxidized under galvanostatic delithiation for 45 seconds at a current of 0.6 mA (current density of ca. 8.6 mA cm^{-2}) and 10.0 μA

(current density of ca. 80.0 μA cm^{-2}) for a LMO-modified glassy carbon electrode (LMO-GCE) and a LMO-modified screen-printed electrode (LMO-SPE), respectively. This first step leading to *partial expulsion* of Li^+ from the spinel structure of LMO (Equation 1).

$$LiMn_2O_4 - x\,e^- \rightleftharpoons Li_{(1-x)}Mn_2O_4 + x\,Li^+ \qquad \text{(Equation 1)}$$

Subsequently, the linear sweep voltammetry (LSV) was performed by sweeping the potential from the end potential of the galvanostatic delithiation to 0.0 V vs SCE (for LMO-GCE) or 0.0 V vs Ag/AgCl (for LMO-SPE) at a scan rate of 5.0 mV s^{-1}. The latter step led to the re-insertion (*lithiation*) of Li^+ in the reverse of reaction (Equation 1). The peak current from the lithiation reflects *both* the amount of Li^+ that was expelled in the first step and that present in the solution phase before the analysis, which one aims to detect. Note that the use of solids to provide a selective approach for Li^+ in the presence of other alkali metals can be compared to the use of Li^+ ionophore-based polymeric membrane, as reviewed by Zdrachek and Bakker[37], but with the advantage that they may be easily screen-printed as demonstrated in this thesis. Moreover, the use of solids may provide a corresponding good selectivity but with significantly lower cost and synthetic requirements.

The transfer of the optimized sensing strategy onto screen-printed electrodes (LMO-SPE) was assessed in an authentic human saliva sample from four healthy volunteers. The results show distinct signals against the background with high reproducibility (RSD <7%) and excellent sensitivity and selectivity, as well as making it simpler, safe, and accessible for point-of-care diagnosis and routine monitoring of Li^+ levels in saliva. More importantly, the linear response range of the sensor spans the therapeutically relevant Li^+ concentrations in human saliva and the total time needed to analyze a sample is less than three minutes.

8.2. Experimental

Details about the chemical reagents here utilized can be found in Chapter 2, Section 2.1. The proprietary formulation of the synthetic saliva (pH 6.8 ± 0.1) reflects the standardized production process pursuant of DIN53160-1.[38] The electrode surface modifier was made of a mixture of $LiMn_2O_4$, carbon black (M 1100, Monarch® donated by Cabot Performance, Billerica, USA) and polyvinylidene difluoride (PVDF, Solef S5130, Solvay, Belgium) with a percent weight ratio of 80:10:10, respectively, and diluted in N-methylpyrrolidone (Sigma Aldrich, UK).[36] The LMO slurry was stirred overnight with a magnetic stirrer. A high purity N_2 flow (BOC Gases plc, UK) was used to remove oxygen thoroughly in all aqueous solutions prior to the electrochemical measurements. Neither synthetic saliva nor authentic human saliva was bubbled with N_2 (see Section 8.3.2 and 8.3.3) as the analysis does not require the removal of oxygen or other dissolved from the saliva.

The freshly polished glassy carbon electrode (GCE) and glassy carbon disc (GCD) were modified by drop-casting 5.0 µl of the LMO slurry and annealing it at 65 ^oC for 10 min to evaporate the solvent, resulting in a LMO-GCE or LMO-GCD, respectively. Electrochemical studies of LMO-GCE in aqueous solution were first conducted by cyclic voltammetry (CV). LMO-GCE was immersed in a solution of 1.0 M $LiClO_4$ and voltammograms were recorded by sweeping the potential from 0.0 to 1.2 V and back to 0.0 V vs SCE at different scan rates. The influence of the use of Faraday cage and temperature was also studied by performing CV at a scan rate of 0.5 mV s^{-1}. Next, the LMO-GCE was immersed in solutions of $LiClO_4$, LiCl, $NaClO_4$, NaCl, KCl and $MgCl_2$, each 1.0 M respectively, and then the potential was swept as described above at a scan rate of 0.5 mV s^{-1}. The concentration of 1.0 M was selected in order to obtain clear signals for the delithiation steps. In further CV experiments, initially, a reductive sweep was

performed after holding the potential of 1.0 V for zero or 10 min by immersing the LMO-GCE in 50.0 mM $LiClO_4$ solution and sweeping the potential from 1.0 to 0.0 V and back to 1.0 V vs SCE at different scan rates.

The selectivity studies were performed using LSV by immersing the LMO-GCE either in a solution of NaCl, KCl, $CaCl_2$ or $MgCl_2$, 10.0 mM each respectively, or in a mixture of these. The concentration of 10.0 mM was selected to study the lithiation, which underpins the sensor performance for practical purposes. LSV was recorded after a delithiation step of 10 min at 1.0 V vs SCE, followed by sweeping the potential directly to 0.0 V vs SCE at a scan rate of 5.0 mV s^{-1}. The lower scan rate of 0.5 mV s^{-1} is selected when performing CV for the modified electrode in *both* aqueous solution and synthetic saliva. The aim of using this low scan rate is to study the electrode response within delithiation steps. Meanwhile, the higher scan rate of 5.0 mVs^{-1} selected to speed up the lithiation step (Li^+ detection) of the sensor in aqueous solution, synthetic saliva, and authentic human saliva. By improving the scan rate (5.0 mVs^{-1}), reasonable analytical times can be achieved without compromising the sensitivity or selectivity of the measurement.

Electrochemical studies of LMO-GCE in synthetic human saliva were evaluated first by CV at different scan rates. The components of commercial synthetic saliva recipes vary depending on the supplier (see Table 8.1). In this thesis, the synthetic saliva used contains inorganic ions such as Mg^{2+}, Ca^{2+}, K^+, Cl^-, CO_3^{2-}, $HPO_4^{2-,}$ and unknown organic substances in order to adjust the viscosity level and pH 6.8 ± 0.1.[38] Next, both LMO-GCE, and LMO-GCD were analyzed by performing galvanostatic measurements with a current density of 8.6 mA cm^{-2} (which is based on the geometrical area of the electrode, not the particle surface area) at different times in order to optimize the delithiation steps prior to the detection of Li^+. The optimization

of chronoamperometric time was studied in 5.0 mM Li^+-spiked synthetic saliva through LSV at a scan rate of 5.0 mV s^{-1}. The powder X-ray diffraction (PXRD) measurements were performed to analyze the structure of the LMO before and after the delithiation at different times. Next, a measurable lower limit of the LMO-GCE was assessed in synthetic saliva through galvanostatic delithiation followed by LSV measurement.

Table 8.1. Compositions of different synthetic saliva recipes.

Composition		Concentration (g L^{-1})					
		S.U. [38]	**AFNOR** [39]	**Fusayama-Meyer** [40]	**SAGF** [41]	**Klimek** [42]	**Shellis** [43]
Inorganic	NaCl	0.33	6.70	0.40	0.13	0.58	-
	KCl	0.75	1.20	0.40	0.96	1.27	1.16
	Na_2HPO_4	-	0.26	-	-	0.34	0.375
	KH_2PO_4	-	0.20	-	0.66	0.33	0.35
	$K_2HPO_4.3H_2O$	0.76	-	-	-	-	-
	$NaHCO_3$	-	1.50	0.10	0.63	-	0.54
	K_2CO_3	0.53	-	-	-	-	-
	KSCN	-	0.33	-	0.19	0.16	0.22
	$CaCl_2.2H_2O$	0.15	-	0.69	0.23	0.17	0.21
	$Na_2S.9H_2O$	-	-	0.005	-	-	-
	Urea	-	-	1.00	0.20	0.20	0.17
	$NaH_2PO_4.H_2O$	-	-	0.69	-	-	-
	NH_4Cl	-	-	-	-	0.16	0.233
	$Na_2SO_4.10H_2O$	-	-	-	0.76	-	-
	$MgCl_2.6H_2O$	0.17	-	-	-	-	0.043
	Sodium Citrate	-	-	-	-	-	0.013
Organic	Ascorbic Acid	-	-	-	-	0.002	-
	Glucose	-	-	-	-	0.03	-
	Uric Acid	-	-	-	-	-	0.0105
	Creatinine	-	-	-	-	-	0.0001
	Choline	-	-	-	-	-	0.013

	Mix. of Vitamins	-	-	-	-	-	0.0008
Protein/ Poly-peptide	Mucin	-	-	-	-	2.70[a]	-
	Glycoprotein	-	-	-	-	-	2.5
	α-Amylase	-	-	-	-	-	3×10^5 Somogyi's unit L^{-1}[b]
	Albumin	-	-	-	-	-	0.025
	Mixture of Amino Acids	-	-	-	-	-	0.041

[a] Bacto-Mucin Bacteriological.

[b] Somogyi's unit L^{-1} is a measure of the level of activity of amylase in blood serum. One Somogyi unit is defined as the amount of amylase required to produce the equivalent of 1 mg of glucose when acting on a standard starch solution under a defined condition.

As proof of concept, this thesis demonstrates the application of the established sensing strategy for the analysis of Li^+ in authentic human saliva. Authentic human saliva is primarily composed of water (99%), several inorganics (Na^+, K^+, Ca^{2+}, Cl^-, HPO_4^{2-}, etc.) and organic (uric acid, creatine, etc.) substances and others.[9] Details about authentic human saliva and its preparation procedure can be found in Section 8.2 and Chapter 2 (Section 2.1). The measurements of Li^+ levels in authentic human saliva samples were performed using the $LiMn_2O_4$-modified screen-printed electrode (LMO-SPE) comprised of three electrodes, which were screen printed by Sun Chemical Ltd (Bristol, UK). The reference electrode was a silver-silver chloride electrode formed using a 60:40 weight ratio of silver to silver chloride, stabilized by 1.0 M Cl^- in aqueous solution, 0.02 M chloride in synthetic saliva[41] and by natural chloride content found in authentic human saliva which is similar to the value in synthetic saliva. The counter electrode was made of carbon (graphite/carbon black), whilst the working electrode was made from carbon and $LiMn_2O_4$.

8.3. Results and Discussion

This section outlines the method for the electrochemical detection and quantification of Li^+ ion in aqueous solution, synthetic saliva, and authentic human saliva. First, electrochemical characterizations of the LMO-GCE immersed in 1.0 M $LiClO_4$ aqueous solutions inside and outside of a Faraday cage, at various temperatures and at various scan rates using CV were carried out. Then CV analysis of the LMO-GCE in solutions containing different cations was performed at a scan rate of 0.5 mV s^{-1}. Selectivity in respect of possible interfering ions and the measurable lower limit of the LMO-GCE were analyzed through linear sweep voltammetry (LSV). Second, the LMO-GCE performance was optimized by galvanostatic delithiation followed by a LSV measurement in synthetic saliva. Finally, with the knowledge about the galvanostatic delithiation and LSV, the successful application of the LMO-SPE to detect Li^+ level in four different authentic human saliva samples is demonstrated.

8.3.1. Electrochemical Behaviour of LMO-GCE in Aqueous Solution

The LMO-GCE was immersed in a solution of 1.0 M $LiClO_4$ and a CV was recorded by sweeping the potential from 0.0 to 1.2 V vs SCE and back to 0.0 V at a scan rate of 0.5 mV s^{-1}. On the forward scan (Figure 1), two quasi-reversible redox waves (as judged by the peak-to-peak potential separation) are observed at a potential of ca. 0.87 V vs SCE (peak-A1) and ca. 1.00 V vs SCE (peak-A2). Peak-A1 and peak-A2 correspond to the two delithiation steps in $LiMn_2O_4$. The first step (peak-A1) yields a phase with the approximate composition $Li_{0.5}Mn_2O_4$ and the second step (peak-A2) is the lithium free λ-MnO_2.[42] On the backward scan, two peaks (C2 and C1) were observed at ca. –0.86 V and ca. –0.67 V vs SCE that correspond to the re-insertion of the Li^+ (lithiation) into the spinel structure of the LMO.[36]

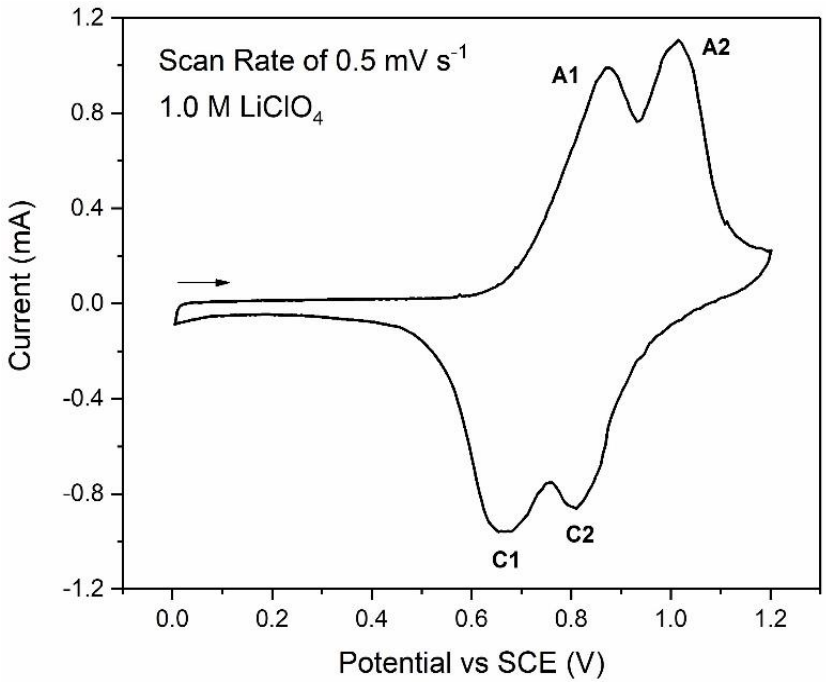


Figure 1. The CV of the LMO-GCE immersed in 1.0 M $LiClO_4$ at a scan rate of 0.5 mV s^{-1}.

The use of a thermostatted vessel or within a Faraday cage follows standard analytical practice; it is not needed for the analytical measurement. To confirm this, the LMO-GCE immersed in 1.0 M $LiClO_4$ both inside (at 25 ^oC) and outside (at ambient temperature) of the Faraday cage. The CVs were recorded by sweeping the potential from 0.0 to 1.2 V vs SCE and back to 0.0 V vs SCE at a scan rate of 0.5 mV s^{-1}. As shown in Figure 2a, the two forward peaks resulting from the experiment performed outside the Faraday cage (solid red curve) are clear; all redox waves can be distinguished and seen at the same peak potential position, suggesting good reproducibility of the modified electrode. The Faraday cage was not used for screen-printed electrode (SPE) measurements, mimicking the condition for potential sensor applications outside of the laboratory.

The temperature influence on the electrode response was verified by performing the CV of the LMO-GCE immersed in a degassed solution of 1.0 M $LiClO_4$ with a temperature setting of 20, 25, and 35 ^oC, all carried out inside the Faraday cage.

CV experiments were performed as described above. As shown in Figure 2b, the resulting cyclic voltammograms are very similar for all temperatures studied. This result suggests that the temperature does not significantly affect the modified electrode response, at least over the temperature range studied.

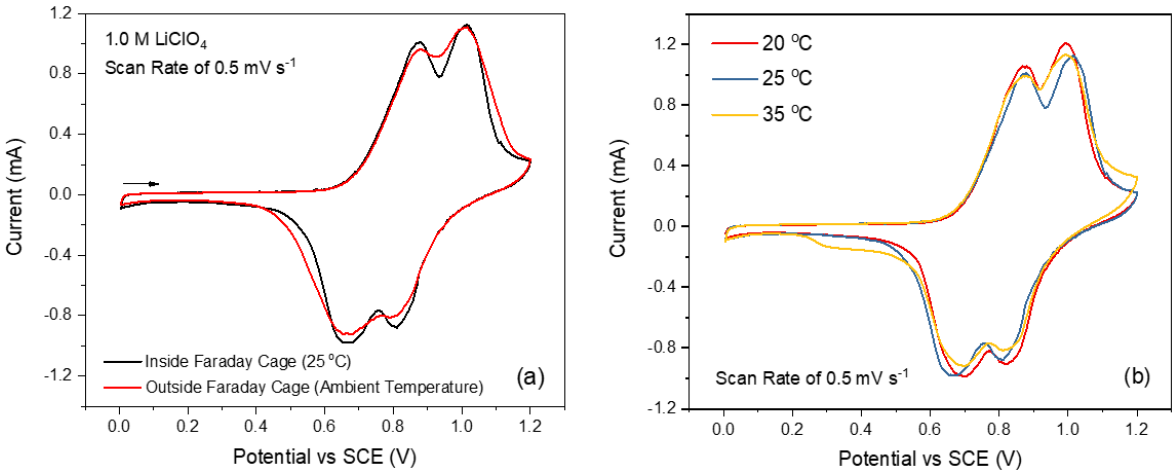


Figure 2. CVs of LMO-GCE immersed in 1.0 M $LiClO_4$ at a scan rate of 0.5 mV s^{-1}. (a) Inside and outside the Faraday cage, and (b) in various temperatures.

Next, the effect of the scan rate was studied. The LMO-GCE was immersed in a 1.0 M $LiClO_4$ and CVs were undertaken by sweeping the potential at 0.0 V to 1.2 V vs SCE and back to 0.0 V vs SCE at scan rates of 0.5, 1.0, 2.0 and 5.0 mV s^{-1}. Note that each experiment was undertaken using a freshly prepared LMO-GCE and degassed solution. As shown in Figure 3a, the two forward peaks can be distinguished using a scan rate of 0.5 mV s^{-1}. Higher scan rates result in distorted voltammograms likely due to the kinetic limitations of the permeation of lithium cations through the deposited LMO at the electrode surface. Note that this low scan rate is exclusively used for CV experiments when the delithiation steps are studied. Figure 3b presents a plot of peak current vs scan rate with an $R^2 = 0.999$ and $R^2 = 0.993$ for peak-A1 and peak-A2, respectively. The

two linear dependencies of the peak current values on the scan rate suggest that the delithiation step is a surface-controlled process.

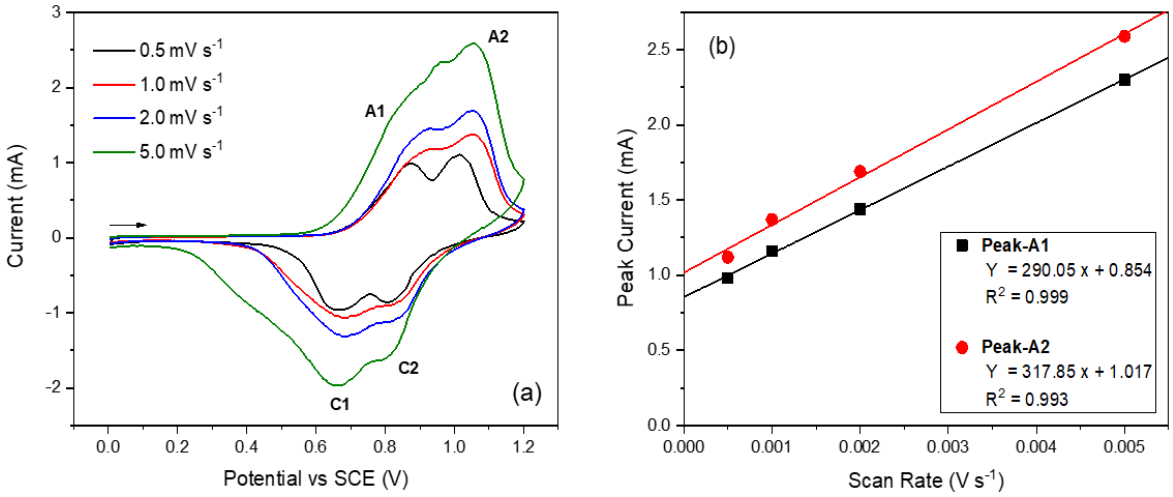


Figure 3. CVs of LMO-GCE immersed in 1.0 M $LiClO_4$. (a) at various scan rates and (b) linear peak current behavior at various scan rates.

Next, the LMO-GCE was immersed in solutions of $LiClO_4$, $NaClO_4$, LiCl, NaCl, KCl or $MgCl_2$ at a concentration of 1.0 M for each cation, then the CVs were recorded in the same potential window (see above) with a scan rate of 0.5 mV s^{-1}. As shown in Figure 4, oxidation peaks are observed in all solutions but the peak potentials of both peak-A1 and peak-A2 are shifted to more positive values by ca. 60 mV and 90 mV, respectively, in $LiClO_4$ and LiCl compared to other solutions. These first forward peaks indicate the delithiation steps are exclusively related to the oxidation of the manganese centers of the LMO. That two forward peaks appear at more negative potentials (for $NaClO_4$, NaCl, KCl and $MgCl_2$ solutions) suggests an easier expulsion of lithium cations out of the LMO structure. The backward peaks C2 and C1 (the re-insertion or lithiation steps) are only observed in $LiClO_4$ and LiCl solutions (Figure 4, solid and dotted black curves). Therefore, lithiation only occurs if the bulk solution contains Li^+.

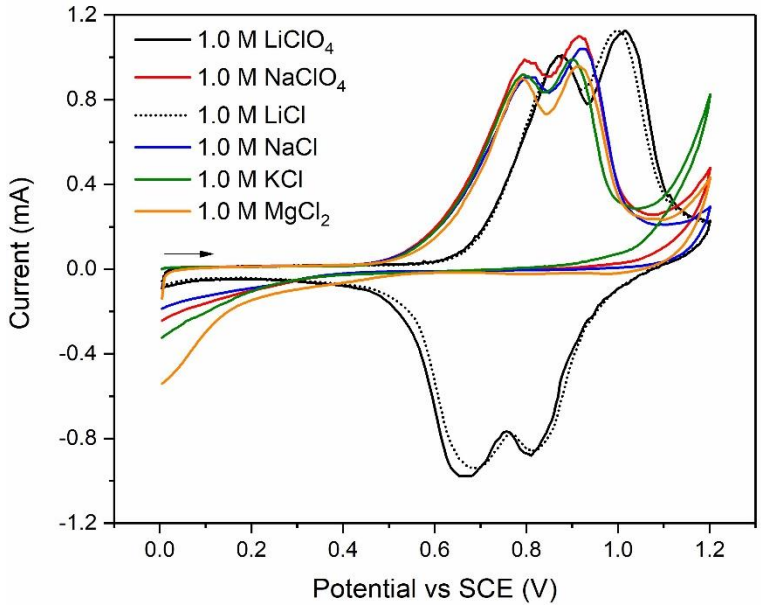


Figure 4. CVs of LMO-GCE immersed in various aqueous solutions at a scan rate of 0.5 mV s^{-1}.

The lithiation process was next studied at different delithiation step times under different scan rates. First, the LMO-GCE was immersed in a solution of 50.0 mM KCl or 50.0 mM $LiClO_4$. The potential was held at 1.0 V vs SCE for either zero or 10 min followed by sweeping the potential from 1.0 V to 0.0 V vs SCE and back to 1.0 V vs SCE, at a scan rate of 5.0 mV s^{-1}. As shown in Figure 5a (solid and dotted red curves), two backward peaks are observed at the peak potential of –0.64 V and –0.42 V vs SCE denoted as peak-C2 and peak-C1, respectively. Consistently, in the absence of Li^+ in the solution, no backward peaks were observed. The peak current values increase with lengthier delithiation step from ca. 0.1 mA to ca. 0.2 mA for peak-C2 and ca. 0.2 mA to ca. 0.3 mA for peak-C1. Second, the LMO-GCE was immersed in a solution of 50.0 mM $LiClO_4$ and the potential held at 1.0 V vs SCE for 10 min. CVs were recorded in the same potential window (see above) at scan rates of 0.5, 2.0, 5.0 and 10 mV s^{-1}. As shown in Figure 5b, the two backward peaks are not clearly seen at scan rates above 5.0 mV s^{-1}. The result indicates that the lithiation step is likely limited to the low permeation of Li^+ and slow absorption kinetics of Li^+ into the LMO, at least for the $LiClO_4$ concentration

studied. Therefore, for the analytical measurements reported below (for the lithiation analysis), a "potentiostatic" delithiation step of 10 min and a scan rate of 5.0 mV s^{-1} were selected.

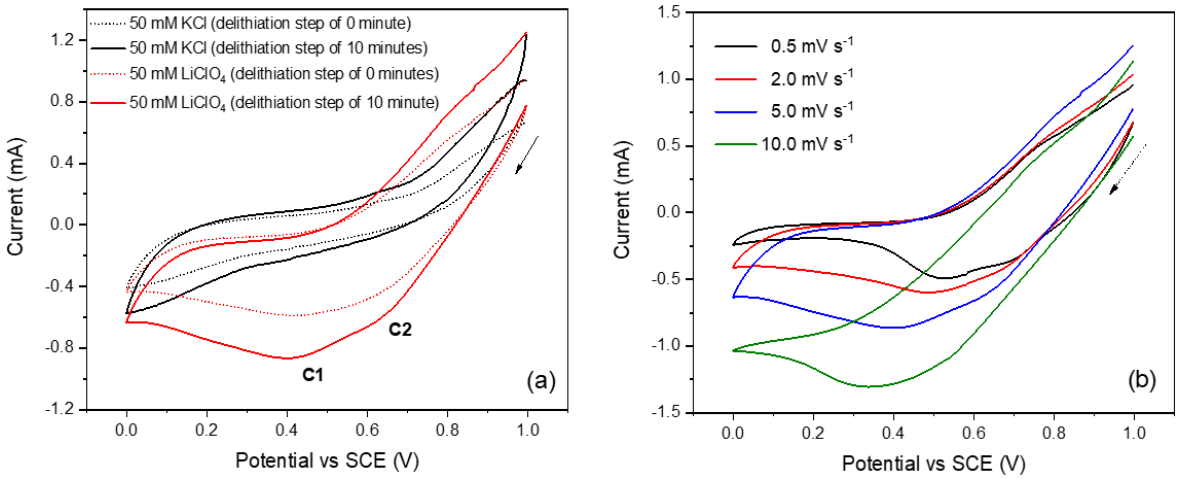


Figure 5. CVs of LMO-GCE immersed in (a) 50.0 mM KCl or 50.0 mM $LiClO_4$ at a scan rate of 5.0 mV s^{-1} with different delithiation step times and (b) 50.0 mM $LiClO_4$ with delithiation step of 10 min at 1.0 V vs SCE with different scan rates.

The selectivity of the LMO-GCE towards the ion of interest (Li^+) in the presence of potentially interfering ions, such as Na^+, K^+, Ca^{2+}, and Mg^{2+}, was investigated next. To assess this, a LMO-GCE was exposed to 10.0 mM of $LiClO_4$, NaCl, KCl, $CaCl_2$ or $MgCl_2$, respectively and LSV was recorded by employing a delithiation step of 10 min at 1.0 V vs SCE followed by sweeping the potential from 1.0 V to 0.0 V vs SCE at a scan rate of 5.0 mV s^{-1}. As shown in Figure 6a, the backward peak is observed at all studied solutions namely at a peak potential of 0.42, 0.54, 0.65, 0.60, and 0.57 V vs SCE, respectively. The result indicates that these cations may insert into the LMO structure during the LSV scan. To validate the sensor's selectivity, the LMO-GCE was assessed in the presence of binary and all cation mixtures, at a selected concentration of 10.0 mM for each cation. As shown in Figure 6b (black and red curves), two backward peaks

were observed at a peak potential of 0.65 V (or 0.58 V in the red curve) and 0.42 V vs SCE that correspond to other cations and Li^+ insertions, respectively. However, in the mixture of all cations (Figure 6b, blue curve), no significant interference from these cations toward Li^+ was observed since only one backward peak is seen at a peak potential of ca. 0.42 V vs SCE. These results suggest that the LMO-GCE has a good selectivity towards Li^+ if applied to mixtures of multiple cations, which reflects the conditions as found in authentic human saliva.

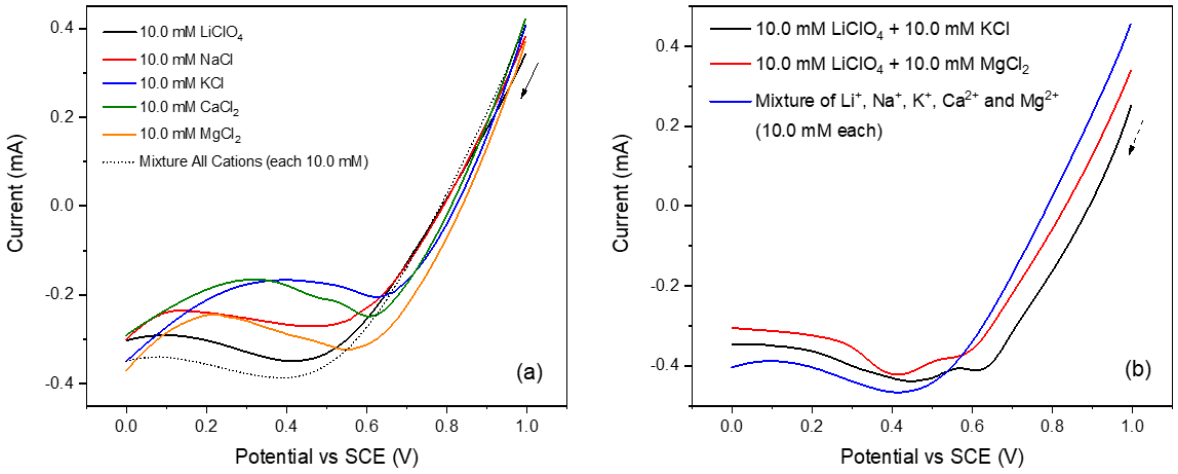


Figure 6. LSVs of LMO-GCE immersed in (a) 10.0 mM solution of different cations, (b) mixture of multiple cations; with delithiation of 10 min at 1.0 V vs SCE and at a scan rate of 5.0 mV s^{-1}.

Having defined the delithiation step time, scan rate and evaluated the selectivity of LMO-GCE, the sensitivity of the sensor is investigated in the following. The LMO-GCE was immersed in solutions of various Li^+ concentrations, from 50.0 µM to 5.0 mM, and LSVs were recorded by employing the method as described above (Figure 7a). The absolute peak current value at the cathodic peak position was used rather than using linear baseline correction to determine the peak current values as discussed below. As shown in Figure 7b, the absolute peak current values increase on increasing the Li^+ concentration. At concentrations below 50.0 µM Li^+, the backward peak is no longer

discernible, revealing the measurable lower limit of the LMO-GCE. For Li^+ detection, a linear peak current behaviour was observed at concentrations ranging from 50.0 μM to 0.5 mM Li^+ with an R^2 = 0.996 (Figure 7b, inset).

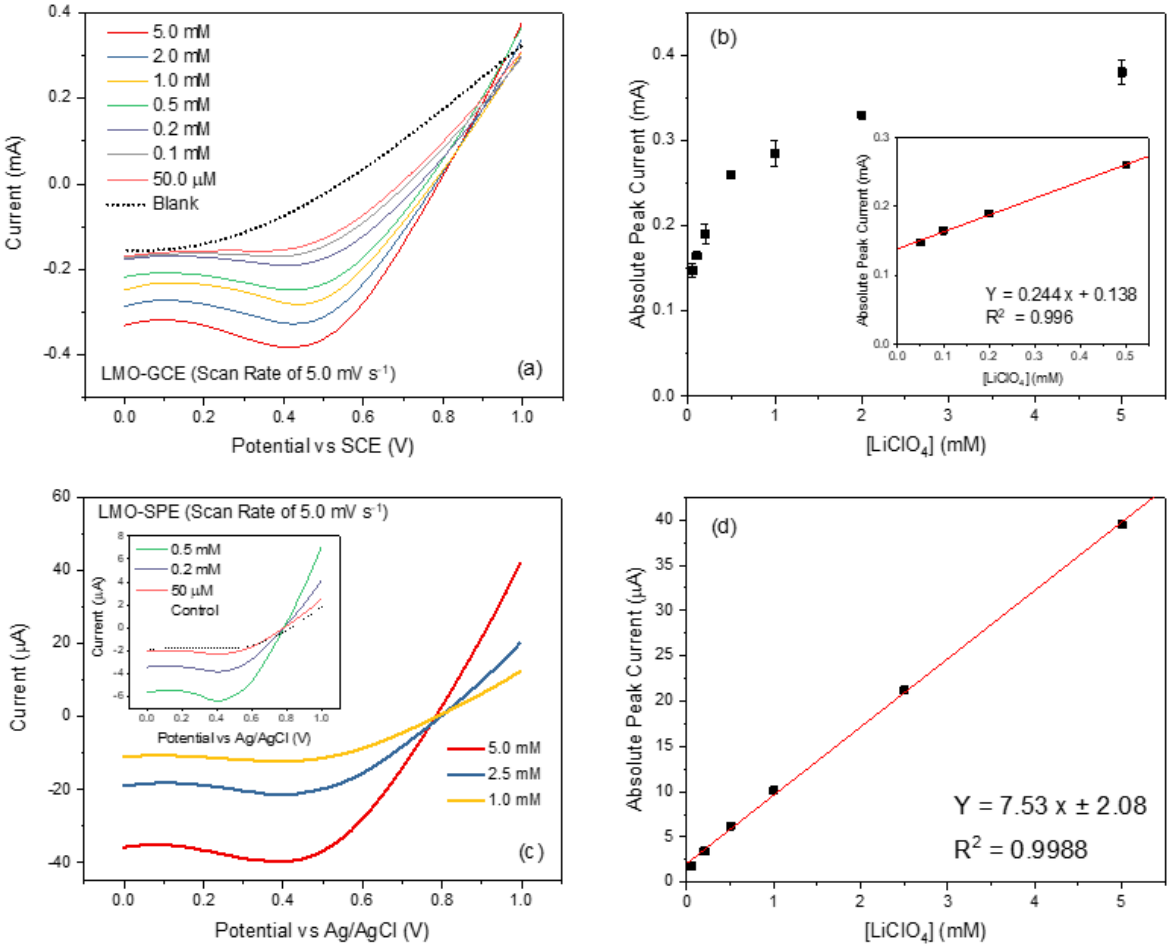


Figure 7. The measurable lower limit and linearity analyses of the modified electrodes immersed in different $LiClO_4$ concentrations: (a) LSVs of LMO-GCE, (c) LSVs of LMO-SPE. (b) and (d) are the plot of the peak current values against various $LiClO_4$ concentrations, generating from (a) and (c), respectively.

Following this, the linearity of the measurement was further verified using a lithium manganese oxide-modified screen-printed electrode (LMO-SPE) in an aqueous solution containing various $LiClO_4$ concentrations. The LSV was recorded by employing a potentiostatic delithiation of 10 min at potential 1.0 V vs Ag/AgCl followed by

sweeping the potential from 1.0 V to 0.0 V vs Ag/AgCl at a scan rate of 5.0 mV s^{-1} (Figure 7c). As shown in Figure 7d, the absolute peak current value of the LMO-SPE increases linearly with increasing Li^+ concentrations, showing excellent linearity from 50.0 μM to 5.0 mM Li^+. This result demonstrates the high applicability of the LMO-SPE to detect Li^+ in analyte covering the therapeutic range of 1.5-2.5 mM. The practicability of the LMO-SPE will be discussed further in Section 8.3.3, which is after optimization of the galvanostatic delithiation and LSV measurement for the analysis of human saliva.

The above demonstrates a possible sensing method of Li^+ in an aqueous solution. However, the identified required potentiostatic delithiation step of 10 min at 1.0 V vs SCE before LSV being recorded is disadvantageous for the routine monitoring of samples. For practical and regular purposes, a direct-and-quick use of the sensor is required by the user. In the following section, this aspect can be improved by performing galvanostatic delithiation followed by LSV measurement.

8.3.2. Detection of Li^+ in Synthetic Saliva

This section will describe the electrochemical behavior of the LMO-GCE in synthetic saliva, the optimization of the sensing performance via galvanostatic delithiation-LSV and the sensitivity of the sensor.

First, the LMO-GCE was immersed in synthetic saliva and then CV was recorded by sweeping the potential from 0.0 V to 1.2 V vs SCE and back to 0.0 V at a scan rate of 0.5 mV s^{-1}. Note that the synthetic saliva was not bubbled with N_2 in order to better reflect conditions for practical purposes (direct-and-quick use of the sensor in authentic human saliva). Figure 8 shows that the resulting peak significantly decreased after 10 minutes of bubbling with N_2. Moreover, the observation shows that synthetic saliva becomes whitish or opaque if bubbled with N_2 thoroughly before the

voltammetric measurement. This whitish color of synthetic saliva after N_2 bubbling is likely caused by the denaturation of protein due to mechanical stress.

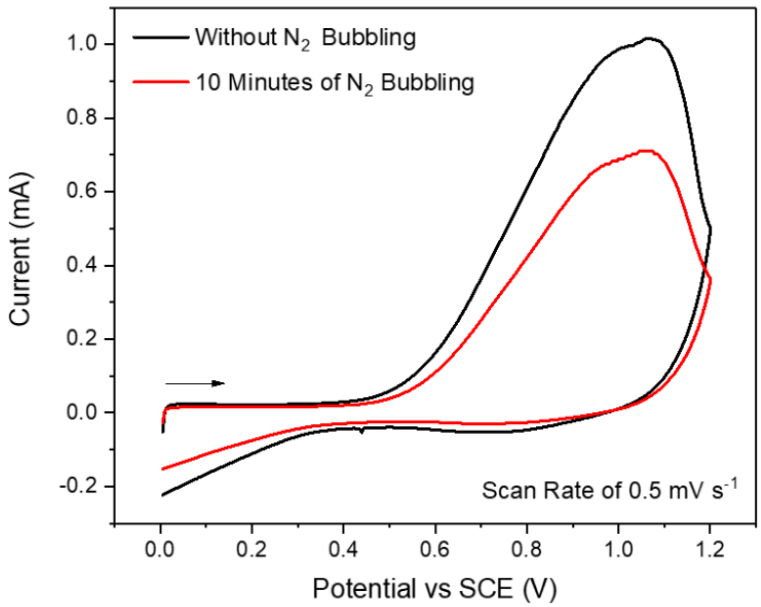


Figure 8. CVs of LMO-GCE immersed in synthetic saliva, without and with 10 min N_2 bubbling, at a scan rate of 0.5 mV s^{-1}.

As shown in Figure 9a, two oxidation peaks are seen at a peak potential of ca. 0.96 V and ca. 1.07 V vs SCE that likely corresponds to the two delithiation steps of deposited LMO on the electrode surface. Relatively no backward peaks are observed on the backward CV scan, suggesting no Li^+ (from the delithiation) re-insert back into the LMO. However, the cyclic voltammogram becomes distorted when applying higher scan rates, or even at 5.0 mV s^{-1} (Figure 9b), and extraction or absorption of unknown species (from components of the synthetic saliva) may arise as shown in a backward peak at a peak potential of ca. 0.5 V vs SCE. This scan rate influence, again (see Section 8.3.1), is likely related to the kinetic limitations of the permeation of Li^+ through the deposited LMO at the electrode surface.

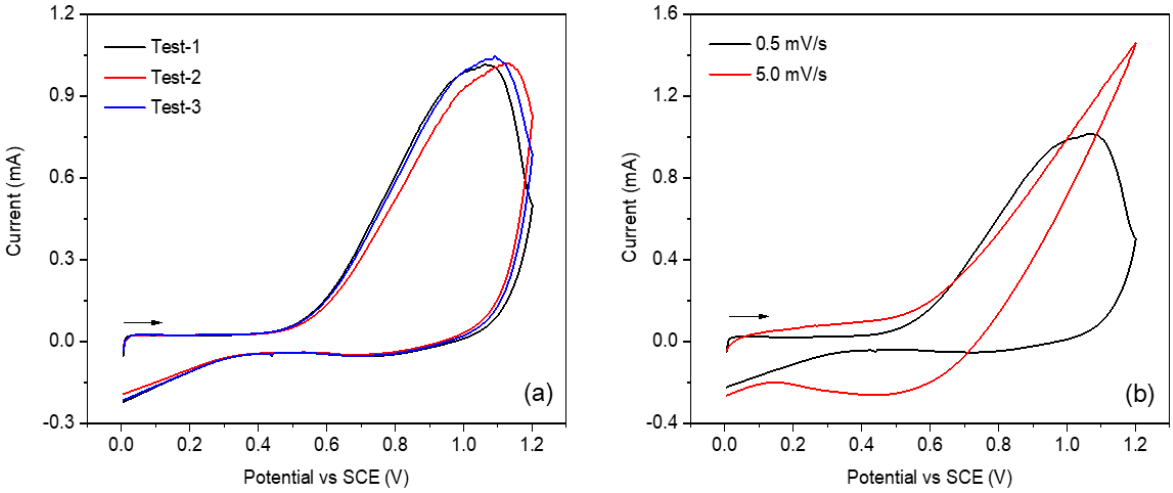


Figure 9. CVs of LMO-GCE immersed in synthetic saliva without N_2 bubbling. (a) Reproducibility of the LMO-GCE at a scan rate of 5.0 mV s^{-1}, (b) at two different scan rates.

Second, the LMO-GCE was immersed either in 1.0 M $LiClO_4$ or in synthetic saliva, and then galvanostatic delithiation was performed at an applied current density of 8.6 mA cm^{-2} for a particular period. In 1.0 M $LiClO_4$, two delithiation steps were found at ca. 0-420 s (up to the first plateau) and ca. 420-1800 s (up to the second plateau) (Figure 10a, red curve). Meanwhile, in synthetic saliva two delithiation steps were found at ca. 0-2000 s (up to the first plateau) and ca. 2000-4500 s (up to the second plateau) (Figure 10a, black curve). The results suggest both delithiation steps in 1.0 M $LiClO_4$ aqueous solution is faster than in synthetic saliva, possibly due to the higher ionic strength. At a higher concentration in aqueous solution (high ionic strength), the rate of delithiation at the electrode-bulk solution interface may increase due to a higher electrical field at the electrode-bulk solution interface. Therefore, this leads to a faster flow of the charge into and out of the interface.

Next, the LMO-GCE was immersed in 5.0 mM Li^+-spiked synthetic saliva and then the galvanostatic delithiation with a current density of 8.6 mA cm^{-2} was performed at different times, ranging from 20 s to 20 min. In the same analyte, immediately LSV measurements were performed by sweeping from the ending potential of the

galvanostatic delithiation to 0.0 V vs SCE at a scan rate of 5.0 mV s^{-1}. Figure 10b shows the response in the LSV becomes broadened for very long delithiation times and weaker for very short delithiation times. After a galvanostatic delithiation of 45 s (within the first plateau of the delithiation) the signal is very sharp and the peak current already close to values at longer times. Indeed, 45 s is also a realistic time scale of analysis for routine monitoring purposes and was therefore selected for all further experiments described below.

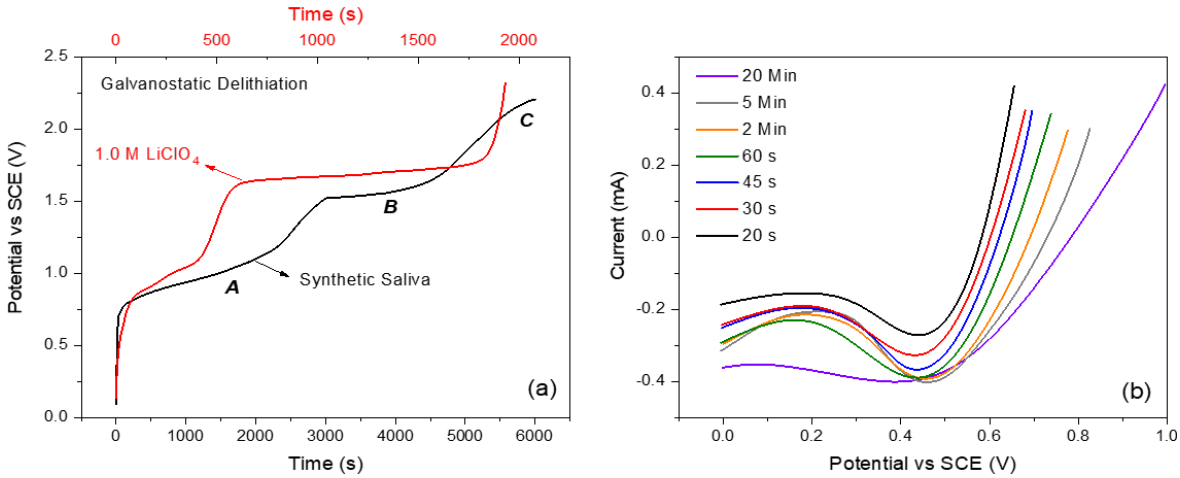


Figure 10. Optimizing galvanostatic delithiation time. (a) Comparison of galvanostatic delithiation response of LMO-GCE in 1.0 M $LiClO_4$ vs synthetic saliva, (b) LSVs of LMO-GCE immersed in 5.0 mM Li^+-spiked synthetic saliva at a scan rate of 5.0 mV s^{-1}.

An explanation for the different responses during the lithiation after different times in the galvanostatic delithiation can be found in the structural changes of LMO concomitant with the delithiation process. The structural changes of LMO before and after the delithiation steps were studied using the powder X-ray diffraction (PXRD) analysis, which requires compatible substrate (disc type) for the measurements. To assess this, a freshly polished glassy carbon disc (GCD) was first modified by drop-casting 5.0 µl of the LMO slurry and annealing at 65 ^oC until completely dry, resulting

in LMO-GCD. Next, the LMO-GCDs were immersed in synthetic saliva and then first underwent a galvanostatic delithiation for different times followed by PXRD measurements on a powder diffractometer. Subsequently, the LMO-GCDs were re-immersed in synthetic saliva to perform the lithiation in LSV as described above. The galvanostatic for the three samples was performed so that the first sample was stopped within the first plateau, the second sample after the first step within the second plateau and the third sample after the second step (Figure 10a, denoted as *A*, *B,* and *C*).

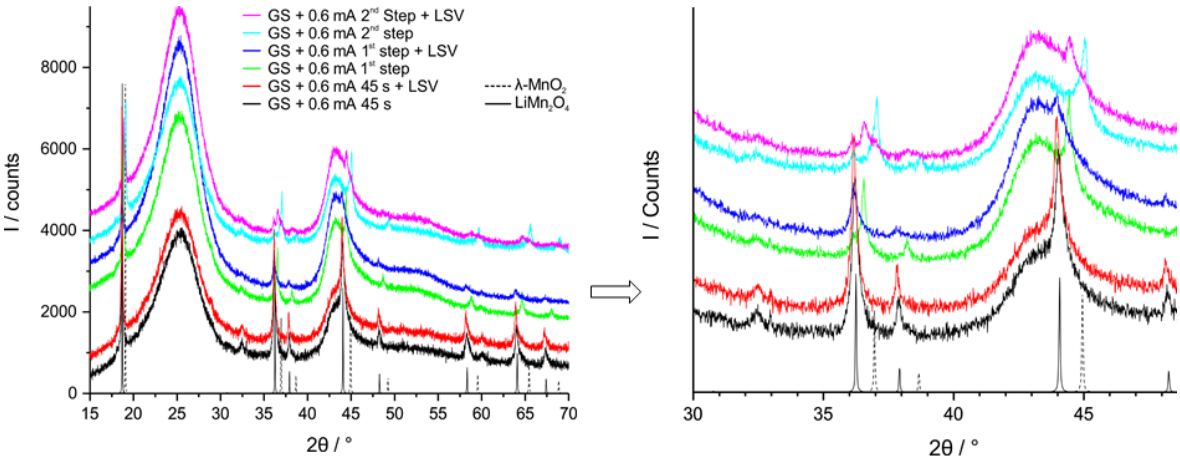


Figure 11. PXRD analysis of LMO-GCD before and after galvanostatic-LSV measurements in synthetic saliva.

From PXRD analysis, three different structures can be distinguished, which are the structure of the initial $LiMn_2O_4$, of $Li_{0.5}Mn_2O_4$ and of the fully delithiated λ-Mn_2O_4, as expected for the delithiation steps of $LiMn_2O_4$.[42] As shown in Figure 11, the PXRD patterns taken for the first, second and third sample (black, green and turquoise, respectively) imply that the initial $LiMn_2O_4$ structure type remains intact during the first plateau (with the composition $Li_xMn_2O_4$, with $0.5<x\leq1.0$) whilst the $Li_{0.5}Mn_2O_4$ structure type is formed after the first step and remains intact during the second plateau (with the composition $Li_xMn_2O_4$, with $0.0<x\leq0.5$). The λ-Mn_2O_4 is formed after

the second step only when the structure contains no lithium. For the latter two, a small part of the sample remains in the initial $LiMn_2O_4$ structure type, possibly due to larger particles that are not completely delithiated. After the (re-)lithiation in the LSV experiment, for the first sample, no structural differences can be seen, while the second sample is mainly transformed back to the initial $LiMn_2O_4$ structure type. For the sample that mainly consisted of the λ-MnO_2, after the LSV measurement, a mixture of all three structure types (dominantly the $Li_{0.5}Mn_2O_4$ structure type) was found. These results demonstrate how the delithiation/lithiation process becomes more irreversible with each structural transition passed in the delithiation process. This effect is already obvious in the LSV experiment after delithiation of 20 min (Figure 10b). While after the 20 min delithiation step only the first structural transition is approached, the LSV response already becomes broadened compared to all experiments with shorter delithiation steps. On the other hand, for delithiation times where the initial structure of $LiMn_2O_4$ remains intact (Figure 10b: 20 s to 5 min), the resulting LSV signal is sharp and well defined with the peak current mainly varying with the delithiation time, meaning the amount of delithiated lithium. Therefore, the galvanostatic delithiation has to remain within the first plateau (Figure 10a) to avoid any structural changes.

In summary, the working mechanism of the electrode toward the detection of lithium ions is as follows. The $LiMn_2O_4$ was first oxidized under galvanostatic delithiation control leading to *partial* expulsion of Li^+ from $LiMn_2O_4$ (Equation 1). Typically, the galvanostatic oxidation was stopped when a substantial amount of delithiated $Li_{(1-x)}Mn_2O_4$ had formed (x = 0.13), taking care not to go beyond x = 0.5 which would involve a phase transition.[42] This requires driving the electrode for a period of 45 seconds at a current density of ca. 8.6 mA cm^{-2} and ca. 80.0 µA cm^{-2} for LMO-GCE and LMO-SPE, respectively. The electrode potential then usually reached a

value of ca. 0.70 V vs SCE (for LMO-GCE) or ca. 0.52 V vs Ag/AgCl (for LMO-SPE). Subsequently, the potential was swept directly from the ending potential of the galvanostatic delithiation to 0.0 V vs SCE (for LMO-GCE) or 0.0 V vs Ag/AgCl (for LMO-SPE). This led to the re-insertion (lithiation) of Li^+ in the reverse of the reaction in Equation 1 as revealed by a cathodic peak in the linear sweep voltammogram.

The sensitivity of the sensor was studied by employing the established sensing strategy as described above. The LMO-GCE was exposed in various concentrations of Li^+-spiked synthetic saliva samples, ranging from 50.0 µM to 5.0 mM (Figure 12a). The measurable lower limit was determined by the *absolute* peak current value at the minimum peak position. As shown in Figure 12b, the absolute peak current value is increased with increasing Li^+ concentrations added into the synthetic saliva. A linear peak current behaviour was found at concentrations ranging from 50.0 µM to 0.5 mM Li^+ with an R^2 = 0.9906 (Figure 12b, inset). A measurable lower limit of 50.0 µM was achieved, the same value as found in aqueous solution (see Section 8.3.1).

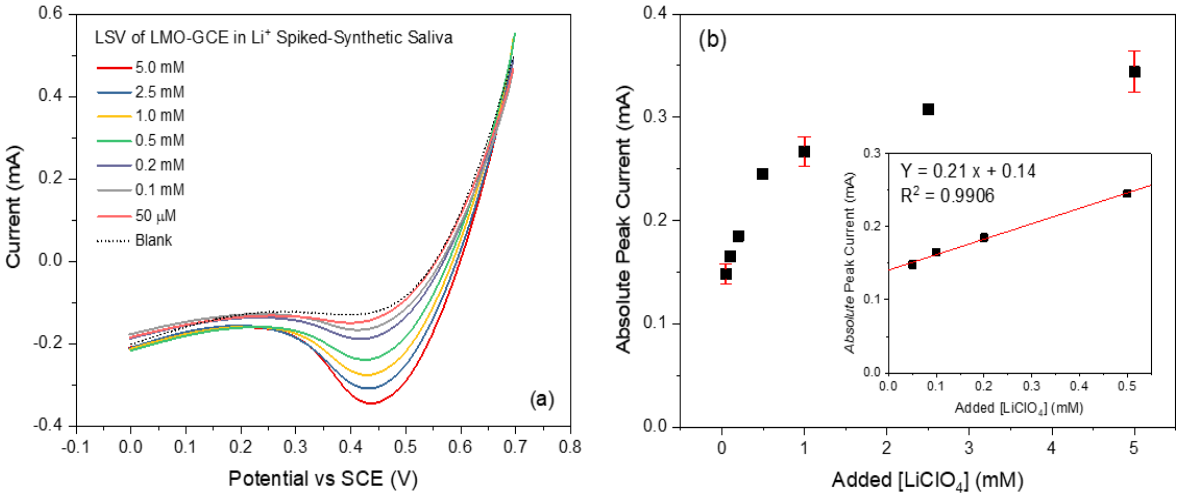


Figure 12. The measurable lower limit of the LMO-GCE in different concentrations of Li^+-spiked synthetic saliva at a scan rate of 5.0 mV s^{-1}. (a) LSVs of LMO-GCE, (b) A plot of the peak current values against various Li^+-spiked synthetic saliva concentrations.

Having defined a measurable lower limit of Li^+ at the LMO-GCE in both aqueous solution and synthetic saliva, the following section will describe the applicability of the optimized system in authentic human saliva.

8.3.3. Detection of Li^+ in Authentic Human Saliva

Next, the optimized methodology developed above was transferred to screen-printed electrodes and used to analyze Li^+ in authentic human saliva. The analysis was conducted by standard addition method in triplicate, each from the same time of sample collection (see below).

Initially, the LMO-SPE performance was characterized using CV in 1.0 M LiCl, synthetic saliva or authentic human saliva. 50.0 μL of the selected analyte was deposited onto the LMO-SPE surface, covering all three electrodes. A CV was recorded by sweeping the potential from 0.0 to 1.2 V and back to 0.0 V vs Ag/AgCl at a scan rate of 0.5 mV s^{-1}. The experiment was performed in triplicate in order to ensure the reproducibility of the result. As shown in Figure 13 (red curve), two forward peaks are observed at a peak potential of ca. 0.74 V and ca. 0.88 V vs Ag/AgCl, which correspond to the two delithiation steps in LMO. On the backward scans, two peaks were also observed at a peak potential of ca. –0.70 V and ca. –0.82 V vs Ag/AgCl that correspond to the re-insertion of the Li^+ into the LMO structure. This result suggests an excellent analytical performance of LMO-SPE than LMO-GCE (Figure 1) with two well-distinguished peaks observed clearly. In addition, exposing either synthetic saliva or authentic human saliva to the LMO-SPE the forward peaks (ca. 0.55 V and ca. 0.71 V vs Ag/AgCl) and backward peaks (ca. –0.60 V and ca. –0.47 V vs Ag/AgCl) are again clearly observed (Figure 13, blue and black curves). Figure 13 shows that the SPE gives a clearer electrochemical response compared to the GCE (Figure 9).

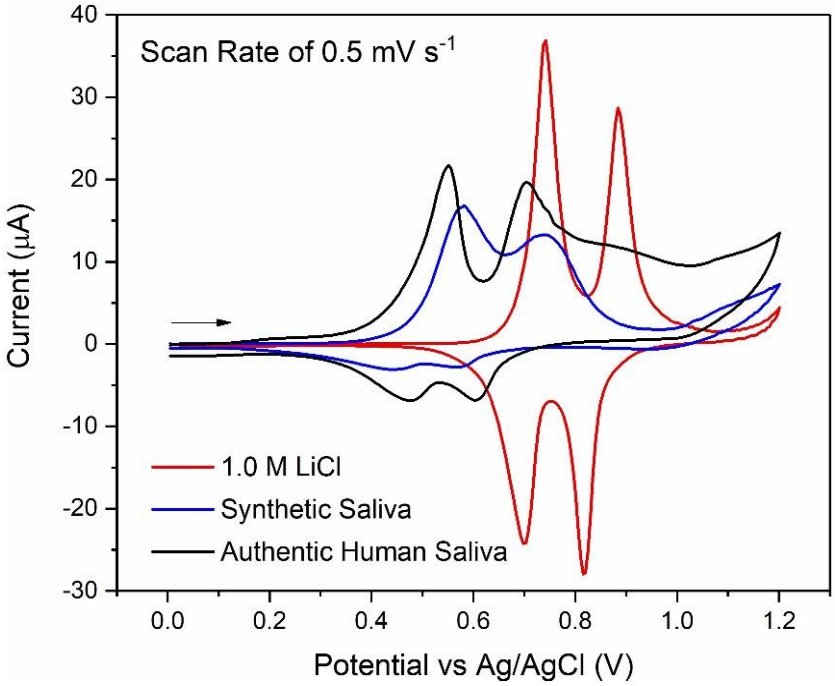


Figure 13. The CV of LMO-SPE with different analytes at a scan rate of 0.5 mV s^{-1}. Note that the potential of the SPE Ag/AgCl reference electrode is poised by the chloride ion levels present explaining the shift in peak potentials between analytes.

To conduct an analysis of Li^+ in authentic human saliva, a ca. 50.0 µL sample of pristine authentic human saliva was put onto the LMO-SPE surface. Subsequently, galvanostatic delithiation was performed with a current density of 80.0 µA cm^{-2} for 45 seconds (see above). Next, an LSV measurement was undertaken immediately by sweeping the potential from the ending potential of the galvanostatic step (approximately 0.5 V vs Ag/AgCl) to 0.0 V vs Ag/AgCl at a scan rate of 5.0 mV s^{-1} (Figure 14a, solid red curve). To determine the Li^+ concentration in authentic human saliva, the standard addition procedure was conducted by adding a $LiClO_4$ standard solution with a known concentration of 100.0 mM in subsequent steps to the sample (Figure 14a). Three different authentic human saliva samples were measured up to 1.0 mM Li^+ added, while for a fourth sample the added concentration range was extended up to a concentration of 5.0 mM Li^+ to cover the therapeutic range (1.5-2.5 mM Li^+). For each

step, the same galvanostatic delithiation and LSV measurements were performed. This procedure was repeated for three fractions from each of the four different authentic human saliva samples to ensure the reproducibility of the result and to determine the relative standard deviation. A plot of the absolute peak current values against the total concentration of Li^+ was then generated. In a control experiment, synthetic saliva containing no Li^+ was used. As shown in Figure 14b and Appendix A.5, the absolute peak current values increase linearly with increasing concentration of Li^+-spiked authentic human saliva for the triplicate measurements of all four different samples in the respective concentration ranges. Additionally, the recovery of Li^+ was determined for the same authentic human saliva samples as before with an added 0.2 mM concentration of Li^+. The recovery was calculated from the differences between the Li^+ concentrations found from standard addition (before spiking) and the Li^+ concentrations found in the recovery test (after spiking) in relation to the spiked amount of 0.2 mM Li^+. The summary of these results is reported in Table 1.

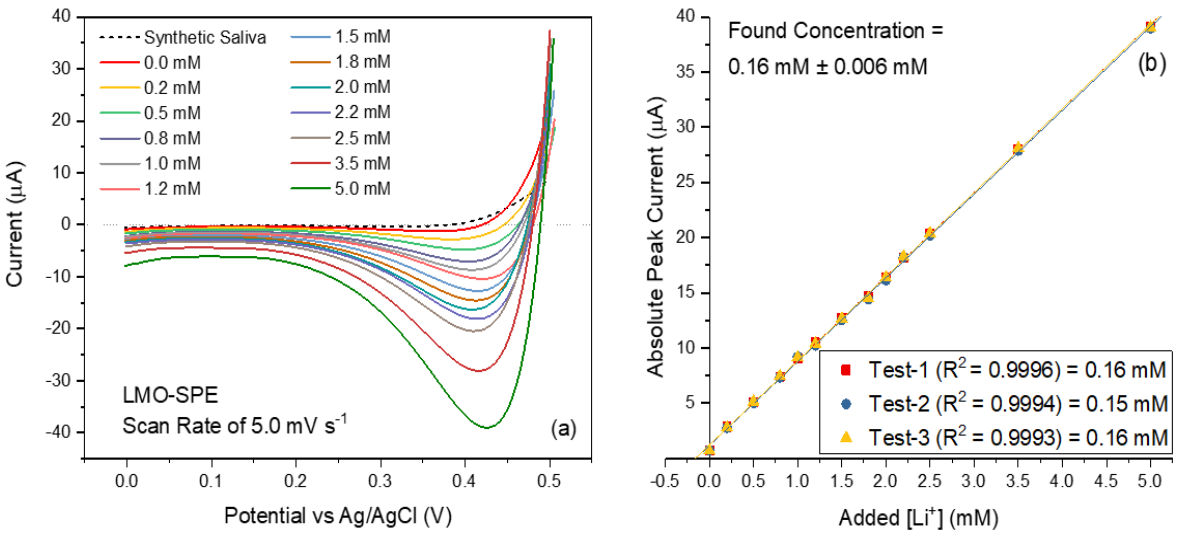


Figure 14. (a) Representative LSVs of LMO-SPE with different Li^+-spiked authentic human saliva concentrations, at a scan rate of 5.0 mV s^{-1}. (b) Linear peak current behavior at various Li^+-spiked authentic human saliva concentrations.

The first three samples analyzed are similar (ranging from 0.13 to 0.16 mM) in around the value for a healthy person. Moreover, the relative standard deviation (% RSD) from the random error was found to be 6.3%, 6.9% and 4.6% for sample-1, sample-2, and sample-3, respectively. Together with the measurement of the zero Li^+ current, the systematical and random errors add up to 0.05, 0.05 and 0.04, respectively. For the fourth sample, the standard addition method was extended towards the therapeutic range and beyond, demonstrating the linearity of the sensor response in the whole relevant range. As shown in Figure 14b, the found concentration in the fourth sample is 0.16 ± 0.006 mM (RSD 3.8%) comparable to the values from the first three samples. This result shows a reproducible linear response of the sensor also in an extended range, including the therapeutically relevant concentrations as a linear response is seen up to 5.0 mM Li^+. This is also in agreement with the experiments shown previously (see 8.3.1) using the LMO-SPE with potentiostatic delithiation (holding the potential of 1.0 V vs SCE for 10 min prior to the LSV) for detection of Li^+ in aqueous solution. The result demonstrates the practicality of the sensor for routine monitoring of Li^+ in saliva for a patient with bipolar disease.

Table 1. Li^+ quantification in authentic human saliva samples and recovery results.

Sample	**Concentration (before spiking) (mM)**	**RSD**	**Recovery (after spiking with 0.2 mM Li^+)**
1	0.16 ± 0.0100	6.3%	99.2%
2	0.14 ± 0.0096	6.9%	99.0%
3	0.13 ± 0.0060	4.6%	98.6%
4	0.16 ± 0.0060	3.8%	99.4%

8.4. Conclusions

The electrochemical sensor based on a lithium manganese oxide ($LiMn_2O_4$)-modified screen-printed electrode (LMO-SPE) exhibits a good selectivity towards possible interfering cations, a sensitivity of 50.0 μM (in both aqueous solution and synthetic saliva) and an excellent sensing performance in authentic human saliva. The linear response range of the sensor spans the therapeutically relevant Li^+ concentrations in human saliva (0-5.0 mM) and allows analysis in reasonable times of less than three minutes. The sensor offers a low cost and easy to utilize alternative that is applicable for routine monitoring of Li^+ levels. With the non-invasive sampling approach, the sensor can be used directly by either patients or clinicians. For instance, patients with bipolar disease can benefit from the point-of-care diagnosis with this sensor, as during dose adjustment or change in the medication schedule, immediate feedback is possible. This ensures that the Li^+ levels remain within the therapeutic range, so patients are treated appropriately and safely.

Bibliography

(1) Merikangas, K. R.; Jin, R.; He, J. P.; Lee, S.; Sampson, N. A.; Viana, M. C.; Andrade, L. H.; Hu, C.; Karam, E. G.; et al. Prevalence and Correlates of Bipolar Spectrum Disorder in the World Mental Health Survey Initiative. *Arch. Gen. Psychiatry* 2011, *68(3)*, 241–251.

(2) Rybakowski, J. K. Recent Advances in the Understanding and Management of Bipolar Disorder in Adults [Version 1; Peer Review: 2 Approved]. *F1000Research* 2017, *6* (2033), 1–7.

(3) NHS. www.nhs.uk/conditions/bipolar-disorder/treatment/. Accessed 5 April 2019.

(4) WHO. 20th World Health Organization (WHO) Essential Medicines List www.who.int/medicines/publications/essentialmedicines/en. Accessed 9 April 2019.

(5) Murru, A.; Torra, M.; Callari, A.; Pacchiarotti, I.; Romero, S.; de la Presa, B. G.; Varo, C.; Goikolea, J. M.; Pérez-Sola, V.; Vieta, E.; et al. A Study on the Bioequivalence of Lithium and Valproate Salivary and Blood Levels in the Treatment of Bipolar Disorder. *Eur.*

Neuropsychopharmacol. 2017, *27* (8), 744–750.

(6) Albero, M. I.; Ortuño, J. A.; García, M. S.; Cuartero, M.; Alcaraz, M. C. Novel Flow-through Bulk Optode for Spectrophotometric Determination of Lithium in Pharmaceuticals and Saliva. *Sensors Actuators B Chem.* 2010, *145* (1), 133–138.

(7) Ben-Aryeh, H.; Naon, H.; Szargel, R.; Gutman, D.; Hefetz, A. Salivary Lithium Concentration—A Tool for Monitoring Psychiatric Patients. *Oral Surgery, Oral Med. Oral Pathol.* 1980, *50* (2), 127–129.

(8) Lima, D. P.; Diniz, D. G.; Moimaz, S. A. S.; Sumida, D. H.; Okamoto, A. C. Saliva: Reflection of the Body. *Int. J. Infect. Dis.* 2010, *14* (3), e184–e188.

(9) Ngamchuea, K.; Chaisiwamongkhol, K.; Batchelor-McAuley, C.; Compton, R. G. Chemical Analysis in Saliva and the Search for Salivary Biomarkers – a Tutorial Review. *Analyst* 2018, *143* (1), 81–99.

(10) Hirayama, E.; Sugiyama, T.; Hisamoto, H.; Suzuki, K. Visual and Colorimetric Lithium Ion Sensing Based on Digital Color Analysis. *Anal. Chem.* 2000, *72* (3), 465–474.

(11) Dai, L.; Wigman, L.; Zhang, K. Sensitive and Direct Determination of Lithium by Mixed-Mode Chromatography and Charged Aerosol Detection. *J. Chromatogr. A.* 2015, *1408*, 87–92.

(12) Vrouwe, E. X.; Luttge, R.; van den Berg, A. Direct Measurement of Lithium in Whole Blood Using Microchip Capillary Electrophoresis with Integrated Conductivity Detection. *Electrophoresis* 2004, *25* (10–11), 1660–1667.

(13) Lewen, N.; Nugent, D. The Use of Inductively Coupled Plasma-Atomic Emission Spectroscopy (ICP-AES) in the Determination of Lithium in Cleaning Validation Swabs. *J. Pharm. Biomed. Anal.* 2010, *52* (5), 652–655.

(14) Stubing, D. B.; Heng, S.; Abell, A. D. Crowned Spiropyran Fluoroionophores with a Carboxyl Moiety for the Selective Detection of Lithium Ions. *Org. Biomol. Chem.* 2016, *14* (15), 3752–3757.

(15) Cloete, K. J.; Jenčič, B.; Šmit, Ž.; Kelemen, M.; Mkentane, K.; Pelicon, P. Detection of Lithium in Scalp Hair by Time-of-Flight Secondary Ion Mass Spectrometry with High Energy (MeV) Primary Ions. *Anal. Methods* 2017, *9*, 5249–5253.

(16) Sweilam, M. N.; Varcoe, J. R.; Crean, C. Fabrication and Optimization of Fiber-Based Lithium Sensor: A Step toward Wearable Sensors for Lithium Drug Monitoring in Interstitial Fluid. *ACS Sensors* 2018, *3* (9), 1802–1810.

(17) Novell, M.; Guinovart, T.; Blondeau, P.; Rius, F. X.; Andrade, F. J. A Paper-Based Potentiometric Cell for Decentralized Monitoring of Li Levels in Whole Blood. *Lab Chip* 2014, *14* (7), 1308–1314.

(18) Kadian, S.; Arya, B. D.; Kumar, S.; Sharma, S. N.; Chauhan, R. P.; Srivastava, A.; Chandra,

P.; Singh, S. P. Synthesis and Application of PHT-TiO_2 Nanohybrid for Amperometric Glucose Detection in Human Saliva Sample. *Electroanalysis* 2018, *30* (11), 2793–2802.

(19) Gugoasa, L. A.; Stefan-van Staden, R.-I.; van Staden, J. F.; Coroș, M.; Pruneanu, S. Electrochemical Determination of Bisphenol A in Saliva by a Novel Three-Dimensional (3D) Printed Gold-Reduced Graphene Oxide (RGO) Composite Paste Electrode. *Anal. Lett.* 2019, 1–24.

(20) Ngamchuea, K.; Batchelor-McAuley, C.; Compton, R. G. The Fate of Silver Nanoparticles in Authentic Human Saliva. *Nanotoxicology* 2018, *12* (4), 305–311.

(21) Hardcastle, J. L.; West, C. E.; Compton, R. G. The Membrane Free Sonoelectroanalytical Determination of Trace Levels of Lead and Cadmium in Human Saliva. *Analyst* 2002, *127*, 1495–1501.

(22) Khairy, M.; Kadara, R. O.; Kampouris, D. K.; Banks, C. E. In Situ Bismuth Film Modified Screen Printed Electrodes for the Bio-Monitoring of Cadmium in Oral (Saliva) Fluid. *Anal. Methods* 2010, *2* (6), 645–649.

(23) Kämäräinen, S.; Mäki, M.; Tolonen, T.; Palleschi, G.; Virtanen, V.; Micheli, L.; Sesay, A. M. Disposable Electrochemical Immunosensor for Cortisol Determination in Human Saliva. *Talanta* 2018, *188*, 50–57.

(24) Pasha, S. K.; Kaushik, A.; Vasudev, A.; Snipes, S. A.; Bhansali, S. Electrochemical Immunosensing of Saliva Cortisol. *J. Electrochem. Soc.* 2014, *161* (2), B3077–B3082.

(25) Goodwin, A.; Banks, C. E.; Compton, R. G. Tagging of Model Amphetamines with Sodium 1,2-Naphthoquinone-4-Sulfonate: Application to the Indirect Electrochemical Detection of Amphetamines in Oral (Saliva) Fluid. *Electroanalysis* 2006, *18* (18), 1833–1837.

(26) Ponnaiah, S. K.; Prakash, P.; Vellaichamy, B.; Paulmony, T.; Selvanathan, R. Picomolar-Level Electrochemical Detection of Thiocyanate in the Saliva Samples of Smokers and Non-Smokers of Tobacco Using Carbon Dots Doped Fe_3O_4 Nanocomposite Embedded on g-C_3N_4 Nanosheets. *Electrochim. Acta* 2018, *283*, 914–921.

(27) Goodwin, A.; Banks, C. E.; Compton, R. G. Graphite Micropowder Modified with 4-Amino-2,6-Diphenylphenol Supported on Basal Plane Pyrolytic Graphite Electrodes: Micro Sensing Platforms for the Indirect Electrochemical Detection of Δ^9-Tetrahydrocannabinol in Saliva. *Electroanalysis* 2006, *18* (11), 1063–1067.

(28) Lee, P. T.; Compton, R. G. Electrochemical Determination of Free and Total Glutathione in Human Saliva Samples. *Sensors Actuators, B Chem.* 2015, *221*, 962–968.

(29) Ngamchuea, K.; Batchelor-McAuley, C.; Cowen, P. J.; Williams, C.; Gonçalves, L. M.; Compton, R. G. Can Saliva Testing Replace Blood Measurements for Health Monitoring? Insights from a Correlation Study of Salivary and Whole Blood Glutathione in Humans. *Analyst* 2016, *141* (15), 4707–4712.

(30) Ngamchuea, K.; Batchelor-McAuley, C.; Compton, R. G. Understanding Electroanalytical Measurements in Authentic Human Saliva Leading to the Detection of Salivary Uric Acid. *Sensors Actuators, B Chem.* 2018, *262*, 404–410.

(31) dos Santos, W. T. P.; Amin, H. M. A.; Compton, R. G. A Nano-Carbon Electrode Optimized for Adsorptive Stripping Voltammetry: Application to Detection of the Stimulant Selegiline in Authentic Saliva. *Sensors Actuators, B Chem.* 2019, *279*, 433–439.

(32) dos Santos, W. T. P.; Compton, R. G. A Simple Method to Detect the Stimulant Modafinil in Authentic Saliva Using a Carbon-Nanotube Screen-Printed Electrode with Adsorptive Stripping Voltammetry. *Sensors Actuators B Chem.* 2019, *285*, 137–144.

(33) Zhu, Q.; Zheng, S.; Lu, X.; Wan, Y.; Chen, Q.; Yang, J.; Zhang, L.; Lu, Z. Improved Cycle Performance of $LiMn_2O_4$ Cathode Material for Aqueous Rechargeable Lithium Battery by LaF_3 Coating. *J. Alloys Compd.* 2016, *654*, 384–391.

(34) Özgür, C. Preparation, and Characterization of LiMn2O4 Ion-Sieve with High Li^+ Adsorption Rate by Ultrasonic Spray Pyrolysis. *Solid State Ionics* 2010, *181* (31), 1425–1428.

(35) Ryu, T.; Shin, J.; Ghoreishian, S. M.; Chung, K.-S.; Huh, Y. S. Recovery of Lithium in Seawater Using a Titanium Intercalated Lithium Manganese Oxide Composite. *Hydrometallurgy* 2019, *184*, 22–28.

(36) Zampardi, G.; Batchelor-McAuley, C.; Kätelhön, E.; Compton, R. G. Lithium-Ion-Transfer Kinetics of Single $LiMn_2O_4$ Particles. *Angew. Chemie* 2017, *129* (2), 656–659.

(37) Zdrachek, E.; Bakker, E. Potentiometric Sensing. *Anal. Chem.* 2019, *91* (1), 2–26.

(38) Synthetic Urine e.K. www.synthetic-urine.de/en/produkt/synthetic-saliva-din-53160-1-din-en-6462006-07/. Accessed on 14 August 2019.

(39) Elagli, K.; Traisnel, M.; Hildebrand, H. F. Electrochemical Behaviour of Titanium and Dental Alloys in Artificial Saliva. *Electrochim. Acta* 1993, *38* (13), 1769–1774.

(40) Meyer, J.-M. Corrosion Resistance of Nickel-Chromium Dental Casting Alloys. *Corros. Sci.* 1977, *17* (12), 971–982.

(41) Gal, J.-Y.; Fovet, Y.; Adib-Yadzi, M. About a Synthetic Saliva for in Vitro Studies. *Talanta* 2001, *53* (6), 1103–1115.

(42) Klimek, J.; Hellwig, E.; Ahrens, G. Fluoride Taken Up by Plaque, by the Underlying Enamel and by Clean Enamel from Three Fluoride Compounds in Vitro. *Caries Res.* 1982, *16* (2), 156–161.

(43) Shellis, R. P. A Synthetic Saliva for Cultural Studies of Dental Plaque. *Arch. Oral Biol.* 1978, *23* (6), 485–489.

Chapter 9

Overall Conclusions

The motivation behind a significant proportion of the works reported in this thesis is the increasing awareness of the toxicity of particular metal ions and the known associated risks to the human body and environment. This thesis has addressed specific sensing strategies of detecting and quantifying different toxic metal ions (Hg^{2+}, Al^{3+}, Zn^{2+}, and Li^{+}) in aqueous solutions including real-world samples. It has been shown that these metal ions can be determined sensitively and selectively by voltammetric methods with specific sensing protocols.

A sensor for inorganic Hg^{2+} was achieved by monitoring the change in the AgNPs stripping peak with Hg^{2+} presence in the analyte, resulting from the galvanic displacement of silver by mercury under suitable applied potential. The measurable lower limit of 100.0 pM more than meets the guideline value set by the World Health Organization (WHO) of 30.0 nM for Hg^{2+} in drinking water.

A sensor for Al^{3+} or Hg^{2+} was achieved by utilizing tannic acid (TA)-capped gold nanoparticles-modified carbon electrodes through complexation and by employing square wave voltammetry (SWV) using a suitable starting potential during voltammetry, which controls which species are taken up by the TA capping agent and/or are electrochemically visible. The starting potential and optimization of SWV parameters become essential to achieve selectivity between Al^{3+}, Hg^{2+}, and Zn^{2+} and to eliminate other possible interference ions. Meanwhile, the nano-impacts method has successfully characterized the role of TA capping agents in the detection of metal ions.

The TA has been shown to markedly control the redox activity of the gold nanoparticle, prior to and after the complexation with metal ions. The nano-impacts method shows how the TA complexes with Zn^{2+} and Hg^{2+} in a reversible and Langmuirian manner in both cases. The sensitivity of detection is thus determined by the amount of TA capping agent present on the gold nanoparticles. The measurable lower limit of 10.0 pM and 100.0 fM were achieved for Al^{3+} and Hg^{2+}, respectively. These sensor sensibility meet the permissible level of 7.4 μM and 30.0 nM for inorganic Al^{3+} and Hg^{2+} in drinking water as defined by the World Health Organization (WHO), respectively.

The nano-impacts method also has successfully characterized the reactivity and mechanism of gold nanoparticle dissolution at the single-particle level in cyanide-containing solution, drawing contrasts to what is seen at the nanoparticle ensemble level. The result shows that ensembles of AuNPs@CA undergo the partial oxidation (incomplete stripping) through various KCN concentrations studied. Meanwhile, at the single-particle level, nearly complete oxidation of the gold nanoparticle was achieved at ≥35.0 mM KCN and at an applied potential of 1.0 V vs SCE.

A sensor for Li^{+} determination in authentic human saliva was successfully developed using a lithium manganese oxide ($LiMn_2O_4$)-modified screen-printed electrode. The sensor realizes a low cost, fast analysis and high reproducibility and applicability for routine monitoring purposes. With the non-invasive sampling approach, the sensor can be used directly by either patients or clinicians.

All these original findings and developed sensing protocols have generic values that contribute notably to the field of electroanalysis. Recent advances in this field have brought us closer to replacing conventional analytical methods with excellent voltammetric techniques, providing simplified sensing platforms for in situ determination of toxic metal ions in the real world samples.

Appendix A. Calculation Details

A.1. Calculation Details for Chapter 3

A.1.1. Expected Charge of Silver Stripping Peak

The lognormal distribution of the particle size gave a mean radius, r_p, of 11.9 (*/2.2) nm. The amount of AgNPs (in mole), $N_{NP,}$ is calculated as follows

$$N_{NP} = \frac{\rho . V_{NP}}{Ar}$$

where ρ is the density of silver (10.5 x 10^6 g m^{-3}), Ar is the atomic mass of silver (107.9 g mol^{-1}) and V_{NP} is the volume of a single nanoparticle, calculated as:

$$V_{NP} = \frac{4}{3}\pi . r_p{}^3$$

A N_{NP} was calculated to be 7.1 x 10^{-24} moles or 4.3 x 10^5 of silver atoms (Avogadro's number, 1 mole = 6.022 x 10^{23} atoms) in a single nanoparticle.

A known concentration of AgNPs suspension is 5.0 x 10^{15} particles dm^{-3}. Therefore, an expected (theoretical) number of AgNPs in 5.0 μL of drop cast is

Drop cast volume * [AgNPs suspension]

= 5.0 x10^{-6} dm^3 * (5.0 x 10^{15} particles dm^{-3})

= ca. 2.5 x 10^{10} particles.

Therefore, a total number of silver atoms (the number of species undergoing electrochemical processes) is calculated as

= Number of AgNPs * (number of silver atom per single AgNPs)

= 2.5 x 10^{10} particles * (4.3 x 10^5 silver atoms $particle^{-1}$)

= ca. 1.1 x 10^{16} Ag atoms.

An expected (theoretical) charge, Q, assuming that each silver atom transfers one electron, e^- = 1.602 x 10^{-19} C, is found to be ca. 1.8 mC as calculated from:

Number of silver atom * (1.602 x 10^{-19} C $atom^{-1}$)

A.1.2. Surface Coverage

The mean radius of GCE, r_e, is 1.48 ± 0.02 mm and the mean radius of AgNPs is 11.9 (*/2.2) nm. The surface area of GCE, A_e, is calculated as below:

$A_e = \pi r_e^2$ * (close packing of 91%)

= $\pi(1.48 \times 10^{-3}\ m)^2 * 91\%$

= 6.2 x 10^{-6} m^2.

The surface area of single silver nanoparticle, A_{NP}, calculated as $\pi.r_e^2$

= $\pi(1.19 \times 10^{-10}\ m)^2$

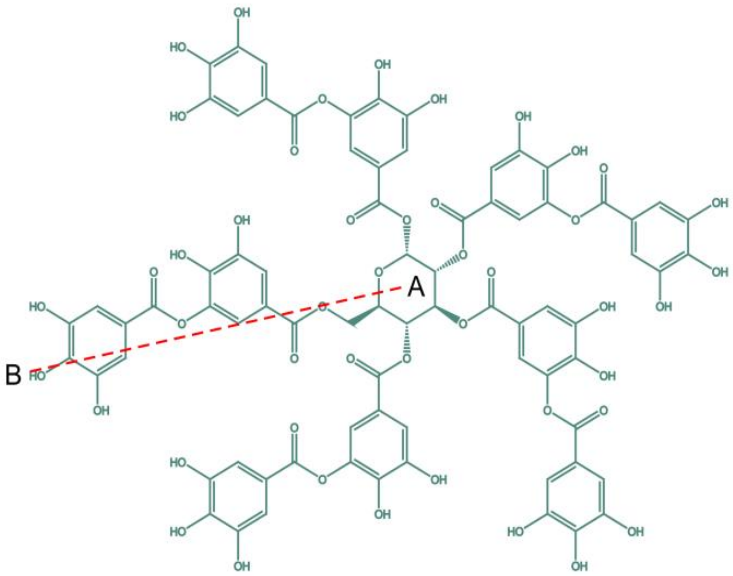
= 4.45 x 10^{-16} m^2.

The total number of AgNPs occupied the GCE surface for approximately one-monolayer surface coverage is calculated by dividing A_e with A_{NP}, and found to be approximately 1.43 x 10^{10} nanoparticles (ca. one-monolayer). Therefore, a surface coverage for 5.0 μL drop cast of AgNPs suspension onto the GCE surface is

$$\frac{\text{Number of AgNPs in 5.0 μL drop cast}}{\text{Number of AgNPs for one} - \text{monolayer}} \times \text{monolayer}$$

Surface coverage $= \frac{2.5 \times 10^{10}\ \text{particles}}{1.43 \times 10^{10}\ \text{particles}}$ * monolayer = ca. 1.75-monolayer.

A.2. Calculation Details for Chapter 4 and Chapter 5



An estimated effective radius of a single tannic acid (TA) molecule was approximately determined by measuring the length from its center (denoted as "*A*") to one of its hydroxyl groups (denoted as "*B*") based on the known bond lengths and angles. The length of *A to B* was measured to be ca. 1.3 nm. The surface area of a single molecule of tannic acid, A_{TA}, crudely estimate that molecule is symmetrical and planar, is calculated as $[2 * (1.3 \times 10^{-9}\ m)]^2$, which is ca. $6.46 \times 10^{-18}\ m^2$.

A mean diameter size distribution of single AuNPs@TA, according to SEM micrographs, is 60.0 ± 3.0 nm. The surface area of a single nanoparticle, A_{NP}, is calculated as $4\pi(30 \times 10^{-9}\ m)^2$, which is ca. $1.13 \times 10^{-14}\ m^2$.

The amount of TA in one-monolayer surface coverage of single nanoparticle is calculated as follow,

$$\frac{\text{The surface area of a single AuNPs@TA } (A_{NP})}{\text{The surface area of a singe TA } (A_{TA})}$$

$$= \frac{1.13 \times 10^{-14}\ m^2}{6.46 \times 10^{-18}\ m^2}$$

= ca. 1,750 TA molecules occupied per single nanoparticle.

An expected (theoretical) amount of AuNPs@TA for one-monolayer surface coverage of GCE is calculated as follow:

$$\frac{\text{The surface area of GCE } (A_e)}{\text{The surface area of a single AuNPs@TA } (A_{NP})}$$

$$= \frac{6.2 \times 10^{-6}\ m^2}{1.1 \times 10^{-14}\ m^2}$$

= ca. 5.6×10^8 nanoparticles.

An expected (theoretical) number of TA molecules associated with a one-monolayer coverage of nanoparticles is then calculated as follow

= 1,750 TA molecules per nanoparticle * (5.7×10^8 nanoparticles)

= ca. 1.0×10^{12} molecules.

An expected (theoretical) charge, Q, for one-monolayer surface coverage and assuming that each TA molecule transfers one electron (e^- = 1.602×10^{-19} C), is calculated as Q = number of TA molecule * 1.602×10^{-19} C, which is ca. 0.16 μC.

Drop cast mass needed to make one-monolayer coverage is calculated as follow:

$$\frac{\text{Expected number of AuNPs@TA for one} - \text{monolayer coverage}}{\text{The concentration of AuNPs@TA suspension (indicated by the manufacturer)}}$$

$$= \frac{5.6 \times 10^8 \text{ nanoparticles}}{2.2 \times 10^{10} \text{ nanoparticles mL}^{-1}}$$

= ca. 25.0 μL.

Relative Error Calculations

1) Standard error of linear regression for quantification of Al^{3+} ions, $[Al^{3+}] = y$

   Error progression calculation, $\Delta[Al^{3+}]$, is calculated as follow

$$\Delta[Al^{3+}] = \frac{\partial(10^y)}{\partial y}\,\Delta y$$

$$\Delta[Al^{3+}] = \ln 10 * 10^y * \Delta y$$

$$\Delta[Al^{3+}] = 2.303 * [Al^{3+}] * \Delta y$$

$$\frac{\Delta[Al^{3+}]}{[Al^{3+}]} = 2.303 * \Delta y$$

$$\frac{\Delta[Al^{3+}]}{[Al^{3+}]} = 0.392$$

1) Standard error of linear regression for quantification of Hg^{2+} ions $[Hg^{2+}] = y$

Error progression calculation, $\Delta[Hg^{2+}]$, is calculated as follow

$$\Delta[Hg^{2+}] = \frac{\partial(10^y)}{\partial y}\,\Delta y$$

$$\Delta[Hg^{2+}] = \ln 10 * 10^y * \Delta y$$

$$\Delta[Hg^{2+}] = 2.303 * [Hg^{2+}] * \Delta y$$

$$\frac{\Delta[Hg^{2+}]}{[Hg^{2+}]} = 2.303 * \Delta y$$

$$\frac{\Delta[Hg^{2+}]}{[Hg^{2+}]} = 0.263$$

A.3. Calculation Details for Chapter 6

Concentration of AuNPs@TA suspension = 2.2 x 10^{10} particles mL^{-1}. Surface area of GCE (πr_e^2) = ca. 6.9 x 10^{-6} m^2 and mean radius of the core AuNP, r_p, is 31.1 nm.

A.3.1. Ensembles of AuNPs@TA (Cyclic Voltammetry)

Number of AuNPs@TA particles onto GCE surface for one-monolayer surface coverage, N_{NP}, considering closest packing of the equal sphere of 91%, is calculated as

$$N = 0.91 * \frac{\text{The surface area of GCE}}{\text{The surface area of AuNPs@TA}}$$

= ca. 2.0 x 10^9 particles.

Total surface area of AuNPs@TA drop casted onto GCE surface, A_{NP}, calculated as:

$A_{NP} = N*(4\pi r_p^2)$

= 2.0 x 10^9 particles * (1.2 x 10^{-14} m^2)

= ca. 2.4 x 10^{-5} m^2.

A.3.2. Single AuNPs@TA (Nano-impacts)

From the oxidative nano-impacts experiments with the absence of the metal cations (oxidation of TA capping agent), the experimental average spikes charge, Q, was found to be ca. 0.3 pC. The number of moles, n, of TA molecule involved in the reaction is calculated using Faraday's first law:

$$n = \frac{Q}{zF}$$

where z is the number of electron transfer during oxidation of TA (assuming fully oxidized, z = 20) and F is the Faraday's constant (96485.33 C mol^{-1}). The number of moles TA was found to be ca. 1.6 x 10^{-19} or equal to ca. 1.0 x 10^5 molecules.

The apparent number of TA molecules incorporated in a single core AuNP, N_{TA}, was calculated by dividing volume of core AuNP with known volume of a single TA molecule of 8.6 x 10^{-28} m^3 (B. Madhan, A. Dhathathreyan, V. Subramanian and T. Ramasami, *J. Chem. Sci.*, 2003, 115, 751–766).

$$N_{TA} = \frac{1.07 \text{ x } 10^{-22} \text{ m}^3}{8.6 \text{ x } 10^{-28} \text{ m}^3}$$

= **ca. 1.2 x 10^5 molecules**

A.3.3. Underpotential deposition of Zinc onto Ensembles of AuNPs@TA

From CV experiments, the reductive charge of the Zn (UPD), *Q*, is ca. 17.2 μC. An effective surface coverage of 0.2 mM Zn^{2+} UPD (considering $z = 2$) calculated as follow

$$= \frac{Q}{zFA} = \frac{17.2 \text{ x } 10^{-6} \text{ C}}{2 * 96485.33 \text{ C mol}^{-1} * 0.24 \text{ cm}^2}$$

= 3.7 x 10^{-10} mol cm^{-2} or approximately 2.2 x 10^{14} atoms cm^{-2}.

A.4. Calculation Details for Chapter 7

A known concentration of AuNPs@CA concentration is 2.6 x 10^{10} particles mL^{-1}

Average radius of AuNPs@CA (indicated from TEM sizing), r_p = 31.45 ± 1.33 nm

The volume of single-particle ($V_{NP} = \frac{4}{3}\pi r_p^3$) = 1.30 x 10^{-22} m^3

Estimate number of AuNPs@CA in one-monolayer surface coverage (considering closest packing of equal spheres 91%), N_{NP}, is calculated as follow

$$N_{NP} = \frac{\text{Surface area of GCE } (6.26 \text{ x } 10^{-6} \text{ m}^2)}{\text{The surface area of the single AuNPs@CA } (1.12 \text{ x } 10^{-14} \text{ m}^2)} * 91\%$$

= ca. 5.1 x 10^8 particles.

Drop cast mass needed to make one-monolayer coverage is calculated as follow

$$\text{Volume} = \frac{N_{NP}}{\text{The concentration of AuNPs@CA suspension}}$$

$$= \frac{5.1 \text{ x } 10^8 \text{ particles}}{2.6 \text{ x } 10^{10} \text{ particles mL}^{-1}}$$

= ca. 20.0 μL drop cast.

A.4.1. CV Experiments

An expected (theoretical) charge for a single AuNPs@CA, assuming 1e^- transfer and $z = 1$, is calculated as follow:

$$= \frac{\text{Density of Au} * \text{Volume of AuNPs@CA}}{\text{Atomic Mass of Au}} * z * F$$

$$= \frac{1.93 \times 10^{7}\ \text{g m}^{-3} * 1.30 \times 10^{-22}\ \text{m}^{3}}{1.97 \times 10^{2}\ \text{g mol}^{-1}} * 1 * 96485.3\ \text{C mol}^{-1}$$

= ca. 1.2×10^{-12} C per single particle of AuNP@CA.

An expected charge, *Q*, for one-monolayer surface coverage is calculated as follow

= 1.2×10^{-12} C particle^{-1} * 5.0×10^{8} particles

= ca. 600.0 μC.

The percent conversion is determined as a ratio between the experimental charge of the peak-2 recorded from the CV experiments and the expected charge for complete particle oxidative dissolution. The results can be found in Table 1.

Table A.1. The percent conversion of the oxidized ensembles of AuNPs@CA.

[KCN] (mM)	Experimental Charge (Q_{Exp})	% Converted AuNPs@CA
1.0	9.6 μC	ca. 1.6%
5.0	12.5 μC	ca. 2.1%
15.0	28.7 μC	ca. 4.8%
35.0	37.1 μC	ca. 6.2%
50.0	47.0 μC	ca. 7.8%

A.4.2. Nano-impacts Experiments

The number of Au atom per particle:

$\left(\frac{\text{Density of Au} * V_{AuNP}}{\text{Atomic Mass of Au}}\right)$ * Avogadro's number = 7.6×10^{6} atoms per single particle

Number of Au particle added in the system

= 0.7 mL * 2.6×10^{10} particles mL^{-1}

= 1.8×10^{10} particles

The number of Au atoms (number of species undergoing electrochemical process) is

= 7.6 x 10^6 atoms per single particle * (1.8 x 10^{10} particles)

= ca. 1.4 x 10^{17} atoms.

Expected (maximum) charge for 0.7 mL of AuNPs@CA suspension (each atom transfers e^- = 1.602 x 10^{-19} C) is calculated as follow

= 1.4 x 10^{17} atoms * 1.602 x 10^{-19} C $atom^{-1}$

= ca. 0.02 C.

Expected charge, Q, for a single AuNPs@CA particle is calculated as follow

$$= \frac{0.02\ \text{C}}{1.8\ x\ 10^{10}\ \text{particle}}$$

= 1.1 x 10^{-12} C per single AuNPs@CA.

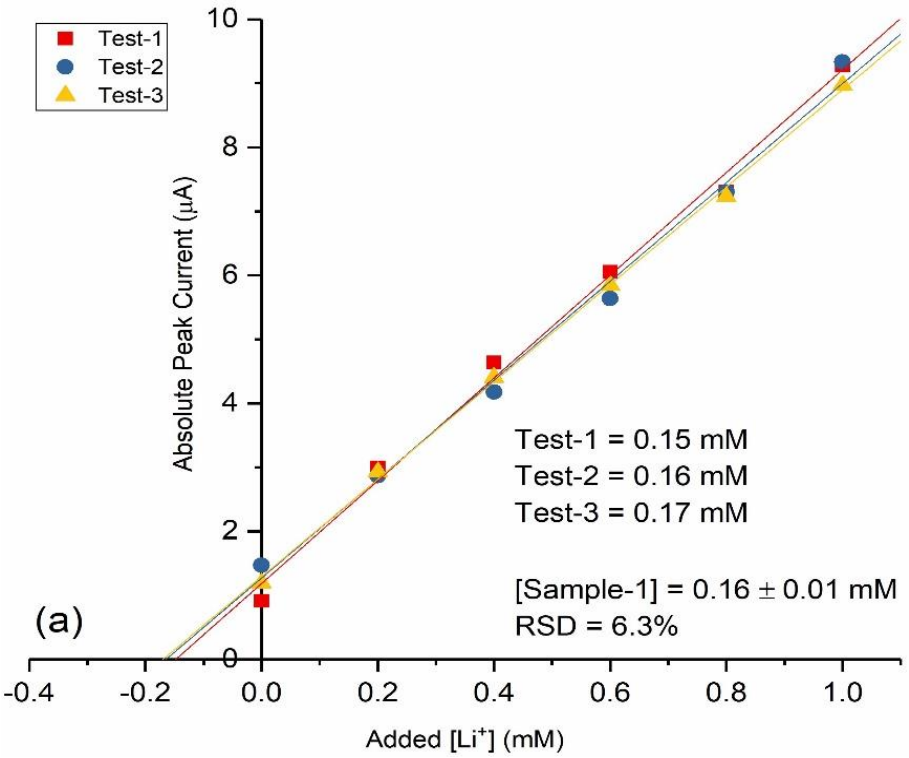
The ratio between the experimental nano-impacts and expected (maximum) charge values at the single-particle level was considered as the percent conversion of the oxidized AuNPs@CA. Table A.2 summarises the percent conversion of the single AuNP@CA level at different CN^- concentrations.

Table A.2. The percent conversion of the oxidized single AuNP@CA level.

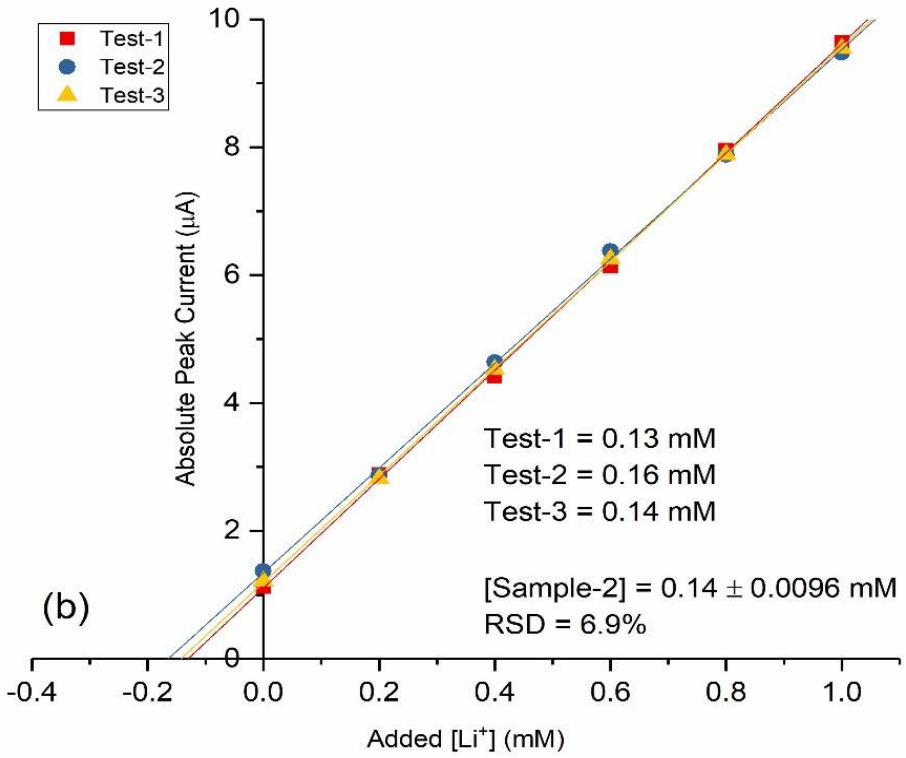
[KCN] (mM)	Experimental Charge (Q_{Exp})	% Converted AuNPs@CA
1.0	0.29 pC	ca. 26.4%
5.0	0.55 pC	ca. 50.0%
15.0	0.76 pC	ca. 69.1%
35.0	1.03 pC	ca. 93.6%
50.0	1.04 pC	ca. 94.2%

A.5. Calculation Details for Chapter 8

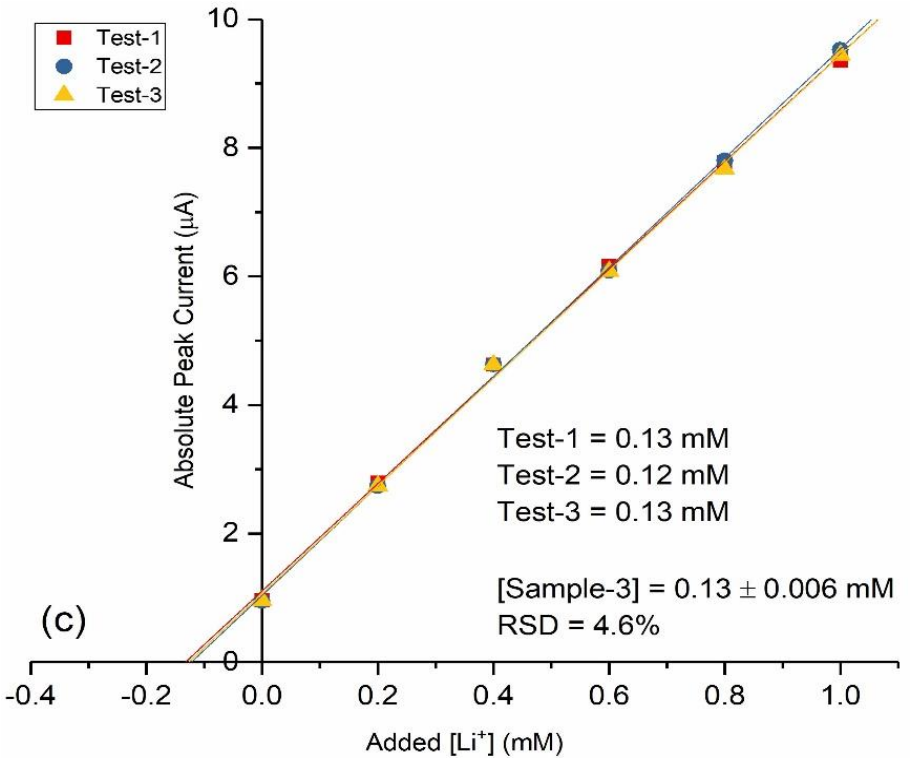
Linear plots between the absolute peak current value and different concentrations of Li^+-added authentic saliva, from the first three different samples, denoted as (a), (b) and (c), are presented (see below). The found concentration (Li^+ levels in the analyte) was calculated by dividing the intercept with the slope.



Equation	y = a + b*x		
Plot	|Peak Current|-1	|Peak Current|-2	|Peak Current|-3
Weight	No Weighting	No Weighting	No Weighting
Intercept	1.18E-6 ± 1.9E-7	1.27E-6 ± 1.94E-7	1.29E-6 ± 8.53E-8
Slope	8.03E-6 ± 3.14E-7	7.72E-6 ± 3.20E-7	7.61E-6 ± 1.41E-7
Sum of Squares	2.76936E-13	2.86108E-13	5.55436E-14
Pearson's r	0.9969	0.9966	0.9993
R-Square(COD)	0.9939	0.9932	0.9986
Adj. R-Square	0.9924	0.9915	0.9983



Equation	**y = a + b*x**		
Plot	|Peak Current|	|Peak Current|	|Peak Current|
Weight	No Weighting	No Weighting	No Weighting
Intercept	1.11E-6 ± 5.66E-8	1.34E-6 ± 6.54E-8	1.19E-6 ± 2.42E-8
Slope	8.51E-6 ± 9.34E-8	8.18E-6 ± 1.08E-7	8.37-6 ± 3.99E-8
Sum of Squares	2.44E-14	3.23E-14	4.46E-15
Pearson's r	0.9998	0.9997	0.9999
R-Square(COD)	0.9995	0.9993	0.9999
Adj. R-Square	0.9994	0.9991	0.9999



Equation	y = a + b*x		
Plot	|Peak Current|	|Peak Current|	|Peak Current|
Weight	No Weighting	No Weighting	No Weighting
Intercept	1.11E-6 ± 9.36E-8	1.04E-6 ± 7.94E-8	1.06E-6 ± 9.16E-8
Slope	8.35E-6 ± 1.54E-7	8.50E-6 ± 1.31E-7	8.39E-6 ± 1.51E-7
Sum of Squares	6.67E-14	4.81E-14	6.41E-14
Pearson's r	0.9993	0.9995	0.9994
R-Square(COD)	0.9986	0.9991	0.9987
Adj. R-Square	0.9983	0.9988	0.9984

Galvanostatic delithiation experiment

Surface area of the GCE (r_e = 1.48 ± 0.02 mm) is ca. 0.07 cm^2.

Surface area of the screen-printed electrode (r_e = 2.0 mm) is ca. 0.125 cm^2.

The current density (based on the geometrical area of the electrodes) in galvanostatic delithiation is 8.6 mA cm^{-2} (for LMO-GCE) or 80.0 μA cm^{-2} (for LMO-SPE).

Appendix B. Characterisation of the Materials

This appendix comprises a supplementary of the characterization result of the materials utilized within this thesis. Some results of the material characterization are also presented and discussed in the relevant chapter.

B.1. Characterization of Silver Nanoparticles (AgNPs)

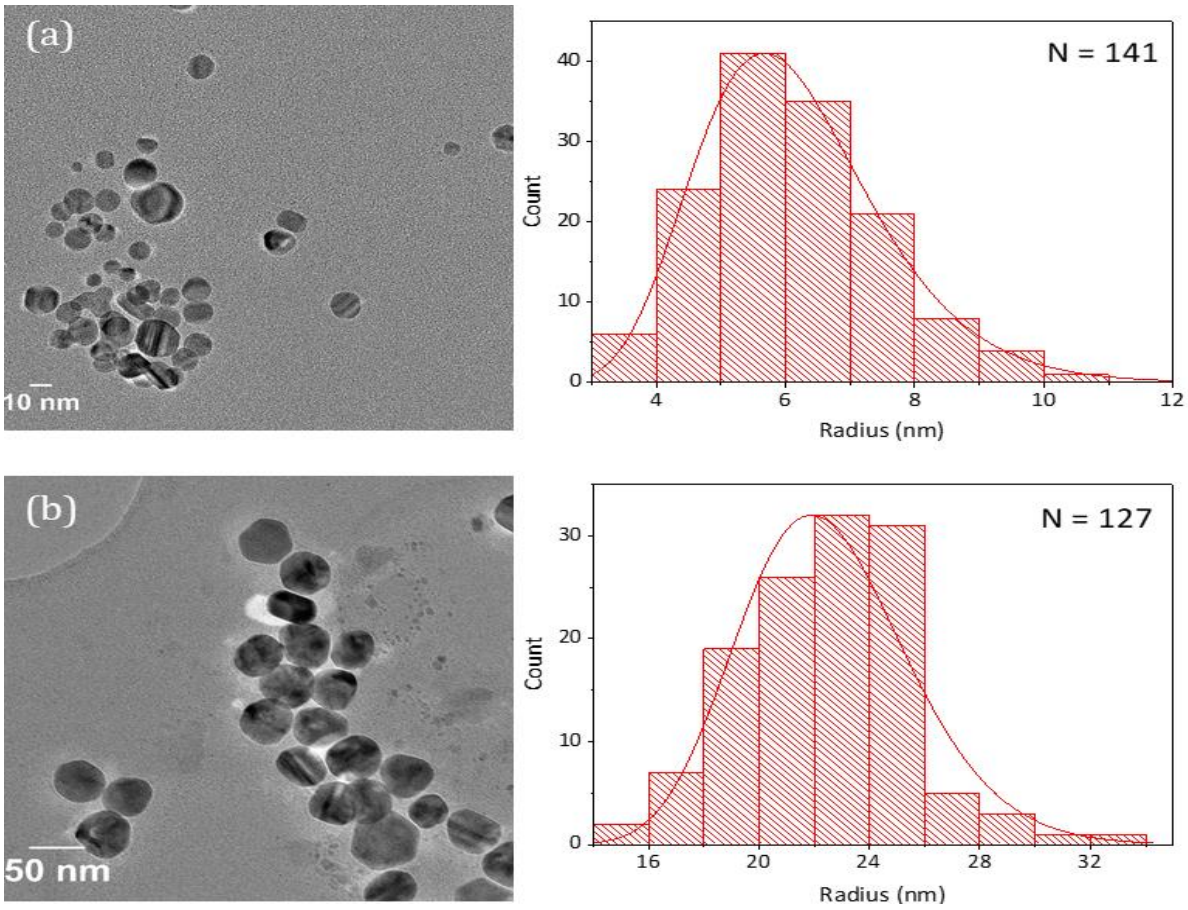


Figure B.1. TEM micrographs of citrate-capped silver nanoparticles (AgNPs) and sizing histograms displaying the statistical distribution of the particle size of (a) Batch "B" and (b) "nominally 50 nm diameter". A lognormal curve is used to fit the data. The AgNPs revealed a lognormal distribution of the particle size with a mean radius of 6.2 (*/1.5) nm and 22.5 (*/3.1) for Batch "B" and "nominally 50 nm diameter", respectively.

B.2. Characterization of Tannic Acid-capped Gold Nanoparticles

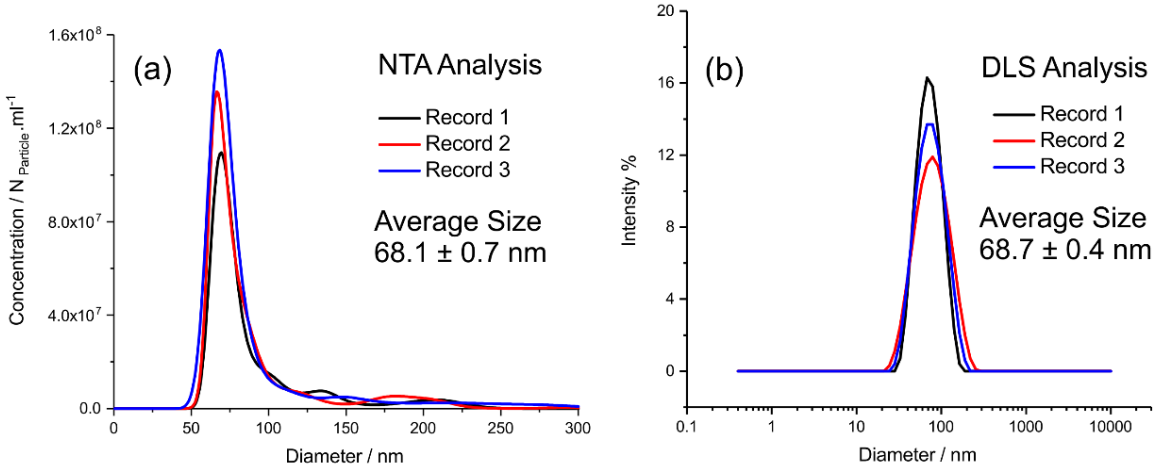


Figure B.2. Size characterization of the AuNPs@TA using (a) NTA and (b) DLS analysis.

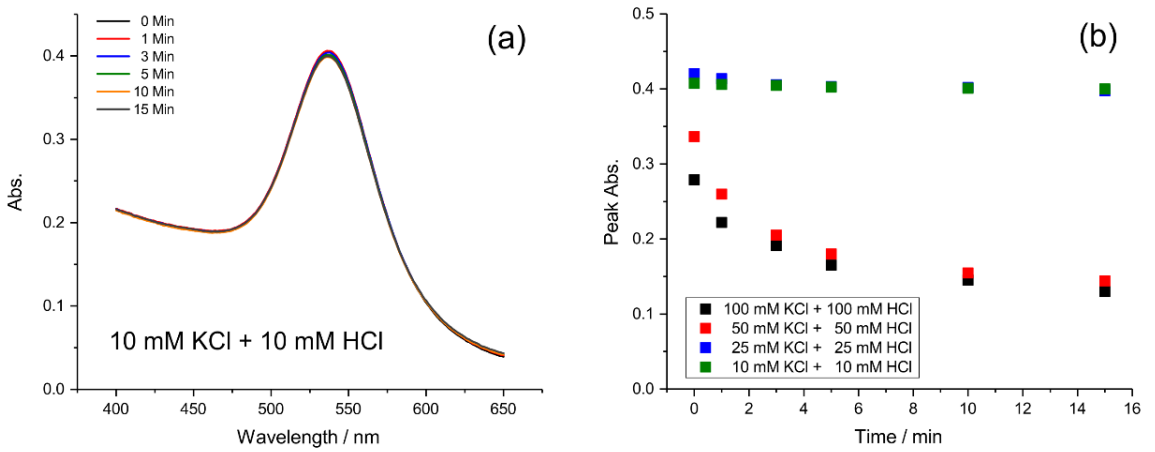


Figure B.3. UV-vis analysis of the AuNPs@TA. (a) UV-vis spectra of 10.0 pM AuNPs@TA suspension in a solution of 10.0 mM KCl + 10.0 mM HCl. (b) The plot of peak absorbance of AuNPs@TA in various electrolyte concentrations during 15 min measurement.

Zeta Potential analysis of the AuNPs@TA at 25 °C

Dispersant	Record	Zeta Potential (mV)	Mobility (µm cm/Vs)	Conductivity (mS cm^{-1})
Deionised Water	1	-30.9	-2.42	0.023
	2	-29.6	-2.40	0.025
	3	-32.2	-2.44	0.022
	Mean	**-30.9 ± 1.9**		

B.3. Characterization of Citrate-capped Gold Nanoparticles

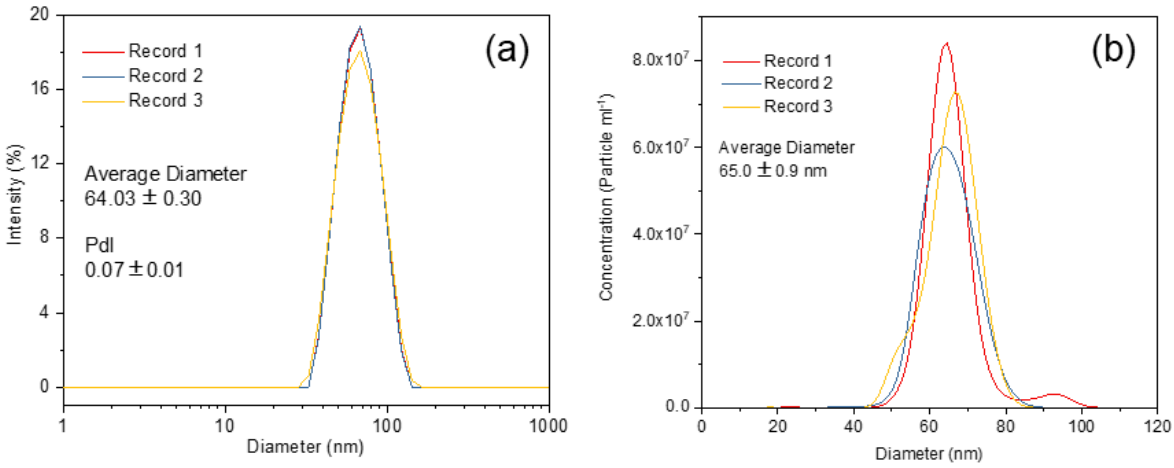


Figure B.5. Size characterization of the AuNPs@CA using (a) DLS and (b) NTA.

Zeta Potential analysis of the AuNPs@CA at 25 °C

Dispersant	Record	Zeta Potential (mV)	Mobility (µm cm/Vs)	Conductivity (mS/cm)
Deionised Water	1	-42.0	-3.29	0.004
	2	-42.6	-3.34	0.004
	3	-46.2	-3.62	0.004
	Mean	**-43.6 ± 2.3**		
10.0 mM NaOH	1	-44.8	-3.51	1.06
	2	-44.8	-3.52	1.110
	3	-47.2	-3.70	1.140
	Mean	**-45.6 ± 1.4**		
50.0 mM KCN + 10.0 mM NaOH	1	-36.1	-2.83	12.700
	2	-37.4	-2.93	13.000
	3	-36.6	-2.87	13.200
	Mean	**-36.7 ± 0.7**		

Appendix C. Nano-impacts Analysis

This appendix complements the nano-impacts analysis discussed in Chapter 6 (for AuNPs@TA) and Chapter 7 (for AuNPs@CA).

C.1. Nano-impacts Analysis of AuNPs@TA

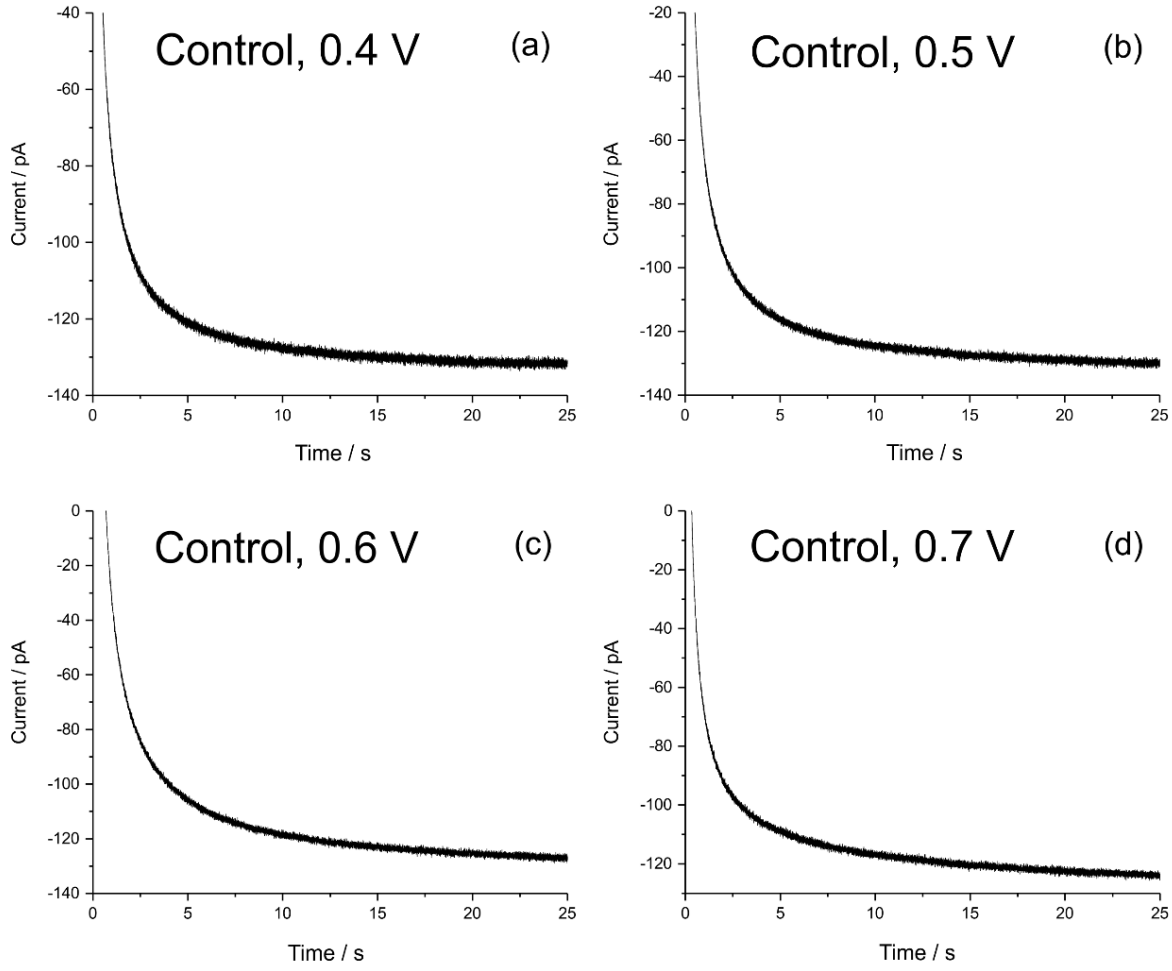


Figure C.1. Oxidative nano-impacts analysis of the AuNPs@TA. Representative chronoamperograms of microelectrode disc immersed in solution containing of 10.0 mM KCl + 10.0 mM HCl (blank solution) at applied potential of 0.4, 0.5, 0.6 and 0.7 V vs SCE.

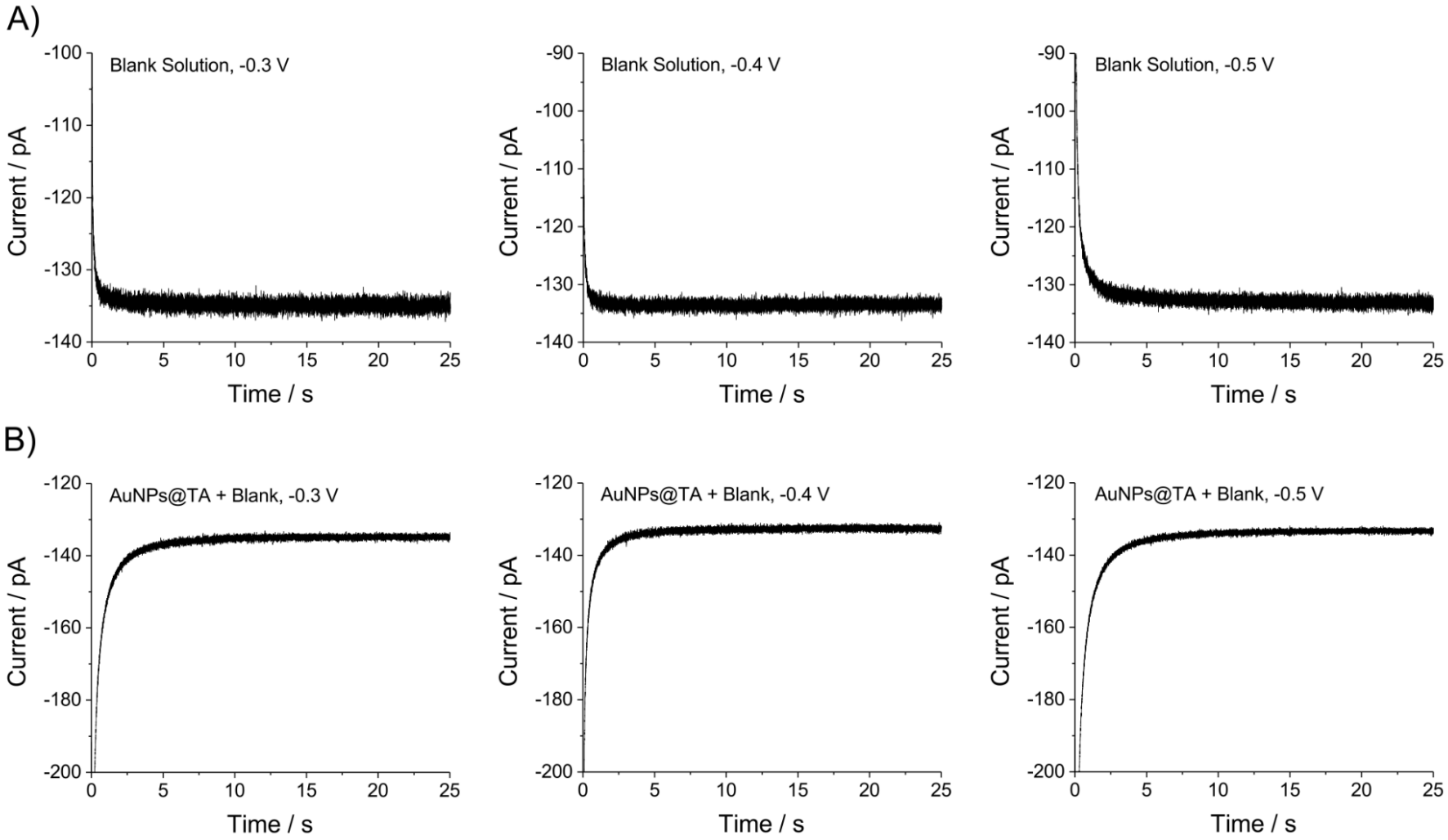


Figure C.2. Reductive nano-impacts analysis of AuNPs@TA. Representative chronoamperograms of carbon microelectrode immersed in solution containing of (a) 10.0 mM KCl + 10.0 mM HCl (blank solution) and (b) AuNPs@TA + blank at applied potential of -0.3, -0.4 and -0.5 V vs SCE.

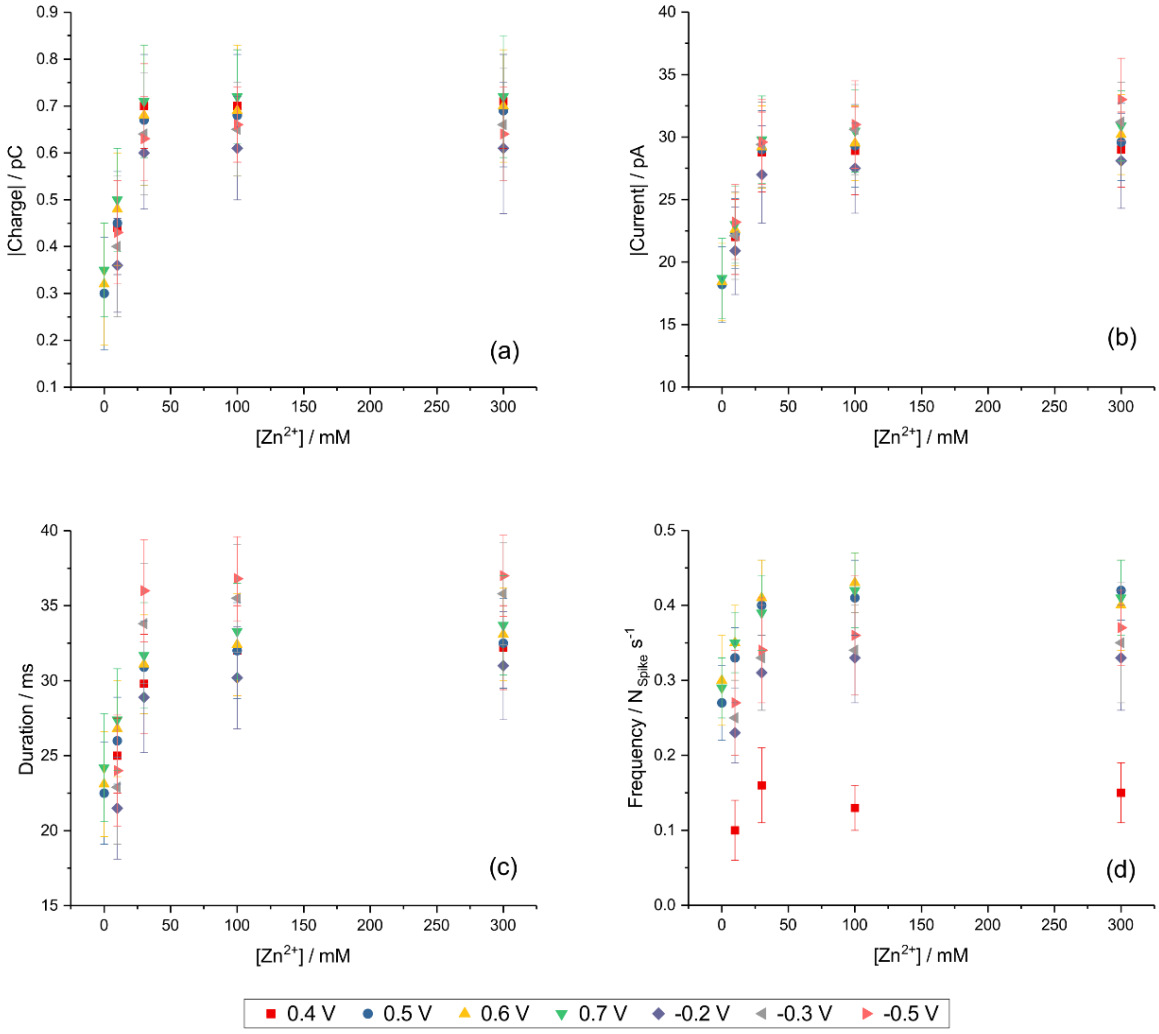


Figure C.3. The linear relationship between average spikes: (a) charge, (b) current, (c) duration and (d) frequency with different potentials at various Zn^{2+} concentrations, resulting from oxidative and reductive nano-impacts method.

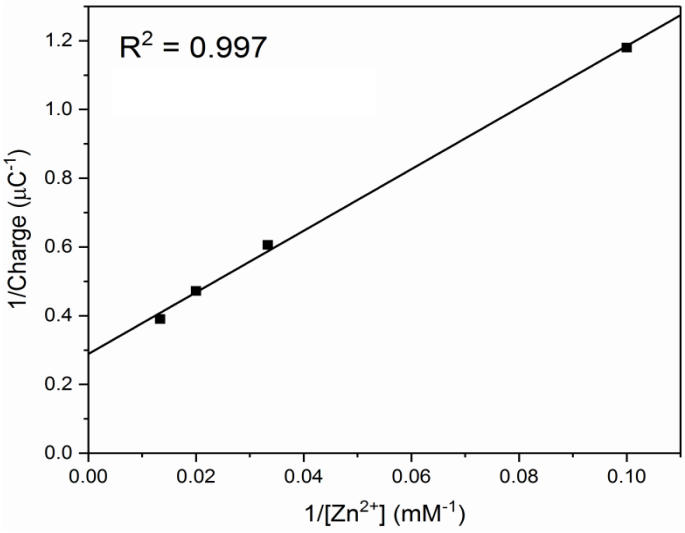


Figure C.4. Langmuir plot of Zn^{2+} on ensembles AuNPs@TA (before saturation).

C.2. Nano-impacts Analysis of AuNPs@CA

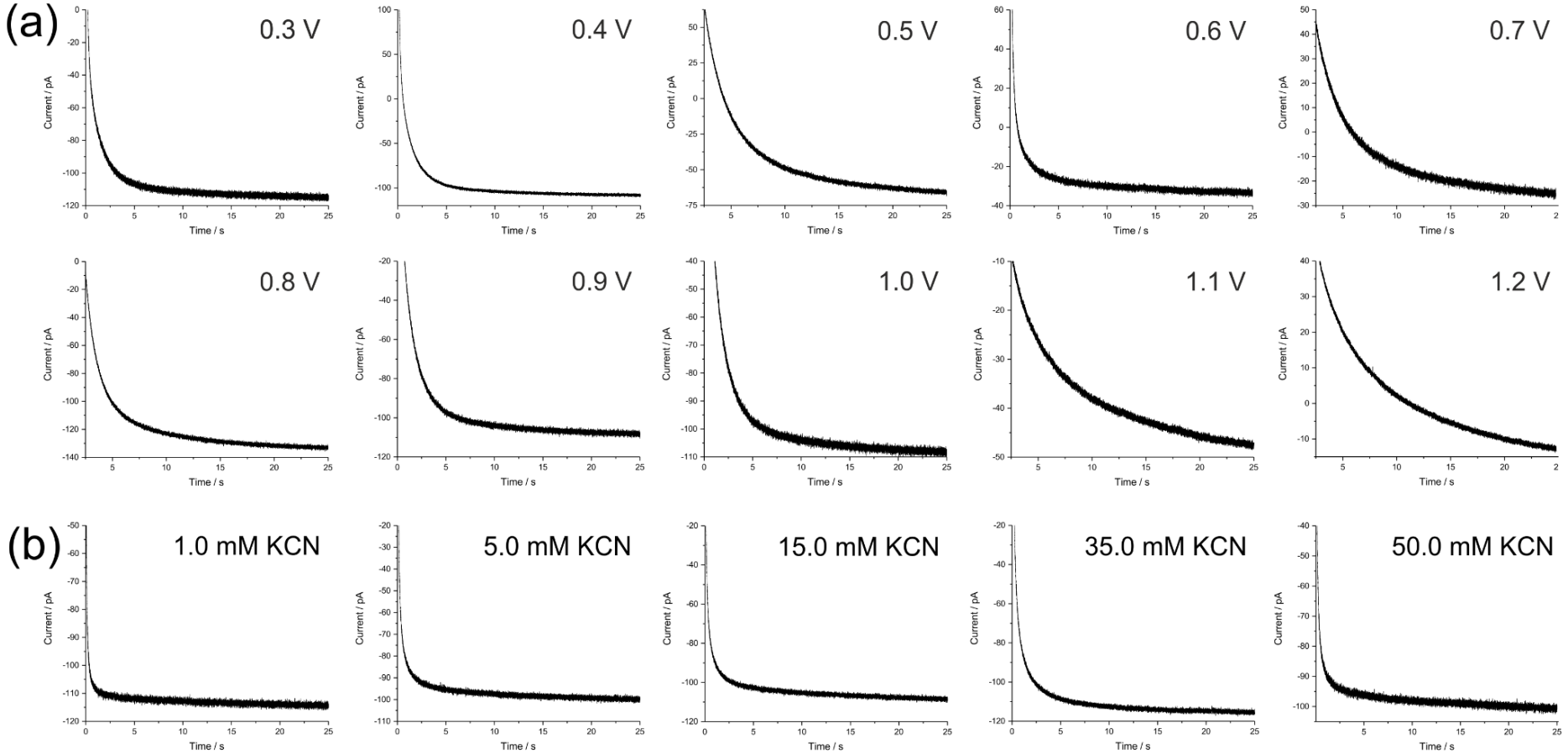


Figure C.5. Representative chronoamperograms of carbon microelectrode immersed in solution of (a) 42.0 pM AuNPs@CA + 10.0 mM NaOH at varying potential of 0.3 V to 1.2 V vs SCE. (b) 1.0 mM to 50.0 mM KCN + 10.0 mM NaOH at applied potential of 1.0 V.

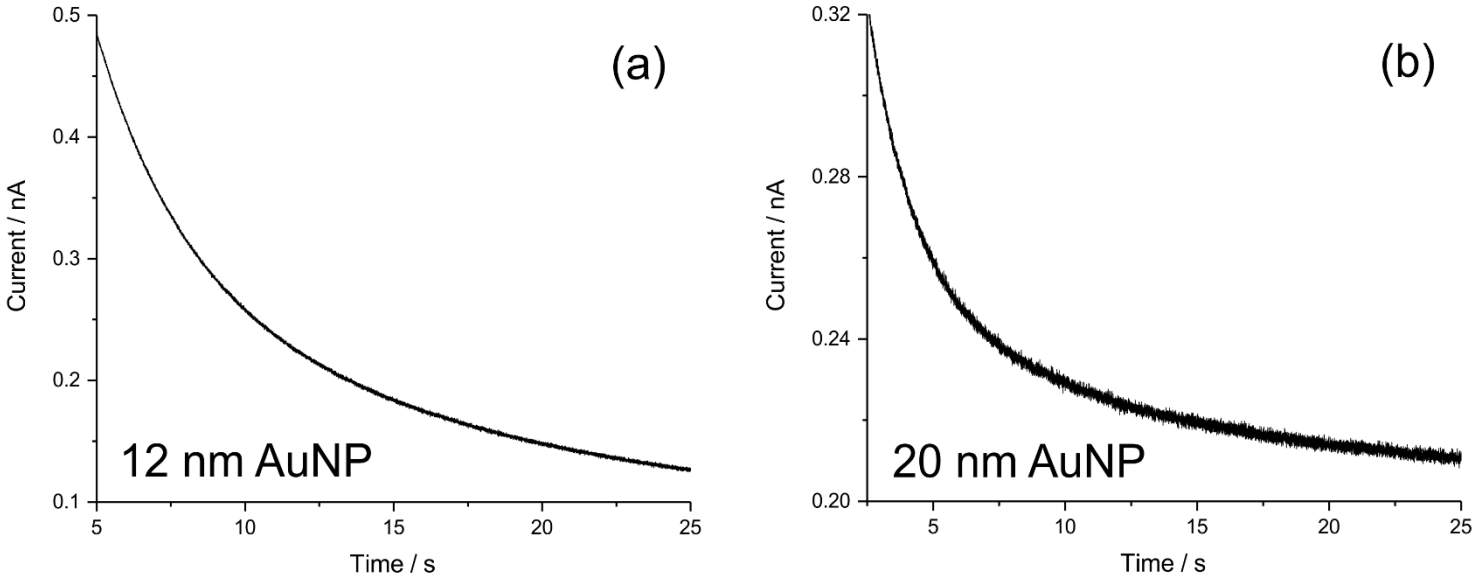


Figure C.6. Chronoamperograms of 42.0 pM AuNPs@CA added in 5.0 mM KCN + 10.0 mM NaOH at a potential of 1.0 V vs SCE. No spikes were observed at both (a) "nominally 12 nm diameter" and (b) "nominally 20 nm diameter" AuNPs@CA.

I have fought the good fight, I have finished the race, I have kept the faith.

2 Timothy 4:7 (NIV)

D.Phil. Viva Voce Examination

Internal Examiner : Prof. Dr. John S. Foord

External Examiner : Prof. Dr. Frank Marken (University of Bath, UK)

Date : 31st October 2019 (1.45-3.15 pm BST)

Place : St. Catherine's College

Soli Deo Gloria